UCSF
UC San Francisco Electronic Theses and Dissertations

Title

Distribution and dynamics of DNA topoisomerase II in drosophila chromosomes

Permalink

https://escholarship.org/uc/item/2fg0t422

Author

Swedlow, Jason R.

Publication Date

1994

Peer reviewed|Thesis/dissertation

eScholarship.org
Powered by the California Digital Library
University of California

DISTRIBUTION AND DYNAMICS OF DNA TOPOISOMERASE II IN DROSOPHILA CHROMOSOMES

by

JASON R. SWEDLOW

DISSERTATION

Submitted in partial satisfaction of the requirements for the degree of

DOCTOR OF PHILOSOPHY

in

BIOPHYSICS

in the

GRADUATE DIVISION

of the

UNIVERSITY OF CALIFORNIA

San Francisco

[redacted]

Preface

Much of the data presented in the fifth chapter of this thesis has been published as Swedlow, J. R., Sedat, J. W. and Agard, D. A. (1993). Multiple chromosomal populations of topoisomerase II detected in vivo by time-lapse, three-dimensional wide field microscopy. Cell *73*, 97-108 and is reprinted here by permission. Chapter 3 will be submitted for publication to the Journal of Microscopy. Parts of Chapter 4 will be submitted to the Journal of Cell Biology.

Dedication

This work is dedicated to the memory of my father, Jerold L. Swedlow, my grandfather, Philip F. Lauer, my grandmother, Rose Lauer, and my great uncle, David Swedlow, all of whom passed away while this work was in progress. Throughout my life, they were my guiding lights: they encouraged me to do only the best that I could, and to keep a sense of humor in the process. I miss them terribly, and hope that this work stands as a symbol of what they taught me.

Acknowledgments

No six and a half year enterprise is accomplished by one person alone. Many people and institutions have contributed directly and indirectly to this work. I feel the utmost appreciation and gratitude to all those who have helped me during the last years. I especially thank:

The National Institutes of Health and The Howard Hughes Medical Institute for funding;

David Agard for answering all the questions, providing the right guidance at the right time, sending me to all the meetings, and being a friend;

John Sedat for allowing me to reside in his lab and sharing daily guidance, thoughts, wierd jokes, and a truly exceptional view of life;

Neil Osheroff for providing topoisomerase II and anti-topoisomerase II antibody, and discussions about topoisomerase II purification;

Tim Karr for doing the fusions;

Hans Chen, Mel Jones, Angus McDonald, Warren Clyborne, Diana Diggs, Paul Chan, and Bill Stock for not driving a stake through my heart, but instead helping to fix hardware and software;

Sue Parmelee for taking care of everything and smiling on (some of) even of the worst days;

Jennifer Fung for tolerating the EM jokes and coaching the volleyball team;

Abby Dernburg for being messier than I and a joy to work with, and for collaborating;

Wallace Marshall for mathematical rigor and an introduction to death metal;

Yoji Urata for an introduction to Kanji and the suggestion of bleed-through alignment;

Hirosumi Itoi for sharing good sushi and the woes of microinjection;

Michael Paddy for sharing a bench and lots of programs;

Yasushi Hiraoka for help learning the microscopy ropes;

Olga Ionescu for faithfully cleaning all the glassware;

John Addison for keeping the flies healthy and fecund;

David and Sandy Swedlow for their love and support;

Chuck Wilson, Lydia Gregoret, Brian Shoichet, Leslie Taylor, John Altman, Abby Dernburg, Jeremy Minshull, Nicole Valtz, and Ted Lowenkopf for friendship, warmth, and understanding;

Jerold, Patricia, Pam and Kathy Swedlow for proving that blood is thicker than anything;

My wife and best friend, Inke Näthke, for sharing the best and worst of times, and everything in between;

My son Jan, for always smiling, no matter how late I came home.

The Distribution and Dynamics of Topoisomerase II in *Drosophila* Chromosomes

Jason R. Swedlow

Abstract

DNA topoisomerase II catalyzes the passage of DNA strands through one another and is required for proper chromosome condensation and segregation. The enzyme is localized at the bases of "radial loops" of DNA in histone-depleted chromosomes. This work describes the localization of topoisomerase II *in vivo* and *in situ*. For *in vivo* studies, purified *Drosophila* topoisomerase II was conjugated with tetramethylrhodamine using a protocol that produced labeled, active enzyme, and microinjected into nuclear cycle 9-10 *Drosophila* embryos. Time-lapse three-dimensional movies of these embryos were then recorded with a CCD-based, wide field optical sectioning fluorescence microscope. For *in situ* localization, enzyme distribution relative to chromatin and DNA in fixed embryos was measured by immunofluorescence and recorded with the three-dimensional microscope. Topoisomerase II is distributed throughout the interphase nucleus, and is also concentrated in at least one, but no more than two sites on the periphery of each nucleus. These sites disappear as nuclei enter prophase and chromosomes condense. During mitosis, topoisomerase II was not localized to an axial chromosome core, but instead was distributed throughout the chromosome. Approximately 60% of the enzyme present in the early prophase chromosome leaves and diffuses into the cytoplasm during prophase and prometaphase. During the transition from metaphase to anaphase, the concentration of chromosomal topoisomerase II decreases by another 10%. The prophase and anaphase transitions occur immediately after the completion of chromosome condensation and segregation and suggest that separate populations of enzyme are responsible for these activities. The distribution of topoisomerase II along the chromosome arm is similar to that of chromatin and DNA at prophase; the mitotic loss of topoisomerase II leaves a distribution at anaphase that significantly differs from that of chromatin and DNA. This suggests that topoisomerase II decorates all parts of the chromosome during chromosome condensation, possibly to ensure adequate strand passing activity during condensation. The interphase site of topoisomerase II concentration was characterized by simultaneous *in situ* DNA hybridization and immunofluorescence. The site exactly coincides with the distribution of the 359 bp 1.688 g/cc^3 satellite in the centric heterochromatin of the X chromosome. A second dimmer site was identified on the Y chromosome. Both sites are immediately proximal to arrays of rDNA sequences. Pairing of prophase X chromosomes was observed exclusively at the topoisomerase II/359 bp site, suggesting a role for this chromosomal region and topoisomerase II in communication between two X, and possibly X and Y, chromosomes. The localization of topoisomerase II is therefore spatially and temporally regulated throughout the cell cycle.

Table of Contents

	Page Number
Title Page	i
Preface	ii
Dedication	iii
Acknowledgments	iv
Abstract	vi
Table of Contents	viii
List of Tables	xi
List of Figures	xi
Chapter 1: Chromosome Structure and Topoisomerase II	**1**
Chapter 2: Three-Dimensional Multi-Wavelength Imaging With High Numerical Aperature Lenses	
Summary	**7**
Introduction	**7**
Results	**10**
Discussion	**12**
Materials and Methods	**13**
Chapter 3: Alignment of Multi-Wavelength Fluorescence Microscopic Images Using Simplex Minimization	
Summary	**16**
Introduction	**16**
Results	**17**
Discussion	**24**
Materials and Methods	**25**

Chapter 4: The Distribution of Topoisomerase II During the Early Cell Cycles of the *Drosophila* Embryo

Summary 30
Introduction 30
Results 33
Discussion 52
Materials and Methods 56

Chapter 5: Multiple Chromosomal Populations of Topoisomerase II Detected In Vivo by Time-Lapse, Three-Dimensional Wide Field Microscopy

Summary 60
Introduction 60
Results 62
Discussion 83
Materials and Methods 89

Chapter 6: Conclusion 97

References 103

Appendix 1: Focal points for chromosome condensation and decondensation revealed by three-dimensional *in vivo* time-lapse microscopy. *Nature 342: 293-296 (1989).* 121

Appendix 2: Role of neurogenic genes in establishment of follicle cell fate and oocyte polarity during oogenesis in Drosophila. *Cell 66: 433-449 (1991).* 126

Appendix 3: Association of p60$^{c\text{-}src}$ with endosomal membranes in mammalian fibroblasts. **143**

J. Cell Biol. 118:321-333 (1992).

Appendix 4: Defining interactions and distributions of cadherin and catenin complexes in polarized epithelial cells. **155**

J. Cell Biol., submitted

List of Tables

Page Number

Table 5.1 Loss of Chromosomal Topoisomerase II During Mitosis 74

List of Figures

Page Number

Figure 2.1 Schematic Drawing of the Objective Lens and Sample 9

Figure 2.2 PSFs of Two High Numerical Aperture Lenses at Different Wavelengths 11

Figure 3.1 Alignment of Anti-Histone Images 19

Figure 3.2 Analysis of Image Overlap 20

Figure 3.3 Alignment of Images with Differing Intensity Distributions 22

Figure 4.1 The Effect of Fixation Conditions on Localization of Topoisomerase II 34

Figure 4.2 Changes in Topoisomerase II Distribution During the Cell Cycle 36

Figure 4.3 Chromosomes That are not Assembled into Telophase Nuclei Retain Topoisomerase II 37

Figure 4.4 Anti-topoisomerase II is not Localized in Sites of Initial Chromatin Condensation 40

Figure 4.5 High Resolution Localization of DAPI, Anti-histone, and Anti-topoisomerase II 41

Figure 4.6 Distribution of DAPI, Anti-histone, and Anti-topoisomerase II Along the X Chromosome 43

Figure 4.7 Topoisomerase II Site Localizes to X Heterochromatin and Site of Homologue Pairing During Prophase 47

Figure 4.8 Topoisomerase II Colocalizes with the 359 bp Satellite in the X Heterochromatin 49

Figure 4.9 Topoisomerase II Concentrates on both X and Y Chromosomes, Proximal to the rDNA 51

Figure 5.1 Characterization of Purified Topoisomerase II and Rhod-topo II. 64

Figure 5.2 Comparison of Image Processing Techniques for Time-Lapse Three-Dimensional Data 66

Figure 5.3 Nuclear and Chromosomal Distribution of Topoisomerase II *In Vivo* 68

Figure 5.4 Cell Cycle Changes in Nuclear and Cytoplasmic Topoisomerase II and Histone Concentration 72

Figure 5.5 Topoisomerase II Concentrates at Specific Sites in Interphase 77

Figure 5.6 Topoisomerase II is Located Throughout the Chromosome 79

Figure 5.7 Low Resolution Dual-Wavelength Time Lapse Movie of Histones and Anti-topoisomerase II 82

Figure 5.8 Summary of Distribution of Topoisomerase II During the Cell Cycle 84

Chapter 1: Chromosome Structure and Topoisomerase II

The replication, transcription and segregation of DNA in eukaryotes occurs within the context of chromatin and chromosomes. Chromatin shifts from condensed to decondensed states during transcriptional activation and during the transition from mitosis to interphase. Two extremes, the 10,000-fold linear compaction of the DNA in heterochromatin or the mitotic chromosome, and the completely unfolded DNA present at replication forks and highly transcribed loci, define the limits of a range of structures that can occur simultaneously in a single cell. To mediate these changes, a host of proteins are available that promote efficient packaging by neutralizing the high negative charge of DNA phosphate backbone and forming specific nucleoprotein structures.

The most fundamental unit of structure in chromatin is the 11 nm nucleosome fiber. It consists of naked DNA wound about a disk shaped octamer of the core histones H2A, H2B, H3, H4 and accounts for a 6-7 fold linear compaction of the DNA (Kornberg, 1974; Kornberg and Thomas, 1974; Richmond et al., 1984). In the presence of histone H1 or appropriate ionic conditions, the 11 nm fiber then folds into a fiber with a width of 25-30 nm (Widom, 1989; Freeman and Garrard, 1992). The structure is important since the 30 nm fiber appears to be somewhat disrupted around transcriptionally active genes, possibly through the partial depletion of H1 (Ericsson et al., 1990; Zlatanova and van Holde, 1992). Most of the models for this structure are based on studies of isolated chromatin fibers and suggest various forms of helical folding of the nucleosome fiber into the 30 nm fiber (reviewed in Freeman and Garrard, 1992). However, the structure of the 30 nm fiber is easily deformed by the ionic and enzymatic treatments used for fiber isolation (Giannasca et al., 1993). Electron micrographic tomography of sperm chromatin *in situ* and a theoretical prediction based solely on heterogeneity in the length of linker DNA indicate that the chromatin fiber is a 'zig-zag' ribbon of nucleosomes (Woodcock et al., 1992; Woodcock et al., 1993). In this structure, the separation between nucleosomes both parallel and perpendicular to the local fiber axis remains constant, with the fibers occupying, on average, a cylindrical space. However, since the nucleosomal ribbon folds in a highly localized manner, there does not appear to be a single 30 nm fiber structure. Rather, there is a general organization which appears quite flexible and could therefore assume the various structural states that must accompany DNA replication, transcription, and chromosome condensation. Regardless of the model favored, the chromatin fiber only accounts for an additional 6-7 fold linear compaction of the chromosome.

How the 30 nm fiber folds into 'higher-order' condensed structures like heterochromatin and linear chromosomes remains to be determined. The study of chromosomes either *in vivo*, *in situ*, or after isolation has provided evidence of helical coiling of the chromatid axis (Ohnuki, 1965; Ohnuki, 1968; Rattner and Lin, 1985; Boy de la Tour and Laemmli, 1988). The presence of helically coiled smaller fibers (60-100 nm) has suggested that the chromosome arm is comprised of a series of progressive helical coils (Inoué and Sato, 1964; Sedat and Manuelidis, 1977). However, the delicate structure of the chromosome is easily perturbed during sample preparation (Belmont et al., 1989; Giannasca et al., 1993), and a recent report has described the misinterpretation of the zig-zag chromatin ribbon as a helix in stereo projections (Woodcock et al., 1991). Unfortunately, there is to date no definitive description of the structure of chromosomes, although some sort of progressive hierarchical folding of smaller fibers into larger ones appears to be the fundamental theme which guides the folding of the chromosome (Belmont et al., 1987).

The source of free energy required to generate the folded chromosome is likely a product of the interaction of DNA sequences with chromosomal proteins. The histones clearly function in this manner. A much larger group of proteins, the nonhistone chromosomal proteins, have been fractionated from interphase nuclei and chromosomes and at least some of these appear to function in the organization of chromatin and chromosomes (Elgin et al., 1973). A desire to unify biochemical characteristics with chromosome structural functionality led a number of groups to digest or extract chromosomes to remove histones and DNA and examine the residue (Stubblefield and Wray, 1971; Paulson and Laummli, 1977; Marsden and Laemmli, 1979; Lewis and Laemmli, 1982). The retention of the basic shape of the chromosome after these treatments led to the suggestion that the post-digestion remnants represented the underlying framework, or 'scaffold', of the chromosome. Experiments that retained the chromosomal DNA demonstrated the existence of DNA loops whose ends were embedded in the scaffold, suggesting the presence of specific factors and DNA sequences which organized the genome into scaffold-associated fraction and DNA 'radial loops' (Marsden and Laemmli, 1979). DNA sequences called scaffold (or matrix) attachment regions (SARs) have been identified which bind specifically to the scaffold *in vitro* (Amati and Gasser, 1988; Izaurralde et al., 1988; Mirkovitch et al., 1988). The finding of a proteinaceous fibrillar remnant in extracted interphase nuclei provided an attractive function to the scaffold model: the scaffold might contain the set of proteins which mediate the structural transition between interphase chromatin and metaphase chromosome (Laemmli et al., 1992). The relevance of the scaffold to the *in vivo* structure of the chromosome has been a source of much controversy, since a proteinaceous chromosome core has never been seen in unextracted chromosomes and the recovery of the scaffold and its component proteins are dependent on a heat 'stabilization' step and the absence of any reducing agents to preserve thiols (Gasser et al., 1986). In addition, some published chromosome scaffolds suggest a condensed axial core while others appear as a fine fibrillar mesh distributed throughout the chromosome (Paulson and Laummli, 1977; Paulson, 1989). It is quite possible that the structural framework of the chromosome is a network of proteins distributed throughout the chromosome, and not just a central core (Earnshaw and Heck, 1985).

Regardless of the ultimate fate of the scaffold model, it has proven a powerful method for the fractionation of chromatin and chromosome proteins, especially those of molecular weight greater than 100 kD (Hirano et al., 1988; Bickel and Pirrotta, 1990; Yen et al., 1991). The first protein identified as a component of the scaffold was DNA topoisomerase II (Berrios et al., 1985; Earnshaw et al., 1985; Earnshaw and Heck, 1985; Gasser et al., 1986). This enzyme catalyzes strand passing of double-stranded DNA in an ATP-dependent fashion and is necessary for replication termination, when intertwined sister chromatids created during DNA replication are decatenated (Liu et al., 1980; Sundin and Varshavsky, 1980). The active enzyme is required *in vivo* and *in vitro* for proper chromosome condensation and chromosome segregation during mitosis (DiNardo et al., 1984; Newport and Spann, 1987; Uemura et al., 1987; Holm et al., 1989; Wood and Earnshaw, 1990; Adachi et al., 1991; Downes et al., 1991; Shamu and Murray, 1992; Hirano and Mitchison, 1993). A/T-rich consensus sites for topoisomerase II identified *in vitro* are often found in SARs, although, to date, most topoisomerase II consensus sites in SARs are not available to topoisomerase II *in vivo* (Sander and Hsieh, 1983; Gasser and Laemmli, 1986; Reitman and Felsenfeld, 1990; Udvardy and Schedl, 1991; Käs and Laemmli, 1992). The identification of an enzyme that mediated DNA topology as a significant component of the chromosome suggested that proteins which modified DNA and possibly chromatin structure might be intimately associated with the chromosome itself, and not freely diffusing soluble proteins in the nucleoplasm or cytoplasm. The nature of this association may be fixed, such that topoisomerase II might bind to SARs or other sequences throughout the cell cycle, and therefore would play a fundamental role in the organization of the genome (Mirkovitch et al., 1988). In this case, it might mediate chromosome condensation by aggregating with itself or other scaffold proteins once the cell enters M Phase (Adachi et al., 1989). Alternatively, the localization of the enzyme may be highly regulated and targeted to sites requiring its activity. This appears to be the case in interphase where changes in the localization of topoisomerase II at specific sequences have been observed upon activation of transcription (Reitman and Felsenfeld, 1990; Udvardy and Schedl, 1991; Kroeger and Rowe, 1992). A high chromosomal concentration of the enzyme might be maintained to ensure that any requirement for the enzyme is met immediately and not dependent on passive diffusion. This would ensure that all catenated sister chromatids are resolved during mitosis and prevent the breakage of DNA.

The purpose of the work described here was to characterize the distribution of topoisomerase II in interphase nuclei and mitotic chromosomes. The goal was to localize the enzyme either in nuclei and chromosomes whose structure was preserved during preparation, or simply in a living cell, and determine what the distribution of the enzyme is and if it changes during the cell cycle. In general, fixed or living cells were treated with a fluorescent probe for the enzyme and examined under a fluorescence microscope. This assay provided a direct and quantifiable measure of the localization of the enzyme, although at somewhat limited resolution. For example, although the data presented in the following Chapters shows that the localization of the enzyme is spatially and temporally specified, no information was gleaned about the molecular events controlling localization. However, the recent finding of a cell cycle-dependent phosphorylation of topoisomerase II suggests there may be a correlation between its localization and molecular state (Heck et al., 1989; Cardenas et al., 1992; Shiozaki and Yanagida, 1992).

Since chromosomes are inherently three-dimensional objects, the distribution of the enzyme was studied using a microscope capable of recording a series of images at sequential focal planes, thus generating a three-dimensional image. The need to simultaneously colocalize probes specific for DNA and topoisomerase II in three-dimensional images required characterization and correction of aberrations inherent in multi-wavelength imaging of a real sample in a light microscope. These experiments showed that there are significant wavelength-dependent deviations from ideality in microscopic images of biological specimens. The chromatic aberrations could be minimized with some knowledge of their behavior and completely corrected using an image alignment scheme developed in the course of this work. This method allowed the accurate comparison of the distribution of multiple components at diffraction-limited resolution in fluorescence microscopy.

With this ability in hand, the relative localization and behavior of topoisomerase II and chromosomes were studied in fixed *Drosophila* embryos by immunofluorescence cells and in living embryos by microinjection of a fluorescently labeled anti-topoisomerase II antibody or fluorescently labeled topoisomerase II enzyme. In these experiments, most of the enzyme present in the chromosome leaves the chromosome during the cell cycle. Enzyme which leaves the chromosome is presumably not involved in maintaining the structure of the chromosome. In addition, all detectable topoisomerase II can be extracted from chromosomes with no detectable effect on their morphology. In cases where the chromatid axis was visible, topoisomerase II was always distributed throughout the chromosome; no evidence for localization to an axial chromosome core was found. During interphase, the enzyme is distributed throughout the nucleus, but also concentrates in a specific region of X centric heterochromatin, adjacent to but distinct from the rDNA and nucleolar organizer, and colocalizing with the 359 bp 1.688 g/cc^3 A/T-rich satellite sequence. The distribution of the enzyme along the rest of the chromosome arm relative to the DNA is quite heterogeneous suggesting a specificity in the localization of the enzyme to regions of the chromosome. Taken together, these results describe a number of different populations of topoisomerase II which appear to have specific functions at specific times in the cell cycle.

Chapter 2: Three-Dimensional Multi-Wavelength Imaging With High Numerical Aperature Lenses

Summary

High resolution digital microscopy requires an accurate characterization of the performance of the imaging system. The design of high numerical aperture objective lenses assumes conditions which are often not met in biological microscopy in general, as well as in the studies presented in the following chapters. The severity of the aberrations present in two nominally similar high numerical aperture lenses was measured by recording their point-spread functions at different wavelengths and different optical path lengths. An Olympus Plan ApoChromat 60x/N.A. 1.4 possesses slight axial chromatic and spherical aberrations, whereas a Nikon Plan ApoChromat 100x/ N.A. 1.4 is well corrected, but transmits approximately 30% less intensity than the Olympus 60x lens. The optical path length of both lens increases with increasing wavelength, suggesting the presence of dispersion in the mounting media, coverslip, or immersion oil. The changes in optical path length create spherical aberration, which can be corrected by subsequent processing of images with transfer functions which include similar aberration.

Introduction

A microscopic image is generated when light emitted from an object is focused by an objective lens onto the focal plane of the microscope. The relationship between the object and the image is given by

$$\mathrm{Img}(x, y, z) = \mathrm{Obj}(x, y, z) * S(x, y, z)$$

where Obj(x, y, z) and Img(x, y, z) are the three-dimensional spatial distributions of light intensity in the object and image respectively and S(x, y, z) is the three-dimensional point-spread function of an objective lens and the symbol '*' signifies a convolution

(Bracewell, 1986). In theory, any aberrations in the lens or other parts of the light path are included in S(x, y, z) and are therefore correctable either by suitable additional lens elements or by computational processing of Img(x, y, z). In practice, the distortion of images by aberrations must be minimized to allow an observer to view an undistorted image in the microscope and allow the modifications of the light path for confocal, differential interference, dark field, or phase optics common in modern light microscopy. Objective lenses are therefore designed to eliminate most of the common aberrations like coma, astigmatism, distortion, and chromatic aberration (Inoué, 1986). However, especially in high numerical aperture objective lenses, these corrections assume a thin specimen that is immediately juxtaposed to the coverslip and mounted in a media of homogeneous refractive index (Fig. 2.1).

Unfortunately, these criteria are rarely met in biological microscopy. The sample is often a complex architecture of cellular components that create refractive index heterogeneity. In images of cell layers grown in culture, the problem is probably minimal, but becomes significant in images of tissues or whole organisms. Also, many biological samples are thick and require adjusting the focal plane many micrometers beyond the coverslip. In both these conditions, the lens corrections are now inappropriate and the system contains significant spherical aberration, observed as the smearing of signal along the optical axis (Born & Wolf). Extensive theoretical and experimental treatments of these phenomena have described the dependence of spherical aberration on the refractive indices of the immersion oil, coverslip, and mounting media and the focus position relative to the coverslip in both confocal and wide-field microscopes (Hiraoka et al., 1990; Gibson and Lanni, 1991; Hell et al., 1993). For a given lens and sample, it is possible to chose an immersion oil that restores the optical path length to the lens design and minimizes spherical aberration (Hiraoka et al., 1990). Since this correction is only appropriate at a given focal plane, spherical aberration will still be present in objects thicker than 5 μm. Moreover, the sensitivity of the optical path length suggests a further

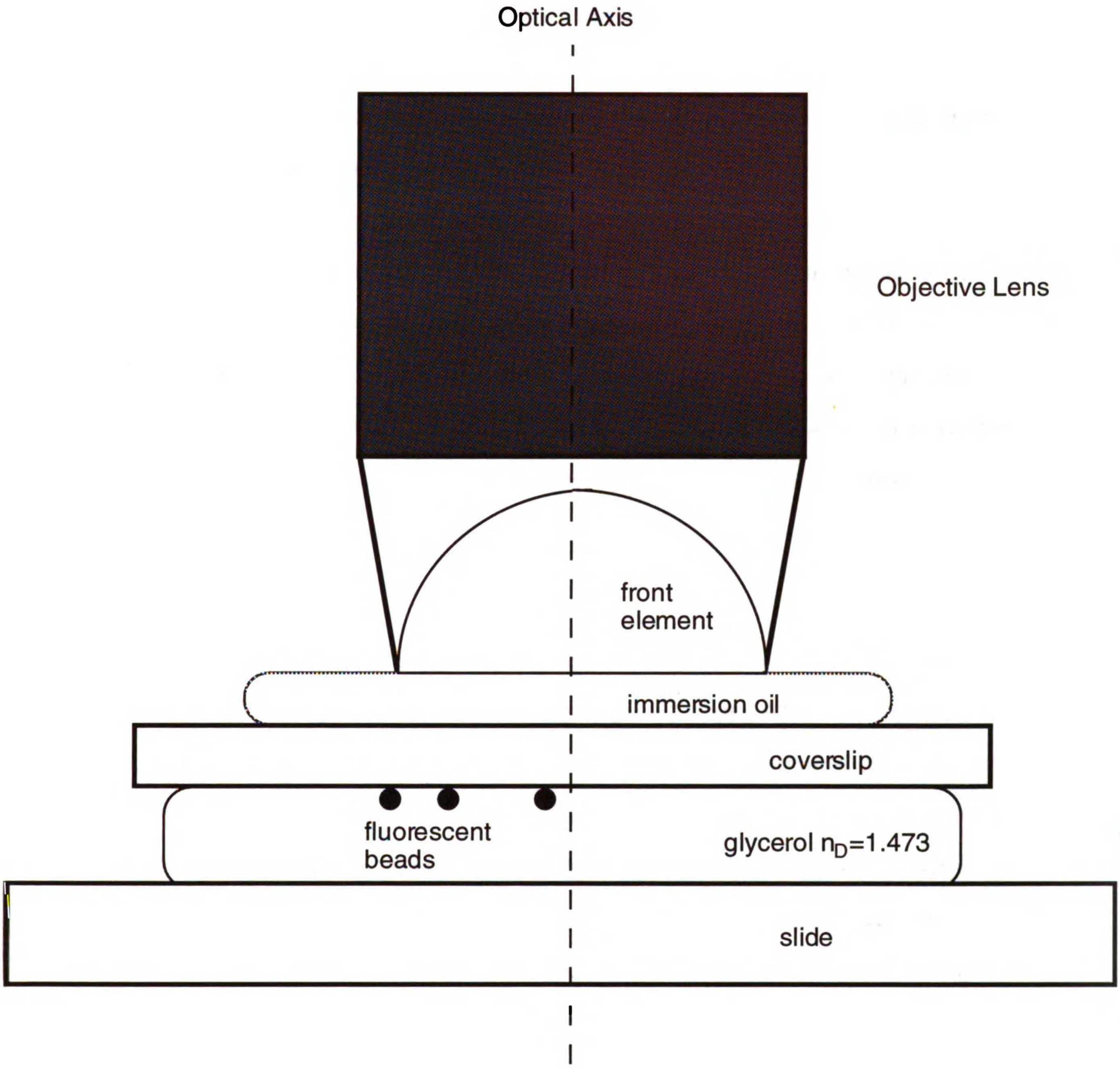
Optical Axis
Objective Lens
front element
immersion oil
coverslip
fluorescent beads
glycerol n_D=1.473
slide

Figure 2.1. Schematic Drawing of the Objective Lens and Sample. The elements of the optical path running from the sample to the front element of an oil immersion lens are indicated. The sizes of the different elements are drawn to emphasize the optical path, but are not to scale. Ideally, the sample is mounted in a medium of homogeneous refractive index, near the surface of the coverslip. For the lenses used in this study, the mounting media is glycerol, $n_D = 1.4730$. The refractive index of the coverslip is nominally 1.5150, but recent measurements suggest it may be as high as 1.522 (Gibson and Lanni, 1991). The refractive index of the immersion oil varies, as described in the text.

UC
San Francisc
LIBRARY
UC
San Franci
LIBRAR

complication: dependence of the optical path length on wavelength due to dispersion in the optical path. A given oil may be correct for a limited range of wavelengths, but incorrect for others. In fluorescence microscopy then, spherical aberration will affect images of samples containing multiple fluorophores.

This chapter presents the measurements of point-spread functions (PSFs) of two nominally similar high numerical aperture lenses at different wavelengths and optical path lengths. The PSFs of the lenses differ dramatically and at least some of the difference appears to be uncorrected intrinsic spherical aberration in one of the lenses. The immersion oil required to minimize spherical aberration is dependent on wavelength, suggesting that spherical aberration will always be present in multi-wavelength microscopy.

Results

The dependence of the point-spread function (PSF) on wavelength and optical path length of two high numerical aperture lenses, an Olympus S Plan ApoChromat 60x/NA 1.4 and a Nikon Plan ApoChromat 100x/NA 1.4, was measured by collecting three-dimensional images of 0.12 μm spherical beads impregnated with dyes fluorescing at 515 nm or 605 nm. For an ideal lens and optical path, the point spread function is circularly symmetric in the image plane and symmetric along the optical axis (Hiraoka et al., 1990; Gibson and Lanni, 1991; Hell et al., 1993). If the refractive indices of any of the elements in the optical path (see Fig. 2.1) deviate from ideality, the optical path length changes and spherical aberration, detected as axial asymmetry, is present in the recorded image. For example, as the refractive index of the immersion oil is varied from below the point that generates an axially symmetric PSF to aboveit, the optical path length increases, and the distribution of intensity in the PSF moves from below the object (in this case, a fluorescent bead) to above it (Hiraoka et al., 1990). To determine the effect of wavelength on the optical path length and spherical aberration, three-dimensional PSFs were collected using immersion oils with a range of refractive indices (Fig. 2.2). An oil

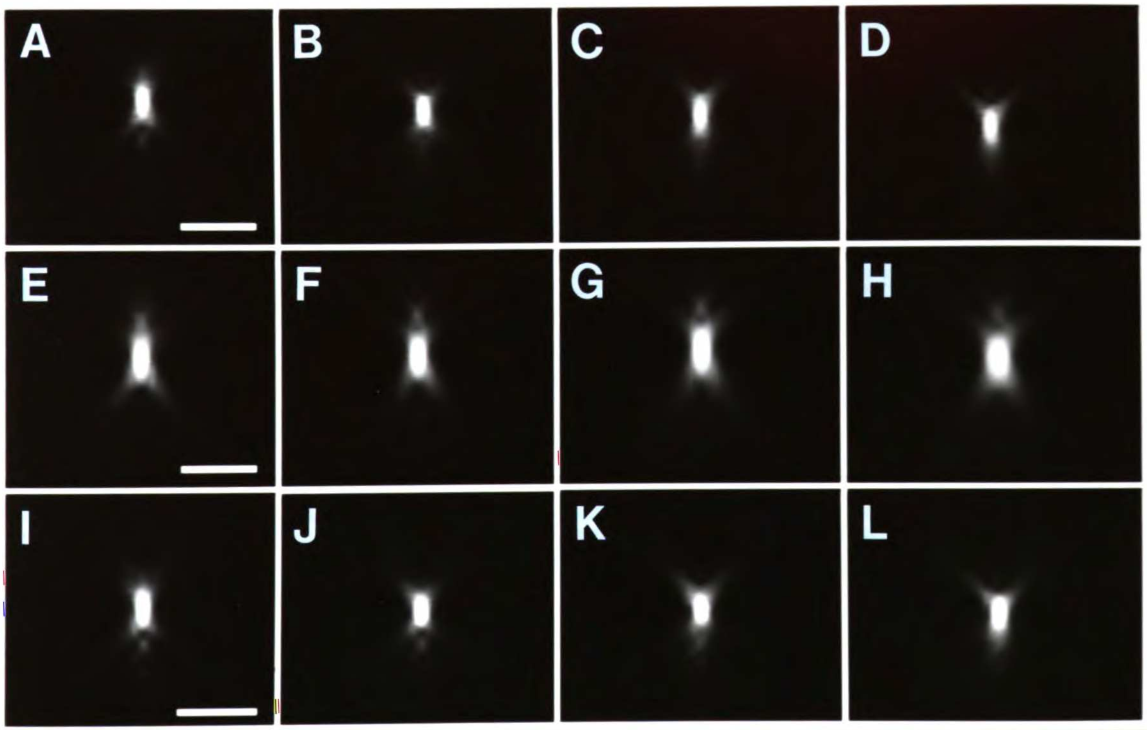

Figure 2.2. PSFs of Two High Numerical Aperture Lenses at Different Wavelengths. PSFs for the Olympus 60x/NA1.4 and Nikon 100x/NA1.4 lenses were collected using immersion oils with a range of refractive indices at 515 nm and 605 nm. (A-D) Fluorescence at 515 nm recorded with Olympus 60x lens with immersion oils with n_D = 1.5120, 1.5124, 1.5128, and 1.5136, respectively. (E-H) Fluorescence at 605 nm recorded with Olympus 60x lens with immersion oils with n_D = 1.5128, 1.5144, 1.5150, and 1.5160, respectively. (I-L) Fluorescence at 515 nm recorded with Nikon 100x lens with immersion oils with n_D = 1.5120, 1.5124, 1.5128, and 1.5140, respectively. All measurements were made at 22°C. Scale bars = 2 μm.

with $n_D = 1.5124$ produced the most axially symmetric PSF with the Olympus 60x lens at 515 nm (Fig. 2.2B). At 605 nm, an oil in this range produces a very asymmetric PSF; the optical path length is too short (Fig. 2.2D). An oil with $n_D = 1.5150$ produces the most symmetric PSF in this series, although the cross-section shows brighter intensity above the bead than below it and the distribution of intensity above and below the bead differs. The dependence of the optical path length on wavelength indicates that elements of the optical path either inside or outside of the lens are exhibiting dispersion. These differences suggest the presence of axial chromatic aberration in this lens. In addition, the lens possesses uncorrected spherical aberration, especially at 605 nm. Interestingly, a lens designer from Olympus, Inc. informed me that this behavior is predicted by the lens design (M. Yamagishi, personal communication).

A similar set of measurements were made using the Nikon 100x lens. In general the PSFs from this lens are much better defined than those from the 60x lens. At 515 nm, an oil with $n_D = 1.5124$ gives a fairly symmetric PSF (Fig. 2.2J), and there is a smooth transition in the integrated intensities of PSFs recorded with oils of refractive indices above and below this point. For this lens, the symmetric oil at 605 nm is $n_D = 1.5150$ (data not shown). The similarity in oils that produce symmetric PSFs for both lenses suggests that either both lenses contain similar dispersion properties or that the oil, coverslip, and mounting media contribute to dispersion in the optical path.

Discussion

The use of objective lenses to image samples that deviate from the lens design generates aberrations in the final image. Deviations in optical path length from the design limits cause spherical aberration, visible as a loss of intensity and smearing along the optical axis of the signal (Hiraoka et al., 1990; Gibson and Lanni, 1991; Hell et al., 1993). The data presented here were generated during an attempt to record PSFs for different lens at a variety of wavelengths. Clearly, different degrees of spherical aberration are generated using the same immersion oil at different wavelengths of light. In practice, this implies that a symmetric, non-aberrated light path may be designed for the imaging of a given fluorophore, but not more than one. A solution to this problem is to minimize it with the appropriate immersion oil, and using an empirical measure of the PSF which includes an appropriate amount of spherical aberration, reconstruct Obj(x, y, z) by deconvolution. Perhaps an ideal situation would be the addition of adjustable lenses behind the objective lens that would correct wavelength dependent spherical aberration.

The effects of spherical aberration differ in the two types of microscopes used for optical sectioning. For a confocal microscope, this phenomenon will cause a significant loss of signal intensity in at least one of the channels of a multi-wavelength image (Hell et al., 1993). For a wide-field microscope, the loss of intensity is not as severe (Fig. 2.2), but the blurring of signal along the optical axis degrades the resolution of the image. Correct restoration of multi-wavelength images will require the use of appropriately aberrated PSFs for each of the wavelengths used in the image. However, tests of the efficacy of various asymmetric PSFs in image restoration have shown that the asymmetry of the PSF need not perfectly match the asymmetry of the data. In general, an adequate reconstruction is produced by ensuring that the sign of the spherical aberration in the PSF, or the side of the bead on which the intensity concentrates, is identical to that in the data (B. A. Scalettar, J. R. S, D. A. Agard, J. W. Sedat, manuscript in preparation).

Materials and Methods

Measurement of PSFs

Spherical 0.12 μm latex sulfate beads with emission maxima at 605 nm or 515 nm (Molecular Probes, OR) were used for PSF measurement. These beads are exceptionally bright and do not appear to bleach significantly during extended data collection. 10 μl of a 1:10^6 dilution of bead suspension in 100% ethanol was placed in the center of a clean coverslip (22x22 mm #1 $^1/_2$, Gold Seal, available through VWR) on a clean slide warmer heated to 40°C. Higher temperatures caused the beads to melt. Extended exposure of the beads to ethanol caused a slow diminution in their intensity, so dilutions were used immediately after preparation. After allowing five minutes for the suspension to dry, a 7 µl drop of 0.1 M Tris Base, 2% n-propyl gallate, 95% glycerol (NPG glycerol) was placed in the center of the coverslip and used to pick up the coverslip with a slide. The coverslip was sealed with nail polish and allowed to dry for a minimum of six hours to allow the nail polish to dry completely. This extended drying time prevents motion of the bead as the nail polish is drying. An alternative method which eliminated the need for nail polish was also used. In this case, the coverslips were taped to the underside of tool steel mount with a hole cut in its center so that the beads were exposed through the hole. A drop of NPG glycerol was placed on the beads and the whole assembly was mounted on the microscope stage.

The details of the wide-field optical sectioning microscope used in this study are described in Chapter 3. PSFs were collected for two objectives, an Olympus S Plan ApoChromat 60x/NA 1.4 (Olympus, Inc.) and a Nikon Plan ApoChromat 100x/NA 1.4 (Nikon, Inc.). These lenses were chosen because the Olympus 60x was the brightest high numerical aperture lens with a 160 mm tube length obtainable from any lens manufacturer. The Nikon 100x was somewhat dimmer, but produced PSFs closest to the theoretical case. The lenses were cleaned with optical quality chloroform ("Photrex" Grade, Baker) before measurement of a PSF. This step was critical for the collection radially symmetric PSFs, probably because it eliminated mixtures of different immersion oils from the lens surface. A three-dimensional PSF was recorded by collecting optical sections from 4 µm above the bead to 4 µm below the bead at 0.1 or 0.2 µm intervals. The 515 nm beads were imaged using 485/22 nm bandpass excitation and 535/40 nm emission filters; the 605 nm beads were imaged using 560/40 nm excitation and 635/50 nm emission filters. At both wavelengths, PSFs were collected using immersion oils with a range of refractive indices (Series 5610, Cargille Laboratories). Exposure times were

1.5 - 2.0 s for the 515 nm beads and 0.2 - 0.4 s for the 605 nm beads. Cross-sectional views of each PSF were generated by rotating the PSF about the horizontal axis (x) axis 90° and resampling the voxel so that its dimensions along the optical axis were equivalent to the dimensions in the image plane. This transformation is necessary so that the displayed cross-section image is geometrically correct. The calculation was done using quadratic interpolation . To obtain a numerical measure of the intensity distribution in the PSF, the total intensity above background was calculated for each section in a PSF and then expressed as a fraction of the maximum total intensity. In all PSFs, the section with the maximum single pixel intensity was the section closest to focus. Because of the variability in fluorescence intensity between beads, it was not possible to compare the maximum intensity of PSFs using different optical path lengths.

Chapter 3: Alignment of Multi-Wavelength Fluorescence Microscopic Images Using Simplex Minimization

Summary

The use of multiple fluorophores to simultaneously localize different molecules in a single sample presumes that the microscope light path is free of chromatic aberrations. By localizing a single antigen with two fluorophores, I demonstrate small but significant registration and magnification differences between two images of the same sample recorded with different wavelengths of light. A method to align multi-wavelength images based on a simplex minimization of the image differences has been used to accurately correct lateral and axial chromatic aberrations, even in cases of limited overlap between images. When there is no overlap between images, alignment is achieved based on the bleed-through of emitted fluorescence.

Introduction

The use of multiple fluorescent probes with different spectral properties within a single sample allows the simultaneous localization of many cellular components (Tsien and Waggoner, 1990). Typically, a fluorescence microscope equipped with bandpass excitation and emission filters and multiple-wavelength dichroic mirrors is used to record the distribution of each fluorophore in a sample. With the advent of microscopic digital imaging systems, multiple wavelength images are now used to obtain high resolution measurements of the distance between different cellular components. These measurements assume the absence of any significant registration or magnification differences between images of individual fluorophores. While the use of well-corrected objective lenses and multiple wavelength dichroic mirrors substantially reduces the severity of these problems, there are still elements in any high resolution microscopic imaging system which introduce significant registration and magnification differences between images recorded using different wavelengths of light. For instance, the exact refractive index of the immersion oil used will vary with the wavelength of light passed through it and therefore cause differing amounts of spherical aberration at different wavelengths of light (Hiraoka et al., 1990; Gibson and Lanni, 1991; Hell et al., 1993). In addition, dramatic effects will be caused by the sample itself. As long as the refractive index of the sample material differs from that of the mounting medium, the final image will be affected by chromatic and spherical aberration generated by the sample. This will affect the exact position of the focal plane as well as the final magnification of the image. Once these aberrations are recorded in an image, they will affect any measurements of distances or sizes of image objects.

This problem can be corrected by aligning the multi-wavelength images based either on fiducial markers (e.g., fluorescent beads) or properties of the images themselves. The latter is preferable as it eliminates the possibility of markers coinciding with interesting sample structures and the difficulty of penetration into thick samples. I describe here such a method that is quick, stable, and applicable to cases where components of multi-wavelength images are exactly, partially, and even not at all colocalized. The method uses a multi-parameter minimization of the difference between two images to find appropriate translation and magnification corrections in all three spatial dimensions. The minimization is calculated using the simplex method, a widely used minimization scheme known for its speed and stability (Nelder and Mead, 1965; Parkinson and Hutchison, 1972). The method generates a polygon whose vertices represent each of the variables in the minimization. These vertices are progressively expanded and contracted until the minimum value of a function, in this case a measurement of the difference between two images, is found.

Results

I have developed a three-dimensional alignment scheme based on simplex minimization which is rapid and seems to be widely applicable. In general, I have worked with very small objects and lenses with high numerical aperture. For example, the method presented here was used with images of the mitotic chromosomes of the early *Drosophila* embryo which, at their largest, are 0.4-0.5 µm in diameter. To evaluate the simplex alignment scheme, I used a control system that would produce two perfectly coincident images in the absence of chromatic aberration. *Drosophila* embryos were stained by indirect immunofluorescence with an anti-histone antibody and two secondary antibodies, one labeled with Cascade Blue and one labeled with Texas Red. The anti-histone antibody recognizes the histones H1, H2A, H2B, H3, and H4, the structural proteins of all eukaryotic chromosomes. Before alignment, optical sections from the same focal position of the Cascade Blue and Texas Red three-dimensional images show substantial differences, primarily due to a wavelength-dependent translation of the position of the focal plane along the optical axis (Fig. 3.1A, B). It should be noted that these images were collected using a multiple-pass dichroic mirror and therefore are not due to registration shifts caused by a movement in this part of the optical path. Also, it is unlikely that the misalignment is caused by the use of different excitation and emission filters for the two images since previous measurements of image alignment of fluorescent beads showed measurable but much smaller magnification and translation differences (Hiraoka et al., 1991). Thus, much of the misalignment is caused by optical dispersion effects in the sample itself that cannot be systematically corrected in the microscope optics. Alignment is therefore crucial for accurate measurements of colocalization in multi-wavelength fluorescence images.

After alignment by simplex minimization, the overlap is substantially better as evidenced by the increased amount of white intensity in Figures 3.1C and 3.1D. If the ratio of intensities between the two three-dimensional images are binned and displayed as a histogram, there is a increase in the population of pixels with a ratio of intensities around 1:1 (Fig. 3.2). Simplex minimization therefore can correct wavelength-dependent registration and magnification differences in images containing signals that are largely colocalized.

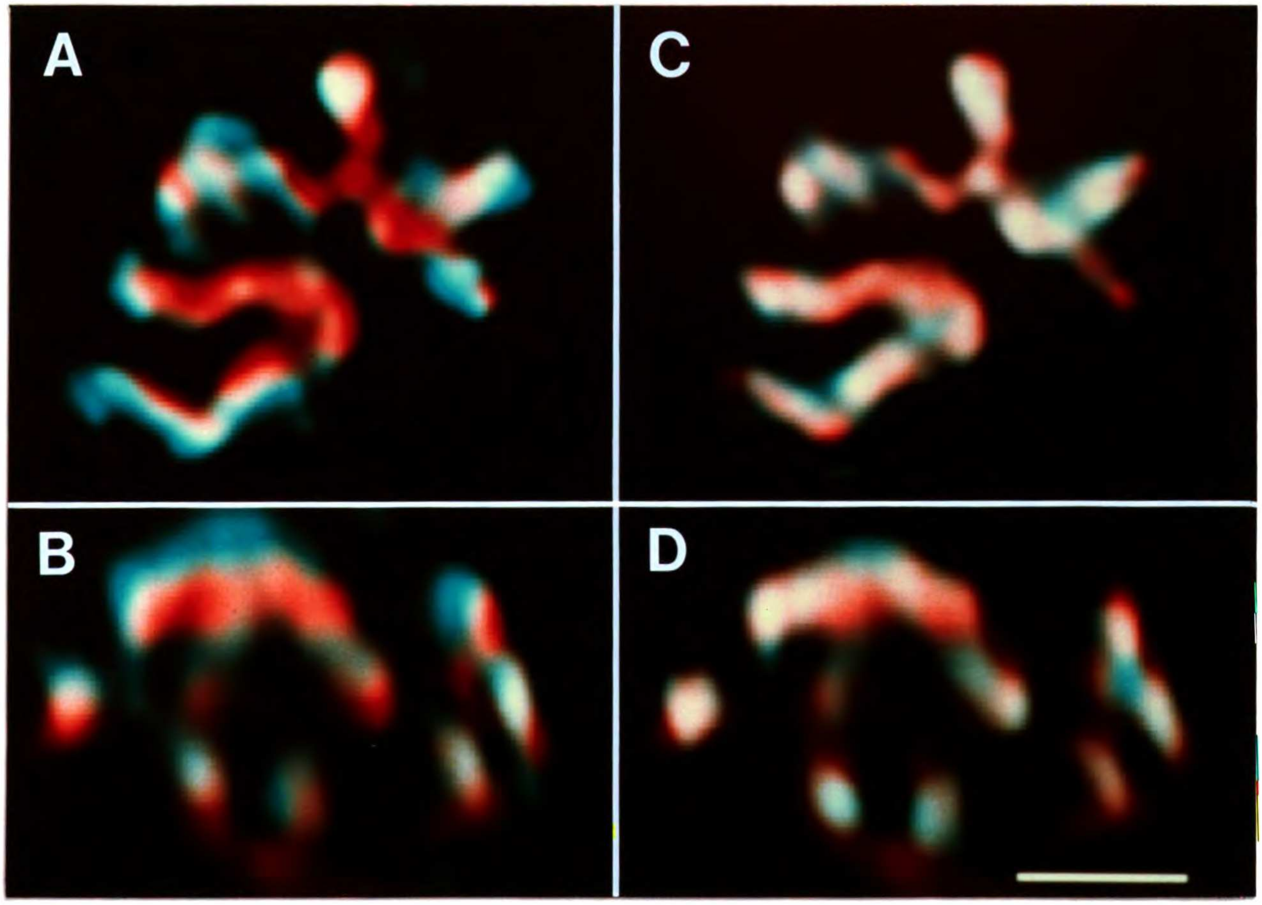

Figure 3.1. Alignment of Anti-Histone Images. Images of *Drosophila* embryonic cycle 12 metaphase nucleus stained with mouse anti-histone and Texas Red-conjugated goat anti-mouse IgG (red) and Cascade Blue-conjugated goat anti-mouse IgG (blue) before (A, B) and after (C, D) alignment. (A, C) Optical sections from three-dimensional data set. (B, D) Transverse views of data sets after 90° rotation with optical axis running vertically. The size of the voxel in x, y, z was 0.0744 x 0.0744 x 0.2 µm. To align the Cascade Blue image to the Texas Red image, translations in x, y, and z of 0.110, 0.176, and -0.329 µm and in-plane and axial magnification changes of 1.22 and 6.5% were required. This compares with translations of -0.016, 0.050, and -0.078 µm and an in-plane magnification change of 1.001% for images of red and blue fluorescent beads (Hiraoka et al., 1991). Scale = 2 µm.

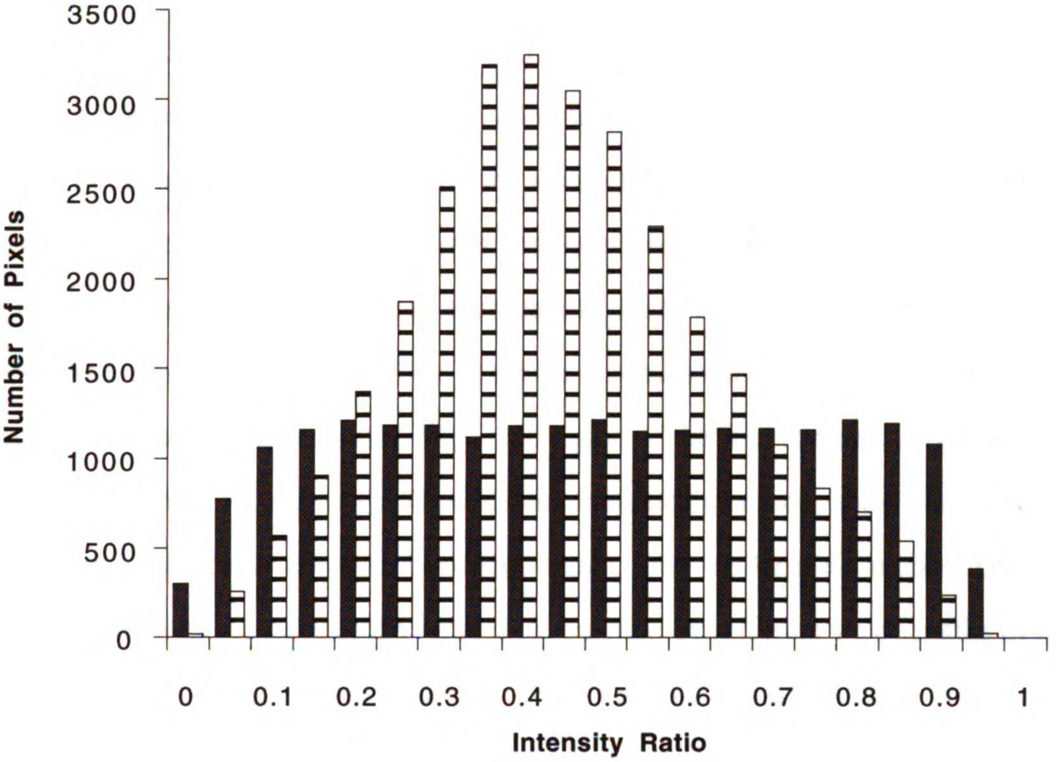

Figure 3.2. Analysis of Image Overlap. The ratio of the Cascade Blue image to the sum of the intensity of both the Cascade Blue and Texas Red images was calculated for all the voxels in the three-dimensional image of the nucleus shown in Figure 3.1. The number of pixels with a given ratio was added into bins of 5%. Pixels with intensity less than 1% of the maximum were ignored. Filled bars, distribution of image ratios before alignment. Stippled bars, distribution of image ratios after alignment.

Any general alignment scheme for multi-wavelength fluorescence microscopy must be applicable to systems where there is only partial or even no pixel-by-pixel correlation between images. *Drosophila* embryos were therefore stained with a rabbit polyclonal antibody against topoisomerase II (anti-topo II), the anti-histone monoclonal antibody used above, and DAPI, a fluorescent DNA binding drug. The distribution of the antibodies was detected with Texas Red anti-rabbit and fluorescein anti-mouse secondary antibodies. While all three probes detect chromatin and chromosomes, there are significant differences in their distributions along chromosome arms. Anti-histone stains *Drosophila* chromatin and chromosomes homogeneously whereas DAPI stains heterochromatin more intensely than euchromatin (Gatti et al., 1976; Hiraoka et al., 1990). Anti-topo II stains most of the prophase chromosomes used in this study uniformly, but also concentrates in a specific region of the X chromosome centric heterochromatin (see Chapter 4). Thus, this combination of probes should produce related, but not perfectly correlated images. Again, there are large differences between the optical sections recorded at the same focal position by different wavelengths of light (Fig. 3.3A, B). After alignment of the anti-topo II and DAPI images to the anti-histone image the intrinsic differences in the positions of the probes are maintained, but the general paths of the chromosomes are coincident (Fig 3.3C, D). This demonstrates that similar, but not identical images can be accurately aligned using simplex minimization.

A more difficult problem occurs when imaging components that are not spatially colocalized or structurally correlated. In this case, minimization of the r-factor would lead to nonsensical results. However, because of the long tail present in the emission spectra of most fluorophores, an image of fluorophore distribution generated by a given excitation light and emission filter designed for a different, longer wavelength fluorophore can be used to record an image which is spatially correlated to an image taken with the normal emission filter; the only difference will be the wavelength-dependent registration and magnification errors described above. For example, if

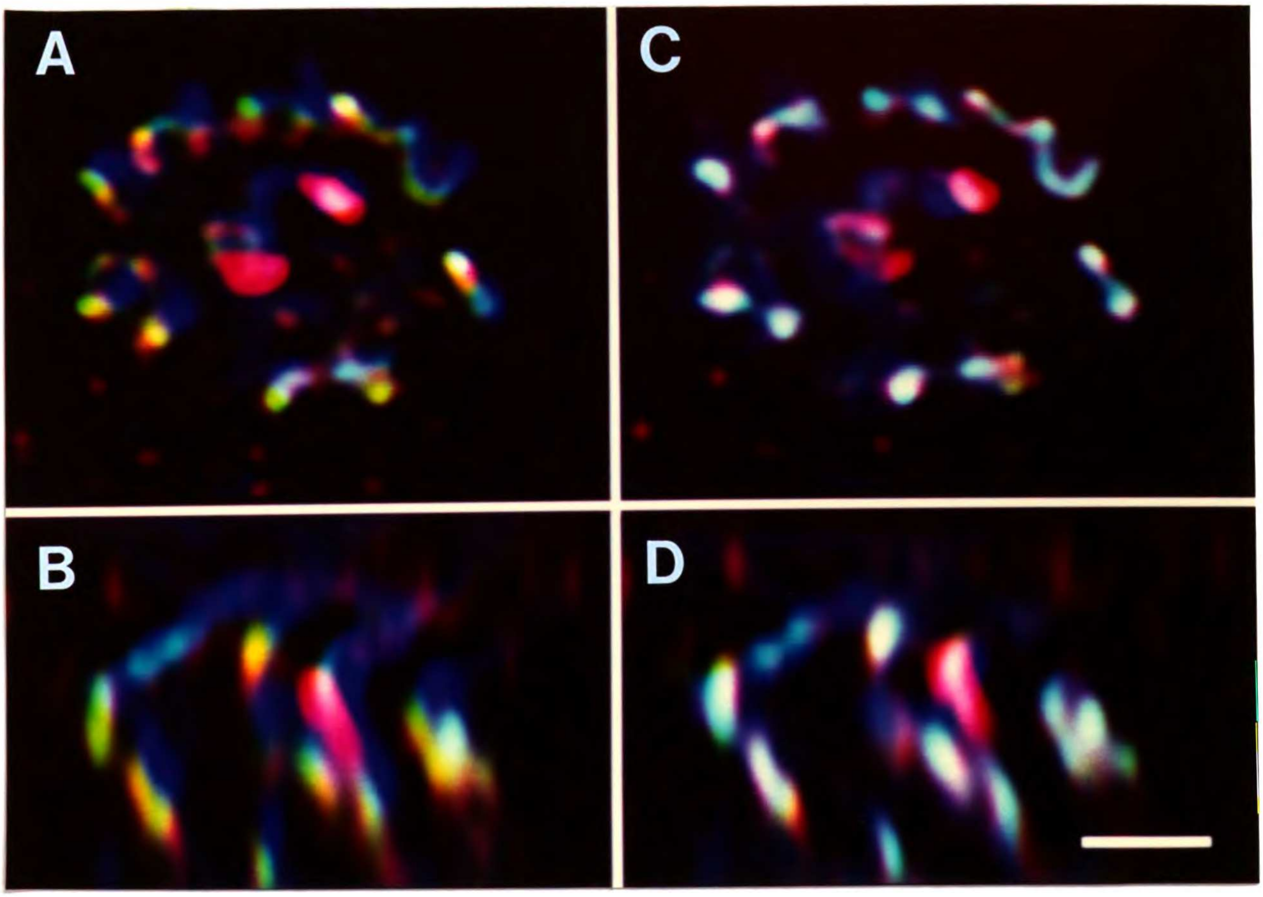

Figure 3.3. Alignment of Images with Differing Intensity Distributions. Images of *Drosophila* embryonic cycle 12 prophase nucleus stained with rabbit anti-topoisomerase II/Texas Red-conjugated goat anti-rabbit IgG (red), mouse anti-histone/fluorescein-conjugated goat anti-mouse IgG (green), and DAPI (blue) before (A, B) and after (C, D) alignment. (A, C) Optical sections from three-dimensional data set. (B, D) Transverse views of data sets after 90° rotation with optical axis running vertically. The size of the voxel in x, y, z was 0.0678 x 0.0678 x 0.2 μm. To align the anti-topo II image to the anti-histone image, translations in x, y, and z of -0.001, 0.025, and 0.199 μm and in-plane and axial magnification changes of 0.0 and -4.5% were required. To align the DAPI and anti-histone images, translations in x, y, and z of -0.103, -0.006, and -0.352 μm and in-plane and axial magnification changes of -1.3 and 0.0% were required. Scale = 2 μm.

uncorrelated DAPI and fluorescein images are to be aligned, the alignment parameters can be calculated by simplex minimization of the DAPI image and image recorded with the DAPI excitation and fluorescein emission filters. While the latter image typically requires exposures of 5-15 seconds on our charge-coupled device based microscope, inclusion of free radical scavengers in the mounting media effectively inhibits photobleaching (Giloh and Sedat, 1982). This technique was used to align images of two *in situ* DNA hybridization signals on a *Drosophila* polytene chromosome to the image of the chromosome itself (data not shown). Before simplex alignment, there are significant registration errors between the image measured with the DAPI emission filter and that measured in either fluorescein or Texas Red (data not shown). After alignment, the DAPI images coincide, ensuring that the positions of the *in situ* hybridization signals after alignment correction represent their true positions (data not shown). This type of experiment is used to determine the relationship of molecular distance in the genome to distance in the chromosome, and thus directly measure the packaging of DNA in the chromosome. The accurate alignment of the *in situ* signals to the chromosome is therefore crucial for correct interpretations in these experiments.

I have compared the quality of image alignment achieved by simplex minimization with that attained by cross-correlation (Bracewell, 1986). A phase-based cross-correlation scheme was used to minimize the effects of noise and provide a sharper cross-correlation peak (Shaw et al., 1989). While the cross-correlation method successfully aligned images of identical objects like those shown in Figure 3.1, it could not attain an accurate alignment of partially correlated images, like those shown in Figure 3.3. In general, it misaligned the images along the optical axis, probably because of image noise and the limited sampling along the optical axis. It may be possible to enhance the accuracy of this method by appropriate image filtering and by padding the image along the optical axis, thus fulfilling the condition of a cyclical transform.

However, the cross-correlation method was at least three fold slower than the simplex minimization, so these enhancements were not attempted.

Discussion

I have developed a new scheme to correct position and magnification differences in microscopic images caused by lateral and axial chromatic aberration. The alignment method uses a six parameter simplex search to minimize the differences between two images, as measured by the r-factor. It is relatively quick, stable, and can be used for highly or poorly correlated images. Wavelength dependent magnification and registration differences between images of different fluorophores vary in different samples and are also different from those measured for fluorescent beads. In three-dimensional multi-wavelength images of *Drosophila* embryos and polytene nuclei, quantitative and visual analyses showed that the most severe aberration occurs along the optical axis. These aberrations probably occur in images of any biological tissue and therefore must be corrected before any accurate measurement of colocalization is performed. Unfortunately, because much of the measured aberrations appear to be generated in the sample, a set of pre-measured parameters cannot be applied to all images from a given objective. However, the speed of the alignment calculation makes it practical to calculate alignment parameters for every data set.

Even though the data used in this study was recorded using high numerical aperture, apochromatic lenses, significant misalignment occurred between images recorded at different wavelengths. While I recorded multi-wavelength three-dimensional images, it is clear that even in single two-dimensional images, the physical position of the focal plane differs in images of different fluorophores. Therefore for critical measurements, e.g., genomic mapping by *in situ* DNA hybridization to chromosome spreads , the presence of small but significant aberrations will have to be considered. Ideally, short stacks of optical sections should be recorded and then aligned. The appropriate focal plane for each wavelength would then be chosen and analyzed as necessary.

Two aspects of sample-dependent chromatic aberration probably degrade the resolution of the image. First, it is likely that the sample-dependent aberrations measured here vary continuously as a function of wavelength. This suggests that a given fluorescence image, measured as the light passing through an emission filter, is blurred by the registration and magnification differences characteristic of the range of wavelengths passed by the emission filter. If most of these aberrations are generated by the sample, it is difficult to imagine how they could be corrected. Second, I have treated sample-dependent aberrations as a single global phenomenon of the image. This clearly generates a valid image correction, but it ignores local refractive index variations that may affect the colocalization of two fluorophores at some specific small volume. At the moment this problem is not treated, but it may be possible to use a Nomarski image of the same field to directly measure the local refractive index gradients and correct multi-wavelength fluorescence images for these effects.

Since multi-wavelength images must be aligned, it might be possible to use lenses with much less correction for chromatic aberration, and subsequently less elements. The advantage would be higher light transmittance, although, because of chromatic aberration, such a lens would probably only be suitable for multi-wavelength fluorescence and not transmitted or reflected light imaging.

Materials and Methods

Fixation and Immunofluorescence

Oregon R *Drosophila melanogaster* embryos were fixed for 15 minutes in a 1:1 mixture of heptane and 37% formaldehyde in Buffer A salts (15 mM PIPES pH 7.0, 80 mM KCl, 20 mM NaCl, 1.5 mM 2-mercaptoethanol, 2 mM Na_2 EDTA, 0.5 mM EGTA). Embryos were then devitellinized as described previously (Mitchison and Sedat, 1983).

Briefly, embryos were removed from the interface of the fixation mixture and transferred to 10:9:1 mixture of heptane:methanol:50mM EGTA pH7.4 cooled to -78°C. After a 10 minute incubation, the mixture was quickly warmed to 37°C and then rapidly shaken. Devitellinized embryos fell to the bottom of the tube. The embryos were then washed for 10 minutes each in 10%, 30%, 50%, 70%, 90%, and 100% Buffer A (Buffer A salts with , 0.5 mM spermidine, 0.2 mM spermine) in methanol (v/v). The embryos were then washed twice in 0.1% Triton X-100 (Pierce, Inc.) in Buffer A^- (Buffer A without ß-mercaptoethanol). Non-specific binding of antibodies was blocked with 5% normal goat serum (Jackson, Inc.) in 0.1% Triton X-100/Buffer A^- (NGS/Tx/A^-) for 3 hours. For double-labeled histone staining, the embryos were then incubated with an anti-histone monoclonal antibody (Chemicon, Inc.) diluted 1:1000 in NGS/Tx/A^- for 3-16 hrs. According to the manufacturer, the anti-histone antibody recognizes all of the core histones and H1 from a wide-range of species. After extensive washing in Tx/A^-, the embryos were incubated with Texas Red-conjugated goat anti-mouse IgG and Cascade Blue-conjugated goat anti-mouse IgG antibodies (Jackson, Inc.) diluted 1:200 in Tx/A^- for 3-5 hours. Again after extensive washing, embryos were mounted in Buffer A between two #1 coverslips (Gold Seal, Inc.), covered with a #1 1/2 coverslip, and then sealed with nail polish. For topoisomerase II/histone/DNA triple staining, the first antibodies were a polyclonal rabbit anti-*Drosophila* topoisomerase II antibody kindly provided by Dr. Neil Osheroff (Vanderbilt Univ.) diluted 1:500 in NGS/Tx/A^- and the anti-histone antibody used above. The second antibodies were Texas Red-conjugated donkey anti-rabbit IgG and fluorescein-conjugated goat anti-mouse IgG (Jackson, Inc.). After washing as above, embryos were washed three times with Buffer A^- and chromosomal DNA was stained with 0.5 µg/ml DAPI for 15 minutes, washed three more times, and then mounted as above.

Multiple-label *in situ* DNA hybridization of *Drosophila* salivary gland giant polytene chromosomes was performed as described (Y. Urata, S. J. Parmelee, J. W. Sedat, manuscript in preparation).

Optical Sectioning Fluorescence Microscopy and Deconvolution

Three-dimensional images of immunostained *Drosophila* embryos were recorded using a Peltier-cooled digital camera (Photometrics, Inc.) housing a charge-coupled device (CCD) camera (Eastman Kodak). The camera was mounted on an IMT-2 fluorescence microscope (Olympus, Inc.) workstation controlled by a MicroVax III computer (Digital Equipment Corp.; Maynard, MA) (Hiraoka et al., 1991) and equipped with bandpass excitation and emission filters (Omega, Inc.; Brattleboro, VT) mounted on motorized, computer-controlled filter wheels, a multi-wavelength dichroic mirror (Omega, Inc.; Brattleboro, VT) , and a 60x/NA1.4 (Olympus, Inc.) or a 100x/NA1.4 (Nikon, Inc.) oil immersion lens. Most of the design and specifications of the system have been described previously (Hiraoka et al., 1991). Fluorescence excitation light was collected from a 100 watt mercury arc lamp, and delivered to the back focal plane of the objective using a 1 mm diameter UV grade quartz fiber (Mitsubishi, Inc.). This arrangement scrambles the spatial intensity variation from the arc, and fills the back focal plane of the objective with spatially homogeneous light (Kam et al., 1993). Optical sections (512x512 pixels; effective pixel size is 0.0744 μm for the 60x lens, 0.0678 μm for the 100x lens) were recorded at 0.2 μm intervals by changing the microscope focus with a computer-controlled stepper motor (Compumotor, Inc.). Multiple wavelength three-dimensional images were recorded in a single focal series by alternating the appropriate excitation and emission filters for DAPI, Cascade Blue, fluorescein isothiocyanate, or Texas Red at each focal plane. To correct for temporal fluctuations in illumination intensity due to power instabilities in the Hg-arc lamp, the mean intensities of the individual sections were fit to a third-order polynomial and corrected for bleaching assuming a first-order decay. For some of the data, the intensity of the lamp was directly measured using a avalanche photodiode-based photon counting module (EG & G, Vaudreuil, Quebec). The section-to-section variations in intensity were then corrected by scaling the photon counts for each section to a reference. The out-of-focus information in these images was then removed using iterative, constrained, three-dimensional deconvolution (Agard et al., 1989; Hiraoka et al., 1991). This technique uses an empirical measure of the blurring of an image caused by the limited resolution of the objective lens (the "point-spread" function) to deblur an image by moving out-of-focus intensity back to its originating point.

Alignment of Three-Dimensional Images Using Simplex Minimization

Three-dimensional images of individual nuclei were aligned with the FORTRAN program SIMPLEX_ALIGN. This program uses a simplex minimization algorithm to find a three-dimensional magnification (M_{xyz}) and translation (T_{xyz}) relationship between two images that minimizes an r-factor function:

$$r = \frac{\sum |\mathrm{Image1}(x,y,z) - \mathrm{Image2}(x,y,z) \bullet S^{-1}|}{\sum |\mathrm{Image1}(x,y,z)|}$$

where (x, y, z) are the spatial coordinates for the two different images and S is a multiplicative factor which ensures that the intensities in the two images are on the same relative scale. The magnification in the plane of the image (x and y coordinates) is assumed to be isotropic. Each evaluation of the r-factor involves the application of a given M_{xyz}, T_{xyz}, and S to Image2 using a quadratic interpolation routine. The r-factor for that interpolation is then evaluated. The simplex routine used in SIMPLEX_ALIGN was from the Numerical Algorithms Group Library, Mark 14.

Alignment of Images Using Fourier-Space Cross-Correlation.

A phase-based cross-correlation function was calculated for two images at a series of magnifications in the image plane and along the optical axis using the FORTRAN program HYPER_CORREL (Shaw et al., 1989). For two images $f_1(x, y, z)$ and $f_2(x, y, z)$ and their Fourier transforms, $F_1(S_{x,y,z})$ and $F_2(S_{x,y,z})$, this modified cross-correlation function $X(S_{x,y,z})$ takes the form:

$$X(S_{x,y,z}) = \frac{F_1(S_{x,y,z}).F_2(S_{x,y,z})^*}{(|F_1| + \alpha_1)(|F_2| + \alpha_2)}$$

where $F_2(S_{x,y,z})^*$ denotes the complex conjugate and α_1 and α_2 are constants chosen to limit the contribution of noise in small amplitude coefficients and are similar to those in a Wiener filter (Castleman, 1979). This form of the function gives a much sharper peak than that provided by a straight cross-correlation scheme (Shaw et al., 1989).

Characterization of Aligned Images

To measure the degree of overlap between two images, each image was normalized to relative minima and maxima and scaled to an intensity range of 0 to 1000. The pixel-by-pixel ratio of the intensity of one image to the sum of both images was calculated and the numbers of pixels with ratios of 0.0-0.05, 0.05-0.10, etc. were counted and then displayed as a histogram.

Acknowledgments

I thank Dr. Zvi Kam for discussions of image alignment and for originally suggesting simplex minimization for image alignment. Dr. Yoji Urata originally suggested the use of bleed-through images for alignment.

Chapter 4: The Distribution of Topoisomerase II During the Early Cell Cycles of the *Drosophila* Embryo

Summary

DNA topoisomerase II is required for proper condensation and segregation of chromosomes during M phase of the cell cycle. This chapter describes the localization of topoisomerase II in the nuclei and chromosomes of fixed early *Drosophila* embryos. Fixation conditions that preserve the localization of the enzyme observed *in vivo* were developed. At prophase, the distribution along the chromosome arm is similar to the distribution of DNA and histones. There is much less topoisomerase II in the anaphase chromosome arm and its distribution is much scarcer than histones and DNA. The change in amount and localization of the enzyme suggest that the presence of much of the enzyme is not required after condensation is complete. The site of high concentration of enzyme in interphase was identified using a combination of immunofluorescence and *in situ* DNA hybridization and found to colocalize with the concentration of the 359 bp 1.688 g/cc^3 satellite sequence in the X centric heterochromatin. The complexity of the localization suggests the presence of many different forms of the enzyme, which function in different parts of the genome and different times of the cell cycle.

Introduction

DNA topoisomerase II is a strand passing enzyme that catalyzes the interconversion of DNA topoisomers (Wang, 1985; Osheroff, 1989). Topoisomerase II *ts* mutations of *Saccharomyces cerevisiae* and *Schizosaccharomyces pombe* cause sister chromatid crossbridges upon the onset of anaphase (DiNardo et al., 1984; Uemura and Yanagida, 1986; Uemura et al., 1987; Holm et al., 1989). In *S. pombe*, a *ts* mutation also appears to disrupt the proper condensation of chromosomes before mitosis (Uemura et al., 1987). Removal from or inhibition of topoisomerase II in *in vitro* mitotic extracts also prevents condensation of DNA or nuclei into chromosomes. (Newport and Spann, 1987; Wood and

Earnshaw, 1990; Adachi et al., 1991; Hirano and Mitchison, 1993). Administration of a specific topoisomerase II inhibitor to tissue culture cells and developing embryos causes improper chromosome condensation and anaphase crossbridges (Downes et al., 1991; Buchenau et al., 1993). None of these experiments could determine if the requirement at mitosis for topoisomerase II was a function of its activity during condensation, but the recent demonstration that topoisomerase II is required during mitosis in a model *in vitro* anaphase system suggests that chromosome condensation and chromosome segregation are two distinct points during the cell cycle which require topoisomerase II (Shamu and Murray, 1992).

Topoisomerase II is 170 kDa chromosomal protein found in all eukaryotes which fractionates with the nuclear matrix or scaffold, the remnant of nuclei or chromosomes after extraction with high salt or detergents (Berrios et al., 1985; Earnshaw et al., 1985; Gasser et al., 1986). Localization of topoisomerase II to the center of extracted chromosome arms and the identification *in vitro* of DNA sequences which specifically bind the scaffold (SARs) has suggested that topoisomerase II is a structural protein of chromosomes (for review, Gasser and Laemmli, 1987). A second 180 kDa form of the enzyme present in higher eukaryotes has been localized to the nucleolus (Chung et al., 1989; Negri et al., 1992). *S. pombe*, *S. cerevisiae* and *Drosophila* may not have this second form of the protein, but *S. cerevisiae top1 top2* double mutants develop elevated levels of recombination in the genes encoding the ribosomal RNA (rDNA) (Christman et al., 1988; Kim and Wang, 1989). The demonstration of a requirement for topoisomerase II in an *in vitro* chromosome condensation system suggested that topoisomerase II functioned during condensation by binding to SARs and aggregating to form the structural backbone of the mitotic chromosome (Adachi et al., 1991). However, in living *Drosophila* embryos, approximately 70% of the topoisomerase II present in the prophase chromosome is lost from the chromosome during mitosis (Swedlow et al., 1993). In addition, the recent demonstration that all immunodetectable topoisomerase II can be extracted from chromosomes condensed *in vitro* suggests that the enzyme may not be necessary to maintain the structural integrity of the chromosome (Hirano and Mitchison, 1993).

A function for topoisomerase II during interphase was suggested by the mapping of specific binding sites for topoisomerase II at a number of loci *in vivo*. These sites coincide with internucleosomal linker DNA and appear to fall into two categories: those which are not affected by transcription and those which disappear, or become much less frequently used, upon transcriptional activation (Reitman and Felsenfeld, 1990; Udvardy and Schedl, 1991; Käs and Laemmli, 1992; Kroeger and Rowe, 1992). The role these sites might have in transcription is not yet known. Topoisomerase II has also been shown to concentrate in one or two sites in the interphase nucleus *in vivo* (Swedlow et al., 1993). These sites had characteristics that suggested they were associated with specific chromosomal loci: every nucleus had either one or two sites and the size of the single sites was twice that of the double site. Because of the limited spatial resolution available in the *in vivo* experiment, the chromosomal location was not determined.

This chapter presents the results of the localization of topoisomerase II by immunofluorescence in *Drosophila melanogaster* embryonic nuclei and chromosomes. The syncytial *Drosophila* embryo was used for these studies because nearly all of the nuclei in the embryo progress through mitosis simultaneously (Foe and Alberts, 1983), allowing many different examples of a given point in mitosis within one embryo. The localization of topoisomerase II was studied *in situ*, instead of in isolated or extracted chromosomes, using fixation conditions that preserve the structure of nuclei and chromosomes as well as the localization of topoisomerase II observed in the living embryo (Belmont et al., 1987; Belmont et al., 1989; Swedlow et al., 1993). A comparison of the distribution of topoisomerase II to that of bulk DNA and specific DNA sequences suggests that the localization of the enzyme is spatially and temporally regulated and that its strand passing activity is required for chromosome condensation. Except for one case, no evidence was found for a specific distribution of the enzyme along a chromosome arm. The exception was the site of concentration of topoisomerase II in the interphase nucleus, which a combination of immunofluorescence and *in situ* DNA hybridization showed corresponds to the centromeric heterochromatin of the X chromosome.

Results

Fixation Conditions for Topoisomerase II

As a first step in determining the distribution of topoisomerase II on chromosomes, I first determined the optimal fixation procedure for preservation of topoisomerase II staining in *Drosophila* syncytial blastoderm embryos. *In vivo*, topoisomerase II is concentrated at one or two sites in interphase nuclei and is lost from chromosomes during mitosis (Swedlow et al., 1993). A good fixation protocol must preserve these characteristics as well as the overall structure of the chromosome. Three fixation methods which had previously been shown to preserve the structure of chromosomes were tested. Figure 4.1 shows the localization of anti-topoisomerase II and 4',6-diamidino-2-phenylindole (DAPI), a fluorescent DNA binding dye, in embryos fixed in a solution of 90% methanol and 0.1% formaldehyde. Topoisomerase II was localized to interphase nuclei, but the nuclei fixed with methanol appeared to be somewhat extracted. However, fixation with methanol produced no specific localization of topoisomerase II to mitotic chromosomes (Fig. 4.1D). Instead, there is a general localization of topoisomerase II throughout the mitotic spindle, suggesting that topoisomerase II was extracted from the chromosomes and trapped in the surrounding spindle microtubules. This phenomena was seen at all points in mitosis. However, despite the extraction of immunolocalizable topoisomerase II from chromosomes, no effect was seen by DAPI staining on the gross morphology of the chromosomes (Fig. 4.1C). No DNA halos, formed by the extraction of chromosome structural proteins, were observed. This suggests that extraction of the localizable topoisomerase II from mitotic chromosomes has no large effect on chromosome

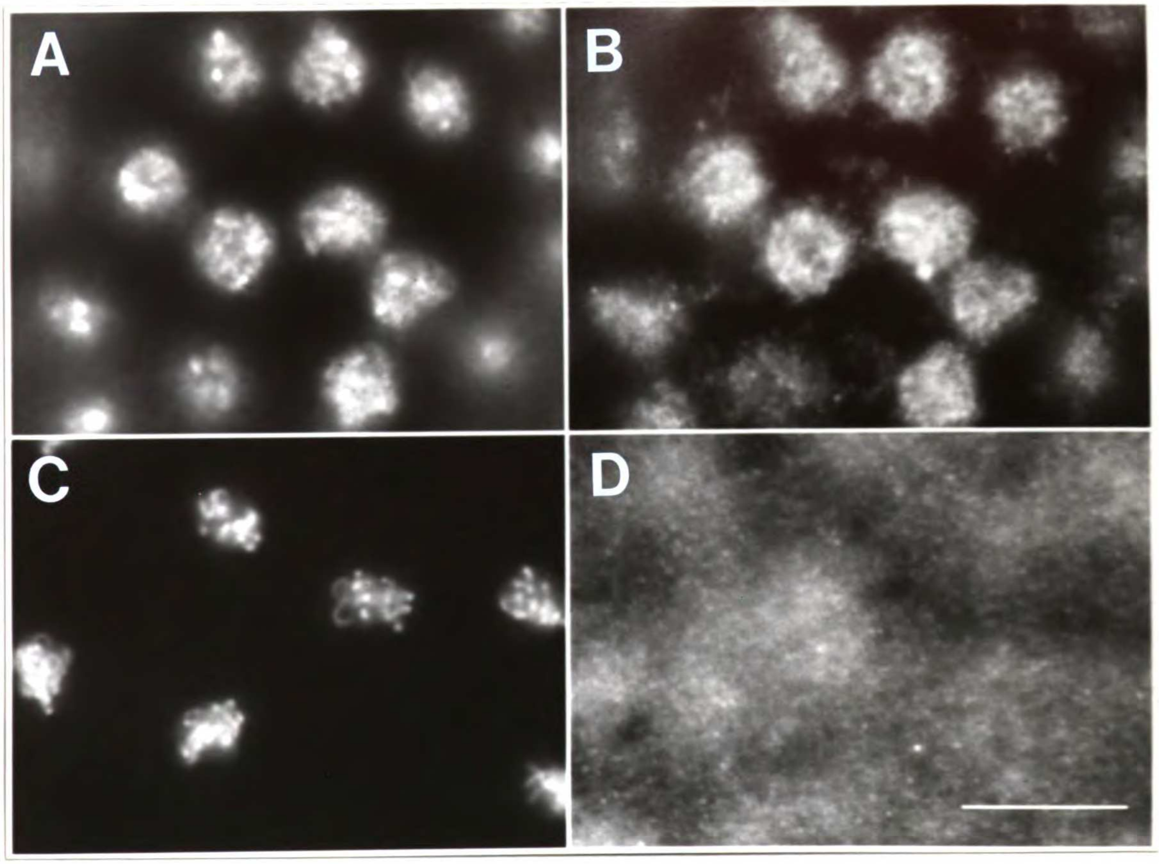

Figure 4.1. The Effect of Fixation Conditions on Localization of Topoisomerase II. Embryos were fixed in 0.1% formaldehyde in methanol and stained with DAPI (A, C) and anti-topoisomerase II (B, D). Anti-topoisomerase II staining is preserved in all interphase nuclei (B) but lost in mitotic chromosomes fixed with methanol (D). Scale = 5 µm.

structure. It is possible that staining of interphase nuclei was preserved in methanol fixed embryos because of the presence of an intact nuclear envelope. By contrast, fixation with 3.7% formaldehyde in Buffer A$^+$ preserves the localization of topoisomerase II to nuclei and chromosomes (Figs. 4.2 and 4.4). For all subsequent experiments, formaldehyde fixation was used for localization of all chromosome proteins in *Drosophila* embryos. While this fixative preserves chromosomes and chromosomal proteins, it alters the morphology of the mitotic spindle and causes the collapse of some anaphase and metaphase figures (Kellogg et al., 1988; J.Swedlow, unpublished results). In addition, while 3.7% formaldehyde preserved most of the features of localization topoisomerase II observed *in vivo*, the nuclear, non-chromosomal topoisomerase II seen in living prophase nuclei was poorly preserved (Swedlow et al., 1993). Therefore, for high resolution protein localization, embryos were fixed with 37% formaldehyde in a buffer containing the salts from Buffer A but missing the polyamines. This high concentration of formaldehyde preserves microtubules in *Drosophila* tissues (Theurkauf, 1992), produces well-ordered anaphase figures, and preserves the localization of topoisomerase II observed *in vivo*.

Cell Cycle Changes in Topoisomerase II Distribution

The changes in overall nuclear and chromosomal content of topoisomerase II varied at different points in the cell cycle. Low resolution, single optical section images of anti-topoisomerase II and DAPI distribution throughout nuclear cycle 12 in different fixed embryos (Fig. 4.2). Anti-topoisomerase II localizes to nuclei and chromosomes throughout mitosis, except at late telophase, where the concentration of nuclear topoisomerase II decreases to approximately cytoplasmic levels. The nuclear concentration presumably then increases during the next interphase. Dramatic examples of this phenomenon were found in two telophase embryos which contained nuclei which had failed to either completely segregate their chromosomes or package the full chromosome in decondensing telophase nucleus (Fig. 4.3). These mitotic faults apparently occur randomly

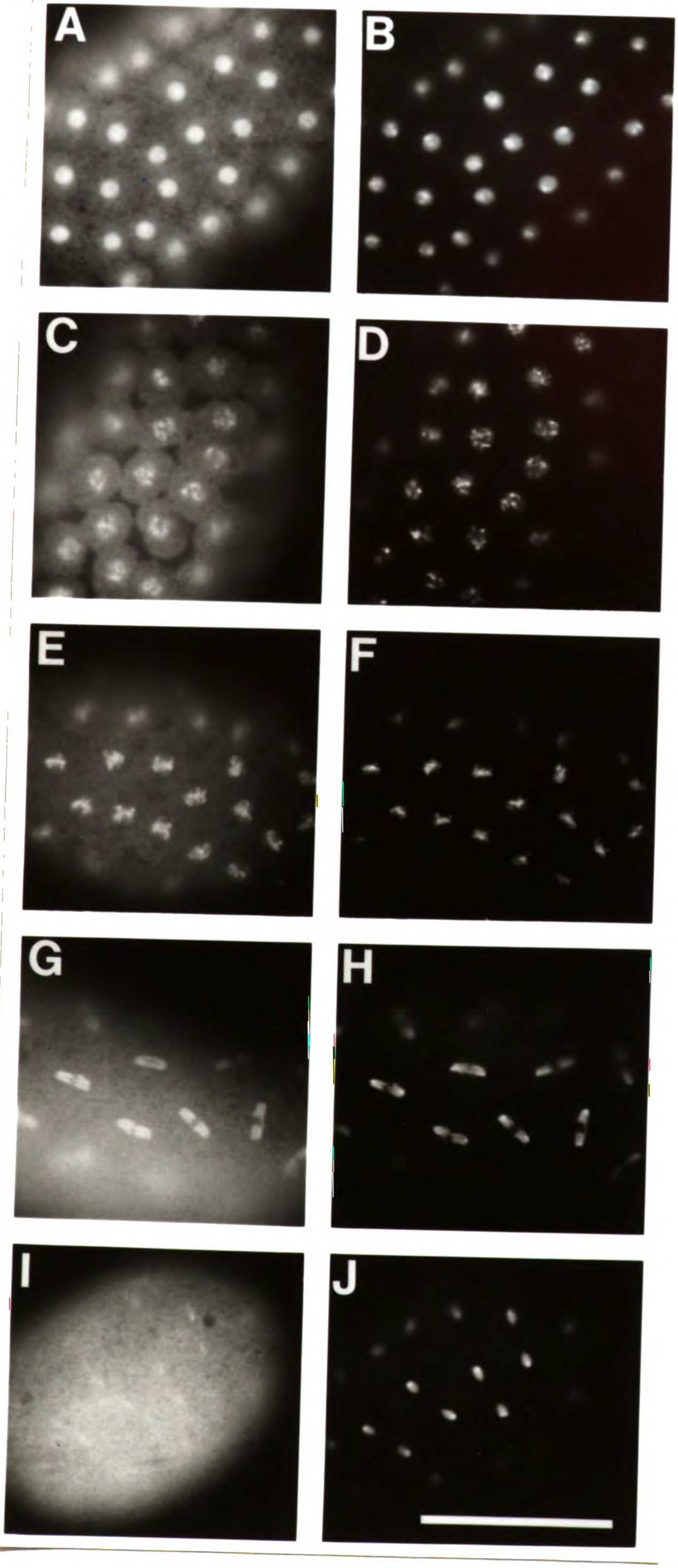

Figure 4.2. Changes in topoisomerase II distribution during the cell cycle. Formaldehyde fixed embryos were stained with DAPI (A, C, E, G, I) and anti-topoisomerase II (B, D, F, H, J). Representative images of interphase (A, B), prophase (C, D), metaphase (E, F), anaphase (G, H), and telophase (I, J) are shown. Scale = 50 µm.

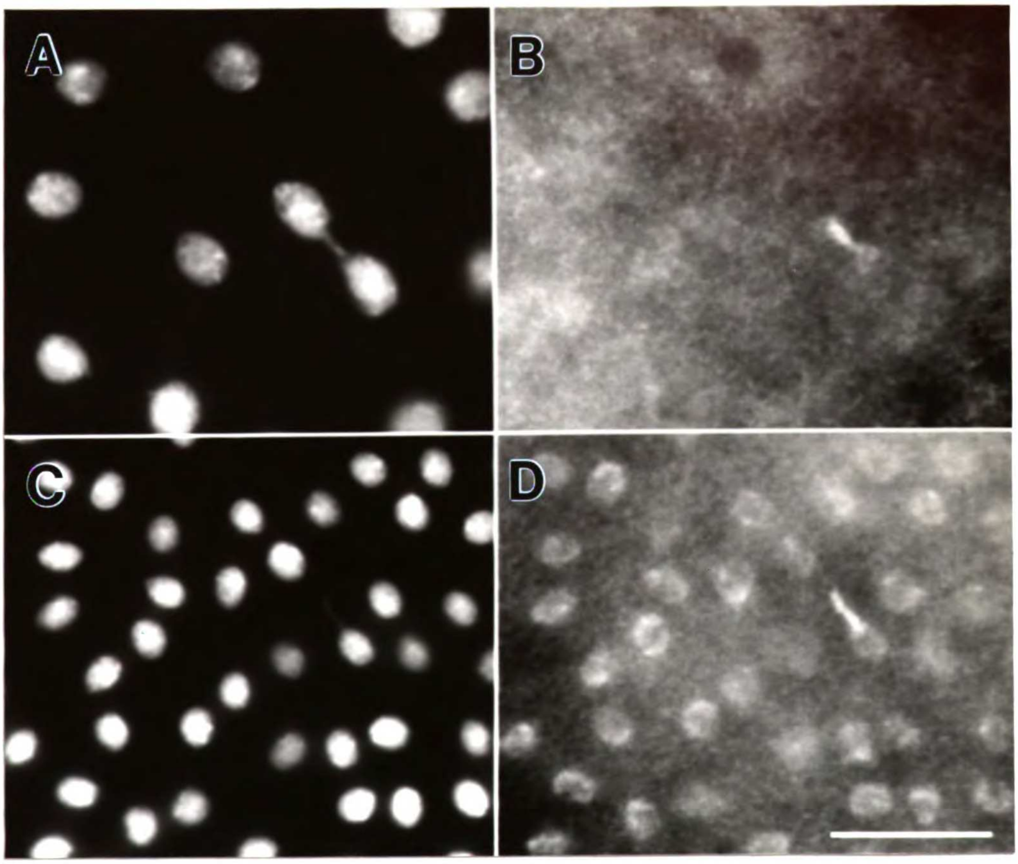

Figure 4.3. Chromosomes that are not assembled into telophase nuclei retain topoisomerase II. Two examples of nuclei from telophase embryos which failed to segregate their chromosome(s) properly. (A, C) DAPI staining. (B, D) Anti-topoisomerase II staining. Only those parts of the chromosome which remain outside of the forming nucleus still possess significant levels of topoisomerase II. Scale = 5 μm.

in wild-type embryos and are tolerated by the embryo (Hiraoka et al., 1989; Minden et al., 1989). In each of these cases, topoisomerase II content of the telophase nucleus had decreased nearly to cytoplasmic levels, while the topoisomerase II content of the extranuclear chromosome remained high. This suggests that the failure to detect significant topoisomerase II levels in late telophase embryos is not due to aberrant fixation or antibody accessibility of telophase embryos, but a regulated change in topoisomerase II content or accessibility in the nucleus itself at telophase.

The localization of topoisomerase II in nuclei and chromosomes was then examined at high resolution. For these experiments three-dimensional images of the distribution of anti-topoisomerase II, anti-histone, and DAPI in nuclear cycle 11, 12, and 13 embryos were recorded and deconvolved to remove out-of-focus blurring. The embryos were mounted in Buffer A with 1 mM dithiothreitol instead of glycerol-based media as glycerol causes a shrinking of the anti-topoisomerase II staining relative to the DAPI staining (data not shown). The triple-wavelength images were corrected for wavelength magnification and optical path differences and aligned using the program SIMPLEX_ALIGN (see Chapter 3). To evaluate the relative distributions of topoisomerase II enzyme and DNA, the distribution of anti-topoisomerase II was compared to the distributions of anti-histone and DAPI. The distribution of the anti-histone antibody serves as a control for general antibody accessibility in the chromosome. It was assumed that the small size of DAPI (mol. wt. 277) would allow it access to even the most condensed DNA. A combination of the affinity of DAPI for AT-rich DNA and the condensation state of the DNA generates a reproducible pattern of DAPI staining along *Drosophila* chromosome arms (Gatti et al., 1976; Hiraoka et al., 1990). The entire length of all the *Drosophila* chromosome arms are stained by DAPI to varying degrees, so the drug can be used to delineate the chromosomes (Hiraoka et al., 1990). None of my results and interpretations depend on a measurement of relative DNA content at two different chromosomal loci, but the use of DAPI for such a measurement would produce results weighted by the local AT-content of the DNA.

The distribution of DAPI, anti-histone, and anti-topoisomerase II generally coincided, but significant differences occurred at specific sites in nuclei and chromosomes and at specific times during the cell cycle. During interphase, most of the anti-topoisomerase II, anti-histone, and DAPI were evenly distributed and colocalized throughout the nucleus. However, sites of intense DAPI staining on the nuclear periphery which earlier work identified as initiation points for chromosome condensation (Hiraoka et al., 1989) do not stain with anti-topoisomerase II (Fig. 4.4). This suggests topoisomerase II is not required for the first stages of condensation. Throughout interphase and during early prophase, a site of intense anti-topoisomerase II staining was observed that coincided with a bright block of DAPI staining that was previously shown to correspond to the X centric heterochromatin (Foe and Alberts, 1985). In early prophase, the site is associated with the end of one of the condensing chromosomes (Fig. 4.5), which appeared to be the X, based on its length and number of heterochromatic blocks visible by DAPI staining (Gatti et al., 1976; Hiraoka et al., 1990). This site of concentration of topoisomerase II in interphase had the same characteristics as that seen *in vivo* in embryos injected with rhodamine-topoisomerase II: every nucleus in all embryos had either one or two sites and the sites were dim but easily distinguished early in interphase, diffuse in mid-interphase, and quite bright in late interphase (Swedlow et al., 1993). In metaphase, the site was still visible, although at significantly reduced intensity. *In vivo*, the high concentration of topoisomerase II at the site was lost by metaphase (Swedlow et al., 1993). This difference is likely due to the reduced spatial resolution and signal-to-noise ratio in the recording of live data. Therefore the sites observed here in fixed embryos are identical to those seen *in vivo*. The sites are characterized in greater detail below.

During prophase, metaphase, and anaphase, all chromosomes are stained with anti-topoisomerase II (Fig. 4.5). In previous studies, topoisomerase II was localized to a central axial core of isolated or extracted chromosomes (Earnshaw and Heck, 1985; Gasser et al., 1986; Taagepera et al., 1993). While extended fibers at least twice the length of the

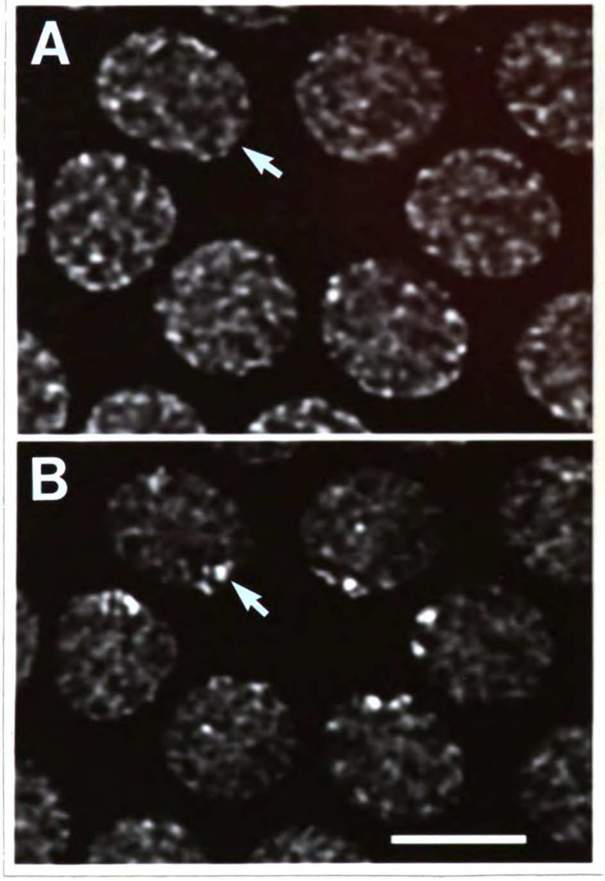

Figure 4.4. Anti-topoisomerase II is not localized in sites of initial chromatin condensation. Optical sections from deconvolved data sets of cycle 12 interphase nuclei. The focal plane is at the midline of most of the nuclei in the field. (A) DAPI staining. Bright spots on nuclear periphery are the first sites of condensation (Hiraoka et al., 1989). (B) Anti-topoisomerase II staining. No enrichment of topoisomerase is detected at condensation sites. Scale = 5 μm.

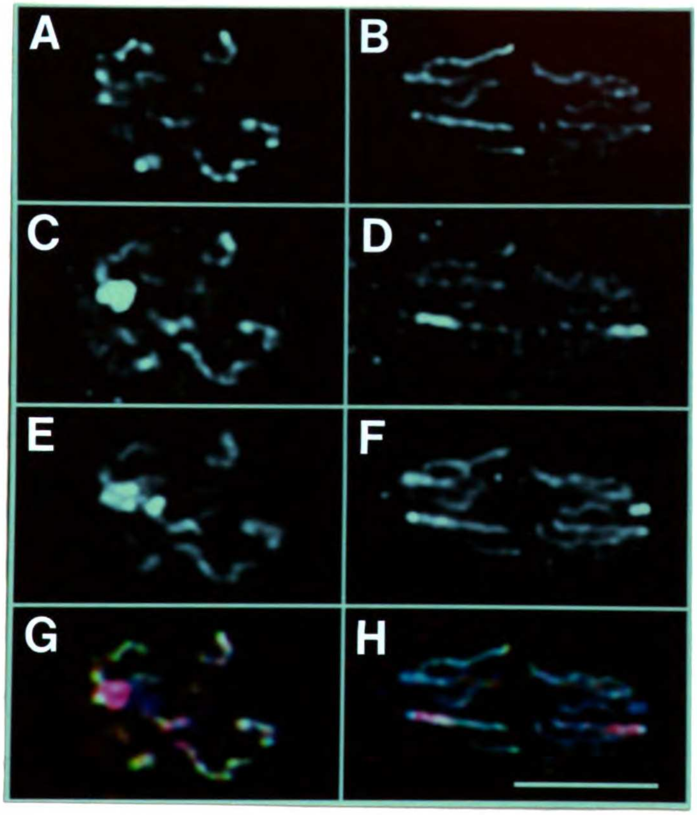

Figure 4.5. High resolution localization of DAPI, anti-histone, and anti-topoisomerase II. Distribution of chromosome probes in 0.2 μm optical sections from three-dimensional data sets of prophase (A, C, E, G) and anaphase (B, D, F, H) nuclei. (A, B) Anti-histone. (C, D) Anti-topoisomerase II. (E, F) DAPI. (G, H) Overlay of images. Red, anti-topoisomerase II. Green, anti-histone. Blue, DAPI. Scale = 5 μm.

final condensed chromosome arm were easily identified in early prophase embryos, no examples of anti-topoisomerase II localizing to an axial chromosome core were found (Fig. 4.5). In general, the distribution of anti-topoisomerase II along the chromosome arm is similar to the distribution of anti-histone and DAPI (Fig. 4.5C). By contrast, there is much less anti-topoisomerase II staining at anaphase and its distribution is much more heterogeneous and dramatically differs from the distribution of anti-histone and DAPI (Fig. 4.5D). In prophase then, topoisomerase II appears to decorate most of the chromatin since its concentration at a particular site in the chromosome appears to correspond to the local concentration of DNA and chromatin.

A quantitative measure of anti-topoisomerase II, anti-histone, and DAPI intensities is shown in Figure 4.6. After collection and deconvolution of three-dimensional images of prophase and anaphase chromosomes stained with DAPI, anti-histone, and anti-topoisomerase II, the chromosome paths were traced using PRISM, an interactive modeling program (Chen et al., 1989; Hiraoka et al., 1990). The chromosomes were identified by their characteristic DAPI staining patterns which are probably generated by a combination of the distribution of AT-rich sequences and differences in condensation along the chromosome arm (Gatti et al., 1976; Hiraoka et al., 1990). Plots of the intensities for X chromosomes at prophase and at anaphase were then generated by averaging the DAPI, anti-histone, and anti-topoisomerase II intensities along the chromosome arm. In prophase, there are regions of significant similarity between DAPI, anti-histone, and anti-topoisomerase II within a given chromosome, but little correspondence between the anti-histone and anti-topoisomerase II staining of chromosomes from two different nuclei (Fig. 4.6A, B). The one exception to this statement is the bright staining of anti-topoisomerase II and DAPI near the centromere of the X chromosome. This is the site of high concentration of topoisomerase II observed throughout interphase and early prophase. At anaphase, there is limited correspondence between the distributions of anti-histone and DAPI, but very little similarity between these and anti-topoisomerase II (Fig. 4.6C, D).

A.

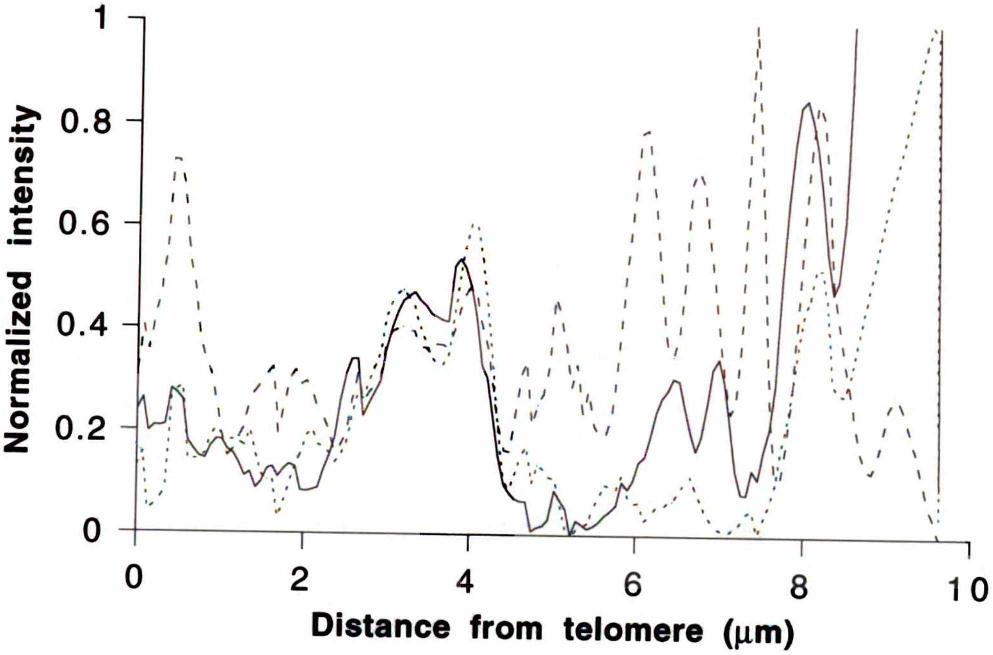

1
0.8
0.6
0.4
0.2
0
Normalized intensity
0
2
4
6
8
10
Distance from telomere (μm)

B.

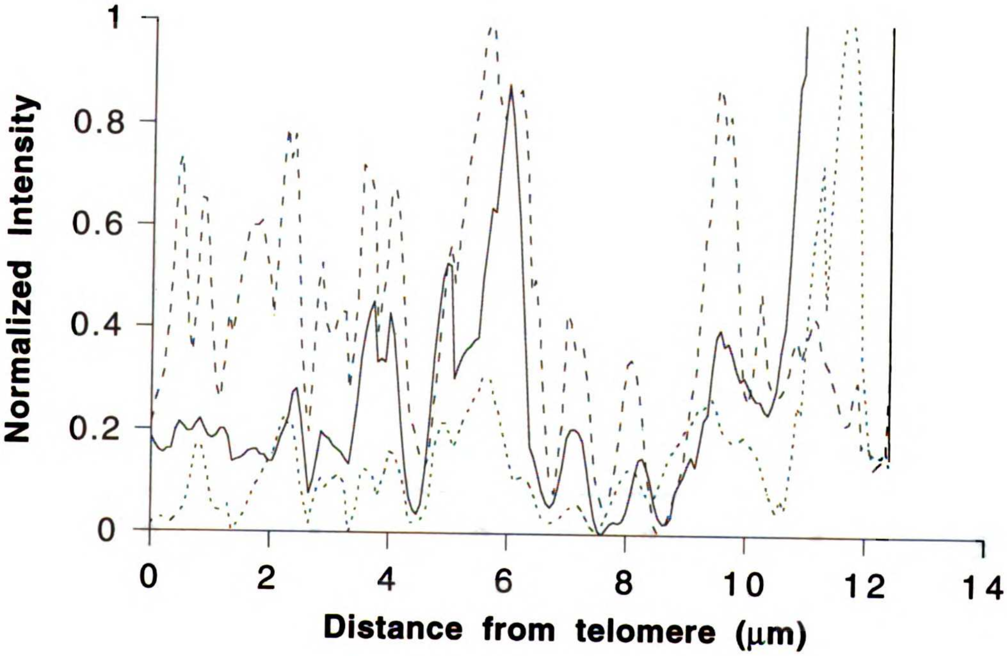

1
0.8
0.6
0.4
0.2
0
Normalized Intensity
0
2
4
6
8
10
12
14
Distance from telomere (μm)

C.

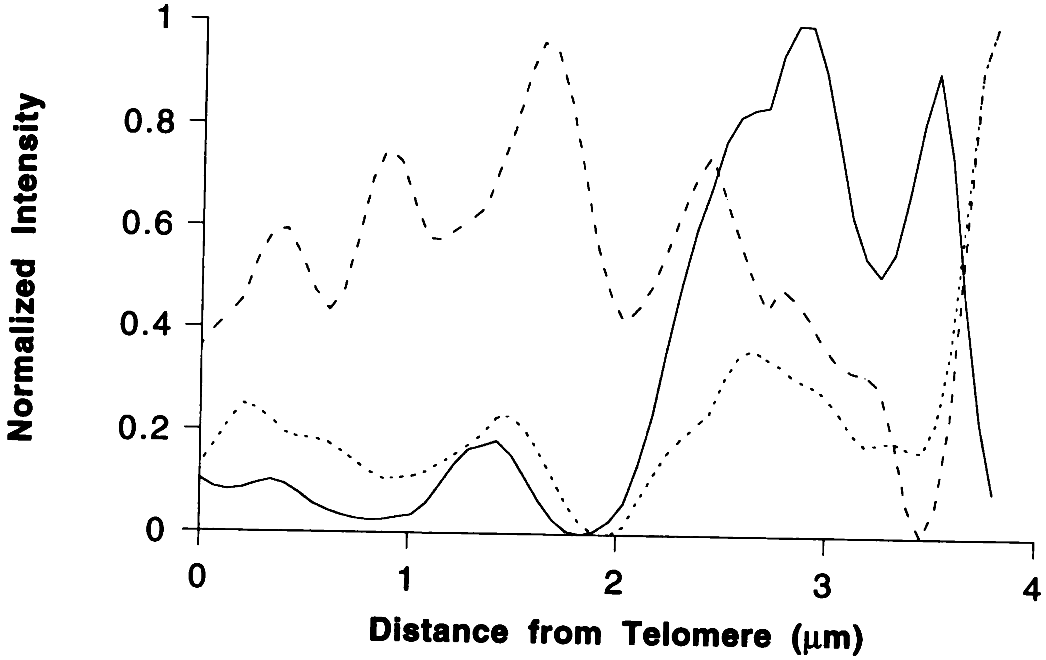

Normalized Intensity
1
0.8
0.6
0.4
0.2
0
0
1
2
3
4
Distance from Telomere (μm)

D.

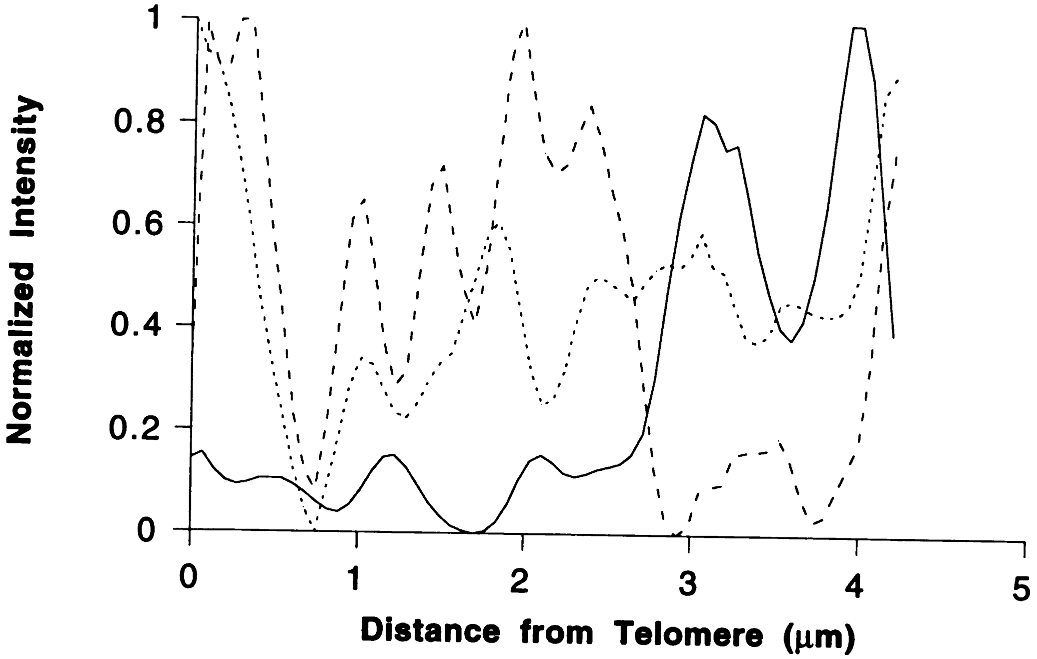

Normalized Intensity
1
0.8
0.6
0.4
0.2
0
0
1
2
3
4
5
Distance from Telomere (μm)

Figure 4.6. Distribution of DAPI, anti-histone, and anti-topoisomerase II along the X chromosome. Normalized intensity of the different chromosomal probes was plotted against the position on the chromosome, expressed as the distance from the telomere. This metric was used because the identification of the exact position of the X centromere is difficult in these preparations. The paths of the chromosomes were traced using PRISM, an interactive modeling program (Chen et al., 1989; Hiraoka et al., 1990). The tracing of the three-dimensional paths of chromosomes was used to define a tube which contained the intensity distribution of DAPI, anti-histone, and anti-topoisomerase II. This tube was then computationally straightened and then projected to produce a map of the intensities along the chromosome arm. Intensity at each point along the arm is plotted as a fraction of the maximum intensity on the arm. Because the intensity of the topoisomerase II site is so much greater that that of the rest of the chromosome, anti-topoisomerase II intensity was normalized to one-third the maximum intensity. (——) Anti-topoisomerase II intensity. (-----) Anti-histone intensity. (······) DAPI intensity. (A, B) Plots of intensity distributions for two X chromosomes from different cycle 12 prophase nuclei from the same embryo. Position on the chromosome is given by the distance from the telomere of the long arm. (C, D) Plots of intensity distributions for two X chromosomes from cycle 12 anaphase nuclei.

Again, except for the concentration of anti-topoisomerase II in the X centric heterochromatin, there is no obvious similarity in the distribution of anti-topoisomerase II in different X chromosome arms (Fig. 4.6C, D). Similar results were obtained from intensity plots of the third chromosome at prophase and anaphase (data not shown). While it is possible that the staining patterns occur because the antibody has limited accessibility to topoisomerase II in the anaphase chromosome, the distribution and relative levels of chromosomal staining are similar to that observed in living embryos injected with rhodamine-topoisomerase II (Swedlow et al., 1993). Therefore, in the chromosome arm, the enzyme's distribution at prophase is similar to the chromatin distribution, but the loss of enzyme during mitosis leaves a distribution that significantly differs from the chromatin distribution at anaphase.

The Interphase Topisomerase II Site Localizes to the X Centric Heterochromatin

The site of high concentration of topoisomerase has been studied *in vivo* by injecting fluorescently-labeled topoisomerase II into *Drosophila* embryos and following the distribution of the enzyme through the cell cycle (Swedlow et al., 1993). In these time-lapse images, one or two sites were seen in every nucleus, suggesting that the site might be a chromosomal locus which paired with its homologue in some nuclei. In addition, images from fixed prophase and anaphase nuclei suggested that the site coincided with the end of one of the chromosome arms (Fig. 4.5). To identify this site, chromosome paths in fixed cycle 12 prophase nuclei were traced as above and the DAPI staining along the chromosome was used to identify the chromosome. Figure 4.7 shows stereo pairs of two chromosomes stained with anti-topoisomerase II, anti-histone, and DAPI. The bright blocks of DAPI staining near the centromeric end of the chromosomes are characteristic of the heterochromatin of the X chromosome (Gatti et al., 1976; Hiraoka et al., 1990). The site of topoisomerase II concentration coincides with this block, thus localizing the site to the X heterochromatin. In addition, the chromosomes appear to be paired at this region and

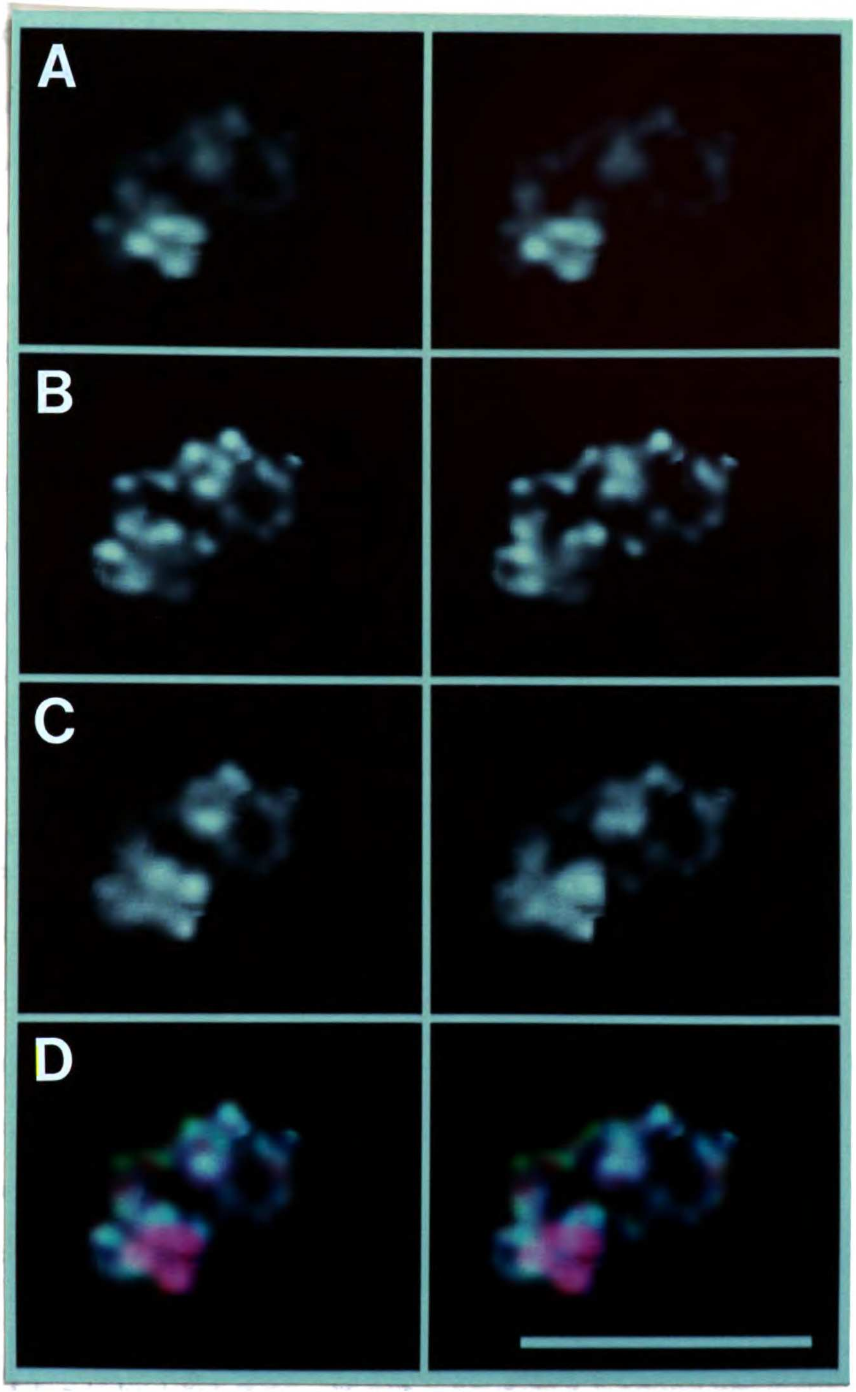

Figure 4.7. Topoisomerase II site localizes to X heterochromatin and site of homologue pairing during prophase. Stereo projections of two X chromosomes from an early prophase nucleus stained with anti-histone, anti-topoisomerase II, and DAPI that contained one large topo II/359 bp site. The three-dimensional paths of all the chromosomes in the nucleus were traced and the paths of the X chromosomes were used to cut out the intensities within 0.47 μm of the traced paths. Stereo pairs were then calculated for each color. (A) Anti-topoisomerase II. (B) Anti-histone. (C) DAPI. (D) Overlay of A, B, and C. Red, anti-topoisomerase II. Green, anti-histone. Blue, DAPI. Scale = 5 μm.

at the telomeres at the opposite end of the chromosomes, but separated throughout the remaining length of the chromosome. At this point, I cannot exclude the possibility that in some cases, pairing may extend to other parts of the chromosome. Nonetheless, this finding confirms the suggestion that the topoisomerase II site might coincide with a chromosomal locus. The pairing of the interphase topoisomerase II site observed *in vivo* then likely reflects the association of the heterochromatin of the X homologues.

The exact position of the site of high concentration of topoisomerase II in interphase nuclei was determined, in collaboration with Abby Dernburg, by sequentially performing *in situ* DNA hybridization and immunofluorescence on syncytial *Drosophila* embryos. After fixation with formaldehyde, embryos were hybridized with appropriate DNA probes labeled with digoxigenin or biotin and then incubated with anti-topoisomerase II. In the final step, the probes and antibody were detected with Cy5-streptavidin, rhodamine-anti-digoxigenin, and FITC goat anti-rabbit IgG. The major site of topoisomerase II localization was identified by simultaneous *in situ* DNA hybridization with probes covering the 18S and 28S rDNA sequences (Karpen et al., 1988), the 359 bp 1.688 g/cc^3 satellite (Hsieh and Brutlag, 1979), and anti-topoisomerase II immunofluorescence. In *Drosophila melanogaster*, there are approximately 220 copies of the 11.8 kb rDNA cistron in the centric heterochromatin of the X chromosome and 180 copies on the short arm of the Y chromosome (for review, see Hawley and Marcus, 1989). These tandemly repeated sequences make up the genetically defined *bobbed* (*bb*) locus, named because flies bearing less than 150 copies of the rDNA sequences are slow growing and have short and thin bristles. The 359 bp 1.688 g/cm^3 satellite is a repeated sequence that is restricted to the region of the X heterochromatin proximal to the rDNA and slightly distal to the centromere (Hsieh and Brutlag, 1979; Hilliker and Appels, 1982; Lohe et al., 1993). Approximately 11 Mb of the 20 Mb of heterochromatin of the X chromosome consist of the 359 bp repeat (Lohe et al., 1993). In addition, the most common *Drosophila* topoisomerase II cleavage

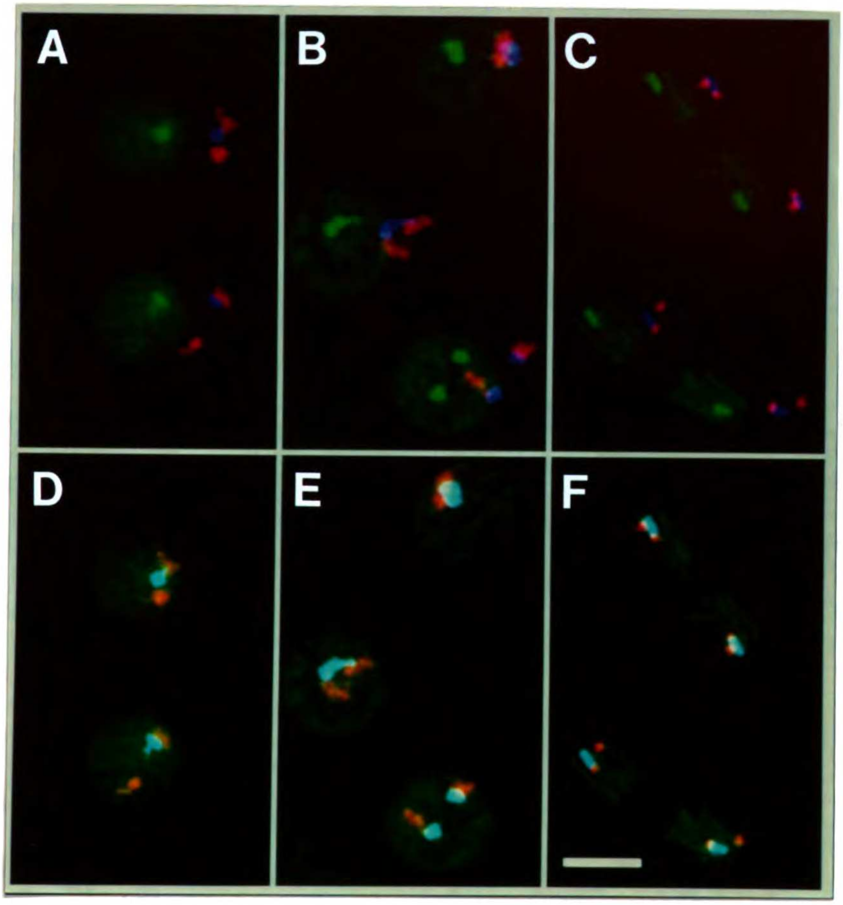

Figure 4.8. Topoisomerase II colocalizes with the 359 bp satellite in the X heterochromatin. Projections of deconvolved three-dimensional data sets showing localization of anti-topoisomerase II and *in situ* DNA hybridization probes. Green, Anti-topoisomerase II. Red, rDNA-digoxigenin. Blue, Biotinylated 359 bp 1.688 g/cc^3 satellite. Overlap of green and blue signals gives turquoise signal. Sex of embryo is determined by the number of 359 bp satellite signals in the nuclei from a given embryo. (A, D) Interphase nuclei from male nuclear cycle 12 embryo. (B, E) Interphase nuclei from female nuclear cycle 12 embryo. (C, F) Anaphase figure from male cycle 11 embryo. (A, B, C) *In situ* hybidization signals are shown offset from anti-topoisomerase II staining to allow comparison of anti-topoisomerase II and 359 bp localization. (D, E, F) *In situ* hybidization signals are shown overlayed with anti-topoisomerase II staining. Scale = 5 μm.

site has been mapped *in vivo* to a specific sequence in this 359 bp satellite (Käs and Laemmli, 1992). In interphase and anaphase, anti-topoisomerase II and the 359 bp satellite exactly coincide at the base of the X chromosome (Fig. 4.8). I will refer to the site as the topo II/359 bp site. In most interphase nuclei, the rDNA was organized in two clusters, generally located on opposite sides of the topo II/359 bp site (Fig. 4.8). By contrast the *Responder of Segregation Distorter* element, a 240 bp repeated sequence located in the centromeric heterochromatin of chromosome 2R (Wu et al., 1988), was always at least 0.5 µm away from the topoisomerase II site (data not shown). Therefore the proximity of the topoisomerase II site, the 359 bp satellite, and the rDNA is not a simple consequence of both being near the centromeres of different chromosomes. In female anaphase embryos, two topo II/359 bp sites were observed proximal and adjacent to each of the rDNA loci of the X chromosomes (Fig. 4.8D). In anaphase figures of male embryos, one topo II/359 bp site was found proximal to the rDNA locus of the X chromosome, and a weaker but reproducible site of topoisomerase II concentration was found slightly proximal to the rDNA locus of the Y chromosome (Fig. 4.9). No significant staining of the 359 bp probe was seen anywhere on the Y chromosome, suggesting the concentration of topoisomerase II near the rDNA of this chromosome occurs by another mechanism. In both sexes, the X topo II/359 bp site was proximal to the centromere relative to the rDNA and overlapped the strong DAPI staining block of heterochromatin near the X centromere. The colocalization of the 359 bp satellite and the topoisomerase II site, along with the mapping of a major topoisomerase II cleavage site to the 359 bp satellite (Käs and Laemmli, 1992), indicates that topoisomerase II concentrates at the base of the X chromosome heterochromatin by binding to the 359 bp satellite.

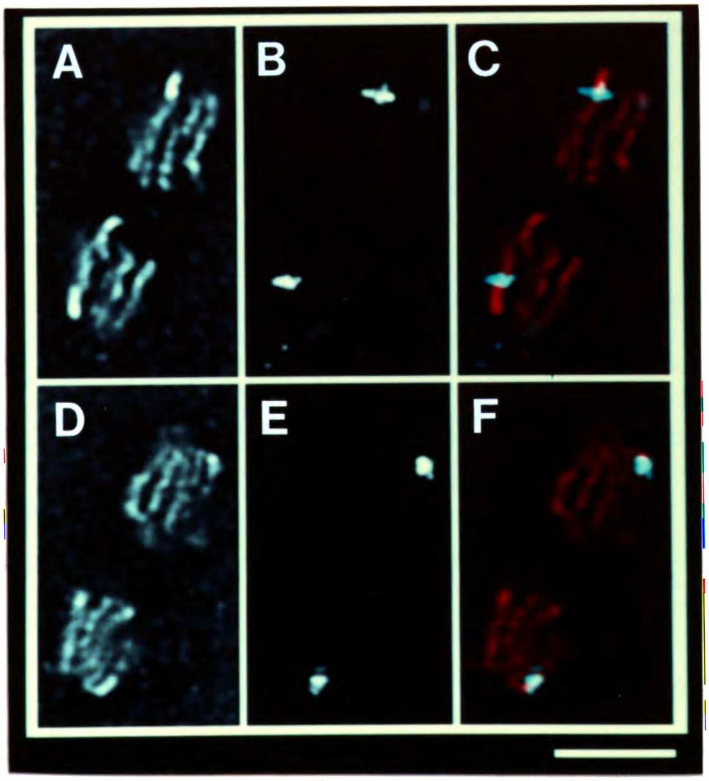

Figure 4.9. Topoisomerase II concentrates on both X and Y chromosomes, proximal to the rDNA. Deconvolved optical sections from three-dimensional data sets showing localization of anti-topoisomerase II (A, D) and *in situ* DNA hybridization probe for the rDNA labeled with digoxigenin (B, E) in a male anaphase chromosomes. (C, F) Overlay of these images showing relative distribution of anti-topoisomerase II (red) and rDNA-digoxigenin (blue). Sex of embryos is deduced from the number of topo II/359 bp sites; embryos with only one site in all nuclei are assumed to be male. (A, B, C) Optical section showing X chromosome. (D, E, F) Optical section showing Y chromosome. Scale = 5 μm.

Discussion

I have studied the distribution of topoisomerase II in *Drosophila* embryonic chromosomes by first finding fixation conditions which preserve the distribution of the enzyme observed *in vivo* and then determining its distribution relative to chromatin and bulk DNA as well as specific DNA sequences. These studies show that the localization of the enzyme is spatially and temporally highly regulated and further support the notion that the enzyme has many functions in nuclei and chromosomes. The description of the enzyme as only a structural protein of the chromosome scaffold likely underestimates the functions of the enzyme.

At the begininng of prophase, the distribution of anti-topoisomerase II, anti-histone, and DAPI along a chromosome arm are surprisingly similar. At this point in the cell cycle, the chromosomes have not folded into the helical coil that is thought to be the final step of chromosome condensation, thus allowing the visualization of the chromosome axis. In agreement with previous reports (Hirano and Mitchison, 1993; Swedlow et al., 1993), no evidence was found for the localization of topoisomerase II to a central axial chromosome core. Topoisomerase II therefore appears to be distributed throughout the chromosome, and with the exception of specific sites on the X and Y chromosomes, its concentration at a given site is determined by the local amount of DNA, or degree of compaction. Chromosome condensation may require a high local concentration of topoisomerase II to help aggregate specific DNA sequences (Adachi et al., 1989) or perhaps to guarantee an abundance of strand passing activity. As the chromatin is driven to a more condensed state, this activity might effectively catenate strands of DNA and thus allow the formation of the densely packed chromosome (Sikorav and Jannink, 1994). Continuing condensation of the chromatids in the presence of topoisomerase II could then cause the first stages of decatenation and separation of the sister DNA molecules. In this view, the length of metaphase might then allow sister separation to proceed as far as possible and thus minimize the number of sister chromatid cross-links awaiting resolution at mitosis. The loss of chromosomal topoisomerase II observed *in vivo* during prometaphase might reflect modifications of the enzyme or simply differences in the accessibility of enzyme binding sites on the condensing chromatin (see Chapter 5).

In anaphase, the distribution of topoisomerase II is much rarer than at prophase, the only point of strong colocalization with DAPI being the topo II/359 bp site. The retention of chromosomal topoisomerase II in chromosomes that have not assembled into the reforming nucleus indicates that the loss occurs specifically in nuclei and not in the cytoplasm (Fig. 4.3). This loss might be due to a specific removal of the enzyme from the nucleus or proteolysis of the enzyme (Heck et al., 1988). The clearance of the enzyme from the nucleus after mitosis might reflect an inability to convert the mitotic form(s) of the enzyme back to an interphase form(s) *in vivo.* A number of serine and threonine residues can be phosphorylated in *S. cerevisiae* and *S. pombe* topoisomerase II, primarily by casein kinase II (Cardenas et al., 1992; Shiozaki and Yanagida, 1992). Phosphorylation increases the activity of the enzyme *in vitro* and the level of phosphorylation of the enzyme increases in M phase cells (Ackerman et al., 1985; Heck et al., 1989; Cardenas et al., 1992), however little is known about the interconversion of individual topoisomerase II molecules between interphase and mitotic states. Alternatively, if the enzyme present in the anaphase chromosome is required to maintain the chromosome's structure, it may be removed to allow the transition back to an interphase nucleus.

In *Drosophila* embryonic chromosomes, topoisomerase II is concentrated on the X and Y heterochromatin, proximal to the rDNA. By far the larger of two concentrations is on the X, and it exactly coincides with the presence of approximately 11 Mb of the 359 bp satellite. This localization probably occurs by direct interaction with the DNA, since the most common drug-stimulated topoisomerase II cleavage site in the *Drosophila* genome is in the 359 bp satellite, at the sequence GAC↓CCCCCT (Käs and Laemmli, 1992). As is the case for topoisomerase II sites located near open reading frames, this site appears to be in the linker DNA between two nucleosomes (Reitman and Felsenfeld, 1990; Udvardy and Schedl, 1991; Käs and Laemmli, 1992; Kroeger and Rowe, 1992) and differs significantly from the AT rich site identified *in vitro* on naked DNA (Sander and Hsieh, 1985). At cycle 14, there are approximately 6000 nuclei in the embryo (Zalokar and Erk, 1976), and with about 3 x10^6 repeats of the satellite in every X chromosome (Lohe et al., 1993), a male embryo has roughly 1.8 x 10^{10} topoisomerase II binding sites just in the 359 bp satellite. Each embryo only has approximately 1.5 x 10^9 copies of topoisomerase II (Shelton et al., 1983; Fairman and Brutlag, 1988), and taking into account the localization of the enzyme in the rest of the genome, less than 5%, and possibly less than 1% of the 359 bp sites can be occupied at any one time. Nonetheless, this amount is enough to generate the highest concentration of topoisomerase II in the genome detectable by light microscopy. This stoichiometry suggests some specificity to the interaction between topoisomerase II and the 359 bp sequence. A small portion of the sequences might be available to the enzyme due to the absence of some other interfering factor(s). Alternatively, a small population of topoisomerase II molecules may be modified to promote interaction with the 359 bp sequence. In either case, since most of the concentration of topoisomerase at this site is lost after prophase (Swedlow et al., 1993), the binding of the enzyme to the 359 bp sequence must change during the cell cycle. It is not yet known which specific sequence, if any, localizes to the position coinciding with the high concentration of topoisomerase II on the Y chromosome. The centromeric heterochromatin of the other chromosomes do not contain concentrations of topoisomerase II (Fig. 4.4) therefore the X and Y sites are likely to function in some aspect specific to these chromosomes.

One possibility, suggested by their adjacency of the X and Y sites to the rDNA clusters, is some function associated with the nucleolus. The coincidence of topoisomerase II and the 359 bp satellite continues after the syncytial cleavages and into cycles 14 and 15, when mature nucleoli are formed (Sonnenblick, 1950; Frasch et al., 1986). In *S. cerevisiae*, low levels of topoisomerases I and II stimulate recombination specifically in the rDNA and the formation of extrachromosomal circles containing rDNA sequences (Christman et al., 1988; Kim and Wang, 1989). However, no effect on rDNA transcription was seen in a single *top2* mutant (Brill et al., 1987). The 180 kDa form of topoisomerase II has been localized to the nucleolus in Hela cells, suggesting some specific function for this form of the enzyme (Negri et al., 1992). It is possible that the centromeres of the X and Y chromosomes may be attached to a nuclear structure, and therefore the high concentrations of topoisomerase II proximal to the rDNA may prevent the propagation of superhelical stress generated by the high levels of transcription at the rDNA genes. However, an X chromosome inversion that moves the rDNA away from the topo II/359 bp site but leaves the site in its normal position, In(1)w^{m51b}, does not cause any phenotypes associated with *bb* mutations (Tartof et al., 1984).

Another aspect of rDNA function that might involve the topo II/359 bp site is rDNA recombination and magnification. In this system, the copy number of rDNA genes on the X and Y chromosomes is maintained by amplification of the rDNA sequences (Hawley and Marcus, 1989). Amplification appears to occur through general cellular recombination systems and can be induced by incorrect pairing between the X and Y chromosomes during meiosis (Hawley and Tartof, 1985). Clearly, two X chromosomes can pair at the topo II/359 bp site in mitotic interphase nuclei, but the site's ability to mediate X-Y pairing and the effect of this pairing on the rDNA association remains to be established. Insertion of a single rDNA sequence into an X chromosome unable to pair with the Y chromosome at meiosis restored limited pairing and consequent X-Y disjunction (McKee and Karpen, 1990). Pairing and nonhomologous disjunction were not induced when the rDNA sequence was inserted on an autosome, suggesting the presence of other X chromosomal elements that mediate X-Y pairing. It will be interesting to determine the localization of topoisomerase II and the 359 bp satellite during spermatogenesis.

It is also possible that the function of the topo II/359 bp site and the Y topoisomerase II sites are not related to the rDNA, but instead to some other phenomenon of these chromosomes. The sites might be required for proper mitotic segregation of the heterochromatin of the X and Y chromosomes. Spreads of mitotic *Drosophila* chromosomes normally show separated sister chromatids, however the X heterochromatin, comprising 40% of the chromosome, rarely separates (Gatti et al., 1976). The importance of this region is underscored by its size, but its function is still unknown.

The distribution of topoisomerase II during the cell cycle clearly suggests functions for the enzyme beyond that of a chromosome scaffold protein. Most of the enzyme present in nuclei and chromosomes redistributes at various points in the cell cycle. The enzyme is localized to specific DNA sequences in interphase, indicating functions in addition to chromosome condensation and segregation.

Materials and Methods

Antibodies and Probes

Rabbit anti-*Drosophila* topoisomerase II antiserum was a kind gift of Dr. Neil Osheroff (Berrios et al., 1985). Buffer A, a chromosome preserving spermine/spermidine buffer, was used for most manipulations (Belmont et al., 1987). Buffer A^- is 15 mM PIPES pH 7.0, 80 mM KCl, 20 mM NaCl, 0.1 mM EDTA, 5 mM EGTA, 2 mM spermidine and 5 mM spermine. Buffer A^+ is A^- with 5 mM β-mercaptoethanol. All fluorescent secondary antibodies (Jackson Laboratories) were affinity purified by the manufacturer and absorbed to fixed *Drosophila* embryos as previously described .

Fixation and Immunofluorescence

Staged embryos 1 - 2.5 hrs or 2.5 - 4 hrs old were collected from Oregon R *Drosophila melanogaster* adult flies grown in population cages. Embryos were fixed using equal volumes of heptane and one of the three following fixatives: 3.7% formaldehyde/Buffer A^+ for 15 minutes (Hiraoka et al., 1990); 37% formaldehyde in Buffer A^- without spermine and spermidine for 10 minutes; or methanol/0.1%

formaldehyde for 1 hour (Hiraoka et al., 1990). Fixed embryos were then devitellinized in equal volumes of heptane and 50 mM EGTA in methanol as previously described (Mitchison and Sedat, 1983). The embryos were then cooled on ice for 15 minutes and exchanged into buffer A+ in steps of 10%, 30%, 50 %, 70%, 90%, 100%, 100% buffer A^+ in methanol. The embryos were allowed to equilibrate at each step for 10 minutes. Embryos were then stained using a 1:500 dilution of anti-topoisomerase II, 1:1000 of a mouse monoclonal anti-histone ascites fluid (Chemicon) and 1:200 dilutions of Texas Red-conjugated donkey anti-rabbit IgG and fluorescein isothiocyanate-conjugated goat anti-mouse IgG. For simultaneous *in situ* DNA hybridization and anti-topoisomerase II immunofluorescence, embryos were hybridized with digoxigenin- or biotin-labeled and then processed for immunofluorescence with anti-topoisomerase II and Texas Red-conjugated donkey anti-rabbit IgG. Details of the *in situ* DNA hybridization procedure will be published elsewhere (A. Dernburg, manuscript in preparation).

Stained embryos were mounted either in 2% n-propyl gallate, 0.1 M Tris Base (not pH'd) in glycerol (Giloh and Sedat, 1982) (NPG/glycerol) or in Buffer A^- with 1 mM dithiothreitol. The glycerol mounting efficiently prevents bleaching but requires several hours of incubation at increasing concentrations of NPG/glycerol to homogeneously penetrate the embryo, however long exposure to glycerol appears to cause a slight collapse of the chromosome arm and thus affects the localization of chromosomal proteins and DNA. Short incubations with NPG/glycerol significantly slow fluorophore bleaching, but cause the formation of heterogeneous gradients of refractive index inside the embryo which effectively act as lenses and therefore can cause the apparent translation of fluorophores detected at different wavelengths of light of as much 0.2 μm in the image plane and 0.4 μm along the optical axis and magnification changes of approximately 1% in plane and along the optical axis. Therefore for high resolution protein localization, embryos were mounted in an aqueous buffer, Buffer A with 1 mM dithiothreitol. This provided enough protection against fading to collect three-dimensional images with short (0.5 - 1.0 s) exposures.

Data Collection and Image Processing

Three-dimensional images were collected with a charge-coupled device (CCD) -based epifluorescence microscope (Agard et al., 1989; Hiraoka et al., 1991). An Olympus IMT-2 inverted microscope (Olympus, Inc.) equipped with either a 60x/NA1.4 (Olympus, Inc.) or a 100x/NA1.4 (Nikon, Inc.) objective lens, a 1024 x 1024 pixel array CCD (Eastman Kodak, Inc.) and microstepper focus motor (Nanomover, Melles Griot, Inc.) was controlled by a 4D-35 workstation (Silicon Graphics, Inc.). A 1 mm diameter quartz fiber optic cable (Mitsubishi, Inc.) collected the radiation from a 100 watt mercury arc lamp, scrambled the spatial intensity variation from the arc, and filled the back focal plane of the objective with spatially homogeneous light (Kam et al., 1993). Multi-wavelength three-dimensional data were collected at a given focal plane by recording an image for each fluorophore using interference filters mounted on computer-controlled motorized wheels and fixed multiple pass dichroic mirrors (Chroma Technology Corp.). The focal plane was then changed by 0.2 μm, and the process repeated. The pixel size for the images was 0.074 μm x 0.074 μm for the 60x lens (with a 1.5x Optivar lens added to the light path) and 0.0678 μm x 0.0678 μm for the 100x lens. Multiple wavelength images were first processed to compensate for temporal fluctuations in lamp intensity and fluorophore bleaching using the program CCDCOR (J. R. S., M. R. Paddy, A. S. Belmont, D. A. Agard, unpublished results). Out-of-focus blurring was removed from images using iterative, constrained, three-dimensional deconvolution (Agard et al., 1989; Hiraoka et al., 1991). This process uses an empirical measure of the blurring of an object imaged by the objective lens to move the out-of-focus photons back to their original positions. Deconvolved images of anti-topoisomerase II, anti-histone, and DAPI were then computationally aligned using a simplex minimization to correct for wavelength-dependent translations, especially along the optical axis, and magnification changes that occur due to the non-ideal refractive index of the sample and residual aberrations in the objective lens (see Chapter 2). DAPI and anti-topoisomerase II images were aligned to anti-histone images. The images of embryos stained by immunofluorescence and *in situ* DNA hybridization were not aligned, since the misregistration, while detectable, did not affect the interpretation of the images.

After alignment, the distribution of anti-topoisomerase II, anti-histone, and DAPI along the chromosome axis was determined by tracing the folding of each chromosome in three-dimensional images of prophase nuclei using an interactive modeling program, PRISM (Chen et al., 1989). The tracing was greatly aided by using the data from all three probes since, for example, ambiguities in the DAPI image often could be resolved in the anti-histone image. This generated a model which followed the center of each chromosome. The model was then used to straighten the intensities within 0.14 μm of the center of the chromosome using the program STRAIGHT3D (Chen et al., 1989; Hiraoka et al., 1990). This produced a cytological map of the distribution of DAPI, anti-histone, and anti-topoisomerase II along the chromosome arm. The mean intensity of each of the three probes was then calculated at every position along the map (defined by the effective pixel size of the original image, 0.0678 μm x 0.0678 μm) and plotted as a per cent of the maximum intensity after subtraction of the minimum mean intensity.

To cut out the chromosomal intensities shown in Figure 4.7, the models of the X chromosomes in nuclei were used to cut out the intensities within 7 pixels, or 0.47 μm, of the model. Stereo projections of the resulting three-dimensional image were then calculated using the program ROTFAST (Agard et al., 1989).

Acknowledgments

I am grateful to Gary Karpen for providing clones for *Drosophila* rDNA and Chung-I Wu for providing a clone of the *Responder* repeat. All of the *in situ* DNA probes, as well as the hybridization, were the work of Abby Dernburg. Many of the ideas in this Chapter are the result of a collaboration with her.

Chapter 5: Multiple Chromosomal Populations of Topoisomerase II Detected In Vivo by Time-Lapse, Three-Dimensional Wide Field Microscopy

Summary

DNA topoisomerase II is required for proper chromosome condensation and segregation during mitosis and may function in the structural organization of chromosomes. The localization of topoisomerase II *in vivo* was studied by recording time-lapse three-dimensional datasets of living *Drosophila melanogaster* embryos injected with rhodamine-labeled topoisomerase II. These images show that topoisomerase II is concentrated at specific sites within the interphase nucleus and that this localization is temporally regulated. During mitosis, topoisomerase II is a component of chromosomes, but pools of topoisomerase II leave the chromosomes after prophase and after anaphase. Overall, 70% of the enzyme present in the early prophase chromosome leaves the nucleus and diffuses into the cytoplasm during mitosis. The enzyme is not restricted to a central chromosome axis, but is distributed uniformly throughout the chromosome. The localization of the enzyme thus correlates with its role in chromosome condensation and segregation. Rather than being solely a structural protein, topoisomerase II appears to localize at the sites on the chromosome where it is required.

Introduction

The replication and transcription of DNA during interphase and the segregation of chromosomes at mitosis all occur within the context of the chromosome. An understanding of these processes must include a description of this compact and highly ordered structure. A number of non-histone proteins have been implicated in the regulation of higher-order chromatin and chromosome structure. Of these, one of the best studied is DNA topoisomerase II, an enzyme that catalyzes strand passing of double-stranded DNA in an ATP-dependent fashion (for review, see Wang, 1985). This activity is necessary for replication termination, when intertwined strands of DNA created during replication are decatenated (Sundin and Varshavsky, 1980). The active enzyme is required for complete condensation of chromosomes as well as the proper segregation of sister chromatids at mitosis (DiNardo et al., 1984; Newport and Spann, 1987; Uemura et al., 1987; Holm et al., 1989; Wood and Earnshaw, 1990; Adachi et al., 1991; Downes et al., 1991; Shamu and Murray, 1992).

While the requirement of topoisomerase II for segregation probably reflects the need for strand-passing activity for replication termination (Uemura et al., 1987; Holm et al., 1989; Downes et al., 1991; Shamu and Murray, 1992), its role in chromosome condensation is not understood. The strand passing activity of topoisomerase II may be required to allow the structural transitions which occur during condensation. Alternatively, the enzyme may simply bind specific sites on the chromosome and thus help to organize the DNA in the chromosome. Such a structural role was suggested by the localization of topoisomerase II to the chromosome scaffold (Earnshaw et al., 1985; Gasser et al., 1986). The scaffold, or nuclear matrix, is defined as the biochemical remnant of chromosomes or nuclei following extraction of histones with high salt or ionic detergents and treatment with DNAase (Lewis and Laemmli, 1982; Mirkovitch et al., 1988). Specific DNA sequences called scaffold (or matrix) attachment regions (SARs) have been identified that bind specifically to the scaffold (Amati and Gasser, 1988; Izaurralde et al., 1988; Mirkovitch et al., 1988). A/T-rich consensus sites for topoisomerase II (Sander and Hsieh, 1983) are often found in SARs (Gasser and Laemmli, 1986), although at least some topoisomerase II consensus sites in SARs are not available to topoisomerase II *in vivo* (Udvardy and Schedl, 1991; Käs and Laemmli, 1992). These data have been used to suggest a role for topoisomerase II in organizing the structure of the chromosome. In this model, SARs attach the bases of chromatin loops to the scaffold and SAR attachment is mediated by topoisomerase II (for review, see Gasser and Laemmli, 1987).

One way to assess the role of topoisomerase II in chromosome structure is to accurately describe its chromosomal localization *in vivo*. I have therefore examined the distribution of topoisomerase II during the cell cycle of living *Drosophila melanogaster* embryos. The *Drosophila* embryo undergoes 14 rapid, nearly synchronous mitotic cycles as a multi-nucleated single cell (Zalokar and Erk, 1976). After the formation of a blastoderm during cycle 10, most of the nuclei pass through the remaining cycles near the surface of the embryo and thus provide a system where the molecular and structural dynamics of the mitotic cycle can be examined (Fuchs et al., 1983; Hiraoka et al., 1990; Paddy et al., 1990). I have microinjected embryos with fluorescently labeled topoisomerase II and monitored the distribution of topoisomerase II *in vivo* by recording time-lapse three-dimensional movies with a charge-coupled device (CCD) -based wide-field fluorescence microscope. These experiments show that the localization of the enzyme in the nucleus and on chromosomes is spatially and temporally regulated. There are at least three separate populations of topoisomerase II in the nucleus. Their behavior suggests that separate pools are responsible for chromosome condensation during prophase and chromosome segregation at mitosis. Most of the enzyme present in the interphase chromatin leaves during mitosis and therefore cannot play a purely structural role in the organization of chromosomes.

Results

Purification and Labeling of Topoisomerase II

The study of the *in vivo* distribution of topoisomerase II required the use of a specific probe for visualization of the enzyme. Our approach was to develop a method to fluorescently label topoisomerase II while maintaining its full enzymatic activity. Topoisomerase II was purified from 6-18 hr old *Drosophila* embryos (Shelton et al., 1983) and shown to be recognized by a monoclonal antibody specific for *Drosophila* topoisomerase II (Fig. 5.1A). The purified fraction decatenated kinetoplast DNA (Fig. 5.1B), a highly catenated substrate, relaxed supercoiled circular DNA in an ATP-dependent fashion (data not shown), and possessed a specific activity similar to that previously reported (Shelton et al., 1983). In an effort to protect the active site of topoisomerase II during labeling, the enzyme was adsorbed onto phosphocellulose and then reacted with tetramethylrhodamine. This approach was based on a protocol developed for the labeling of calf thymus histones (Minden et al., 1989). After the labeling reaction was complete, rhodamine-topoisomerase II (rhod-topo II) was eluted from the phosphocellulose with high salt. This procedure allowed the labeling and recovery at high concentration (~1mg/ml) of small fractions of enzyme (20-150 μg of protein, Fig. 5.1A). Rhod-topo II possesses full ATP-dependent, enzymatic activity (Fig. 5.1B) and can therefore be used for *in vivo* fluorescence experiments.

Data Collection

Rhod-topo II was microinjected into cycle 9-10 *Drosophila* embryos. At this stage in development, the embryos had formed a multi-nucleated syncytium, so the injected rhod-topo II diffused throughout the embryo. After waiting for at least one complete mitosis for the injected rhod-topo II to incorporate into nuclei and chromosomes, I collected time-lapse three-dimensional images of rhod-topo II injected embryos by repeatedly recording 8 or 12 optical sections at 0.25 μm or 0.5 μm intervals, respectively. The out-of-focus information in each three-dimensional data stack was then removed by iterative, constrained deconvolution (Agard et al., 1989). This method uses an experimental measurement of the image blurring caused by the microscope objective lens, the point-spread function, to move the out-of-focus photons back to their correct positions. Comparison of the deconvoluted results to the unprocessed data (Fig. 5.2A) and images generated using only a two-dimensional projection of a three-dimensional image are shown (Fig. 5.2B; Hiraoka et al., 1989). The use of three-dimensional

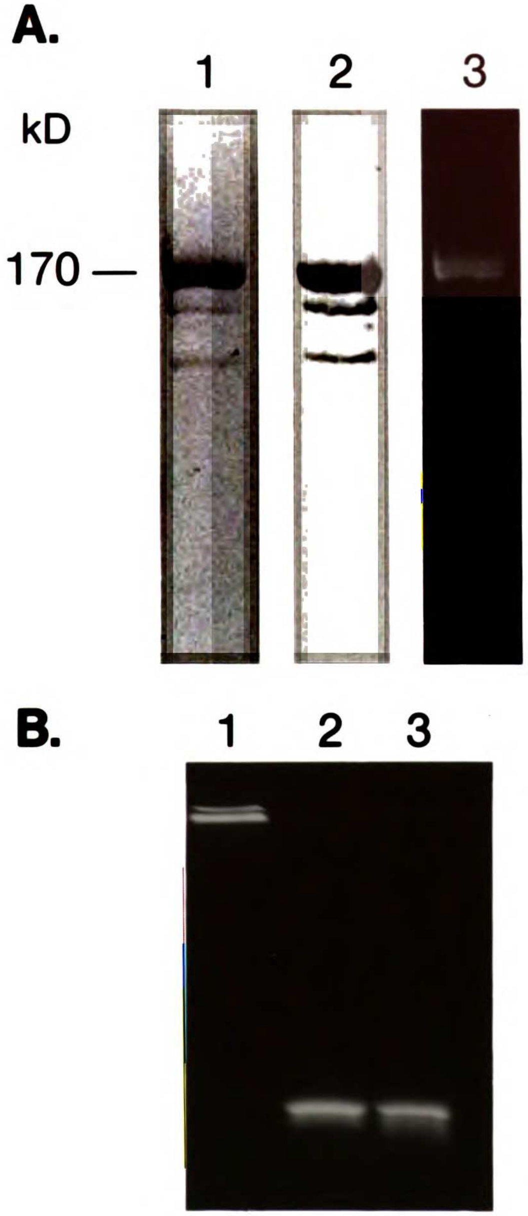
A.
1
2
3
kD
170 —
B.
1
2
3

Figure 5.1. Characterization of Purified Topoisomerase II and Rhod-topo II. (A) SDS-PAGE of topoisomerase II preparations. M_r of band is shown. The major component of the final fraction is a protein of M_r 170 kD, similar to the molecular weight of *Drosophila* topoisomerase II. Two minor contaminating bands are probably derived from the parent 170 kD band. These proteolytic fragments are characteristic of *Drosophila* topoisomerase II preparations, occur even in the presence of high concentrations of protease inhibitors (Hsieh, 1983; Shelton et al., 1983), and have been shown to be generated during the preparation of nuclei from embryos (Whalen et al., 1991; J. Swedlow, unpublished observations). Lane 1, SDS-PAGE of purified topoisomerase II stained with Commassie Blue. Lane 2, Immunoblot after SDS-PAGE of purified topoisomerase II. Blot was probed with monoclonal antibody against *Drosophila* topoisomerase II. Lane 3, SDS-PAGE of rhod-topo II. Fluorescent protein was detected on a UV transilluminator. (B) Decatenation activity assay of topoisomerase II preparations. Highly catenated kinetoplast DNA (kDNA) was incubated with 1 mM ATP and purified topoisomerase II or rhod-topo II (see Materials and Methods). Catenated kDNA networks do not enter the gel and are trapped in the wells. In the presence of strand passing activity (i.e., topoisomerase II), free circular DNA migrates into the gel. Lane 1, kDNA in the absence of topoisomerase II activity. Lane 2, 0.3 µg kDNA incubated with 30 ng purified topoisomerase II. Lane 3, 0.3 µg kDNA incubated with 30 ng rhod-topo II. The specific activity of rhod-topo II was similar to the unlabeled enzyme.

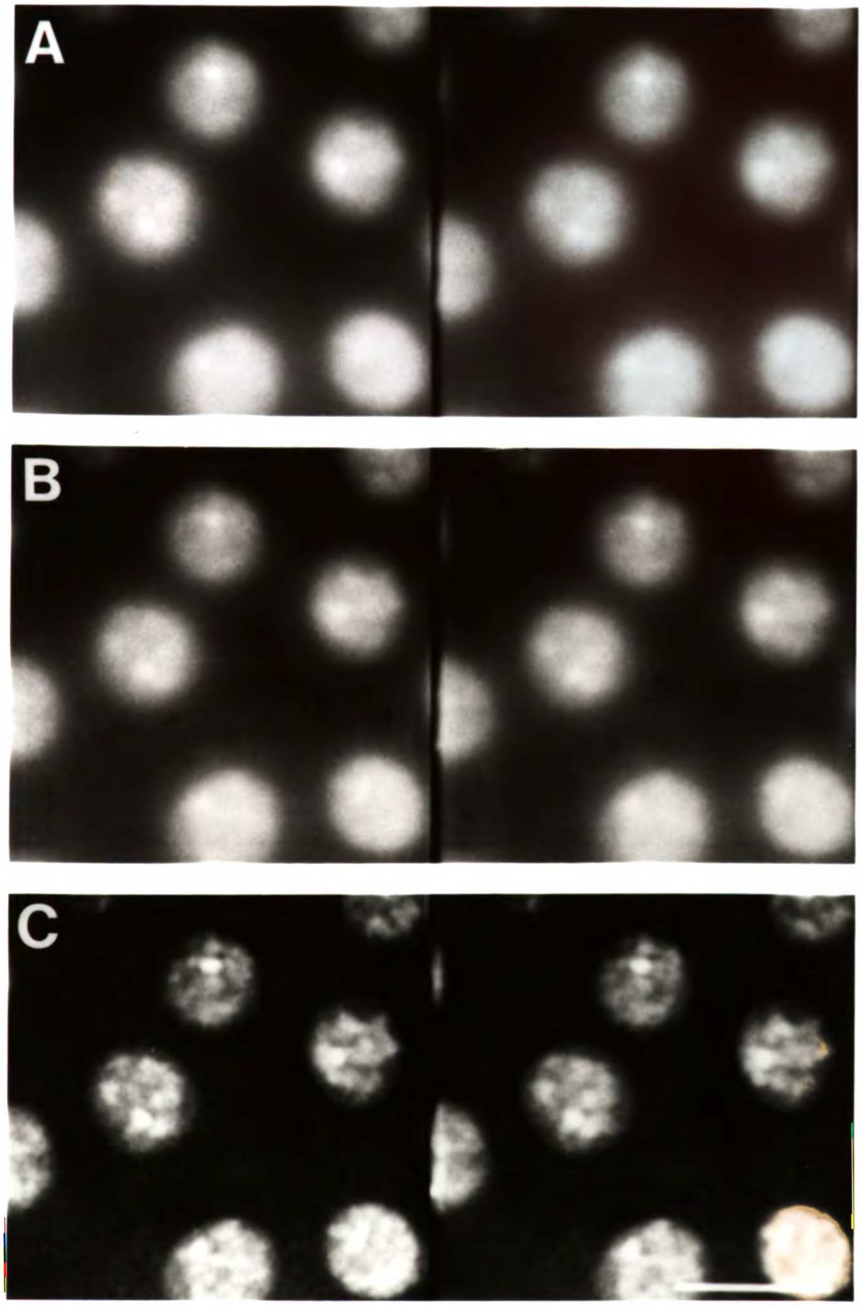

Figure 5.2. Comparison of Image Processing Techniques for Time-Lapse Three-Dimensional Data. Images from a cycle 12 late interphase embryo injected with rhod-topo II were used for the comparison of different processing schemes. Each image is a projection of 12 optical sections separated by 0.5 µm. All images were scaled to their own minimum and maximum grey level values. (A) Projection image without further processing. (B) After projection as in (A), the image was filtered with an iterative, constrained two-dimensional decovolution algorithm using the $Z^*=0$ plane of the optical transfer function (Hiraoka et al., 1989). (C) Projection image after optical sections were processed with an iterative, constrained three-dimensional deconvolution algorithm (Agard et al., 1989). This method uses the original three-dimensional data rather than the two-dimensional projection shown in (A). Scale bar = 10 µm.

deconvolution (Fig. 5.2C) substantially improves the resolution in all three dimensions and therefore allows the study of intranuclear structures that are otherwise difficult to discern. While a properly configured laser scanning confocal microscope could produce three-dimensional images of similar quality from a static specimen, the speed of the embryonic syncytial nuclear cycles and the extreme photosensitivity of embryos microinjected with fluorescent compounds demands short exposures (50-200 msec in these experiments) at very low light levels. This work was only made possible using the high resolution and 10 to 100-fold higher sensitivity provided by a CCD-based wide field microscope coupled with iterative three-dimensional deconvolution.

Topoisomerase II in Living Embryos

After injection into early *Drosophila* embryos, rhod-topo II incorporates into the nuclei and chromosomes of the living embryo. Figure 5.3 shows stereo pairs of selected frames from a time-lapse movie of a cycle 13 embryo. In general, rhod-topo II is distributed throughout the interphase nucleus (Fig. 5.3A), but the distribution changes during the cell cycle and is concentrated in one or two sites on the periphery of each nucleus (Fig. 5.3A, B). At prophase, rhod-topo II was localized in condensing chromosomes, although non-chromosomal rhod-topo II was clearly visible in the nuclei (Fig. 5.3C). In addition, the concentrated sites seen in interphase disappeared as the chromosomes condensed. Rhod-topo II remained a component of chromosomes throughout mitosis (Fig. 5.3C-F). In some cases it was possible to count the arms of the condensed chromosomes detected with rhod-topo II and establish that all chromosomes were stained with rhod-topo II. Fluorescence intensity in the nuclei and chromosomes appears to decrease throughout mitosis. The general features of this localization are similar to those seen in fixed *Drosophila* embryos and larval neuroblasts stained by indirect immunofluorescence with polyclonal and monoclonal antibodies against *Drosophila* topoisomerase II (J. R. Swedlow, unpublished observations; Berrios et al., 1985). These observations, along with *in vivo* experiments using microinjected

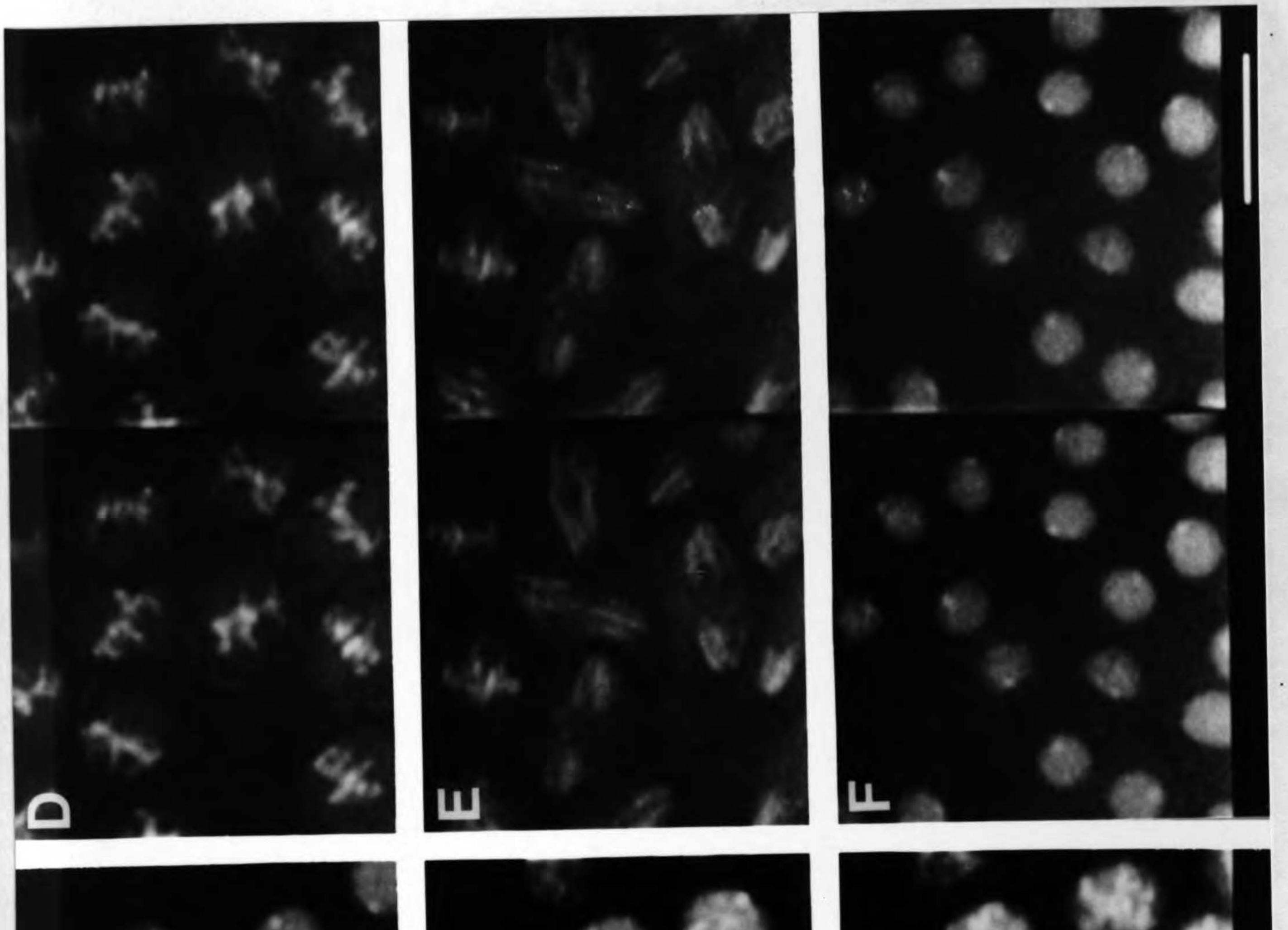
A
B
C
D
E
F

Figure 5.3. Nuclear and Chromosomal Distribution of Topoisomerase II In Vivo. Stereo pairs of selected frames from one movie of a *Drosophila* embryo injected with rhod-topo II. Images shown are from nuclear cycle 13. Exposure time for each section was 0.2 second. Data was processed as in Figure 5.2C and stereo projections were calculated at -5° and 5° tilt (Agard et al., 1989). Cell cycle stages and elapsed time (minutes:seconds) from the beginning of nuclear cycle 13 at 20°C: (A) Early interphase, 1:55; (B) Late interphase, 11:53;. (C) Prophase, 19:10; (D) Metaphase, 22:37; (E) Anaphase, 24:32; (F) Early interphase cycle 14, 29:31. Scale bar = 10 μm.

anti-topoisomerase II antibody (see below) argue that rhod-topo II is a faithful probe for the *in vivo* localization of topoisomerase II.

Multiple Populations of Topoisomerase II During M Phase

A description of the changes of the enzyme's localization should suggest where and when the enzyme is functioning. Since the time-lapse images of the *in vivo* distribution of topoisomerase II are digital data, they provide a method for measuring the changes in topoisomerase II content of the nucleus, chromosomes, and cytoplasm during the cell cycle. The concentrations of nuclear and cytoplasmic topoisomerase II during two sequential mitotic cycles were plotted as a function of time (Fig. 5.4A). Nuclear topoisomerase II increases throughout interphase and reaches a maximum in late interphase, but then decreases throughout prophase and prometaphase. Simultaneously, the cytoplasmic concentration increases. The loss of nuclear topoisomerase II is due to the diffusion of non-chromosomal enzyme (Fig. 5.3C) from the nucleus into the cytoplasm and, as shown below, the loss of enzyme from the chromosome itself. The nuclear concentration continues to decrease during metaphase, but at a much reduced rate. After anaphase movement begins the nuclear concentration decreases again and reaches a minimum in late telophase. Since the embryo nuclei enter mitosis at slightly different times due to the presence of a mitotic gradient (Foe and Alberts, 1983), a steady metaphase topoisomerase II concentration might be masked by averaging of the slightly aynchronous nuclear population used in Figure 5.4. In fact, the mean enzyme concentration in synchronous nuclei remains relatively constant throughout most of metaphase (Fig. 5.4B). It therefore appears that the nuclear topoisomerase II concentration decreases during prophase and prometaphase, changes little during metaphase, and decreases again during anaphase. This behavior was observed in all nuclei in seven time-lapse recordings of rhod-topo II distribution and three recordings of fluorescently labeled anti-topoisomerase II (see below).

These changes in toposiomerase II concentration are strikingly different from those observed in nuclei of embryos injected with fluorescently-labeled histones H2A/H2B (fl-histones): nuclear histone concentration changes little during interphase, increases throughout prophase, reaches a maximum at metaphase, and then decreases during anaphase, but not to the same degree as topoisomerase II (Fig. 5.4C). Furthermore, the cytoplasmic concentration of fl-histones remains constant throughout the cell cycle; there is no significant loss of chromosomal histones. The decrease in chromosomal histone concentration is therefore due to chromosome segregation and decondensation occurring during anaphase.

While this analysis showed the general trends of topoisomerase II localization, the absolute value of the concentration changes varied between datasets. This resulted from the movement of portions of the nuclei out of the optical sectioning volume during the cell cycle (see Materials and Methods). To determine the relative amounts of topoisomerase II lost during the stages of mitosis, the mean chromosomal concentration was measured at early prophase, metaphase, and late telophase. These values were then normalized to the maximum chromosomal concentration at prophase (Table 5.1). A similar analysis was performed on data from embryos injected with fl-histones. While the chromosomal topoisomerase II concentration decreased during the cell cycle, the chromosomal histone concentration increased after prophase and reached a maximum when the chromosomes were most condensed at metaphase (Table 5.1). The histone concentrations were therefore used to normalize the topoisomerase II concentrations for the effects of chromosome condensation, segregation, and decondensation. The chromosomal concentration of topoisomerase II decreased by 60% during prophase and prometaphase and a further 10% during anaphase. This second pool represents 25% of the metaphase chromosomal topoisomerase II. Both of these transitions were complete within 2 minutes and can be accounted for by passive diffusion of topoisomerase II from the chromosomes into the cytoplasm.

A.

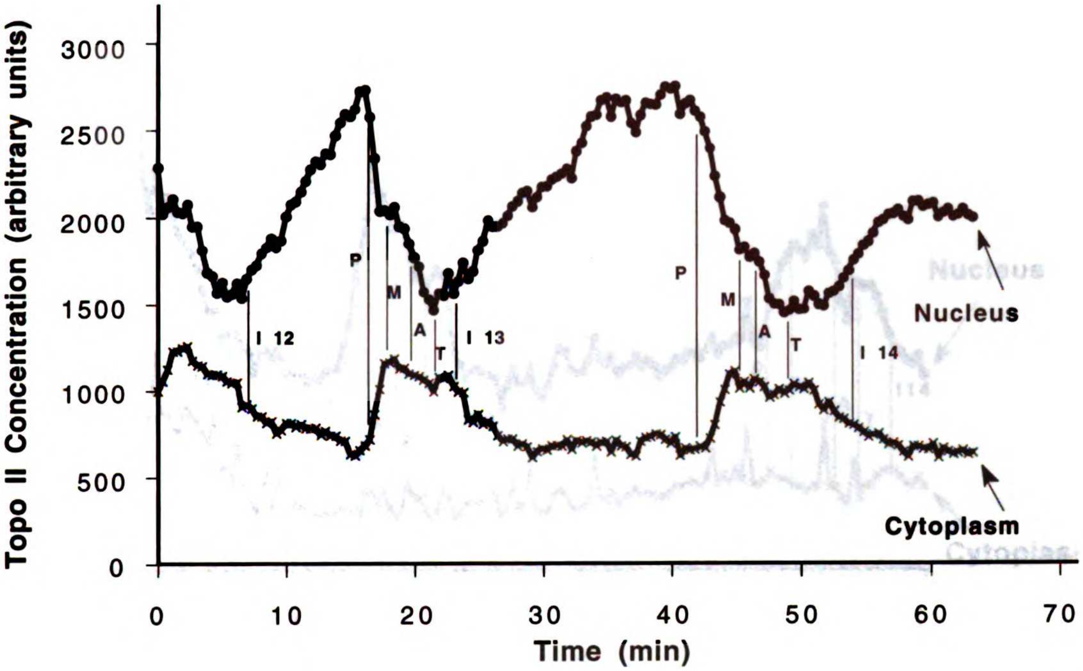
Topo II Concentration (arbitrary units)
3000
2500
2000
1500
1000
500
0
0
10
20
30
40
50
60
70
Time (min)
I 12
P
M
A
T
I 13
P
M
A
T
I 14
Nucleus
Cytoplasm

B.

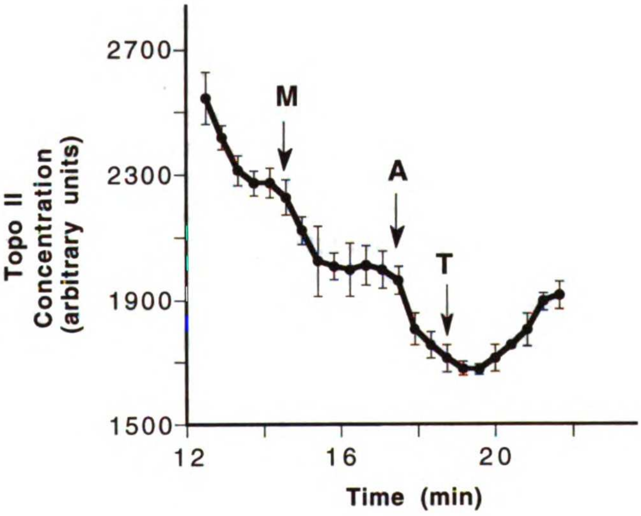
Topo II Concentration (arbitrary units)
2700
2300
1900
1500
12
16
20
Time (min)
M
A
T

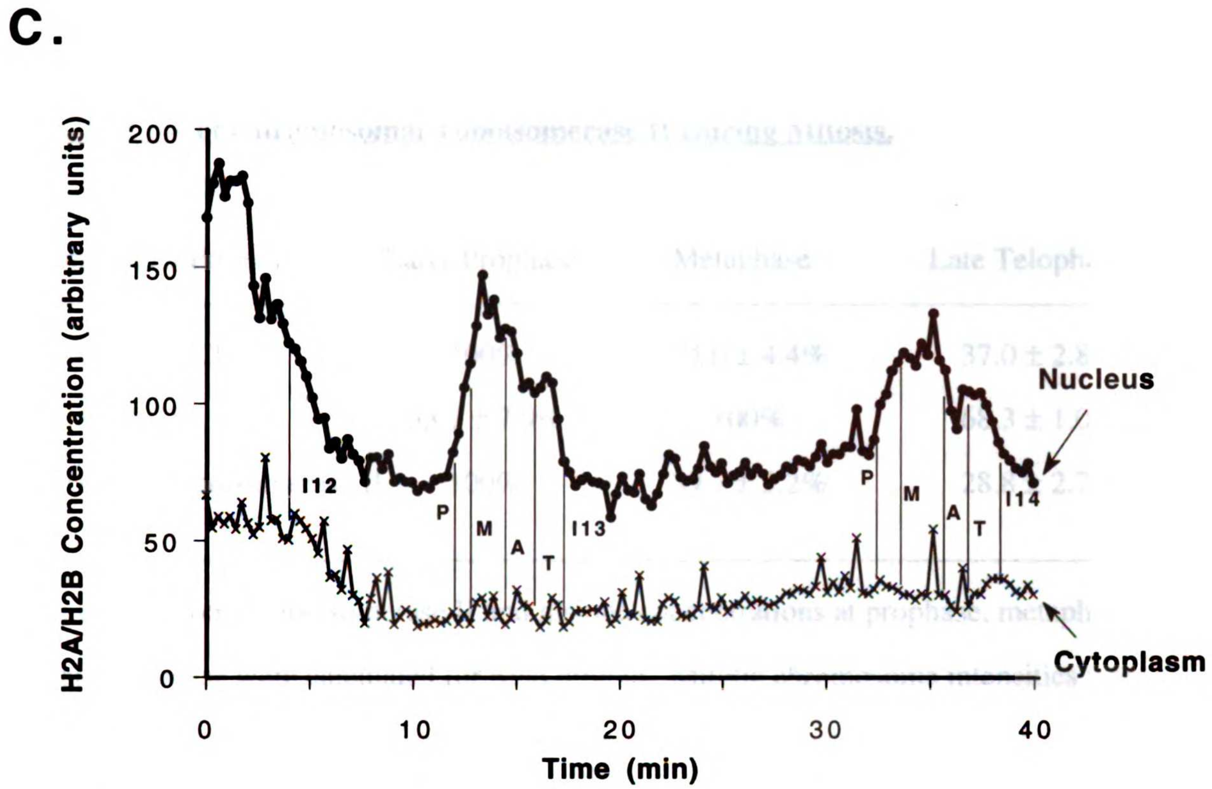

Figure 5.4. Cell Cycle Changes in Nuclear and Cytoplasmic Topoisomerase II and Histone Concentration. The concentration of rhod-topo II or Cy5-histone H2A/H2B inside ("Nucleus") and outside ("Cytoplasm") all of the nuclei or chromosomes in a time-lapse three-dimensional recording of a rhod-topo II-injected embryo. Calculation of concentration (total nuclear or cytoplasmic intensity ÷ number of nuclear or cytoplasmic pixels) normalizes for nuclear volume changes during interphase and division of nuclei at anaphase and also averages over all intranuclear structures. Nuclear and cytoplasmic volumes were defined as described in Materials and Methods. All nuclei in each frame were used for the calculation of nuclear concentration. The term "nuclear" or "nucleus" is used to refer to the volume of nuclei and/or chromosomes throughout the nuclear cycle. The trends in topoisomerase II distribution shown here are similar to the intensity changes shown in Figure 5.3. (A) Nuclear and cytoplasmic concentrations of rhod-topo II. Inset, The mean nuclear topoisomerase II concentration of three synchronous nuclei during mitosis of cycle 13 from a different embryo. Nuclear concentrations from three individual nuclei were normalized using their respective concentration minima and maxima and then averaged. Normalization corrects relative concentration differences between nuclei caused by their different distances from the injection site. Topoisomerase II concentration changes little during the latter part of metaphase. This behavior occurs in all seven of my time-lapse recordings of rhod-topo II *in vivo* and all three recordings of Texas Red-anti-topo II *in vivo*. The error bars represent the standard deviations from the mean for each point. (B) Nuclear and cytoplasmic concentrations of Cy5-labeled histones H2A and H2B. (-•-), nuclear concentration. (x), cytoplasmic concentration. Cytological stages are indicated: I, interphase; P, prophase; M, metaphase; A, anaphase; T, telophase. The number after "I" indicates the beginning of a new nuclear cycle. "I 12" = beginning of cycle 12 interphase; "I 13" = beginning of cycle 13 interphase. The number of nuclei used for the calculation varies during each cycle, but on average there were 7 nuclei in cycle 12, 10 in cycle 13, and 16 in cycle 14.

Table 1. Loss of Chromosomal Topoisomerase II During Mitosis.

Chromosomal Protein	Early Prophase	Metaphase	Late Telophase
Topoisomerase II	100%	74.0 ± 4.4%	37.0 ± 2.8%
Histone 2A/2B	53.7 ± 7.9%	100%	68.3 ± 1.0%
Normalized Topoisomerase II	100%	39.7 ± 3.2%	28.8 ± 2.7%

Mean chromosomal topoisomerase II and histone concentrations at prophase, metaphase, and late telophase were calculated for each protein. Mitotic chromosome intensities were sampled by manually picking pixels contained within chromosomes in each optical section from recordings of 7 mitotic cyles. At least 3000 individual pixels were sampled for each mitosis. The concentrations at each point in the cell cycle were then normalized to the maximum concentration during the cell cycle for each protein. The maximum chromosomal topoisomerase II intensity is at prophase; the maximum histone intensity is at metaphase. To normalize the topoisomerase II concentrations for changes due to chromosome condensation and segregation, the changes in topoisomerase II concentration were normalized by the changes in histone concentration. The errors expressed for each value are the standard deviations of each of the means.

The data shown in Figures 5.3 and 5.4 suggest that there are at least three pools of topoisomerase II in the chromosome: one that leaves the chromosome after prophase, another that leaves after metaphase, and one that remains with the chromosomes throughout the mitotic cycle. Two of these pools leave the chromosome after the completion of an important function of topoisomerase II: one after chromosome condensation and the other after chromosome segregation. This suggests that the different pools might be responsible for the different functions of topoisomerase II.

One intriguing difference between histones and topoisomerase II is that the concentration of topoisomerase II increases during interphase while the concentration of histones remains fairly constant until prophase. Because the amount of fluorescent protein is constant in these experiments, this distinction reflects differences in the net amounts of proteins imported into the nucleus. This presumably occurs either because of differences in the rate of import of the two proteins throught the nuclear pores, or more likely, because of differences in the number of binding sites available to the proteins. This result suggests that while assembly of histones onto DNA occurs during DNA replication, topoisomerase II may associate with DNA independently of replication.

The Interphase Localization of Topoisomerase II is Spatially and Temporally Regulated

Although rhod-topo II is localized throughout the interphase nucleus, it concentrates in specific sites and in a fibrous network at specific times during interphase. I have observed the sites as early as interphase of nuclear cycle 11, however they may be present earlier than this. The sites are first clearly visible in late telophase but in some cases can be identified in anaphase. There is at least one but never more than two sites in each nucleus and they are found close to the nuclear periphery and always located in the half of the nucleus closest to the embryo cortex. This is the region which contains the constitutive heterochromatin (Foe and Alberts, 1985; Hiraoka et al., 1990). They are therefore distinct from the previously described condensation foci observed in late telophase and early prophase (Hiraoka et al., 1989). In early interphase the sites have a diameter of 0.4-0.5 μm; there is no detectable intensity or size difference between sites from single and double site nuclei during early interphase (Fig. 5.3, Fig. 5.5A, B). The intensity of the sites changes during the cell cycle. At roughly 30% of the way through interphase (5.7 ± 0.6 min in cycle 13, number of nuclei = 20; the length of cycle 13 interphase at 25°C is approximately 16 min; Foe and Alberts, 1983), the sites become diffuse and decrease in intensity, sometimes disappearing altogether (Fig. 5.5C, D). However, after approximately 60% of interphase has passed (10.5 ± 1.4 min), the sites reappear (Fig. 5.5E, F) and then continue to grow in intensity until the onset of prophase. There is a clear difference between the sites in single- and double-site nuclei during this part of interphase. Sites from single-site nuclei are 1.1-1.3 μm in diameter while those from double-site nuclei measure 0.55-0.65 μm, however there is no significant difference in the intensity level between the two types of sites (Fig. 5.5F). As interphase ends and prophase begins, the chromosomes condense and the intensity of the sites decreases until they are indistinguishable from the condensed chromosomes in prophase. While I have concentrated I analysis on sites of topoisomerase II concentration in syncytial nuclei, I also observed interphase sites in nuclei after cellularization.

The size and apical position of the sites suggest that they might be part of nucleoli, although it has been reported that syncytial embryonic nuclei do not have nucleoli (Sonnenblick, 1950). To determine if topoisomerase II is a component of the nucleolus in other cell types, intact, unsquashed polytene nuclei were probed with a Texas Red-labeled anti-*Drosophila* topoisomerase II monoclonal antibody (P2G3). While topoisomerase II is detected on all chromosomes, the brightest staining feature in these nuclei is the nucleolus (Y. Urata, S. J. Parmelee, J. R. Swedlow, unpublished observations). Therefore, the syncytial interphase sites may be early nucleoli not previously detected.

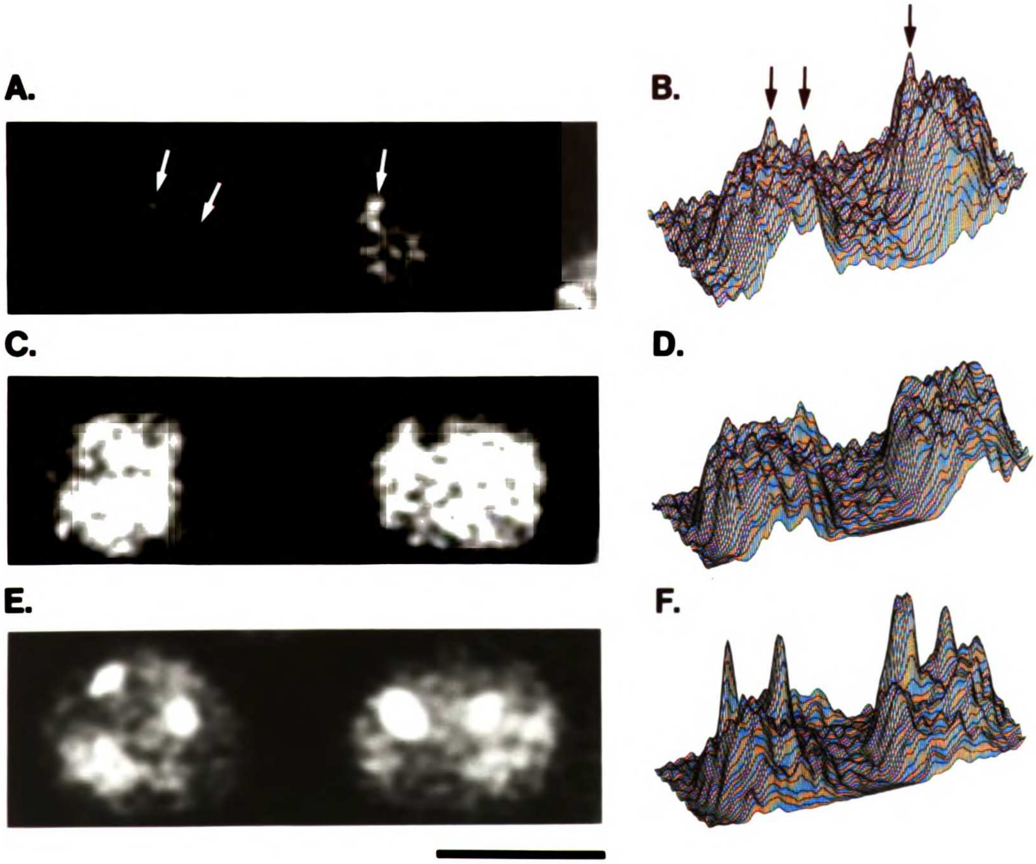

Figure 5.5. Topoisomerase II Concentrates at Specific Sites in Interphase. Two nuclei followed through the three parts of cycle 13 interphase. The nucleus on the left side of the image has two interphase sites; the nucleus on the right side has one. (A,B) First third of interphase. (C,D) Middle interphase. (E,F) Last third of interphase. (A, C, E) Images of nuclei detected with rhod-topo II. (B, D, F) Topographic plots of intensity from images in (A, C, E), respectively. Arrows in (A) and (B) indicate the position of sites in early interphase. Topoisomerase II interphase sites are visible in early interphase, diffuse in mid-interphase, and discrete and much brighter in late interphase. Scale bar = 5 μm.

During the latter part of interphase, rhod-topo II is also assembled into fibers which are clearly visible against an otherwise homogeneous nuclear background (Fig. 5.3B, 5.5E). It has not yet been possible to determine if the fibers seen in the last third of interphase are the precursors of prophase chromosomes.

Topoisomerase II is Distributed Uniformly Throughout Chromosome Arms *In Vivo*

Topoisomerase II has been localized to the mitotic chromosome scaffold in extracted and fixed preparations (Earnshaw and Heck, 1985; Gasser et al., 1986). In general, the scaffold is described as a proteinaceous axial core which runs the length of the extracted chromosome. *Drosophila* cleavage nuclei are an ideal system to study the localization of topoisomerase II in mitotic chromosomes as they are less condensed than chromosomes from metaphase arrested tissue culture cells or from *Drosophila* chromosomes from later in development (Belmont et al., 1987). Figure 5.6 shows sequential frames from a time-lapse, three-dimensional dataset recorded during anaphase of cycle 13. Chromosomes visualized *in vivo* using fluorescently labeled histone H2A/H2B appear to be 0.4-0.5 μm wide at prophase, metaphase, and anaphase (data not shown). The chromosomes detected by rhod-topo II in Figure 5.6 are also uniformly 0.4-0.5 μm wide. Similar sizes were measured at prophase and metaphase. These data are inconsistent with the suggestion that topoisomerase II is a component of an axial protein core running the length of the chromosome (Gasser et al., 1986).

Rhod-Topo II Leaves Chromosomes During Mitosis of Nuclear Cycle 14

The 14th cell cycle of the *Drosophila* embryo is much slower than the initial 13 rapid nuclear divisions, and occurs after cell membranes have formed around each of the nuclei (Foe and Alberts, 1983). The cell cycle passes through a G_2 phase and the mitotic synchrony characteristic of the earlier divisions is replaced by a rough synchrony between groups of cells which appear to share the same fate (Foe, 1989). The different groups, or mitotic domains, progress through mitosis in a defined order. To determine if

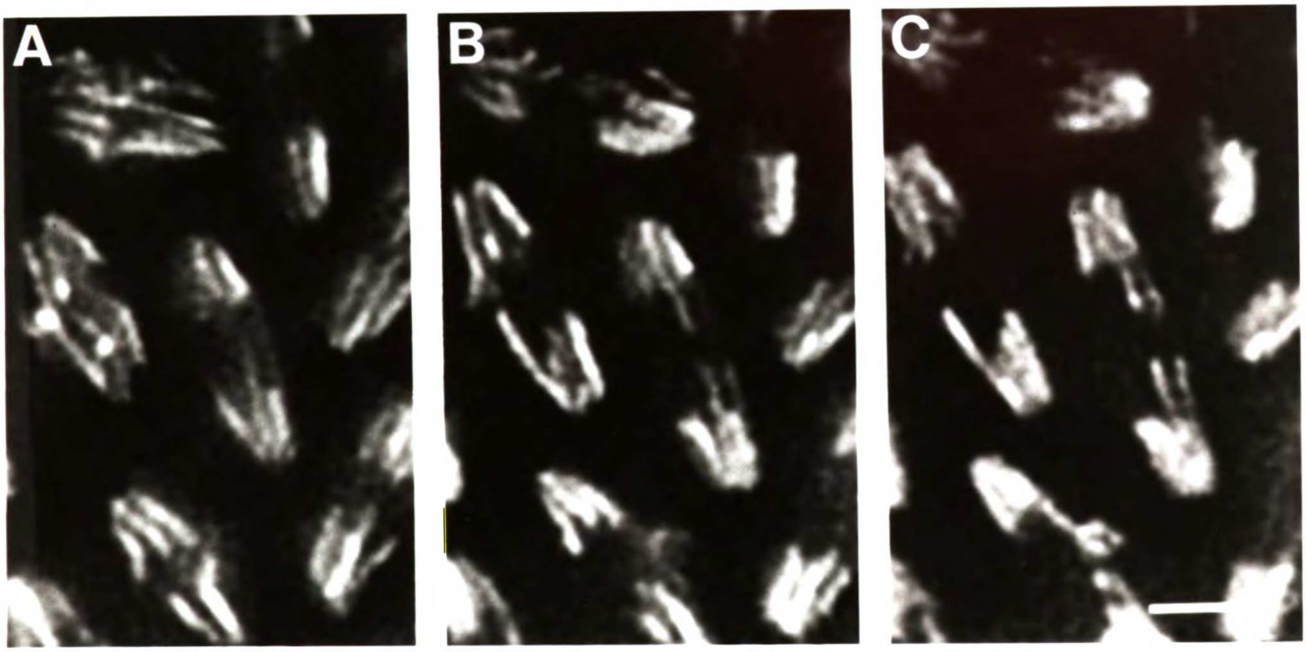

Figure 5.6. Topoisomerase II is Located Throughout the Chromosome. A sequence of projections taken at high resolution (see Materials and Methods) during anaphase when individual chromatid arms are easily seen. Optical sections were recorded at 0.25 µm intervals in order to obtain high resolution images of topoisomerase II distribution. Width of arms is 0.4 - 0.5 µm. Width of chromatid arms visualized with rhodamine-histone H2A, H2B is also 0.4-0.5 µm. Scale = 5 µm.

topoisomerase II changes its distribution during this mitosis, cycle 11 embryos were microinjected with rhod-topo II, but time lapse-three-dimensional images were not recorded until 30 minutes after the beginning of interphase of cycle 14. The regions chosen for analysis were the large mitotic domains 5 and 6 (the fifth and sixth domains to enter mitosis; for a complete description of the cycle 14 mitotic domains, see Foe, 1989), which lie above and below the cephalic furrow, respectively. To observe these domains, embryos were mounted on their lateral surfaces and viewed just dorsal to the lateral midline. Images were collected at lower resolution so the morphological movements of nuclei could be followed. During interphase, all the nuclei contain rhod-topo II (data not shown). As domain 6 progresses through mitosis, nuclear and chromosomal topoisomerase II is lost to the cytoplasm of the cells, creating a zone of uniform intensity. After mitosis, the nuclear staining returns, and the cells of domain 6 now move posteriorly away from the cephalic furrow. Loss of topoisomerase II therefore also occurs after cellularization in the slower mitotic cycles of the *Drosophila* embryo.

Labeled Anti-Topoisomerase II Behaves Identically to Rhod-Topo II

It is formally possible that the labeling of topoisomerase II with tetramethylrhodamine interferes with some of its *in vivo* functions, but the presence of an intact nuclear localization sequence (NLS) directs this damaged protein analogue to the nucleus. In such a case, the observed distribution and dynamics of the enzyme would be those of a damaged protein. It is also possible that the localization of rhod-topo II is artifactually created by the increased amount of topoisomerase II in embryos injected with rhod-topo II. To control for these possibilities, Texas Red- or tetramethylrhodamine-labeled Fab fragments of monoclonal antibody P2G3 were microinjected into embryos. The *in vitro* DNA supercoil relaxation activity of topoisomerase II was not inhibited by the intact antibody or the Fab fragment (data not shown). Embryos were simultaneously injected with Texas Red-conjugated P2G3 Fab fragment and BODIPY-conjugated histones H2A and H2B to allow the direct comparison of the distribution of topoisomerase II and chromatin. Time-lapse three dimensional images were then recorded simultaneously for both fluorophores. All features of the localization observed with rhod-topo II were seen with the labeled Fab fragment. This included staining of nuclei and chromosomes, localization to specific sites in interphase (data not shown), and the loss of topoisomerase II after chromosome condensation and segregation (Fig. 5.7). By contrast, histones remain on the chromosomes throughout mitosis and reach their highest concentration during metaphase (Fig. 5.7). Since the injected labeled Fab has no NLS, it is presumably directed to the nucleus and chromosomes by binding to endogenous topoisomerase II. Therefore, the distribution and dynamics observed with rhod-topo II are not due to the use of a modfied form of enzyme or the alteration of some equilibrium by the addition of exogenous labeled enzyme. Furthermore, the use of labeled Fab fragments for *in vivo* fluorescence experiments may be a general technique which can be applied to other proteins which are difficult to purify. For example, the three-dimensional dynamics of the nuclear lamina in the *Drosophila* embryo has been studied *in vivo* using fluorescently-labeled Fab fragments of anti-lamin antibodies (M. R. Paddy, D. A. Agard, J. W. Sedat, unpublished observations).

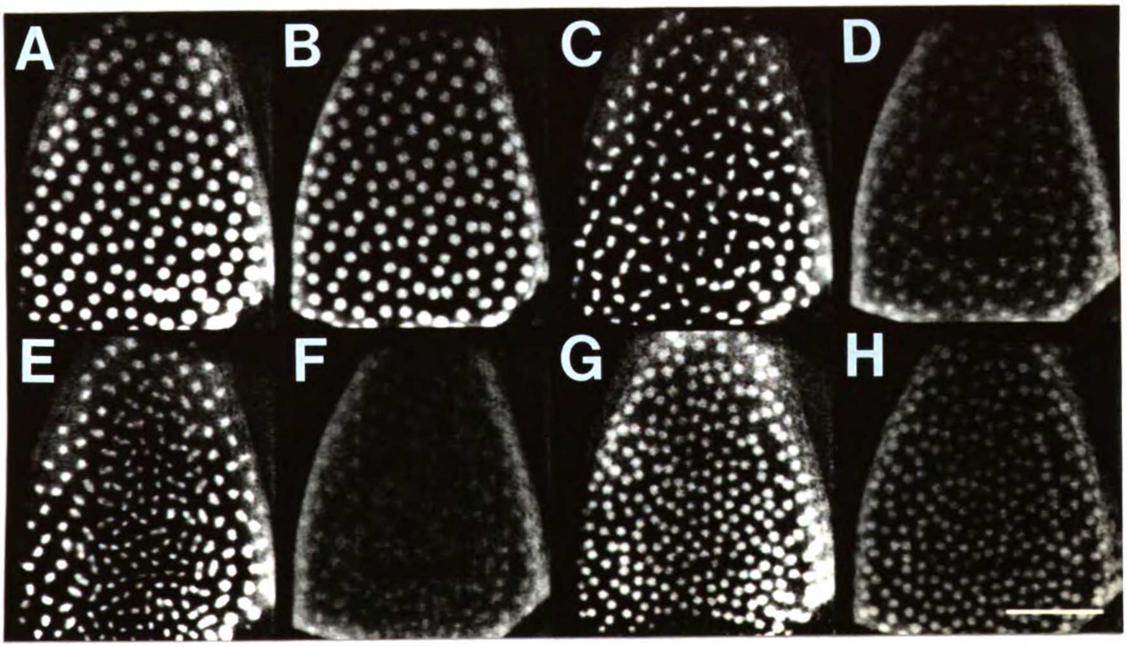

Figure 5.7. Low resolution dual-wavelength time lapse movie of histones and anti-topoisomerase II. Projections of 6 optical sections are shown. (A, C, E, G) BODIPY-histones H2A/H2B. (B, D, F, H) Texas Red-anti-topoisomerase II. (A, B) Interphase nuclear cycle 12. (C, D) Metaphase. (E, F) Anaphase. (G, H) Interphase nuclear cycle 13. Scale bar = 50 µm.

Discussion

This paper describes the *in vivo* distribution of topoisomerase II during the cell cycle in the *Drosophila* embryo. Since the nuclear divisions of the early embryo are nearly synchronous, multiple nuclei and embryos were used for a careful statistical analysis of the changes in distribution of topoisomerase II during the cell cycle. The data presented here, summarized in Figure 5.8, show that roughly 70% of the chromosomal topoisomerase II leaves the chromosome during mitosis in the *Drosophila* embryo. This redistribution occurs in two stages, one after the completion of chromosome condensation and the other after chromosome segregation. These are the two cell cycle events where topoisomerase II is known to function. These observations suggest that most of the enzyme present in the cell is not required for the structural integrity of the chromosome, but instead functions as a DNA strand passing enzyme during chromosome condensation and segregation.

Changes in the overall levels of topoisomerase II in synchronized chicken cells have been reported previously (Heck et al., 1988), but this study had limited temporal resolution and did not discriminate between nuclear and cytoplasmic levels of the enzyme. Also, the majority of the decrease in the levels of topoisomerase II from M to G_1 was attributed to the loss of proteolytic fragments of topoisomerase II. Because the early *Drosophila* embryo is a syncytium and the volume imaged in these movies is ~0.1% of the volume of the embryo, I cannot determine if the enzyme which leaves the nucleus during mitosis is degraded. While proteolytic fragments may exist in chicken cells (Heck et al., 1988), proteolytic degradation of *Drosophila* topoisomerase II in embryos (Fairman and Brutlag, 1988) and Schneider 2 cells has been shown to be artifactual (Whalen et al., 1991; J. R. Swedlow, unpublished observations). Nonetheless, small amounts of topoisomerase II degradation in nuclei at specific points in the cell cycle may not have been detected in these experiments.

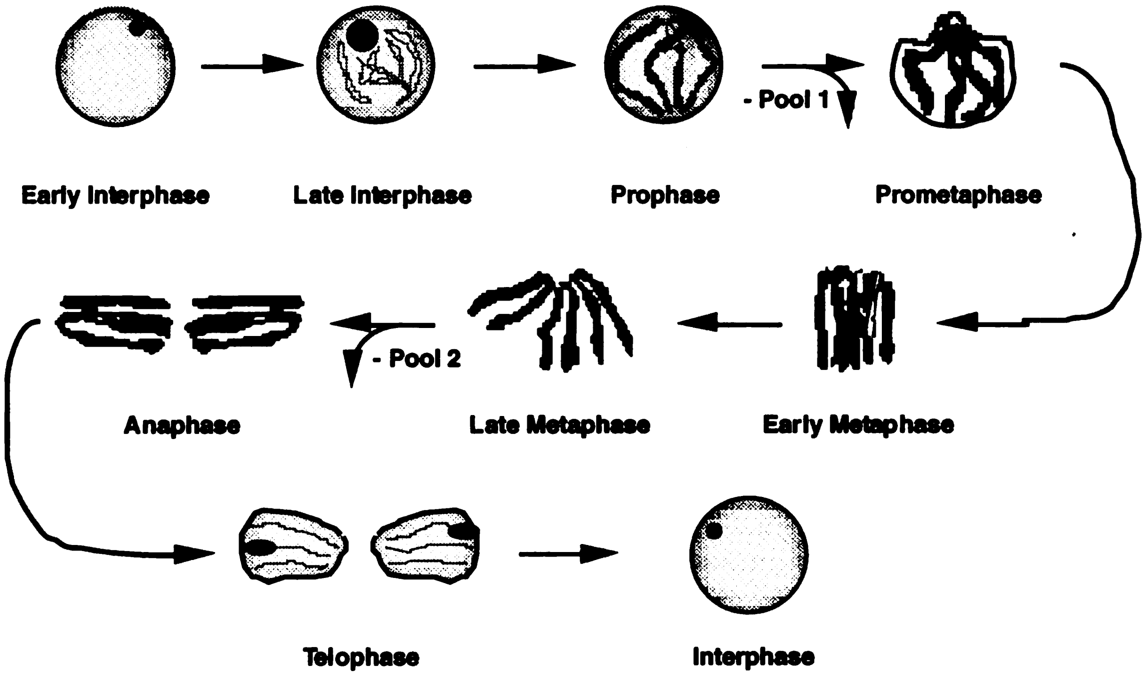
Early Interphase
Late Interphase
Prophase
- Pool 1
Prometaphase
Early Metaphase
Late Metaphase
- Pool 2
Anaphase
Telophase
Interphase

Figure 5.8. Summary of Distribution of Topoisomerase II During the Cell Cycle. Changes in the distribution of topoisomerase II are shown in a schematic embryonic nucleus. The view is a cross-section of the nucleus; the embryo cortex is above the nucleus. The darkness of shading in the nucleus and chromosomes indicates the relative concentration of topoisomerase II. Nuclear and chromosomal topoisomerase II is lost after chromosome condensation ("Pool 1") and after chromosome segregation ("Pool 2"). The interphase site of topoisomerase II concentration is first observed in late anaphase or telophase. The site is found near the apical end of the interphase nucleus, generally close to the nuclear periphery. It becomes diffuse during the middle third of interphase, but then reappears in the latter third of interphase, and finally disappears after prophase.

Why does topoisomerase II leave the nucleus and chromosomes during the cell cycle? During the transition from prophase to metaphase, the non-chromosomal topoisomerase II leaves the nucleus and diffuses into the cytoplasm. The nuclear non-chromosomal enzyme apparently was imported during interphase but was not bound to chromosomes. This effect is not due to the presence of excess topoisomerase II in the embryo following rhod-topo II injection since *in vivo* experiments using a labeled anti-topoisomerase II Fab fragment show the same phenomena. The speed of the early nuclear cycles (Foe and Alberts, 1983) might cause the nuclei to import excess proteins required for replication, chromatin assembly, etc.; non-chromosomal proteins could then leave the nucleus at prometaphase. However, this phenomenon is not seen with core histones, whose nuclear concentration does not change appreciably during interphase. In addtion, this argument does not explain the loss of chromosomal topoisomerase II after chromosome condensation and segregation. These processes may require the localization of topoisomerase II to specific chromosomal sites. After condensation or segregation, either the availability of the site or the affinity of topoisomerase II for the site could be modified, thus causing the enzyme to leave the chromosome and diffuse into the cytoplasm. The existence of such sites is suggested by the presence of preferred binding sites for topoisomerase II *in vivo* (Udvardy and Schedl, 1991; Käs and Laemmli, 1992).

It has been suggested that topoisomerase II binds to chromosomal SARs and upon aggregation serves to mediate chromosome condensation (Adachi et al., 1989; Adachi et al., 1991). Our *in vivo* experiment shows that 60% of the enzyme present in the early prophase chromosome is clearly not acting as a structural chromosome protein. The loss of chromosomal topoisomerase II seen here *in vivo* was not examined in previous *in vitro* chromosome condensation experiments (Wood and Earnshaw, 1990; Adachi et al., 1991), however it should be possible to follow the *in vitro* distribution of enzyme in real time. It will be important to determine if the enzyme required for the *in vitro* condensation reaction leaves the chromosome after condensation is complete. It has been shown that topoisomerase II can be extracted from mitotic chromosomes condensed from Xenopus sperm nuclei in a Xenopus egg extract under mild conditions where the morphology of the chromosome is well preserved (Hirano and Mitchison, 1993).

Our four-dimensional analysis has shown that topoisomerase II concentrates in one or two sites in the embryonic interphase nucleus. Two observations suggest that these sites may be specific chromosomal loci. First, they are visible as early as telophase, but become diffuse and sometimes disappear during the middle of interphase. Then, in the latter part of interphase the sites reappear and have approximately twice the intensity of the early interphase sites. The sites might therefore be disassembled after the first third of interphase, replicated, and then reassembled in the final portion of interphase. Second, in late interphase, the size of the sites in a single-site nucleus is twice that of sites in a double-site nucleus. If the sites are specific chromosomal regions, then in the single-site nucleus, chromosome homologues containing the sites would be paired; in the double-site nucleus, the homologues would not be paired. There is genetic and cytological evidence for the pairing of chromosome homologues in *Drosophila* (Wu and Goldberg, 1989; Hiraoka et al., and references therein).

It is likely that each interphase site is either a nucleolar organizer or a nucleolus. The experiments reported here used a 170 kDa enzyme which was previously reported to be excluded from the nucleoli of fixed larval polytene squashes (Berrios et al., 1985). Our localization of topoisomerase II to the nucleoli of intact, unsquashed polytene nuclei suggests that this structure may be quite delicate and easily perturbed during the preparation of the polytene squash. In fact, a 180 kDa isoform of human topoisomerase II has been localized to the nucleolus of HeLa cells, while the 170 kDa isoform is not found in the nucleoli of cultured human or chicken cells (Earnshaw et al., 1985; Negri et al., 1992). A 180 kDa form of topoisomerase II has not yet been identified in *Drosophila*. Our results suggest that the nucleolar function of topoisomerase II may be performed by a subpopulation of the 170kD enzyme. However, the role of topoisomerase

II in the nucleolus is not yet known. Interestingly, a lack of topoisomerase activity has been correlated with increased recombination of rDNA and the formation of extrachromosomal rings containing rDNA sequences in yeast (Christman et al., 1988; Kim and Wang, 1989). These studies suggested that topoisomerases may be required to relax DNA supercoils created during transcription.

Chromosomal topoisomerase II has been reported to be distributed within a central axial core of isolated chromosomes (Gasser et al., 1986; Boy de la Tour and Laemmli, 1988). These experiments used a variety of reagents to swell the chromosomes or extract chromosomal proteins before fixation and immunolocalization. More recently, in experiments using extracted and even dried chromosomes, topoisomerase II was immuno-localized to an axial core of meiotic chromosomes (Moens and Earnshaw, 1989; Klein et al., 1992). The structural fragility of chromosomes has been well documented (Belmont et al., 1989 and references therein), so it is possible that harsh extraction or isolation conditions might perturb the structure and cause rearrangements of the constituent proteins. The preferable strategy, when possible, is to study localization and structure in unperturbed specimens. In my *in vivo* experiment, the width of the structure detected with rhod-topo II is identical to the width of the chromosome itself. The resolution of the imaging system is sufficient to have detected an axial chromosome core significantly smaller than the loosely condensed chromosome of the *Drosophila* embryo. Therefore if topoisomerase II is a component of the chromosome scaffold, this structure does not appear to form a dense axial core running the length of the chromosome (Gasser et al., 1986; Boy de la Tour and Laemmli, 1988). However, as previously suggested (Earnshaw and Heck, 1985), the scaffold topoisomerase II could be distributed throughout the chromosome. A definitive description of chromosomal topoisomerase II distribution is possible by electron microscopy of embryos injected with gold-labeled topoisomerase II.

I have used the chromosomes of the *Drosophila* embryo to study the distribution of topoisomerase II during the rapid nuclear cycles of the early syncytium as well as the slower mitosis of cycle 14. The amount of topoisomerase II imported into the embryo nuclei may be a consequence of the speed of the nuclear cycle in this system and the possible localization of the 170 kDa form of topoisomerase II to the nucleolus in *Drosophila* may not be seen in higher eukaryotes. However, my most important observations and conclusions are consistent with those made in other systems. As discussed above, a cell cycle variation in the concentration of topoisomerase II was previously reported in chicken tissue culture cells (Heck et al., 1988). The presence of pools of nuclear topoisomerase II with different biochemical extraction properties has been observed in isolated nuclei and chromosomes from 6hr-18hr old *Drosophila* embryos, chicken cells, and human cells (Berrios et al., 1985; Earnshaw et al., 1985; Gasser et al., 1986). Also, the concentration of topoisomerase II in *Drosophila* embryos and HeLa cells is similar (0.25 μM and 0.42 μM, respectively; see Materials and Methods), so the changes in chromosomal content of topoisomerase II are not due to low affinity binding sites specific to an embryonic cell cycle. The similarity of my results with those from other systems suggests that they are representative of fundamental aspects of topoisomerase II function in chromosomes.

The capability of collecting three-dimensional data at each timepoint in the recordings of rhod-topo II *in vivo* is a critical part of the quality and analysis of the data. The high resolution of the images is due to the use of a three-dimensional deconvolution algorithm (Fig. 5.2). Some aspects of topoisomerase II localization are spatially regulated (i.e., the interphase sites) and thus might have been misinterpreted or missed altogether in a time-lapse two-dimensional movie. Finally, the depth of the nuclei in the embryo changes during the mitotic cycle and thus structures may move through many focal planes. The use of three-dimensional imaging allows us to follow features as this movement occurs.

Our results show that the distribution of topoisomerase II in nuclei and chromosomes is spatially and temporally regulated. Rather than serving simply as a structural component of chromosomes, topoisomerase II may localize to regions of the chromosome which require its activity. It may therefore be possible to use the localization of topoisomerase II as an indicator for structural dynamics in chromosomes. It will also be important to determine the molecular basis for the localization of the different populations of topoisomerase II.

Materials and Methods

Purification of and Assay of *Drosophila* Topoisomerase II

Drosophila topoisomerase II was prepared from 6-18 hr old embryos as described (Shelton et al., 1983). Analysis of fractions was performed by SDS-PAGE (Laemmli, 1970) and by immunoblotting with an anti-*Drosophila* topoisomerase II monoclonal antibody (P2G3; J. Swedlow, N. Osheroff, T. Karr, J. W. Sedat, D. A. Agard, unpublished observations). The specific activity of the final fraction (Fraction VI of Shelton et al) was ~1 x 10^6 U/mg (Shelton et al., 1983). Assay of topoisomerase II activity by ATP-dependent supercoil relaxation was performed as described (Osheroff and Zechiedrich, 1987). For decatenation assays, highly catenated kinetoplast DNA (TopoGen) was used in the assay instead of supercoiled DNA.

Fluorescent Labeling of Topoisomerase II

Fluorescent topoisomerase II was prepared using a modification of a previously decribed protocol (Minden et al., 1989). All manipulations were performed at 4°C. Labeling of topoisomerase II was performed on enzyme bound to phosphocellulose. Phosphocellulose (Whatman, Inc.) was washed three times in batch mode with wash buffer (20mM HEPES pH7.6, 200mM NaCl, 1mM DTT, 10% glycerol), three times with elution buffer (20mM HEPES pH7.6, 700mM NaCl, 1mM DTT, 35% glycerol), and three times with wash buffer. 150 μg of purified topoisomerase II was added to a 20 μl bed volume of washed phosphocellulose and diluted with 2 volumes of loading buffer (wash buffer without NaCl). This mixture was incubated for 30 minutes with occasional mixing. The enzyme-bound phosphocellulose was then washed twice with 20mM HEPES pH7.6, 200mM NaCl, 10% glycerol and resuspended in 50 μl of this buffer to form a slurry. 2.5 μl of a 50 mg/ml 5(6)-carboxytetramethylrhodamine N-hydroxysuccinimidyl ester (Molecular Probes, Inc.) in dry dimethylformamide (Aldrich) solution was added to the slurry and mixed by pipetting. The labeling reaction was incubated for 30 minutes with occasional mixing. The slurry was washed once with labeling buffer and then transferred to a P-200 tip plugged with glass wool. This column was washed with ten column volumes of wash buffer. The labeled protein was eluted from the column with elution buffer. 25-30 μl fractions were collected. Fractions were assayed for relaxation and decatenation activity. Incorporation of label was assayed by SDS-PAGE and spectrophotometry. After electrophoresis, fluorescent protein was detected on a standard UV transilluminator. The stoichiometry of tetramethylrhodamine labeling was calculated using $\varepsilon = 50000\ M^{-1}\ cm^{-1}$ for tetramethylrhodamine in solution (Molecular Probes, Inc.). It has been difficult to determine the exact concentration of topoisomerase II in solution, however the concentration was estimated by assuming 1 OD_{280} unit was approximately equal to a protein concentration of 1 mg/ml. This assumption is consistent with the known tyrosine (3.1%) and tryptophan (1.1%) content of *Drosophila* topoisomerase II (Wyckoff et al., 1989). The molar ratio of fluorophore-to-protein in rhod-topo II was determined to be approximately 3:1. Although approximate, these data are consistent with all molecules of topoisomerase II being labeled with at least one molecule of tetramethylrhodamine. The labeling I have achieved might be due to the high content of lysine residues, the target of the N-hydroxysuccinimide reactive group, in the C-terminal domain of *Drosophila* topoisomerase II. 15.1% of the C-terminal 96 residues of the protein are lysine (Wyckoff et al., 1989). After labeling, active fluorescent protein was stored at -80°C.

Preparation and Labeling of Anti-Topoisomerase II

P2G3, an anti-*Drosophila* topoisomerase II monoclonal antibody, was affinity purified by passing supernatant collected from the hybridoma line over a Protein G Sepharose (Pharmacia) column equilibrated in 10mM Tris pH 7.4, 150 mM NaCl (TBS) at a flow rate of 0.5 ml/min. Up to 1 liter of supernatant was passed over a 2 ml column. After washing with at least 20 ml of TBS, the OD_{280} of buffer flowing through the column was determined to be less than 0.001. Antibody was eluted from the column with 0.1M glycine pH 2.7 and collected into tubes containing 10 µl 1M Tris pH 7.9 to immediately neutralize the elution buffer . The protein content of the fractions was determined by measuring OD_{280} of each fraction. Concentration of the final pool was estimated assuming 1.5 OD/mg IgG (Harlow and Lane, 1988).

The isotype of the P2G3 antibody was determined in an ELISA using isotype-specific monoclonal antibodies (Boerhinger Mannheim) were used according to the manufacturer's instructions. P2G3 only reacted with antibodies specific for all IgG's and IgG1, but not IgA, IgM, or any other IgG subtypes. P2G3 also reacted with antibodies specific for κ but not λ light chains. Generation of Fab fragments from mouse IgG1 antibodies is accomplished with papain in 10mM $NaPO_4$ pH7.1, 50mM cysteine HCl, 1 mM EDTA (Parham, 1986). Both agarose-immobilized papain (Pierce) and soluble papain (Worthington) were used for digestion, but agarose-papain produced only $F(ab')_2$ fragments even after 72 hour incubations. Soluble papain quantitatively digested P2G3 to Fab fragments after 2 hr at 37°C. To prepare large amounts of Fab fragments, 10 mg of P2G3 were digested at 37°C with 150 µg papain in a final volume of 2 ml. After 2 hrs, the reaction was stopped with 100 µl 1M Tris HCl pH 8.0 and lodaed onto an 80ml G-100 SF previously equlibrated in PBS. Purified Fab fragments eluted at Ve/Vo = 1.35.

Peak fractions were pooled and concentrated with a Centricon-30 (Amicon) to ~13 mg/ml.

Fab fragments were fluorescently labeled as described (Harlow and Lane, 1988), purified by gel filtration over Sephadex G-25, and then concentrated to approximately 1 mg/ml in a microconcentrator. Aliquots were stored at -80°C.

Microinjection of Rhodamine Topoisomerase II

Drosophila embryos were microinjected with rhod-topo II at 90 minutes after egg deposition as described previously (Hiraoka et al., 1989; Minden et al., 1989). The early embryo contains approximately 1.5×10^9 copies of topoisomerase II protein (Fairman and Brutlag, 1988). Each embryo was injected with approximately 100 picoliters of rhod-topo II at a concentration of 0.5-1 mg/ml. Therefore, the amount of rhod-topo II injected into the embryo was no more than 10% of the endogenous embryonic protein. After injection, rhod-topo II was allowed to incorporate for at least 10 minutes, during which time at least 1 complete nuclear cycle occurred. After injection and data collection, embryos were kept for 24 hours until hatching. 70% of injected embryos hatched.

In Vivo Time Lapse Data Collection and Image Processing

Three-dimensional time lapse data was recorded by a charge-coupled device- (CCD) based wide-field optical sectioning microscope (Hiraoka et al., 1991) equipped with a 10%, 38%, or 50% transmittance neutral density excitation filter, a rhodamine filter set (Olympus, Inc.) and a 60x/NA1.4 oil immersion lens (Olympus, Inc.). Small images (256x256 pixels; effective pixel size = .1117 μm) corresponding to a field size of 28.6x28.6 μm were recorded. Exposure time for each image ranged from 50-200 msec. Data were recorded in two modes: low resolution, or 12 optical sections at each timepoint at 0.5 μm intervals; and high resolution, 8 optical sections at 0.25 μm intervals. The power of the incident illumination in the experiments presented in Figures 5.3 and 5.4 was measured with a photodetector equppied with an attenuator and an optical power meter (Model 835 and Model 818, Newport, Inc.). Both were calibrated at 550nm. The power of the excitation light was 110 nW · μm^{-2} or 1.4 nW · $pixel^{-1}$. Each 200 msec exposure therefore exposed the embryo to 22 nJ · μm^{-2}. The total exposure during the recording of one time-lapse dataset was 43.8 μJ · μm^{-2}. When shorter exposure times are used, a disproportionately greater excitation power is possible with no apparent deleterious effects on the embryos. I believe this is due to repair processes in the embryo which help quench the free radicals created during fluorophore excitation.

After the datasets were recorded, out-of-focus information was removed from each three-dimensional data stack by a constrained, iterative deconvolution algorithm (Agard et al., 1989) based on an empirical knowledge of the objective lens point spread function. Projections separated by 10^{o} of each data stack were calculated to give a series of stereo pairs.

Image Analysis

For the quantitation of nuclear and cytoplasmic topoisomerase II, the mean pixel intensities in the nuclei and cytoplasm were calculated at each timepoint in a dataset. This calculation required the assignment of each pixel as either nuclear or cytoplasmic. The following algorithm was developed to accomplish this and was run on two dimensional projections of each three-dimensional data stack or the full three-dimensional data stack. Images were first convolved with a Fourier space gaussian-edged bandpass filter (Castleman, 1979). The high-pass and low-pass gaussians were constructed with $\sigma = 0.01$ and 0.125 $pixels^{-1}$, respectively. This served to smooth the images and substantially removes any large intensity gradients caused by a concentration of labeled protein near the injection site. At each timepoint, a gradient image is then calculated (Chen et al., 1989). The gradient image is a representation of the edges in the starting image. A gradient threshold based on the cytoplasmic noise was then chosen such that most pixels with a gradient value above the threshold were contained within the nuclei. The spurious pixels in this preliminary mask were removed with a low-pass median filter using an 11x11 pixel box. This filtered mask contained most of the volume of the nuclei, but the nuclei with intranuclear substructure (late interphase) often were not completely included. Therefore, a new gradient image was calculated where pixels already included in the nuclear mask were ignored. A second mask was calculated based on a new threshold. The two masks were added together and then median filtered. This final mask was then used on the original deconvoluted (but not oterwise filtered) images to calculate the mean nuclear and cytoplasmic intensities at each timepoint. Any pixel contained within the mask was considered to be nuclear; otherwise it was considered to be cytoplasmic. The mean nuclear intensity at each timepoint was then calculated by summing the intensities of all nuclear pixels and normalizing by the nuclear volume (the total number of nuclear pixels). An identical calculation was done for the cytoplasmic pixels. These values were then plotted as a function of time. The data can be interpreted assuming that the field of nuclei under observation represent less than 0.1% of the total volume of the embryo. Therefore, the cytoplasmic topoisomerase II seen in these movies is in equilibrium with an effectively infinite volume of topoisomerase II.

While this method reproducibly produced plots like those shown in Figure 5.4 from seven mitotic cycles, the size of the different pools varied in different datasets. This was found to be the result of the movement of nuclei during mitosis. During prometaphase and metaphase, the nuclei move 1.5-2 μm away from the cortex (and the microscope objective lens) into the interior of the embryo. Since the sectioning volume is fixed during the experiment, different volumes of the nuclei are imaged at different parts of mitosis and an accurate comparison of the intensities of whole nuclei is impossible. Therefore direct measurement of chromosomal topoisomerase II and histones H2A/H2B were made by manually picking chromosomal pixels in seven time-lapse three-dimensional movies at early prophase, metaphase, and late telophase. These points in the cell cycle were selected cytologically: prophase was determined by the appearance of distinct chromosome arms, metaphase by the last image before any detectable anaphase movement, and late telophase by the disappearance of distinct chromosome arms. The mean chromosomal intensity at each timepoint was then calculated. The contribution of background intensity at each pixel was estimated by finding the minimum intensity within 1.1 µm of each chromosomal pixel. The mean minimum intensity was subtracted from the mean chromosomal intensity to give the final mean chromosomal intensity. The highest mean intensity for topoisomerase II is in prophase and for histones is in metaphase. The topoisomerase II and histone values at prophase, metaphase, and late telophase were expressed as a percentage of the highest intensity. The normalized topoisomerase II was calculated by dividing the percent change of topoisomerase II intensity by the percent change in histone intensity.

Intracellular Concentration of Topoisomerase II

The concentration of topoisomerase II in the *Drosophila* embryo was calculated assuming a enzyme content of 1.5 x 10^9 copies/embryo (Fairman and Brutlag, 1988) and a volume of 10 nl/embryo (Ashburner, 1989). The concentration of enzyme in HeLa cells was calculated using a value of 1 topoisomerase II molecule/23,000bp DNA (Gasser et al., 1986). Similar values for topoisomerase II concentration were calculated using data from chicken MSB-1 and 3-day-old erythroid cells (Wood and Earnshaw, 1990). Given the difficulty in determining the number of copies of enzyme in a cell, the concentrations reported are approximations and have an error of at least 30% (Gasser et al., 1986).

Acknowledgments

I thank Dr. Michael Paddy for the use of BODIPY-histones and images of embryos injected with Cy5-histones. Also, I thank T. Hirano, S. Holloway, C. Shamu, A. Dernburg, and K. Kaplan for their thoughtful criticism of this manuscript.

Chapter 6: Conclusion

DNA topoisomerase II is a DNA strand passing enzyme required for chromosome condensation and segregation (DiNardo et al., 1984; Uemura and Yanagida, 1986; Newport and Spann, 1987; Uemura et al., 1987; Holm et al., 1989; Wood and Earnshaw, 1990; Adachi et al., 1991; Downes et al., 1991; Buchenau et al., 1993). Biochemical fractionation of chromosomes and nuclei has suggested that topoisomerase II is a structural component of chromosomes (Berrios et al., 1985; Earnshaw et al., 1985; Gasser et al., 1986). The purpose of the experiments in this thesis was to determine the localization of the enzyme *in vivo* or in chromosomes whose *in vivo* structure was preserved during fixation. The major findings of this work are that

-- the chromosomal concentration of topoisomerase II decreases dramatically after chromosome condensation and again after segregation; the loss of concentration occurs as enzyme leaves the chromosome and diffuses into the cytoplasm;

-- topoisomerase II is not localized to an axial chromosome core *in situ* or *in vivo* but instead is distributed throughout the chromosome;

-- there are specific regions of the X and Y chromosome where topoisomerase II concentrates; the site on the X chromosome colocalizes with the 359 bp 1.688 g/ml satellite;

-- while the spatial distribution of topoisomerase II and histones is similar during interphase and prophase, there are marked differences in the way the nuclear and cytoplasmic concentrations of these proteins change during the cell cycle.

The surprising finding was the degree of complexity of the localization of topoisomerase II. The characterization of the enzyme as a structural protein of chromosomes clearly understates the functions of the enzyme. At the moment, the correlation between localization of the enzyme and function is only hypothetical, although a recurring theme in the molecular study of the cell is the degree to which localization of cellular components is tied to function. For example, there is substantial evidence for specific localization of some mRNAs in cytoplasm (Wilhelm and Vale, 1993). In addition, splicing factors are localized to specific regions of the nucleus that appear to be dedicated to transcript processing (Spector, 1993). These and numerous other examples of specific localization suggest that the proper function of many cellular processes requires specific localization of appropriate proteins, nucleic acids, and small molecules. The interactions that result are presumably worth the enthalpy required to generate specific localization at the expense of entropy. In the case of topoisomerase II, the chromosomal localization of high concentrations of strand passing activity during chromosome condensation generates a compact structure which can safely proceed through mitosis.

In order to record and accurately interpret the microscopic data that generated these conclusions, a study was made of the aberrations present in multi-wavelength imaging. This characterization of chromatic and spherical aberrations showed that

-- significant spherical aberration is present in multi-wavelength images recorded with high numerical aperture lenses; the sample will contribute to the degree of aberration; this problem can be largely removed by deconvolution of the recorded image with an optical transfer function that includes an appropriate amount of spherical aberration;

-- sample dependent lateral and axial chromatic aberrations cause wavelength-dependent registration and magnification errors in multi-wavelength images; these errors can be effectively corrected by searching for a translation and magnification that minimize the difference between images recorded with different wavelengths of light.

With these imaging tools and the ability to study the localization of topoisomerase II *in situ* and *in vivo* in hand, a number of outstanding questions can be studied. First, what is the localization of topoisomerase II in chromatin? Using similar chemistry to that described in Chapter 5, it should be possible to label topoisomerase II with undecagold, microinject this preparation into embryos, and then prepare embryos for electron microscopy. The recent demonstration of high pressure freezing as an excellent preparation method for *Drosophila* embryos should eliminate the difficulties in fixation of these specimens (McDonald and Morphew, 1993). In addition, the use of osmium ammine B to specifically stain for DNA will allow a direct comparison between the localization of topoisomerase II and DNA in the electron microscope (Olins et al., 1989; Horowitz and Woodcock, 1992).

The behavior of topoisomerase II in *Drosophila* embryos is reminiscent of results obtained in other systems. In chicken MSB-1 lymphoblastoid cells sorted by elutriation, the content of topoisomerase II is highest in a late G2 and M fraction and lowest in a late M and G1 fraction (Heck et al., 1988). It is therefore important to extend the observations presented here to other species by microinjecting labeled topoisomerase II into tissue culture cells and following the distribution of the enzyme during a slower cell cycle than that of the *Drosophila* embryo. In either an embryonic or tissue culture system, it should be possible to begin a functional dissection of the topoisomerase II molecule. In *S. pombe*, deletion analysis has demonstrated a minimal domain of the protein required for strand passing activity, although this protein does not rescue a *ts top2* mutant at the restrictive temperature (Shiozaki and Yanagida, 1991). One of two domains located on the N- and C-termini of the enzyme are required for nuclear localization (Shiozaki and Yanagida, 1992). In addition, a series of casein kinase II phosphorylation sites have been identified in both the *S. pombe* and *S. cerevisiae* enzymes (Cardenas et al., 1992; Shiozaki and Yanagida, 1992). The *Drosophila* enzyme also contains these sites and is phosphorylated by casein kinase II *in vitro* (Ackerman et al., 1985). Thus, the functional significance of these domains and phosphorylation sites could be addressed by microinjection of fluorescently labeled expressed mutant proteins and following their chromosomal localization during the cell cycle. This type of experiment would determine if specific mutations affect specific aspects of localization. For example, is there a specific region of the enzyme that confers localization to the topo II/359 bp site?

The specificity of the interaction of topoisomerase II with bulk DNA can also be examined. Since the enzyme can readily diffuse from the chromosome at specific points in the cell cycle, there must be a mechanism to keep the enzyme on the chromosome until the appropriate time. It should be possible to use topoisomerase II labeled with caged fluorescein to monitor the equilibrium exchange of chromosomal topoisomerase II with enzyme in the cytoplasm (Mitchison, 1989). This experiment could be carried out during the 3-4 minute long metaphase of the early embryonic cycles (Foe and Alberts, 1983), or if necessary, in embryos injected with colchicine to arrest embryos in metaphase (Raff and Glover, 1988). If chromosomal topoisomerase II does exchange with cytoplasmic enzyme, then the localization of topoisomerase II is likely controlled by availability of enzyme binding sites on the DNA. However, if there is little exchange, then some aspect of the enzyme, most likely a specific modification like phosphorylation, probably confers chromosomal localization. The modification might be delineated by mutational analysis as described above.

The localization of topoisomerase II to sites in the X and Y centric heterochromatin demonstrates the specificity of the interaction of the enzyme and DNA. Unfortunately, the function of this localization is not yet clear. It will be important to examine the localization in contexts where the X and Y chromosomes are known to interact, e. g., during spermatogenesis and male meiosis and during rDNA amplification and in mutants which disrupt this interaction. It is likely that the generation of *Drosophila* topoisomerase II mutants would greatly aid the determination of the importance of this interaction. The cDNA for *Drosophila* topoisomerase II is available (Wyckoff et al., 1989). Unfortunately, expression of the clone does not rescue known chromosomal deficiencies of region 37D2, the location of the gene for topoisomerase II in *Drosophila* (T.-s. Hsieh, personal communication). In lieu of these mutant strains, it might be possible to deplete nuclear topoisomerase II from embryos by microinjecting small (< 0.5 μm) latex spheres coated with anti-topoisomerase II antibodies or even the 359 bp 1.688 g/ml satellite. The structure and localization of the X centric heterochromatin might then be examined. Since topoisomerase II binds in the linker between nucleosomes on the 359 bp sequence *in vivo*, the latter approach may not work (Käs and Laemmli, 1992). In addition, it may not be possible to differentiate the effects generated throughout the chromosomes from those specific to the X and Y centric heterochromatin.

Finally, the difference between the accumulation of topoisomerase II and histones during interphase suggests a regulation of the import of nuclear proteins. This could occur either by specific factors that promote import and/or prohibit export, or by the availability of nuclear targets for imported proteins. A model for control of nuclear import based on the latter mechanism has recently been proposed . It would be interesting to examine the import of other nuclear proteins like lamin, nucleoplasmin, histone H1, or a general transcription factor like SP1 to explore the regulation of import of different proteins.

In conclusion, the study of topoisomerase II *in vivo* and *in situ* has demonstrated the spatial and temporal regulation of its localization. These properties were not suggested from previous work on isolated or extracted nuclei and chromosomes. The data presented here are consistent with the requirement of topoisomerase II for chromosome condensation and segregation, but also suggest other functions. It seems that the strand passing activity of the enzyme is delivered to sites not by passive diffusion, but by specific localization in the dense matrices of nuclei and chromosomes. The next step is therefore the determination of the mechanisms of specific localization.

References

Ackerman, P., Glover, C. V. C. and Osheroff, N. (1985). Phosphorylation of DNA topoisomerase II by casein kinase II: modulation of eukaryotic topoisomerase II activity *in vitro*. Proc. Natl. Acad. Sci. USA *82*, 3164-3168.

Adachi, Y., Käs, E. and Laemmli, U. K. (1989). Preferential, cooperative binding of DNA topoisomerase II to scaffold-associated regions. EMBO J. *8*, 3997-4006.

Adachi, Y., Luke, M. and Laemmli, U. K. (1991). Chromosome assembly *in vitro* - topoisomerase II is required for condensation. Cell *64*, 137-148.

Agard, D. A., Hiraoka, Y., Shaw, P. and Sedat, J. W. (1989). Fluorescence microscopy in three dimensions. Methods in Cell Biol. *30*, 353-377.

Amati, B. and Gasser, S. M. (1988). Chromosomal ARS and CEN sequences bind specifically to the yeast nuclear scaffold. Cell *54*, 967-978.

Ashburner, M. (1989). *Drosophila. A laboratory handbook*. (Cold Spring Harbor: Cold Spring Harbor Laboratory Press).

Belmont, A. S., Braunfeld, M. B., Sedat, J. W. and Agard, D. A. (1989). Large-scale chromatin structural domains within mitotic and interphase chromosme *in vivo* and *in vitro*. Chromosoma(Berl.) *98*, 129-143.

Belmont, A. S., Sedat, J. W. and Agard, D. A. (1987). A three-dimensional approach to mitotic chromosome structure: evidence for a complex hierarchical organization. J. Cell Biol. *105*, 77-92.

Berrios, M., Osheroff, N. and Fisher, P. A. (1985). In situ localization of DNA topoisomerase II, a major polypeptide component of the *Drosophila* nuclear matrix fraction. Proc. Natl. Acad. Sci. USA *82*, 4142-4146.

Bickel, S. and Pirrotta, V. (1990). Self-association of the *Drosophila* zeste protein is responsible for transvection effects. EMBO J. *9*, 2959-2967.

Boy de la Tour, B. and Laemmli, U. K. (1988). The metaphase scaffold is helically folded: sister chromatids have predominantly opposite helical handedness. Cell *55*, 937-944.

Bracewell, R. N. (1986). The fourier transform and its applications. (New York: McGraw-Hill).

Brill, S. J., DiNardo, S., Voelkel-Meiman, K. and Sternglanz, R. (1987). Need for DNA topoisomerase activity as a swivel for DNA replication for transcription of ribosomal RNA. Nature *326*, 414-416.

Buchenau, P., Saumweber, H. and Arndt-Jovin, D. J. (1993). Consequences of topoisomerase II inhibition in early embryogenesis of *Drosophila* revealed by *in vivo* confocal microscopy. J. Cell Sci. *104*, 1175-1186.

Cardenas, M. E., Dang, Q., Glover, C. V. C. and Gasser, S. M. (1992). Casein kinase II phosphorylates the eukaryote-specific C-terminal domain of topoisomerase II *in vivo.* EMBO J. *11*, 1785-1796.

Castleman, K. R. (1979). Digital image processing. (Englewood Cliffs, NJ: Prentice-Hall).

Chen, H., Sedat, J. W. and Agard, D. A. (1989). Manipulation, display, and analysis of three-dimensional biological images. In Handbook of Biological Confocal Microscopy, J. B. Pawley, ed. (New York: Plenum), 141-150.

Christman, M. F., Dietrich, F. S. and Fink, G. R. (1988). Mitotic recombination in the rDNA of S. cerevisiae is suppressed by the combined action of DNA topoisomerases I and II. Cell *55*, 413-425.

Chung, T. D., Drake, F. H., Tan, K. B., Per, S. R., Crooke, S. T. and Mirabelli, C. K. (1989). Characterization and immunological identification of cDNA clones encoding two human DNA topoisomerase II isozymes. Proc. Natl. Acad. Sci. USA *86*, 9431-9435.

DiNardo, S., Voelkel, K. and Sternglanz, R. (1984). DNA topoisomerase II mutant of Saccharomyces cerevisiae: topoisomerase II is required for segregation of daughter molecules at the termination of DNA replication. Proc. Natl. Acad. Sci. USA *81*, 2616-2620.

Downes, C. S., Mullinger, A. M. and Johnson, R. T. (1991). Inhibitors of DNA topoisomerase II prevent chromatid separation in mammalian cells but do not prevent exit from mitosis. Proc. Natl. Acad. Sci. USA *88*, 8895-8899.

Earnshaw, W. C. and Heck, M. M. S. (1985). Localization of topoisomerase II in mitotic chromosomes. J. Cell Biol. *100*, 1716-1725.

Earnshaw, W. C., Halligan, B., Cooke, C. A., Heck, M. M. S. and Liu, L. (1985). Topoisomerase II is a structural component of mitotic chromosome scaffolds. J. Cell Biol. *100*, 1706-1715.

Elgin, S. R. C., Boyd, J. B., Hood, L. E., Wray, W. and Wu, F. C. (1973). A prologue to the study of the nonhistone chromosomal proteins. Cold Spring Harbor Quant. Symp. Biol. *38*, 821-833.

Ericsson, C., Grossbach, U., Björkroth, B. and Daneholt, B. (1990). Presence of histone H1 on an active Balbiani ring gene. Cell *60*, 73-83.

Fairman, R. and Brutlag, D. L. (1988). Expression of the *Drosophila* type II topoisomerase is developmentally regulated. Biochemistry *27*, 560-565.

Foe, V. E. (1989). Mitotic domains reveal early commitment of cells in *Drosophila* embryos. Development *107*, 31-70.

Foe, V. E. and Alberts, B. M. (1983). Studies of nuclear and cytoplasmic behavior during the five mitotic cycles that precede gastrulation in *Drosophila* embryogenesis. J. Cell Sci. *61*, 31-70.

Foe, V. E. and Alberts, B. M. (1985). Reversible chromosome condensation induced in *Drosophila* embryos by anoxia: visualization of interphase nuclear organization. J. Cell Biol. *100*, 1623-1636.

Frasch, M., Glover, D. M. and Saumweber, H. (1986). Nuclear antigens follow different pathways into daughter nuclei during mitosis in early *Drosophila* embryos. J. Cell Sci. *82*, 155-172.

Freeman, L. A. and Garrard, W. T. (1992). DNA supercoiling in chromatin structure and gene expression. CRC Crit. Rev. Eukaryotic Gene Exp. *2*, 165-209.

Fuchs, J.-P., Giloh, H., Kuo, C.-H., Saumweber, H. and Sedat, J. W. (1983). Nuclear structure: determination of the fate of the nuclear envelope in Drosphila during mitosis using monoclonal antibodies. J. Cell Sci. *64*, 331-349.

Gasser, S. M. and Laemmli, U. K. (1986). The organization of chromatin loops: characterization of a scaffold attachment site. EMBO J. *5*, 511-518.

Gasser, S. M., Laroche, T., Falquet, J., Boy de la Tour, E. and Laemmli, U. K. (1986). Metaphase chromosome structure. Involvement of topoisomerase II. J. Mol. Biol. *188*, 613-629.

Gasser, S. M., Laroche, T., Falquet, J., Boy de la Tour, E. and Laemmli, U. K. (1986). Metaphase chromosome structure. Involvement of topoisomerase II. J. Mol. Biol. *188*, 613-629.

[illegible]
[illegible]
[illegible]

Gatti, M., Pimpinelli, S. and Santini, G. (1976). Characterization of *Drosophila* heterochromatin. I. Staining and decondensation with Hoechst 33258 and quinacrine. Chromosoma *57*, 351-375.

Giannasca, P. J., Horowitz, R. A. and Woodcock, C. L. (1993). Transitions between in situ and isolated chromatin. J. Cell Sci. *105*, 551-561.

Gibson, S. F. and Lanni, F. (1991). Experimental test of an analytical model of aberration in an oil-immersion objective lens used in three-dimensional light microscopy. J. Op. Soc. Am. *8*, 1601-1613.

Giloh, H. and Sedat, J. W. (1982). Fluorescence microscopy: reduced photobleaching of rhodamine and fluorescein protein conjugates by n-propyl gallate. Science *217*, 1252-1255.

Harlow, E. and Lane, D. P. (1988). Antibodies: a laboratory manual. (Cold Spring Harbor: Cold Spring Harbor Laboratory).

Hawley, R. S. and Marcus, C. H. (1989). Recombinational controls of rDNA redundancy in *Drosophila*. Ann. Rev. Genet. *23*, 87-120.

Hawley, R. S. and Tartof, K. D. (1985). A two-stage model for the control of rDNA magnification. Genetics *109*, 691-700.

Heck, M. M. S., Hittelman, W. N. and Earnshaw, W. C. (1988). Differential expression of DNA topoisomerases I and II during the eukaryotic cell cycle. Proc. Natl. Acad. Sci. USA *85*, 1086-1090.

[illegible]

Heck, M. M. S., Hittelman, W. N. and Earnshaw, W. C. (1989). *In vivo* phosporylation of the 170-kDa form of the eukaryotic DNA topoisomerase II. J. Biol. Chem. *264*, 15161-15164.

Hell, S., Reiner, G., Cremer, C. and Stelzer, E. H. K. (1993). Aberrations in confocal fluorescence microscopy induced by mismatches in refractive index. J. Microsc. *169*, 391-405.

Hilliker, A. J. and Appels, R. (1982). Pleiotropic effects associated with the deletion of heterochromatin surrounding rDNA on the X chromosome of *Drosophila*. Chromosoma *86*, 469-490.

Hirano, T. and Mitchison, T. J. (1993). Topoisomerase II does not play a scaffolding role in the organization of mitotic chromosomes assembled in Xenopus egg extracts. J. Cell Biol. *120*, 601-612.

Hirano, T., Hiraoka, Y. and Yanagida, M. (1988). A temperature-sensitive mutation of the Schizosaccharomyces pombe gene nuc2+ that encodes a nuclear scaffold-like protein blocks spindle elongation in mitotic anaphase. J. Cell Biol. *106*, 1171-1183.

Hiraoka, Y., Agard, D. A. and Sedat, J. W. (1990). Temporal and spatial coordination of chromosome movement, spindle formation, and nuclear envelope breakdown during prometaphase in *Drosophila melanogaster* embryos. J. Cell Biol. *111*, 2815-2828.

[illegible] LIBRARY
[illegible]
[illegible] LIBRARY

Hiraoka, Y., Dernburg, A. F., Parmelee, S. J., Rykowski, M. C., Agard, D. A. and Sedat, J. W. (1993). The onset of homologous pairing during *Drosophila melanogaster* embryogenesis. J. Cell Biol. *120*, 591-600.

Hiraoka, Y., Minden, J. S., Swedlow, J. R., Sedat, J. W. and Agard, D. A. (1989). Focal points for chromosome condensation and decondensation revealed by three-dimensional *in vivo* time-lapse microscopy. Nature *342*, 293-296.

Hiraoka, Y., Sedat, J. W. and Agard, D. A. (1990). Determination of three-dimensional imaging properties of a light microscope system. Biophysical J. *57*, 325-333.

Hiraoka, Y., Swedlow, J. R., Paddy, M. R., Agard, D. A. and Sedat, J. W. (1991). Three-dimensional multiple-wavelength fluorescence microscopy for the structural analysis of biological phenomena. Semin. Cell Biol. *2*, 153-165.

Holm, C., Stearns, T. and Botstein, D. (1989). DNA topoisomerase II must act at mitosis to prevent nondisjunction and chromosome breakage. Mol. Cell. Biol. *9*, 159-168.

Horowitz, R. A. and Woodcock, C. L. (1992). Alternative staining methods for Lowicryl sections. J. Histochem. Cytochem. *40*, 123-133.

Hsieh, T.-S. and Brutlag, D. (1979). Sequence and sequence variation within the 1.688 g/cm^3 satellite DNA of *Drosophila melanogaster*. J. Mol. Biol. *135*, 465-481.

Hsieh, T.-s. (1983). Purification and properties of type II DNA topoisomerase from embryos of *Drosophila melanogaster*. Methods Enzymol. *100*, 161-170.

[illegible]
[illegible]
[illegible]

Inoué, S. (1986). Video Microscopy. (London: Plenum).

Inoué, S. and Sato, H. (1964). Deoxyribonucleic acid arrangement in living sperm. In Molecular architecture in cell physiology, T. Hayashi and A. G. Szent-Gyorgi, ed. (Englewood Cliffs, New Jersey: Prentice-Hall), 209-248.

Izaurralde, E., Mirkovitch, J. and Laemmli, U. K. (1988). Interaction of DNA with nuclear scaffolds *in vitro*. J. Mol. Biol. *200*, 111-125.

Kam, Z., Jones, M. O., Chen, H., Agard, D. A. and Sedat, J. W. (1993). Design and construction of an optimal illumination system for quantitative wide-field multi-dimensional microscopy. Bioimaging *1*, 71-81.

Karpen, G. H., Schaefer, J. E. and Laird, C. D. (1988). A *Drosophila* rRNA gene located in euchromatin is active in transcription and nucleolus formation. Genes Dev. *2*, 1745-1763.

Käs, E. and Laemmli, U. K. (1992). *In vivo* topoisomerase II cleavage of the *Drosophila* histone and satellite III repeats: DNA sequence and structural characteristics. EMBO J. *11*, 705-716.

Kellogg, D. R., Mitchison, T. J. and Alberts, B. M. (1988). Behaviour of microtubules and actin filaments in living *Drosophila* embryos. Development *103*, 675-686.

Kim, R. A. and Wang, J. C. (1989). A subthreshold level of DNA topoisomerases leads to the excision of yeast rDNA as extrachromosomal rings. Cell *57*, 975-985.

[illegible]
[illegible]
[illegible]

Klein, F., Laroche, T., Cardenas, M. E., Hofmann, J. F.-X., Schweizer, D. and Gasser, S. M. (1992). Localization of RAP1 and topoisomerase II in nuclei and meiotic chromosomes of yeast. J. Cell Biol. *117*, 935-948.

Kornberg, R. D. (1974). Chromatin structure: A repeating unit of histones and DNA. Science *184*, 868-871.

Kornberg, R. D. and Thomas, J. O. (1974). Chromatin structure: Oligomers of histones. Science *184*, 865-868.

Kroeger, P. E. and Rowe, T. C. (1992). Analysis of topoisomerase I and II cleavage sites on the *Drosophila* actin and Hsp70 heat shock genes. Biochemistry *31*, 2492-2501.

Laemmli, U. K. (1970). Cleavage of structural proteins during the assembly of the head of bacteriophage T4. Nature *227*, 680-685.

Laemmli, U. K., Käs, E., Poljak, L. and Adachi, Y. (1992). Scaffold-associated regions: *cis*-acting determinants of chromatin structural loops and functional domains. Curr. Opin. Genet. Dev. *2*, 275-285.

Lewis, C. D. and Laemmli, U. K. (1982). Higher order chromosome structure: evidence for metalloprotein interactions. Cell *29*, 171-181.

Liu, L. F., Liu, C. C. and Alberts, B. M. (1980). Type II DNA topoisomerases: enzymes that can unknot a topologically knotted DNA molecule via a reversible double-strand break. Cell *19*, 697-707.

USAF LIBRARY
[illegible] LIBRARY

Lohe, A. R., Hilliker, A. J. and Roberts, P. A. (1993). Mapping simple repeated DNA sequences in heterochromatin of *Drosophila melanogaster*. Genetics *134*, 1149-1174.

Marsden, M. P. F. and Laemmli, U. K. (1979). Metaphase chromosome structure: evidence for a radial loop model. Cell *17*, 849-858.

McDonald, K. and Morphew, M. K. (1993). Improved preservation of ultrastructure in difficult-to-fix organisms by high pressure freezing and freeze substitution: I. *Drosophila melanogaster* and Strongylocentrotus purpuratus embryos. Microscopy Research and Technique *24*, 465-473.

McKee, B. D. and Karpen, G. H. (1990). *Drosophila* ribosomal RNA genes function as an X-Y pairing site during male meiosis. Cell *61*, 61-72.

Minden, J. S., Agard, D. A., Sedat, J. W. and Alberts, B. M. (1989). Direct cell lineage analysis of *Drosophila melanogaster* by time-lapse, three-dimensional optical microscopy of living embryos. J. Cell Biol. *109*, 505-516.

Mirkovitch, J., Gasser, S. M. and Laemmli, U. K. (1988). Scaffold attachment of DNA loops in metaphase chromosomes. J. Mol. Biol. *200*, 101-109.

Mitchison, T. J. (1989). Polewards microtubules flux in the mitotic spindle: evidence from the photoactivation of fluorescence. J. Cell Biol. *109*, 637-652.

Mitchison, T. J. and Sedat, J. W. (1983). Localization of antigenic determinants in whole *Drosophila* embryos. Dev. Biol. *99*, 261-264.

[illegible] [illegible]
[illegible]
[illegible] [illegible]

Moens, P. and Earnshaw, W. C. (1989). Anti-topoisomerase II recognizes meiotic chromosome cores. Chromosoma *98*, 317-322.

Negri, C., Chiesa, R., Cerino, A., Bestagno, M., Sala, C., Zini, N., Maraldi, N. M. and Astaldi-Ricotti, G. C. (1992). Monoclonal antibodies to human DNA topoisomerase I and the two isoforms of DNA topoisomerase II: 170- and 180-kDa isozymes. Ex. Cell Res. *200*, 452-459.

Nelder, J. A. and Mead, R. (1965). A simplex method for function minimization. Computer J. *7*, 308-313.

Newport, J. and Spann, T. (1987). Disassembly of the nucleus in mitotic extracts: membrane vesicularization, lamin disassembly, and chromosome condensation are independent processes. Cell *48*, 219-230.

Ohnuki, Y. (1965). Demonstration of the spiral structure of human chromosomes. Nature *208*, 916-917.

Ohnuki, Y. (1968). Structure of chromosomes. I. Morphological studies of the spiral structure of human somatic chromosomes. Chromosoma(Berl.) *25*, 402-428.

Olins, A. L., Moyer, B. A., Kim, S. H. and Allison, D. P. (1989). Synthesis of a more stable osmium ammine electron-dense DNA stain. J. Histochem. Cytochem. *37*, 395-398.

Osheroff, N. (1989). Biochemical basis for the interactions of type I and type II topoisomerases with DNA. Pharmacology and Therapeutics *41*, 223-241.

[illegible]

Osheroff, N. and Zechiedrich, E. L. (1987). Calcium-promoted DNA cleavage by eukaryotic topoisomerase II: trapping the covalent enzyme-DNA complex in an active form. Biochemistry *26*, 4303-4309.

Paddy, M. R., Belmont, A. S., Saumweber, H., Agard, D. A. and Sedat, J. W. (1990). Interphase nuclear envelope lamins form a discontinuous network that interacts with only a fraction of the chromatin in the nuclear periphery. Cell *62*, 89-106.

Parham, P. (1986). Preparation and purification of active fragments from mouse monoclonal antibodies. In Handbook of experimental immunology: Immunochemistry, M. Weir, ed. (Boston: Blackwell Scientific Publications), 14.1-14.23

Parkinson, J. M. and Hutchison, D. (1972). An investigation into the efficiency of variants of the simplex method. In Numerical Methods for Nonlinear Optimization, F. A. Lootsma, ed. (New York: Academic Press).

Paulson, J. R. (1989). Scaffold morphology in histone-depleted HeLa metaphase chromosomes. Chromosoma *97*, 289-295.

Paulson, J. R. and Laummli, U. K. (1977). The structure of histone-depleted metaphase chromosomes. Cell *12*, 817-828.

Raff, J. W. and Glover, D. M. (1988). Nuclear and cytoplasmic mitotic cycles continue in *Drosophila* embryos in which DNA synthesis is inhibited with aphidicolin. J. Cell Biol. *107*, 2009-2019.

USAF LIBRARY
[illegible]
[illegible] LIBRARY

Rattner, J. B. and Lin, C. C. (1985). Radial loops and helical coils coexist in metaphase chromosomes. Cell *42*, 291-296.

Reitman, M. and Felsenfeld, G. (1990). Developmental regulation of topoisomerase II sites and DNase I-hypersensitive sites in the chicken beta-globin locus. Mol. Cell. Biol. *10*, 2774-2786.

Richmond, T. J., Finch, J. T., Rushton, B., Rhodes, D. and Klug, A. (1984). Structure of the nucleosome core particle at 7Å resolution. Nature *311*, 532-537.

Sander, M. and Hsieh, T.-S. (1983). Double strand DNA cleavage by type II DNA topoisomerase from *Drosophila melanogaster*. J. Biol. Chem. *258*, 8421-8428.

Sander, M. and Hsieh, T.-s. (1985). *Drosophila* topoisomerase II double-strand cleavage: analysis of DNA sequence homology at the cleavage site. Nucleic Acids Res. *13*, 1057-1072.

Sedat, J. W. and Manuelidis, L. (1977). A direct approach to the structure of eukaryotic chromosomes. Cold Spring Harb. Quant. Symp. Biol. *42*, 331-50.

Shamu, C. E. and Murray, A. M. (1992). Sister chromatid separation in frog egg extracts requires DNA topoisomerase II activity during anaphase. J. Cell Biol. *117*, 921-934.

Shaw, P., Agard, D., Hiraoka, Y. and Sedat, J. (1989). Tilted view reconstruction in optical microscopy: three-dimensional reconstruction of *Drosophila melanogaster* embryo nuclei. Biophys. J. *55*, 101-110.

[illegible]
[illegible] LIBRARY

Shelton, E. R., Osheroff, N. and Brutlag, D. L. (1983). DNA topoisomerase II from *Drosophila melanogaster.* Purification and physical characterization. J. Biol.Chem. *258*, 9530-9535.

Shiozaki, K. and Yanagida, M. (1991). A functional 125-kDa core polypeptide of fission yeast DNA topoisomerase II. Mol. Cell. Biol. *11*, 6093-6102.

Shiozaki, K. and Yanagida, M. (1992). Functional dissection of the phosphorylated termini of fission yeast DNA topoisomerase II. J. Cell Biol. *119*, 1023-1036.

Sikorav, J.-L. and Jannink, G. (1994). Kinetics of chromosome condensation in the presence of topoisomerase: a phantom chain model. Biophysical J. *in press*,

Sonnenblick, B. P. (1950). The early embryology of *Drosophila melanogaster.* In Biology of *Drosophila*, M. Demerec, ed. (New York: Hafner Publishing Co.), 62-167.

Spector, D. L. (1993). Nuclear organization of pre-mRNA processing. Curr. Opin. Cell Biol. *5*, 442-447.

Stubblefield, E. and Wray, W. (1971). Architecture of the Chinese hampster metaphase chromosome. Chromosoma *32*, 262-294.

Sundin, O. and Varshavsky, A. (1980). Terminal stages of SV40 DNA replication proceed via multiply intertwined catenated dimers. Cell *21*, 130-140.

USAF LIBRARY
[illegible]
[illegible]

Swedlow, J. R., Sedat, J. W. and Agard, D. A. (1993). Multiple chromosomal populations of topoisomerase II detected *in vivo* by time-lapse, three-dimensional wide field microscopy. Cell *73*, 97-108.

Taagepera, S., Rao, P. N., Drake, F. H. and Gorbsky, G. J. (1993). DNA topoisomerase II alpha is the major chromosome protein recognized by the mitotic phosphoprotein antibody MPM-2. Proc. Natl. Acad. Sci. USA *90*, 8407-8411.

Tartof, K. D., Hobbs, C. and Jones, M. (1984). A structural basis for variegating position effects. Cell *37*, 869-878.

Theurkauf, W. E. (1992). Behavior of structurally divergent alpha-tubulin isotypes during *Drosophila* embryogenesis: evidence for post-translational regulation of isotype abundance. Dev. Biol. *154*, 205-217.

Tsien, R. Y. and Waggoner, A. (1990). Fluorophores for confocal microscopy: photophysics and photochemistry. In Handbook of Biological Confocal Microscopy, J. B. Pawley, ed. (New York: Plenum), 169-178.

Udvardy, A. and Schedl, P. (1991). Chromatin structure, not DNA sequence specificity, is the primary determinant of topoisomerase II sites *in vivo*. Mol. Cell. Biol. *11*, 4973-4984.

Uemura, T. and Yanagida, M. (1986). Mitotic spindle pulls but fails to separate chromosomes in type II DNA topoisomerase mutants: uncoordinated mitosis. EMBO J. *5*, 1003-1010.

[illegible]

[illegible]

Uemura, T., Ohkura, H., Adachi, Y., Morino, K., Shiozaki, K. and Yanagida, M. (1987). DNA topoisomerase II is required for condensation and separation of mitotic chromosomes in S. Pombe. Cell *50*, 917-925.

Wang, J. C. (1985). DNA topoisomerases. Annu. Rev. Biochem. *54*, 665-697.

Whalen, A. M., McConnell, M. M. and Fisher, P. A. (1991). Developmental regulation of *Drosophila* topoisomerase II. J. Cell Biol. *112*, 203-213.

Widom, J. (1989). Toward a unified model of chromatin folding. Ann. Rev. Biophys. Biophys. Chem. *18*, 365-395.

Wilhelm, J. E. and Vale, R. D. (1993). RNA on the move: the mRNA localization pathway. J. Cell Biol. *123*, 269-274.

Wood, E. and Earnshaw, W. C. (1990). Mitotic chromatin condensation *in vitro* using somatic cell extracts and nuclei with variable levels of endogenous topoisomerase II. J. Cell Biol. *111*, 2839-2850.

Woodcock, C. L., Grigoryev, S. A., Horowitz, R. A. and Whitaker, N. (1993). A chromatin folding model that incorporates linker variability generates fibers resembling the native structures. Proc. Soc. Natl. Acad. USA *90*, 9021-9025.

Woodcock, C. L., Horowitz, R. A. and Agard, D. A. (1992). Three-dimensional organization of chromatin fibers in situ examined by EM tomography. In Proceedings, 50th Annual Meeting Electron Microscopy Society of America., G. W. Bailey, J. Bentley and J. A. Small, ed. (San Francisco: San Francisco Press), 498-499.

Woodcock, C. L., McEwen, B. F. and Frank, J. (1991). Ultrastructure of chromatin. II. Three-dimensional reconstruction of isolated fibers. J. Cell Sci. *99*, 107-114.

Wu, C. and Goldberg, M. L. (1989). The *Drosophila* zeste gene and transvection. Trends Genet. *5*, 189-194.

Wu, C. I., Lyttle, T. W., Wu, M. L. and Lin, G. F. (1988). Association between a satellite DNA sequence and the Responder of Segregation Distorter in D. *melanogaster*. Cell *54*, 179-189.

Wyckoff, E., Natalie, D., Nolan, J. M., Lee, M. and Hsieh, T.-S. (1989). Structure of the *Drosophila* DNA topoisomerase II gene: Nucleotide sequence and homology among topoisomerases II. J. Mol. Biol. *205*, 1-13.

Yen, T. J., Compton, D. A., Zinkowski, R. P., Brinkley, B. R., Earnshaw, W. C. and Cleveland, D. W. (1991). CENP-E, a novel human centromere-associated protein required for progression from metaphase to anaphase. EMBO J. *10*, 1245- 1254.

Zalokar, M. and Erk, I. (1976). Division and migration of nuclei during early embryogenesis of *Drosophila melanogaster*. J. Micros. Biol. Cell. *25*, 97-106.

Zlatanova, J. and van Holde, K. (1992). Histone H1 and transcription: still an enigma? J. Cell Sci. *103*, 889-895.

Appendix 1: Focal points for chromosome condensation and decondensation revealed by three-dimensional in vivo time-lapse microscopy

Introduction

This appendix consists of an article published as Hiraoka, Y., Minden, J. S., Swedlow, J. R., Sedat, J. W. and Agard, D. A. (1989). Focal points for chromosome condensation and decondensation revealed by three-dimensional in vivo time-lapse microscopy. Nature *342*, 293-296. The paper describes the identification *in vivo* of sites of initiation of chromosome condensation along the nuclear periphery. Sites which are the last to decondense after telophase appear to be the first to condense at the end of interphase. J. R. Swedlow's contribution to this work was the identification of these sites in fixed embryos stained with DAPI and the determination, by statistical analysis, that the sites lay at or below the nuclear midline.

© Macmillan Magazines Ltd., 1989

Focal points for chromosome condensation and decondensation revealed by three-dimensional *in vivo* time-lapse microscopy

Yasushi Hiraoka, Jonathan S. Minden,
Jason R. Swedlow*, John W. Sedat
& David A. Agard

Department of Biochemistry and Biophysics, and The Howard Hughes Medical Institute, and * Graduate Group in Biophysics, University of California, San Francisco, San Francisco, California 94143-0448, USA

ALTHOUGH the dynamic behaviour of chromosomes has been extensively studied in their condensed state during mitosis, chromosome behaviour during the transition to and from interphase has not been well documented. Previous electron microscopic studies suggest that chromosomes condense in a non-uniform fashion at the nuclear periphery[1,2]. But chromosome condensation is a complicated and dynamic process and requires continuous observation in living tissues to be fully understood. Using a recently developed three-dimensional time-lapse fluorescence microscopy technique[3], we have observed chromosomes as they relax from telophase, through interphase, until their condensation at the next prophase. This technique has been improved to produce higher-resolution images by implementing new stereographic projection and computational processing protocols[4]. These studies have revealed that chromosomal regions on the nuclear envelope, distinct from the centromeres and telomeres, serve as foci for the decondensation and condensation of diploid chromosomes. The relative positions of the late decondensation sites at the beginning of interphase appear to correspond to the early condensation sites at the subsequent prophase.

In order to study the chromosomal events that occur between telophase and the ensuing prophase, we have followed embryonic nuclei of *Drosophila melanogaster* during the late syncytial blastoderm period. Chromosomes in living *Drosophila* embryos were visualized by imaging chromatin which had assembled fluorescent-labelled histones into nucleosomes. Calf thymus histones H2A and H2B were conjugated with rhodamine and microinjected into *Drosophila* embryos 30 minutes after oviposition to ensure a uniform distribution of the labelled histones

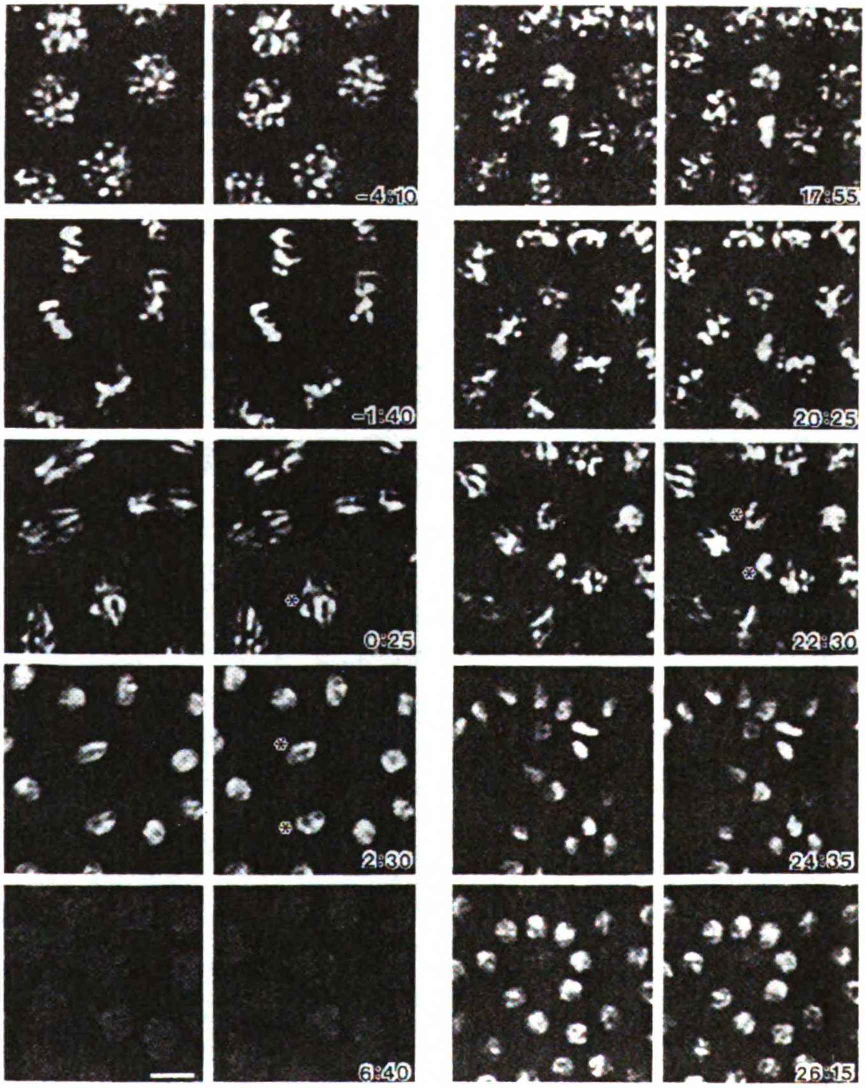

FIG. 1 Stereo pairs selected from the time-lapse data. The numbers represent time in minutes:seconds after the 12th nuclear division. Time is stated relative to the onset of chromosome separation at the metaphase-anaphase transition; a negative sign is given to data dets taken before the 12th nuclear division. Asterisks indicate damaged nuclei (see text and also Fig. 2). Scale bar represents 5 μm.

METHODS. Recording three-dimensional data from living embryos: A standalone, computer workstation CCD system was used which provides real-time capability with a lower digital resolution (12 bits versus 14 bits) but a faster readout rate (200,000 pixel per second versus 50,000 pixel per second) than our previously reported system[5]. All aspects of microscopy, data collection, data storage, image processing and display can be performed on the one workstation. A Peltier-cooled CCD camera (Photometrics, Tucson, Arizona) with a 1340 × 1037 pixel CCD chip (Kodak-Videk) coated to improve short-wavelength response[6], is attached to an IMT-2 Olympus inverted microscope. Microscope shutter, focus movement and CCD data collection are controlled by a MicroVax III workstation coupled to a 20 MFLOPS Mercury Zip 3232 + array processor (Mercury Computer Systems, Lowell, Massachusetts) and a Parallax model 1280 graphic display system having 12 Mbyte of image memory (Parallax Graphics, Santa Clara, California). Calf thymus histones were bound to double-strand DNA cellulose to form nucleosomes, labelled with 5(6)-carboxytetramethyl rhodamine *N*-hydroxysuccinimidyl ester (Molecular Probes, Eugene, Oregon), and eluted with a salt gradient. Rhodamine-labelled histones H2A and H2B, at 0.4 mg ml^{-1}, were microinjected into *D. melanogaster* embryos. Details of the method are reported elsewhere[3]. The rhodamine-histone injected embryos were illuminated with a 100W mercury arc lamp attenuated 20-fold by a neutral density filter and observed using an Olympus 40×/NA1.3 oil immersion objective lens and a high selectivity rhodamine filter combination (Omega Optical, Brattleboro, Vermont). To speed up the image readout, images were taken on a small portion of the CCD, 256 × 256 pixels corresponding to 44 × 44 μm area with a pixel size of 0.17 μm. Five optical section images were recorded at an interval of 1 μm with an exposure time of 0.1 s. It took 5 s to read out correct and store each image; thus, 25 s for one cycle of a focus series. This was repeated 80 times to form a time course. Generation of a time-lapse stereo movie: To make a pair of stereo projections, each set of 5 optical sections was projected to form a single image for each eye. While forming the projection for the left-eye, images were sequentially shifted by 1 pixel to the left, whereas right eye images were shifted 1 pixel to the right. As the optical sections are separated by 1 μm, a shift by one pixel (0.17 μm) per every section (1 μm) corresponds to a tilt of 9.6°, therefore the stereo pair is separated by a tilt of 19.2°. To remove out-of-focus information from the projected images, a three-dimensional optical transfer function was experimentally determined for the objective lens under the conditions used for the data collection of nuclei by imaging very small fluorescent beads (0.1 μm in diameter) as described previously[5]. The projected stereo images were computationally processed to remove out-of-focus information by a constrained iterative deconvolution method using the $Z^* = 0$ plane of the three-dimensional optical transfer function[4]. This approach based on the Fourier projection theorem, can provide nearly perfect signal recovery using data collection conditions that cause minimum exposure to the specimen. Although not precisely correct for the sliding stereo projections used here, the approximation is suitable for the limited spatial regions examined. For rapid movie display, the entire set of time-lapse stereo images was loaded into the Parallax display system with a 12 Mbyte image memory before the display. This permits a pair of the stereo projection images to be displayed side-by-side and rapidly unpdated to form a time-lapse stereographic movie.

the time of observation. The injected rhodamine-labelled ones are stably incorporated into chromatin during periods DNA replication. Under low levels of illumination, these ryos can be observed for more than three hours and develop mally to hatching.

bserving the behaviour of an entire nucleus requires a three- ensional analysis over time. Imaging at low light levels was omplished using a cooled, scientific grade charge-coupled ice (CCD) imager[5,6] operated by a self-contained computer rkstation. Three-dimensional data sets were obtained by itally recording a series of five optical sections taken at 1 μm al intervals every five seconds, as described in the legend to . 1. By repeating this optical sectioning protocol every 25 onds, a time-lapse series of 80 three-dimensional data sets s recorded. The period of analysis spanned nuclear cycles 12 d 13 of syncytial blastoderm stage embryos. During this stage embryonic development, the nuclei form an almost syn-onously replicating monolayer on the embryo surface[7,8]. The clear cycle length for the embryo shown in Fig. 1 was 22 nutes at 23 °C. Embryos were monitored after data collection verify that gastrulation occurred normally.

To facilitate analysis of the large amount of three-dimensional ta over time, a time-lapse stereo movie was constructed using synthetic projection method[4] described in the legend to Fig. Briefly, a stereo pair of projected images is formed from each of optical section data by sequentially shifting each image her left or right and summing to generate the projections. The ojected images are then computationally processed to remove t-of-focus information[4]. For projected images, this is a simple d straightforward process which can provide nearly exact blurring. Furthermore, as no light is rejected in the image ocessing, unlike confocal microscopy, this approach is ideal r the low-light level imaging required for *in vivo* analysis. The resultant in-focus stereo projection images were sequentially displayed in rapid succession as a time-lapse movie. Examples of selected frames of the movie are shown as stereo pairs in Fig. 1.

Examination of the real-time, three-dimensional data revealed that chromosome decondensation terminates and condensation initiates at discrete sites predominantly on the nuclear envelope (visualized as bright spots; Fig. 2*a*–*e*). Chromosomes begin to decondense shortly after chromatid separation, and by the following interphase, nuclei labelled with rhodamine-conjugated histones show an essentially uniform appearance. Surprisingly, examination of the kinetics of chromosome decondensation revealed that a small portion of the chromosomes remained condensed at several sites on the nuclear envelope (2–3 sites per nucleus) after most of the chromosomes had decondensed (about 5 minutes after the metaphase-anaphase transition of the twelfth cycle). The location of these sites can be seen clearly at the nuclear periphery (indicated by arrows in Fig. 2*a*–*e*, column 1). Because these late decondensation sites eventually disappear to make a uniformly stained nucleus during interphase (about 6 minutes after the metaphase-anaphase transition; see Fig. 1, frame at 6:40 min), they are not consistent with the classical definition of heterochromatin.

At the transition from interphase to prophase, bright spots of chromosome condensation were also observed at discrete sites on the nuclear envelope (indicated by arrows in Fig. 2*a*–*e*, columns 3–6). The first of these condensation sites appears 10 minutes after nuclear division, with new sites continuing to appear over a 5-minute interval (Fig. 2*a*–*e*, columns 3–6). Significantly, the relative positions of these early condensation sites were similar to those of the late decondensation sites. Examples of the congruity as shown in Fig. 2*a*–*e* (compare column 1 with columns 3–6). In addition, newly condensed chromosome

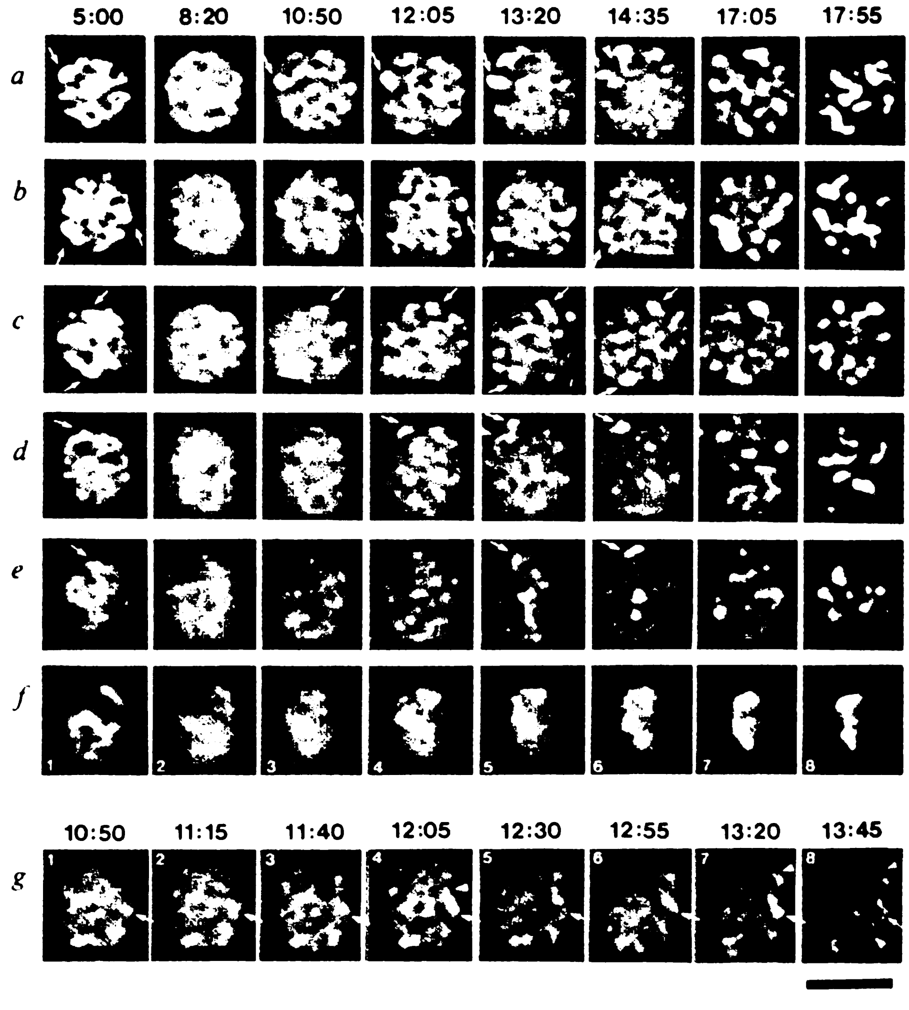

G. 2 Chromosome decondensation and ondensation. Chromosome decondensation nd condensation is shown as a time course. nly one view of the stereo movie is shown or each time point. A damaged nucleus is hown in *f*. Chromosome fibres growing in a ingle nucleus shown in *g* at every 25 s from 0 min 50 s to 13 min 45 s. The numbers at e top of each column or frame represent ime in minutes:seconds as in Fig. 1. ucleation sites are shown by arrows and ibres by arrowheads. Scale bar represents μm.

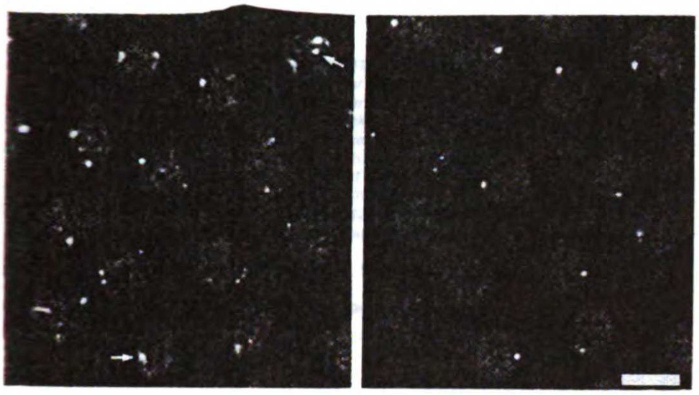

FIG. 3 Sites of condensed chromatin in fixed nuclei. Two optical section images are shown, separated by 2 μm, from a high-resolution three-dimensional data set of a fixed embryo. Because of the curvature of the embryo surface, the focal plane intersects nuclei seen in the upper and lower portions of the field at higher positions than those located in the centre of the field. All of the nuclei shown in the left panel are visualized above the nuclear midline, whereas those in the right panel are all at, or below, the midline. Arrows indicate apparent intranuclear sites above the midline. Scale bar represents 5 μm.

METHODS. *Drosophila* embryos were fixed with 3.7% formaldehyde in heptane/buffer A (15 mM PIPES, pH 7.0, 80 mM KCl, 20 mM NaCl, 0.5 mM EGTA, 2 mM EDTA, 0.5 mM spermidine, 0.2 mM spermine, 0.1% 2-mercaptoethanol). The chorion and vitelline membrane were removed as described previously[17]. The embryos were stained with 0.1 μg ml^{-1} DAPI. Optical section images were collected on the CCD at focus step of 0.2 μm using an Olympus oil-immersion objective lens (60×/NA1.4) and computationally processed to remove the out-of-focus information as described[4].

'fibres' can be seen elongating from these sites at the rate of about 1 μm per min (Fig. 2*a*, *d* and *g*). In one particularly clear case (Fig. 2*g*), the elongation appears to be bidirectional. As the condensation sites were found near the nuclear midline, they are unlikely to be either centromeric or telomeric sites, which are known to be localized to the apical and basal portions of the nucleus respectively[9]. Towards prophase (Fig. 2*a–e*, columns 7, 8), the chromosomes are seen to condense further, forming more contiguous structures. By the time condensation has proceeded sufficiently to identify individual chromosomes, the sites have detached and moved from the nuclear envelope (compare columns 6 and 7 in Fig. 2*a–e*), making it impossible to assign these sites, as yet, to specific chromosomes.

Similar chromosomal bright spots were observed in higher-resolution optical section data of nuclear-cycle-13 embryos that had been fixed and stained with the DNA-specific fluorescent dye, 4′,6-diamidino-2-phenylindole (DAPI), as shown in Fig. 3. Below the nuclear midline, chromosome condensation sites were exclusively observed at the nuclear envelope. By contrast, sites were seen both internally and at the periphery above the midline. It seems that the internal bright spots are associated with, and likely to be a part of, the centrometric heterochromatin. Although such peripheral bright spots had been repeatedly observed in fixed preparations in our laboratory, it is only as a result of continuous observation of chromosome behaviour in individual nuclei that we appreciated the significance of these chromosomal regions.

Using the time-lapse data set, we also have been able to analyse the behaviour of a damaged nucleus (indicated by asterisks in Fig. 1). A chromosomal cross-bridge, the consequence of naturally occurring mitotic failure or photo-induced crosslinking of chromatin, is seen to be extended between daughter nuclei during anaphase. This anaphase bridge was eventually resolved, probably by chromosomal breakage. The resultant damaged nuclei proceeded through chromosome decondensation and condensation with about the same timing as neighboring undamaged nuclei (Fig. 2*f*; see also Fig. 1), but failed to divide at the next nuclear division cycle (Fig. 1). The damaged nuclei then migrated to the embryo interior while normal nuclei divided and remained at the embryo surface. The loss of a small number of islated nuclei at the syncytial blastoderm stage apparently does not affect further embryonic development[3].

These results suggest that sites on chromosomes or on the nuclear envelope function as nucleation points of condensation and decondensation of chromosomes (Fig. 4). Furthermore, the congruity of those sites at telophase and the next prophase suggests that nuclear structures are, in part, preserved during interphase. Previously, we have shown that in *D. melanogaster* polytene interphase chromosomes, there are 15–20 chromosomal sites that are involved in attachment to the nuclear envelope[10-12]. The analysis of chromosomal rearrangements demonstrated that the attachments are chromosomal site-specific, and nuclear-envelope non-specific[13]. As yet, there is no direct evidence for the correlation of these sequences with the condensation initiation loci observed in this report. As many features of chromosome topology are clearly below the resolution of light microscopy, we cannot eliminate the possibility that some limited chromosome condensation might take place at sites other than on the nuclear envelope. Precise determination of the spatial distribution of sites will require analyses of higher resolution.

The real-time, three-dimensional analysis used in this work represents a compromise between temporal and spatial resolution. To speed up the image acquisition rate, data were collected at a spatial resolution lower than we normally use when examining fixed specimens (pixel sizes: 0.17 μm versus 0.06 μm in the microscopic field plane and 1 μm versus 0.2 μm in the focus direction). Nevertheless, examining whole cells in the living state in three dimensions can provide unique insights into cellular structure and function not possible with other structural methods. Improvements in data collection software and the use of a faster CCD readout rate will decrease the time required to record and store an image by fivefold. Storing only final stereo pairs instead of individual section images should provide a further twofold improvement in speed.

To understand cellular events, it is important to visualize macromolecular interactions within the three-dimensional context of the cell as a function of time. Other 'four-dimensional' imaging schemes using polarization or differential interference contrast microscopy have been devised[14], but the molecular specificity of imaging in fluorescence microscopy makes it the technique of choice for our studies of interphase nuclei. In addition, by the use of rapid wavelength-switching, it should be possible to extend the 'four-dimensional' technique described here to the simultaneous analyses of multiple macromolecular components in individual living cells[15,16]. We anticipate that the approach can be extended to a wide range of dynamic biological phenomena. □

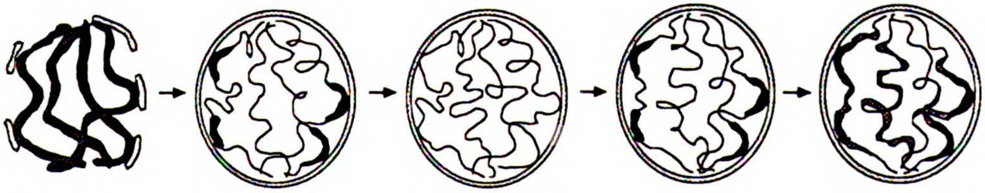

FIG. 4 Schematic diagram of the events of chromosome decondensation and condensation. After the nuclear envelope is reformed on telophase chromosomes, decondensation proceeds sequentially, terminating at specific sites at or near the nuclear envelope. Chromosome condensation starts again at discrete sites, possibly the same as the late decondensation sites, and proceeds with bidirectional growth before the next prophase.

Received 2 May; accepted 4 October 1989.

1. Comings, D. E. & Okada, T. A. *Expl Cell Res.* **63**, 471–473 (1970).
2. Robbins, E., Pederson, T. & Klein, P. *J. Cell Biol.* **44**, 400–416 (1970).
3. Minden, J. S., Agard, D. A., Sedat, J. W. & Alberts, B. *J. Cell Biol.* **108**, 505–516 (1989).
4. Agard, D. A., Hiraoka, Y., Shaw, P. & Sedat, J. W. *Meth. Cell Biol.* **30**, 353–377 (1989).
5. Hiraoka, Y., Sedat, J. W. & Agard, D. A. *Science* **238**, 36–41 (1987).
6. Aikens, R. S., Agard, D. A. & Sedat, J. W. *Meth. Cell Biol.* **29**, 291–313 (1989).
7. Zalokar, M. & Erk, I. *J. Micros. Biol. Cell.* **25**, 97–106 (1976).
8. Foe, V. E. & Alberts, B. M. *J. Cell Sci.* **61**, 31–70 (1983).
9. Foe, V. E. & Alberts, B. M. *J. Cell Biol.* **100**, 1623–1636 (1985).
10. Mathog, D., Hochstrasser, M., Gruenbaum, Y., Saumweber, H. & Sedat, J. W. *Nature* **308**, 414–421 (1984).
11. Hochstrasser, M., Mathog, D., Gruenbaum, Y., Saumweber, H. & Sedat, J. W. *J. Cell Biol.* **102**, 112–123 (1986).
12. Hochstrasser, M. & Sedat, J. W. *J. Cell Biol.* **104**, 1471–1483 (1987).
13. Mathog, D. & Sedat, J. W. *Genetics* **121**, 293–311 (1989).
14. Inoue, S. & Inoue, T. D. *Ann. N.Y. Acad. Sci.* **483**, 392–404 (1987).
15. Taylor, D. L., Amato, P. A., McNeil, P. L., Luby-Phelps, K. & Tanasugarn, L. in *Applications of Fluorescence in the Biomedical Sciences* (eds Taylor, D. L., Waggoner, A. S., Murphy, R. F., Lanni, F. & Birge, R. R.) 347–376 (Liss, New York, 1986).
16. Waggoner, A. *et al. Meth. Cell Biol.* **30**, 449–478 (1989).
17. Mitchison, T. J. & Sedat, J. W. *Devl Biol.* **99**, 261–264 (1983).

ACKNOWLEDGEMENTS. We thank Hans Chen and Mel Jones for their crucial contributions to software and hardware development and Elizabeth Blackburn, Mary Rykowski, Andrew Belmont and Tokuko Haraguchi for critical reading of the manuscripts. This work was supported by the National Institutes of Health and by the Howard Hughes Medical Institute (J.W.S. and D.A.A.). D.A.A. is also a National Science Foundation Presidential Young Investigator. J.S.M. was supported by a fellowship from the Helen Hay Whitney Foundation and Y.H. a Damon Runyon-Walter Winchell Cancer Research Fund Fellowship.

Printed in Great Britain by Turnergraphic Limited, Basingstoke, Hampshire

Appendix 2: Role of neurogenic genes in establishment of follicle cell fate and oocyte polarity during oogenesis in *Drosophila*

Introduction

This appendix consists of an article published as Ruohola H., Bremer K. A., Baker D., Swedlow J. R., Jan L. Y., Jan Y. N. (1991). Role of neurogenic genes in establishment of follicle cell fate and oocyte polarity during oogenesis in *Drosophila*. Cell *66*: 433-449 and is reprinted here by permission. The paper describes the roles of the neurogenic genes, *Notch* and *Delta* in oogenesis in *Drosophila*. Temperature sensitive mutations were used to demonstrate a requirement for these proteins for proper follice cell function during oogenesis. In a fashion reminiscent of *Drosophila* neurogeneis, follicle cells surrounding egg chambers fromN^{ts1} /N^{ts1} flies failed to pinch off from the posterior end of the germarium and form the thin stalk of cells that connect the germarium to the vittelarium. The egg chamber continued to grow in its aberrant location, generating a swollen germarium. J. R. Swedlow's contribution to this work was the use of three-dimensional light microscopy to first show first, that, *Notch* flies bear an improper number of nurse cells, and second, that this phenotype appears in the germarium, around the 10th hour of oogenesis.

Cell, Vol. 66, 433–449, August 9, 1991, Copyright © 1991 by Cell Press

Role of Neurogenic Genes in Establishment of Follicle Cell Fate and Oocyte Polarity during Oogenesis in Drosophila

H. Ruohola,* K. A. Bremer,* D. Baker,† J. R. Swedlow,‡ L. Y. Jan,* and Y. N. Jan*
Howard Hughes Medical Institute
*Departments of Physiology and Biochemistry
†Department of Biochemistry and Biophysics
‡Graduate Group in Biophysics
University of California, San Francisco
San Francisco, California 94143-0724

Summary

Oogenesis in Drosophila involves specification of both germ cells and the surrounding somatic follicle cells, as well as the determination of oocyte polarity. We found that two neurogenic genes, *Notch* and *Delta*, are required in oogenesis. These genes encode membrane proteins with epidermal growth factor repeats and are essential in the decision of an embryonic ectodermal cell to take on the fate of neuroblast or epidermoblast. In oogenesis, mutation in either gene leads to an excess of posterior follicle cells, a cell fate change reminiscent of the hyperplasia of neuroblasts seen in neurogenic mutant embryos. Furthermore, the *Notch* mutation in somatic cells causes mislocalization of *bicoid* in the oocyte. These results suggest that the neurogenic genes *Notch* and *Delta* are involved in both follicle cell development and the establishment of anterior–posterior polarity in the oocyte.

Introduction

Oogenesis in Drosophila melanogaster involves the specialization of both germline and somatic cells (King, 1970; Mahowald and Kambysellis, 1978). One of the 16 cystocytes produced by four consecutive divisions of a germline stem cell becomes the oocyte, whereas the others form nurse cells. The developing oocyte is surrounded by a monolayer of somatic follicle cells. These follicle cells provide the initial cues for the establishment of dorsal–ventral polarity in the oocyte (Anderson, 1987; Schüpbach, 1987; Manseau and Schüpbach, 1989). Some of the asymmetry of the oocyte, therefore, is likely to derive from asymmetric differentiation of its surrounding follicle cells. Consistent with this expectation, follicle cells at different locations of the egg chamber show signs of specialization (Cooley et al., 1988; Grossniklaus et al., 1989; Fasano and Kerridge, 1988). Relatively little is known about the mechanisms by which the fates of different follicle cells are specified. Anterior–posterior polarity of the oocyte is established partly through the anterior localization of the morphogen *bicoid* (*bcd*) (Nüsslein-Volhard et al., 1987; Berleth et al., 1988; St Johnston et al., 1989; Driever et al., 1990). There has been no evidence reported that signals from somatic cells play a role in *bcd* localization.

In studies of the β-galactosidase expression pattern of enhancer-trap lines (Bier et al., 1989) and transcript distributions, we noticed that several neurogenic genes were expressed in somatic and/or germline cells of the ovary. Neurogenic genes play an essential role in the specification of neuroblasts in the Drosophila embryo (for review see Artavanis-Tsakonas, 1988; Campos-Ortega, 1988; Campos-Ortega and Jan, 1991). Loss of function of a neurogenic gene causes an excess of ectodermal cells to become neuroblasts instead of epidermoblasts. Moreover, cell ablation studies in the grasshopper embryo reveal that as a neuroblast forms, it inhibits surrounding ectodermal cells from becoming neuroblasts, a process called lateral inhibition (Doe and Goodman, 1985). These findings suggest that the neurogenic genes are involved in lateral inhibition. Consistent with this notion, two interacting neurogenic genes, *Notch* (*N*) and *Delta* (*Dl*) (Vässin et al., 1985; Fehon et al., 1990) have been found to encode membrane proteins with epidermal growth factor (EGF) repeats (Wharton et al., 1985; Kidd et al., 1986; Vässin et al., 1987; Kopczynski et al., 1988). Several other neurogenic genes, *neuralized* (*neu*) (Boulianne et al., submitted), *mastermind* (Smoller et al., 1990), and genes in the *Enhancer of split* complex (Hartley et al., 1988; Klämbt et al., 1989), which apparently encode globular proteins, appear to be involved in the same pathway as *N* and *Dl* (de la Concha et al., 1988). Another neurogenic gene, *big brain* (*bib*), involves an independent pathway (de la Concha et al., 1988) and encodes a presumed integral membrane protein (Rao et al., 1990).

To determine whether neurogenic genes play a role in oogenesis, we began by studying the existing temperature-sensitive mutants of *N* (Shellenbarger and Mohler, 1975) and *Dl* (Lehmann et al., 1983). In this paper we present evidence that mutations in either gene affect the development of the somatic follicle cells, resulting in an excess of posterior follicle cells due to a cell fate change as well as early defects in the formation of the egg chamber. Abnormalities in the oocytes are also evident at two stages of oogenesis. Because mutant phenotypes such as the mislocalization of *bcd* mRNA can be attributed to the genotype of somatic cells in *N* mutants, it appears that somatic cells are involved in the formation of the anterior–posterior axis of the oocyte. Besides *N* and *Dl*, several other neurogenic genes are also expressed in the ovary, raising the possibility that these neurogenic genes as a group might be involved in oogenesis, perhaps acting as a cassette to mediate cell interactions at multiple stages of development.

Results

Oogenesis in Drosophila occurs within ovarioles, which contain a succession of developmental stages (King, 1970; Mahowald and Kambysellis, 1978) (Figures 1A and 1B). The earliest structure, the germarium (g in Figure 1), is at the anterior end of the ovariole and contains stem cells of the germline lineage and somatic follicle cells. The stem cell divides to produce a 16 cell cyst surrounded by follicle cells, a process that takes 10 hr at 25°C. The egg

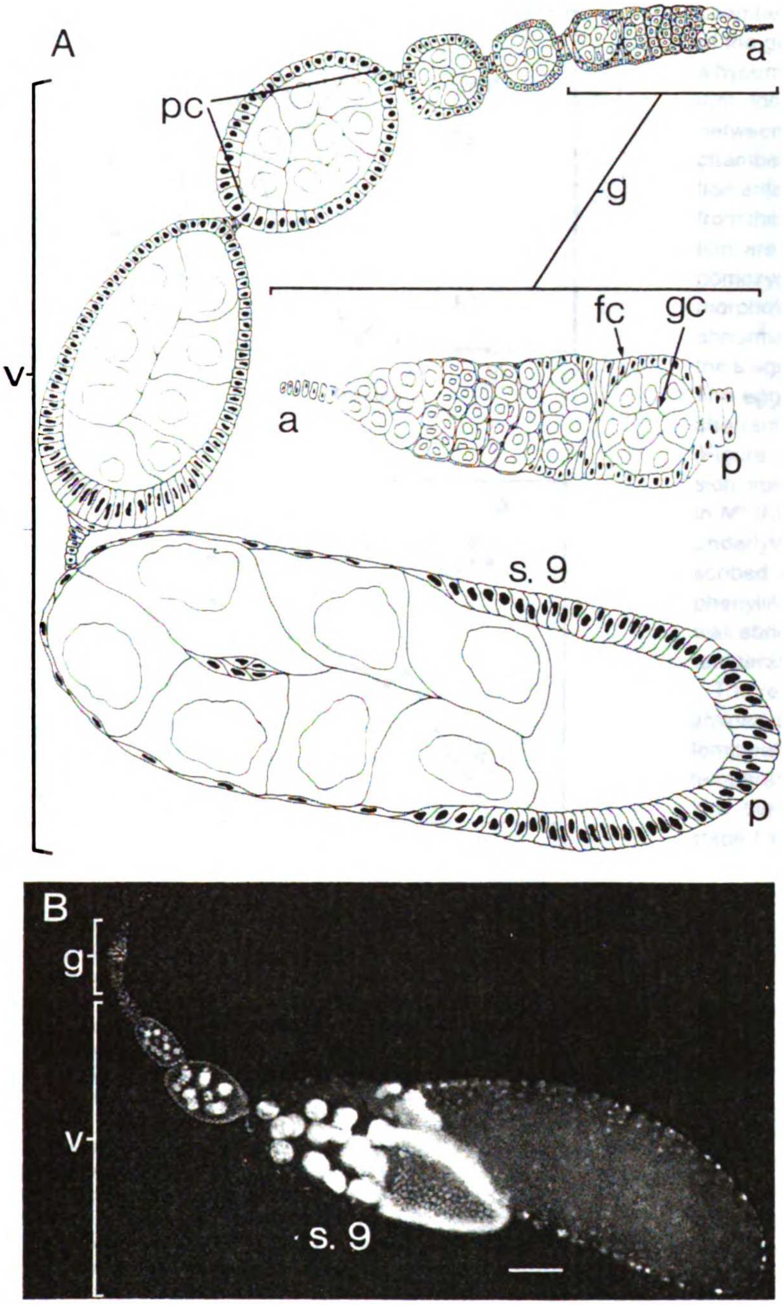

Figure 1. Developmental Sequence in Oogenesis

(A) A diagram of an adult wild-type ovariole. (B) A wild-type ovariole stained with DAPI. a, anterior; p, posterior; g, germarium; v, vitellarium; gc, germline cells; fc, somatic follicle cells; pc, polar cells; s.9, an egg chamber at stage 9 in oogenesis. Scale bar is 1 mm.

chamber containing a cyst then pinches off from the germarium and progresses through 14 developmental stages in the vitellarium (v in Figure 1) over a period of 3 days prior to egg deposition.

We have observed defects at two stages in oogenesis in temperature-sensitive mutants of *N* and *Dl*. We will first focus on the *N* phenotype and then briefly describe the *Dl* phenotype, because mutations of these two genes lead to qualitatively similar defects.

Temperature-Sensitive Defect in Egg Laying by N^{ts1}/N^{ts1} Females

The role of *N* in oogenesis was investigated using a temperature-sensitive mutant (Shellenbarger and Mohler, 1975). Homozygous N^{ts1} embryos were allowed to develop at the permissive temperature (18°C), and adult females were then shifted to the restrictive temperature (32°C; Cagan and Ready, 1989). The rate of egg laying by N^{ts1}/N^{ts1} females was reduced at 32°C compared with that of control females, which were homozygous for N^{ts1} but carried a duplication including the wild-type *N* gene on the second chromosome. Egg laying was reduced by 50% after 20 hr and 97% after 2 days at the restrictive temperature (Figure 2A). Since oogenesis in an adult wild-type female takes approximately 2 days at 32°C, *N* function appears to be essential in early to mid oogenesis.

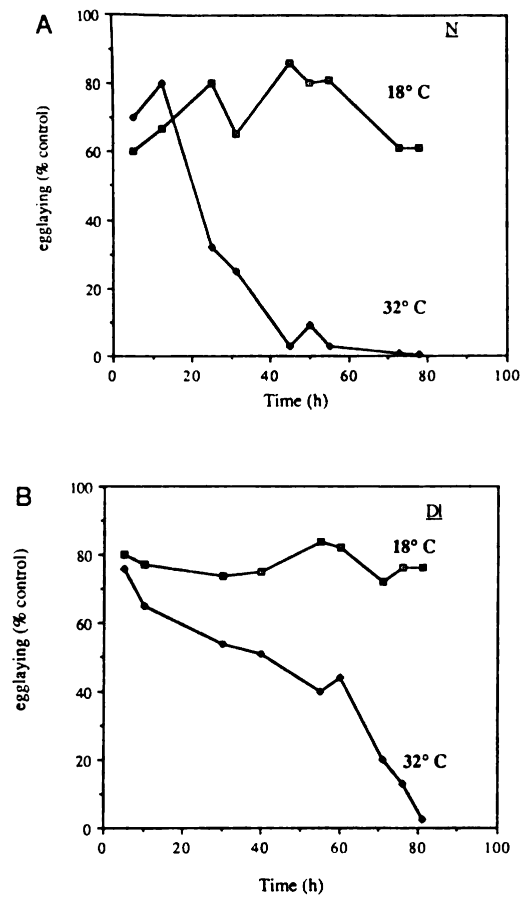

Figure 2. *N* and *Dl* Are Required for Oogenesis

(A) Temperature-sensitive defect in egg laying by homozygous N^{ts1} females. The rates of egg laying by *N* mutant females at the permissive (open squares) and nonpermissive (filled squares) temperatures are plotted as a function of time at the specified temperature. The rates are expressed as a percentage of the rates of egg laying by similarly treated control females bearing a wild-type copy of *N* on the second chromosome. Oogenesis occurs 2.75 times faster at 32°C than at 18°C. A dramatic decrease in the amount of eggs laid by N^{ts1}/N^{ts1} females was detected after 12 hr at 32°C, which is the amount of time required for the progression from stage 8–9 in oogenesis to egg deposition. In 2 days at the restrictive temperature, egg laying by N^{ts1}/N^{ts1} females was reduced to 3% of that of the control females.

(B) Temperature-sensitive defect in egg laying by Dl^{6B37}/Dl^{rev1} females at permissive (open squares) and nonpermissive (filled squuares) temperature. The rates are expressed as a percentage of the egg laying of similarly treated control $Dl^{6B37}/Dp(3{:}3)D2$ females. The rate of egg laying by the control animals was comparable to that of wild type.

To understand the nature of the requirement for the *N* gene in oogenesis, we first analyzed the morphology of ovaries in the temperature-sensitive mutant at the restrictive temperature. As discussed below, morphological abnormalities were observed both in the germarium and in the vitellarium.

Morphological Defects in Germarium and Vitellarium

After 1 day at the restrictive temperature, stage 1 egg chambers did not pinch off properly from the posterior end of the germarium in N^{ts1}/N^{ts1} or N^{ts1}/N^{Placr} mutants (N^{Placr} is a hypomorphic allele) (Figure 3C). In the wild-type germarium, follicle cell delamination and interleafing take place between the stage 1 egg chamber and the immature egg chamber located at its anterior end, resulting in a contraction anterior to the stage 1 egg chamber as it is separated from the germarium (the cells in between after the contraction are called stalk cells; Figure 11A) (King, 1970). In homozygous N^{ts1} mutant females, these follicle cells were morphologically abnormal and failed to form a stalk. These abnormalities were associated with an apparent failure of the stage 1 egg chamber to pinch off from the germarium. The egg chambers appeared to continue growing in the aberrant location, resulting in large and swollen germaria (Figure 3C). This mutant phenotype is recessive; progression from the germarium to the vitellarium was normal in $N^{ts1}/FM6$ females at 32°C (not shown). A defect in the underlying germline was also detected. As will be described elsewhere, the morphology of 4′,6-diamidino-2-phenylindole (DAPI)–stained chromosomes in the oocyte was abnormal in germaria of N^{ts1} females at the restrictive temperature.

The reversibility of the block in the germarium was examined by incubating N^{ts1}/N^{ts1} females at the restrictive temperature for 20 hr and then shifting to the permissive temperature. After 24–30 hr at the permissive temperature, the germarium regained its normal morphology, and stage 1 egg chambers were observed to pinch off from the germarium. Even after longer (29 hr) exposure to 32°C, the mutant females regained their ability to produce eggs after they were shifted to the permissive temperature. The temperature shifts therefore did not destroy the ovariole.

We also observed defects in N^{ts1}/N^{ts1} ovarioles later in oogenesis. Egg chambers that presumably had pinched off prior to the shift to the restrictive temperature developed with no morphological defects until stage 8–9. However, the stage 9 egg chambers had lost their characteristic oval shape, and degradation of the egg chambers was apparent after 2 days at the restrictive temperature (Figure 3A, arrow). After longer exposure to the restrictive temperature there were occasional fusions of two or more egg chambers in the germarium, and sometimes abnormal egg chambers containing 32 or more cells appeared to have pinched off from the germarium (Figure 3A, arrowhead). Five day incubation of N^{ts1}/N^{ts1} females at the restrictive temperature resulted in fully necrotic ovaries (Figure 3F).

Defects in the Anterior–Posterior Polarity of the Oocyte

To characterize further the stage 8–9 oocytes in N^{ts1} mutant females, we examined the spatial distribution of two markers for oocyte anterior–posterior polarity, *bcd* mRNA and *oskar* (*osk*) mRNA.

Previous studies have shown that *bcd* mRNA is localized to the anterior pole of the oocyte and is crucial in the establishment of the anterior–posterior polarity (Nüsslein-Volhard et al., 1987; Berleth et al., 1988; St Johnston et al., 1989). In whole-mount oocytes, in situ hybridization indicated that *bcd* RNA was localized in the posterior end

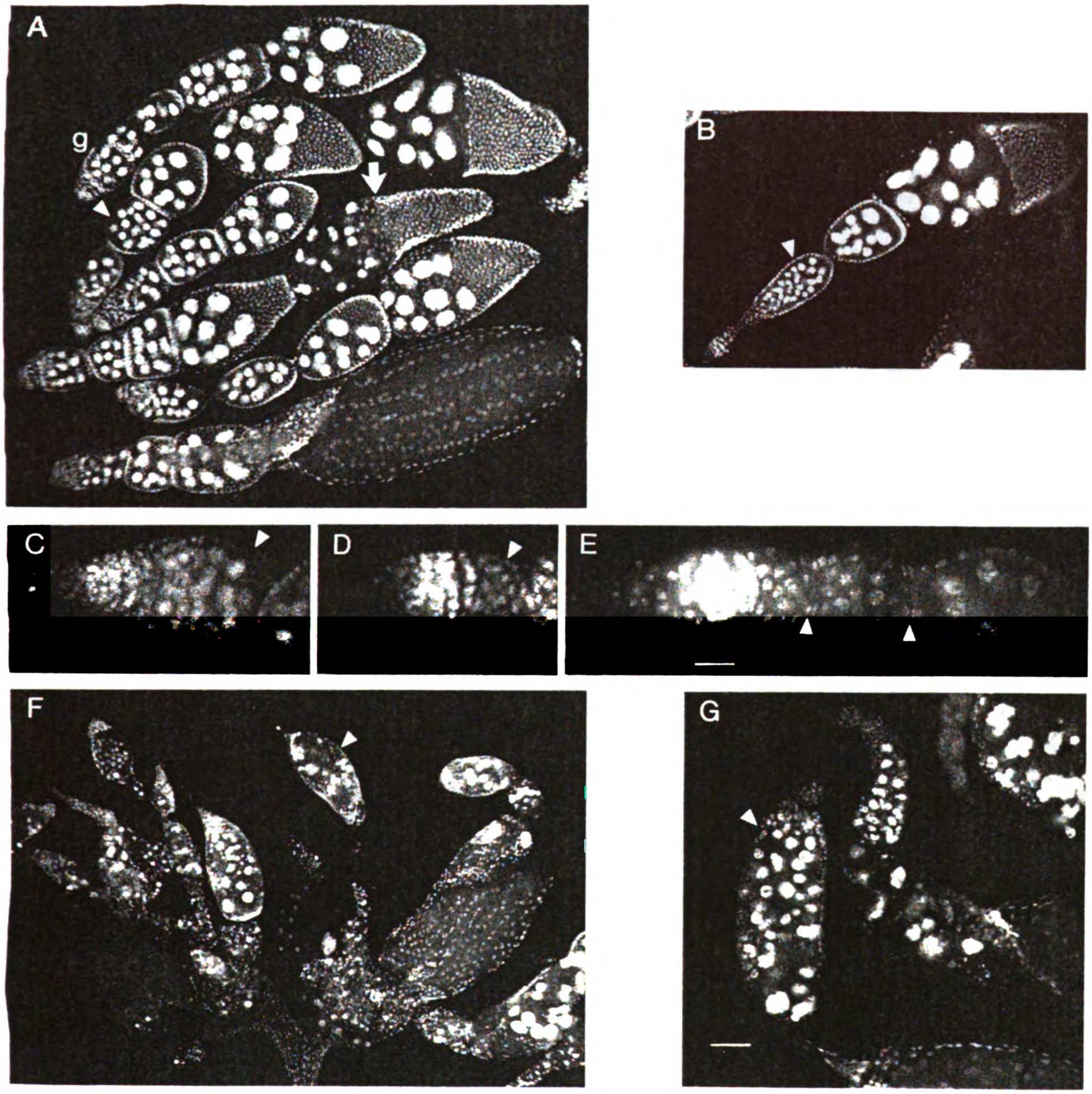

Figure 3. Temperature-Sensitive Defects at Multiple Stages of Oogenesis in N^{ts1}/N^{ts1} and Dl^{6B37}/Dl^{val1} Females

(A) DAPI-stained ovarioles from homozygous N^{ts1} females after exposure to the restrictive temperature (32°C) for 50 hr. Morphological abnormalities are detected in germarium (g) and in stage 8–9 egg chambers. Occasionally two or more egg chambers were fused together, and sometimes abnormal egg chambers containing 32 or more cells appeared to have pinched off from the germarium (arrowhead). The egg chambers that had pinched off from the germarium prior to the shift to the restrictive temperature developed to stage 7–8 and appeared morphologically normal. Most of the stage 9 egg chambers are necrotic (arrow), and only a few egg chambers at later developmental stages are detected.

(B) Ovarioles from Dl^{6B37}/Dl^{val1} females after exposure to the restrictive temperature for 2 days. Compound egg chambers are detected (arrowhead).

(C) Germarium from a homozygous N^{ts1} ovariole after 24 hr at the restrictive temperature. The stage 1 egg chamber failed to pinch off from the germarium (arrowhead) but continued growing, resulting in large swollen germarium.

(D) Stage 1 egg chamber (arrowhead) in wild-type germarium.

(E) Dl^{6B37}/Dl^{val1} germarium after 48 hr incubation at the restrictive temperature. Interleafing of the delaminating follicle cells is defective (arrowheads), resulting in incomplete separation of the stage 1 egg chamber from the germarium and the formation of compound egg chambers.

(F–G) N^{ts1}/N^{ts1} (F) and Dl^{6B37}/Dl^{val1} (G) ovarioles after 5 days at the restrictive temperature. Malformed ovaries are detected with necrotic egg chambers (arrowheads). Scale bar is 250 μm in (E) and 1 mm in (G).

(C), (D), and (E) have the same magnification; (A), (B), and (F) have the same magnification as (G).

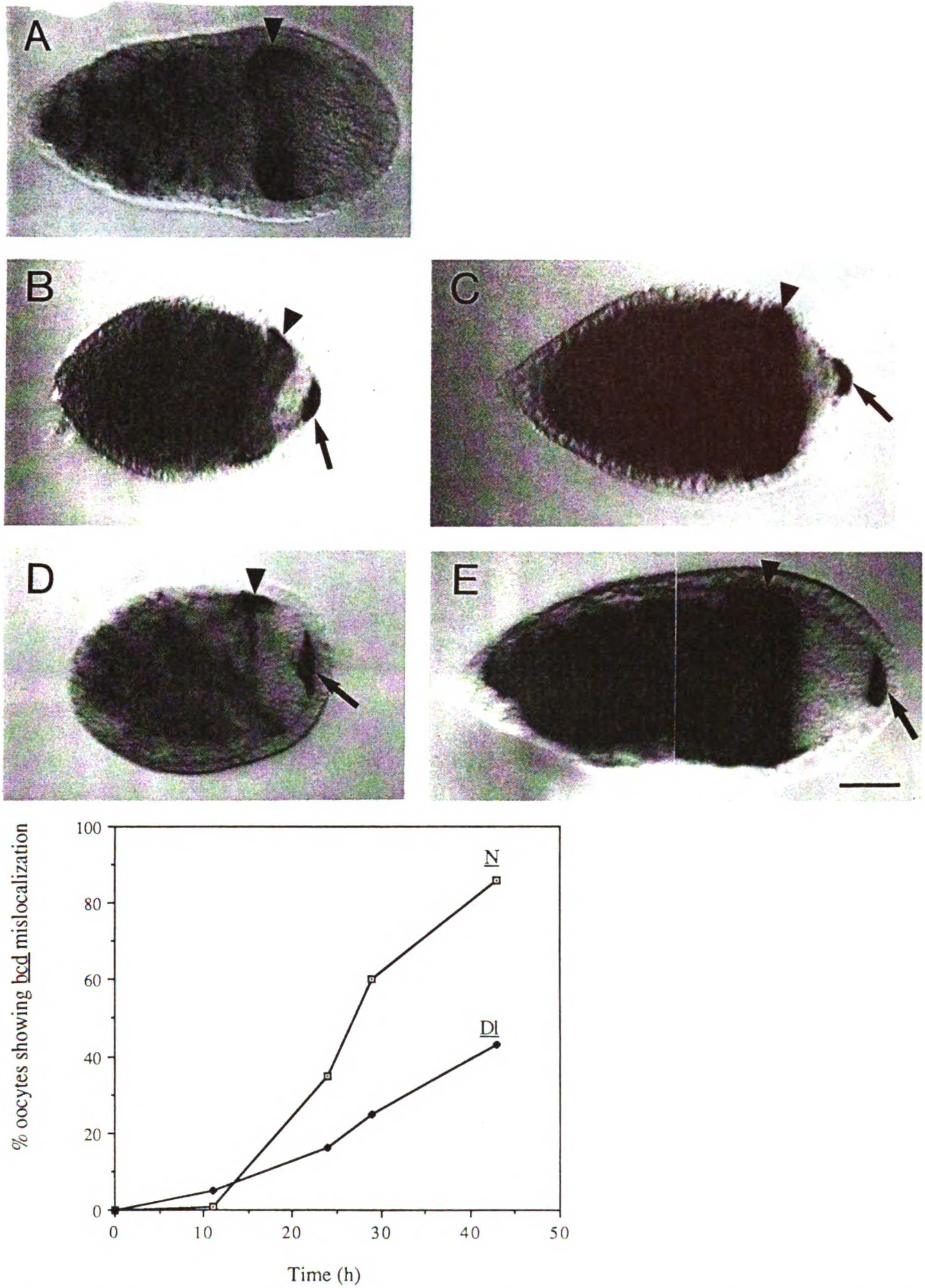

Figure 4. The Anterior–Posterior Axis As Revealed by *bcd* mRNA Localization Is Altered in Oocytes of N^{ts1}/N^{ts1} and $Dl^{6B37}/Dl^{Mal\,1}$ Females at the Restrictive Temperature

The distribution of *bcd* mRNA detected by whole-mount in situ hybridization in stage 6–8 egg chambers of control (A), N^{ts1}/N^{ts1} (B and D), and $Dl^{6B37}/Dl^{Mal\,1}$ (C and E) females. Anterior is to the left.

(A) As a control, N^{ts1}/N^{ts1}, *SM1 Cy Dp(1;2)* w^{+}51b7N^{+}/+, or *st* Dl^{6B37} *e/Dp (3;3)D2* bxd^{110} *pr e* flies were used, and the typical, exclusively anterior localization of *bcd* (St Johnston et al., 1989) was detected (arrowhead).

(B and D) Abnormal posterior *bcd* localization was detected in 57% of stage 8 egg chambers in N^{ts1}/N^{ts1} females after 29 hr incubation at the restrictive temperature (arrow) in addition to the anterior localization (arrowhead).

(C and E) Abnormal *bcd* localization is found in 45% of the oocytes of $Dl^{6B37}/Dl^{Mal\,1}$ females after 48 hr at the restrictive temperature (arrow). Arrowhead marks the anterior localization of *bcd* mRNA. Scale bar is 250 μm in (E); (A–E) have the same magnification.

(Bottom) The percentage of oocytes displaying the defect in *bcd* localization increases as a function of time at the restrictive temperature. Therefore, the mislocalization is temperature sensitive in N^{ts1}/N^{ts1} and $Dl^{6B37}/Dl^{Mal\,1}$ mutants.

[illegible] LIBRARY
[illegible] LIBRARY

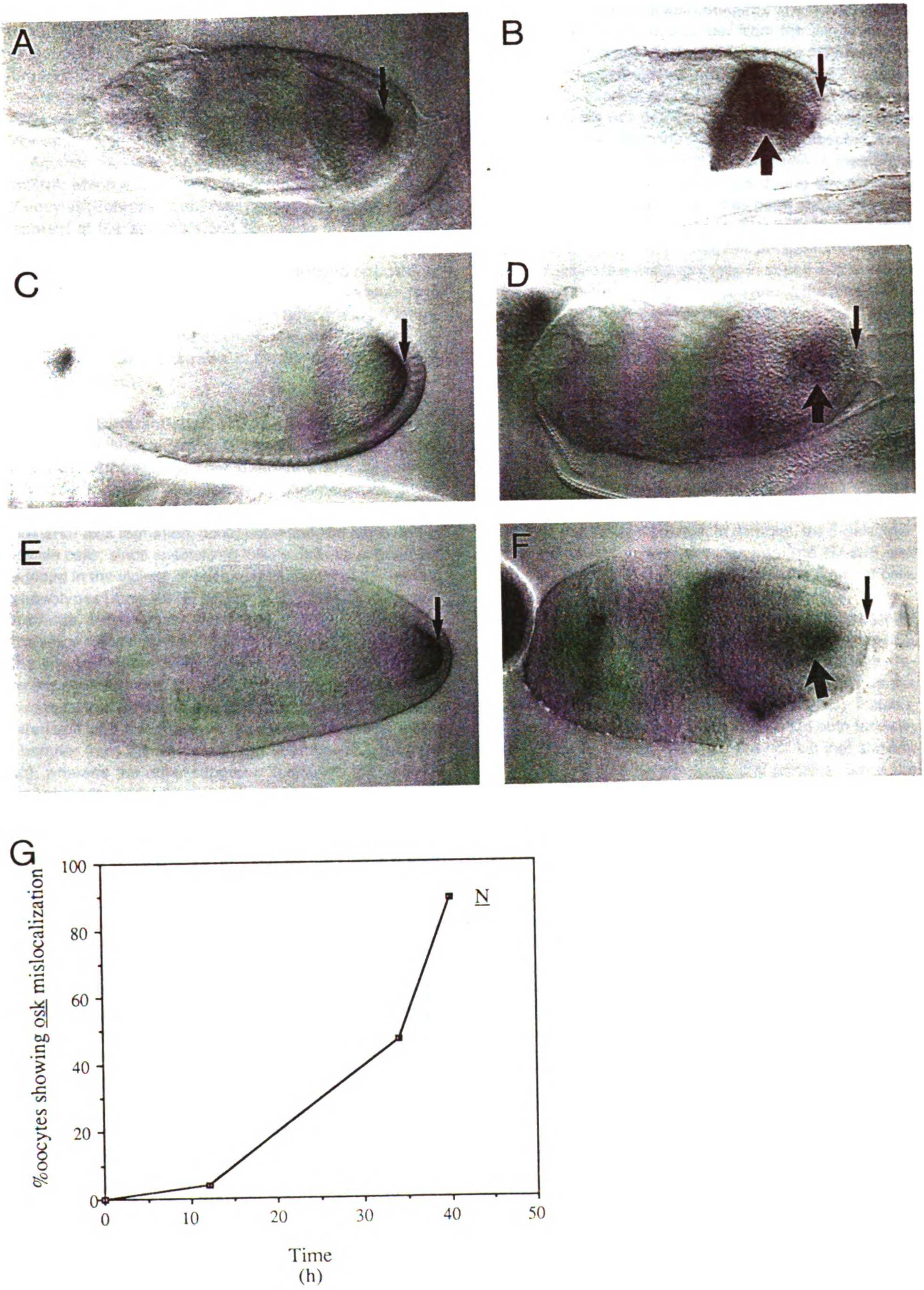
A
B
C
D
E
F
G
%oocytes showing osk mislocalization
0
20
40
60
80
100
Time
(h)
0
10
20
30
40
50
N

USAF LIBRARY
[illegible]
USAF LIBRARY

of 60% (or 86%) of the stage 8 egg chambers from N^{ts1}/N^{ts1} females after 29 hr (or 43 hr) at the restrictive temperature (Figures 4B and 4D). All egg chambers also exhibited an anterior localization of *bcd* mRNA. In control N^{ts1}/N^{ts1} flies containing a wild-type copy of *N* gene on the second chromosome, *bcd* mRNA was localized exclusively to the anterior end of the oocyte (Figure 4A), as in normal oocytes.

Another marker for anterior–posterior polarity is the *osk* mRNA, which is localized to the posterior pole of the stage 7 oocytes (Ephrussi et al., 1991) and is essential for development of the abdomen and formation of the germline precursor cells at the posterior pole of the embryo (Lehmann and Nüsslein-Volhard, 1986). We found no posterior *osk* localization in 47% (or 89%) of the oocytes after 34 hr (or 40 hr) incubation at the restrictive temperature (Figures 5B, 5D, 5F, and 5G), whereas normal posterior localization of *osk* mRNA was observed in control females (Figures 5A, 5C, and 5E).

Abnormal Differentiation of Posterior Follicle Cells

The apparently divergent mutant phenotypes of *N*, namely, the failure of the egg chamber to separate from the germarium, the abnormal morphology of chromosomes in the stage 1 oocyte, and the later defects in oocyte anterior–posterior axis formation, could potentially be attributed to follicle cells, since specialized follicle cells have been described in the vicinity of each manifestation of the mutant phenotypes (King, 1970; Brower et al., 1981; Fasano and Kerridge, 1988; Grossniklaus et al., 1989). Separation of the stage 1 egg chamber from the germarium initiates with the interleafing and delamination of follicle cells anterior to this egg chamber. Morphological analysis (King, 1970) suggests that a subgroup of the delaminating follicle cells interleafs and forms a stalk separating the stage 1 egg chamber from the immature egg chamber (Figure 11A, sc), whereas the other subgroup surrounds the anterior and posterior ends of the egg chambers (Figure 11A, pcp). The plasma membrane of the oocyte that borders the follicle cells at the posterior end of the egg chamber is specialized (Koch and King, 1969), and signals from the posterior follicle cells have been proposed to be important in oocyte differentiation (King, 1970).

The specialized follicle cells could be identified using a number of markers. We found that two neurogenic genes, *bib* and *neu*, were expressed in the delaminating follicle cells in the germarium (Figures 9D and 9B, arrowhead). After the stage 1 egg chamber entered the vitellarium, expression of *neu* and *bib* was evident in only a few follicle cells that were adjacent to the germline cells (Figures 9B and 9D); no expression was detected in the stalk that separated the stage 1 egg chamber from the immature egg chamber. In stage 3–4 egg chambers *neu* expression became even more restricted; only 2 anterior and 2 posterior follicle cells express *neu* mRNA (Figure 9B, arrows). Expression of *bib* was detected in a morphologically similar group of follicle cells in the stage 1 egg chamber but disappeared by stage 2 (Figure 9D). In addition, a membrane protein expressed in many tissues during development, fasciclin III (Patel et al., 1987), has been shown to be expressed in a restricted group of follicle cells during oogenesis (Brower et al., 1981; D. Montell, personal communication). Fasciclin III is first expressed in all of the follicle cells that delaminated in the germarium and in the follicle cells at the anterior and posterior poles of the egg chambers in the vitellarium (Figure 6). The shape of the fasciclin III–expressing posterior follicle cells changes from columnar to round between developmental stages 6 and 8 (Figure 6D). The anterior follicle cells that express fasciclin III migrate between nurse cells to the anterior end of the oocyte in stage 9 egg chambers (Figure 6E). Based on morphological criteria, the cells that express fasciclin III and *neu* appear to be the previously defined "polar cells" (Brower et al., 1981; Fasano and Kerridge, 1988; Grossniklaus et al. 1989) and their precursors. In contrast, the β-galactosidase expression in an enhancer trap line *B1-93F* was found exclusively in the stalk cells and the filament cells at the anterior tip of the germarium (Figure 8A).

N mutation blocks formation of the stalk that separates the stage 1 egg chamber from the germarium (Figure 3C). This was associated with an absence of stalk cells as revealed by the β-galactosidase expression pattern in the *B1-93F* enhancer trap line (Figure 8B, brackets). Instead, an unusual group of cells, which expressed both fasciclin III (Figures 7A and 7C) and *neu* but not *bib* (not shown), were observed in the germaria of *N* females. Since the only cells in wild-type ovarioles that have similar patterns of expression are the polar cells in the vitellarium, one likely possibility is that the *N* mutation caused hyperplasia of polar cell precursors at the expense of stalk cells (Figures 11A and 11C).

In the vitellarium of *N* mutants, there was also an increase in the number of posterior polar cells that expressed fasciclin III and *neu*. After 29 hr at the restrictive temperature, 5 or more (up to 20) fasciclin III–positive posterior polar cells were found in 51% of stage 6–9 egg chambers (Figures 7E and 7F), compared with the normal presence of only 2 such cells (Figures 6B–6E). Similarly, an abnormally large group of follicle cells expressed *neu* in

Figure 5. *osk* mRNA Is Not Localized in N^{ts1}/N^{ts1} Oocytes at the Restrictive Temperature

The figure indicates the distribution of *osk* mRNA detected by whole-mount in situ hybridization in stage 6–8 egg chambers of control ([A], [C], and [E]) and N^{ts1}/N^{ts1} ([B], [D], and [F]) females. Anterior is to the left.

(A, C, and E) As a control, N^{ts1}/N^{ts1}, *SM1 Cy Dp (1;2)* w^{+}51b7N^{+}/+ flies were used, and the typical posterior localization of *osk* (Ephrussi et al., 1991) press) was detected (arrows).

(B, D, and F) No posterior localization of *osk* was detected in 89% of stage 7–8 egg chambers in N^{ts1}/N^{ts1} females after 40 hr incubation at the restrictive temperature (thin arrows). However, an abnormal localization of *osk* mRNA in the middle of the oocyte was detected in these oocytes (thick arrows). Scale bar is 250 μm.

(G) The percentage of oocytes displaying defects in *osk* localization increases as a function of time at the restrictive temperature, with kinetics similar to those of the *bcd* mislocalization (compare with Figure 4F).

USAF LIBRARY
[illegible] LIBRARY

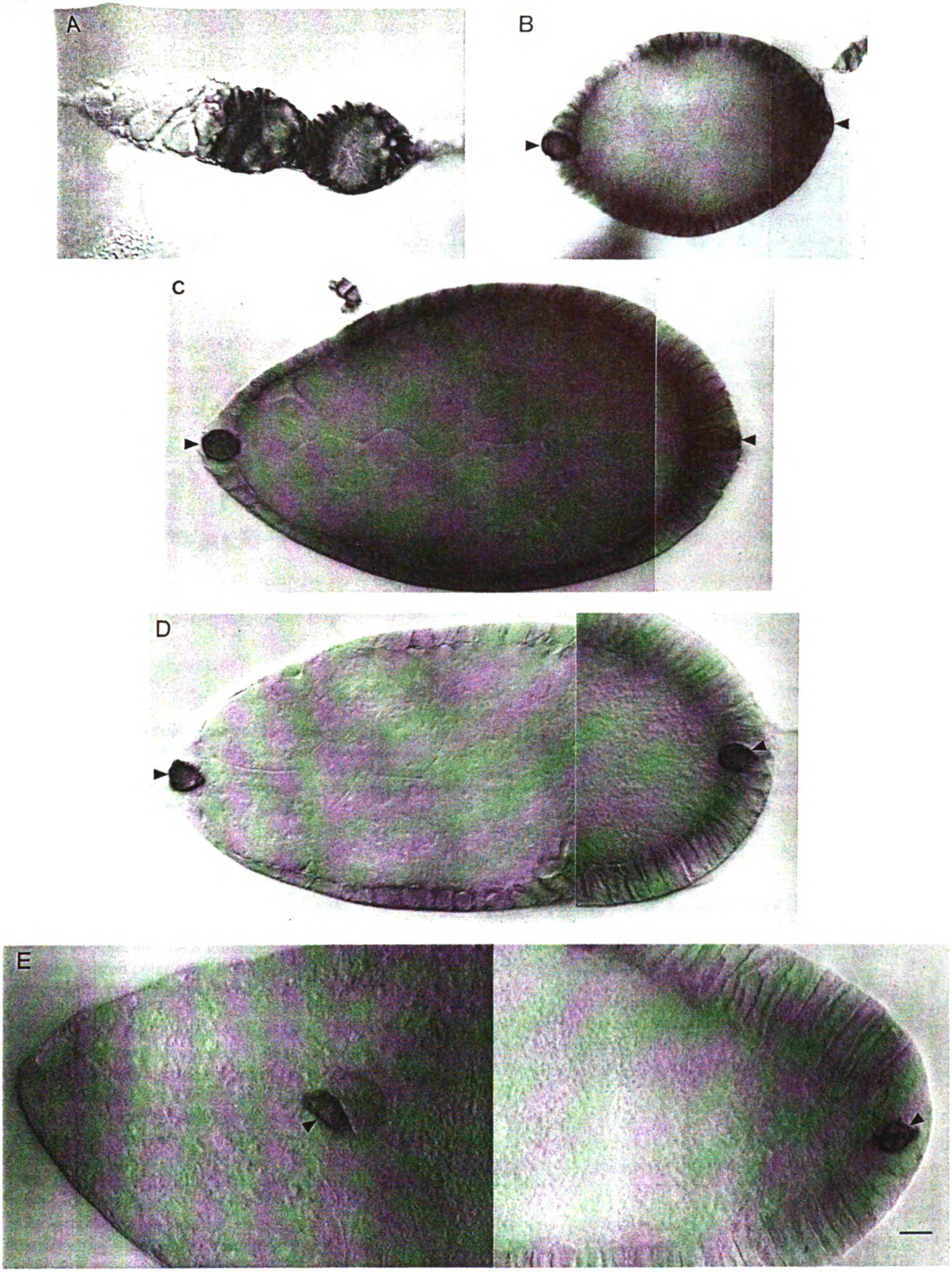

Figure 6. Polar Cells Express Fasciclin III

(A) Fasciclin III is first expressed in all follicle cells that form the constriction in the germarium and continues to be expressed at the anterior and posterior ends of the stage 1 egg chamber.

(B–E) Fasciclin III–positive polar cells (arrowheads) at the anterior (left) and the posterior (right) ends of the egg chamber at stages 6, 7, 8, and 9, respectively. Scale bar is 100 μm.

[illegible] LIBRARY
UCSF LIBRARY

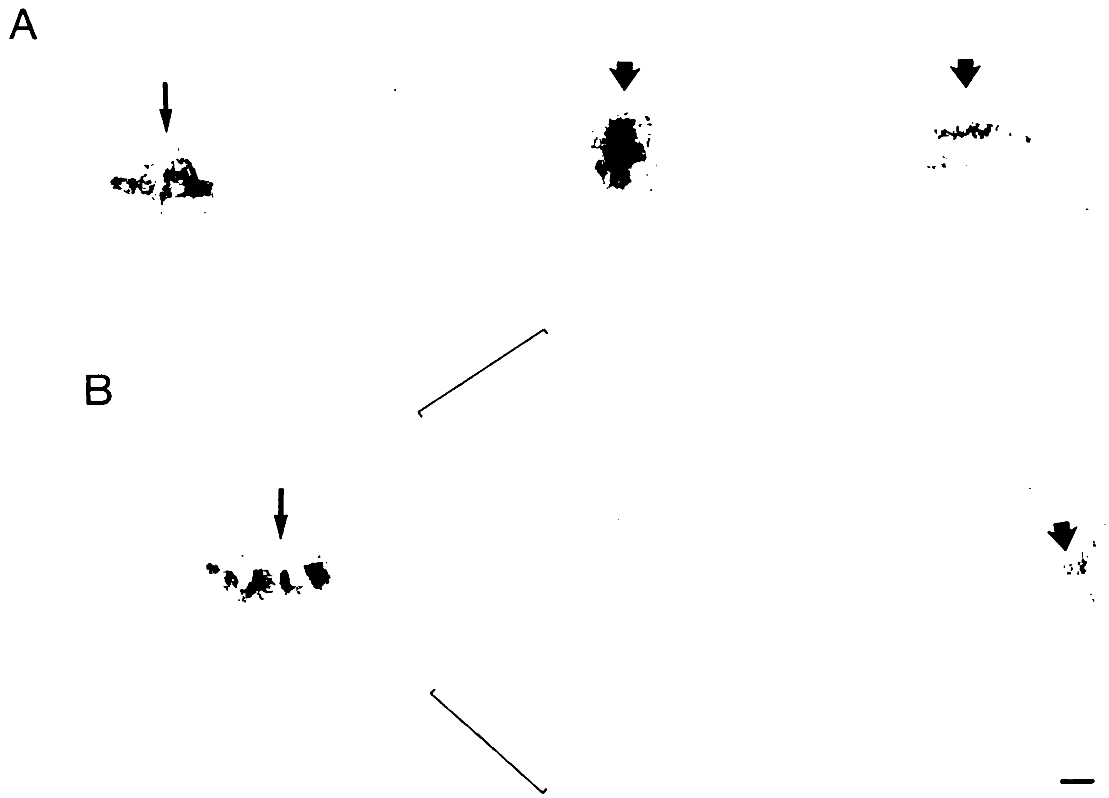

Figure 8. *N* Mutation Blocks Stalk Cell Formation

(A) Stalk cells (thick arrows) and terminal filament cells (thin arrow) are detected by X-Gal staining in an N^{+} enhancer trap line *B1-93F*.

(B) In N^{ts1}/N^{ts1}; *B1-93F/+* germaria, no β-galactosidase-expressing cells are detected after a 2 day incubation at the restrictive termperature (brackets). However, stalk cells that had formed prior to the shift to the restrictive temperature (thick arrow), as well as terminal filament cells (thin arrow), express the *B1-93F* marker. Scale bar is 100 μm.

58% of the homozygous N^{ts1} mutant ovaries after 29 hr at the restrictive temperature (Figure 7J, bracket). These results suggest that the *N* mutation causes hyperplasia of the specialized polar cells at the posterior end of an egg chamber in the vitellarium (Figures 11B and 11C).

Somatic *N* Is Required for Oogenesis

To study the involvement of *N* function in oogenesis, we first examined *N* expression in ovaries and found that *N* mRNA was detected in both the germline and the somatic follicle cells throughout the first seven stages of oogenesis (Figure 9A). The RNA expression pattern correlated well with the distribution of Notch protein in oocytes and follicle cells (T. Xu and S. Artavanis-Tsakonas, personal communication); in the germarium Notch protein is found in those follicle cells that are required for the contraction. Hence, the pattern of *N* expression is compatible with either a somatic or a germline requirement for *N* function in oogenesis.

Mosaic analysis (for review see Wieschaus, 1980) was used to determine whether somatic or germ cell expression of *N* was responsible for the phenotypes in the germarium and in stage 7–9 oocytes. Homozygous *N* germline clones were produced by mitotic recombination, using the dominant female-sterile mutation *ovoDl* (Busson et al., 1983). We found that mosaics with wild-type somatic cells and *N* mutant (N^{ts1} or a stronger, null allele, N^{55e11}) germ cells displayed no detectable defects in oogenesis by either morphological criteria (Figure 10C) or study of the localization of *bcd* mRNA (data not shown); this is consistent with previous studies (Jimenez and Campos-Ortega, 1982). Since *N* function in germ cells did not appear essential for oogenesis, we concluded that *N* is required in the soma for several processes of oogenesis, including proper *bcd* localization in the oocyte. As a consequence, interactions between somatic cells and germ cells appear to be necessary for proper specification of the anterior–posterior polarity.

Dl Is Also Involved in Oogenesis

Besides *N*, four other neurogenic genes, *neu*, *Dl*, *bib* (Figures 9B–9D), and *mastermind* (Don Bettler, personal communication), also showed expression in the ovary. As for the neurogenic gene complex *Enhancer of split* (Klămbt et al., 1989; Hartley et al., 1988), we have only tested two (*m7* and *m8*) of the many transcripts that are associated with this gene complex. Although no detectable expres-

UCSF LIBRARY

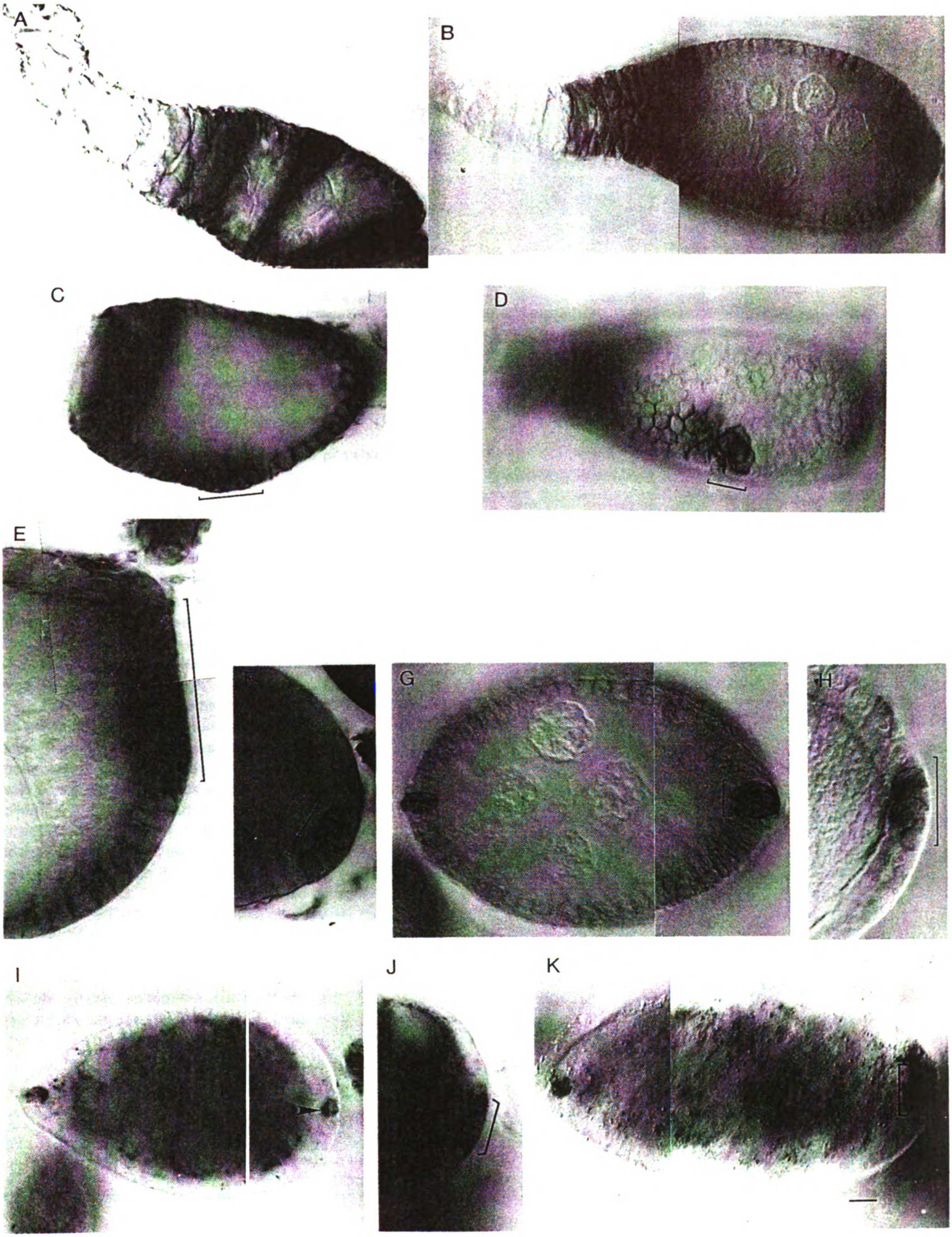
A
B
C
D
E
F
G
H
I
J
K

USAF LIBRARY
[illegible]
USAF LIBRARY

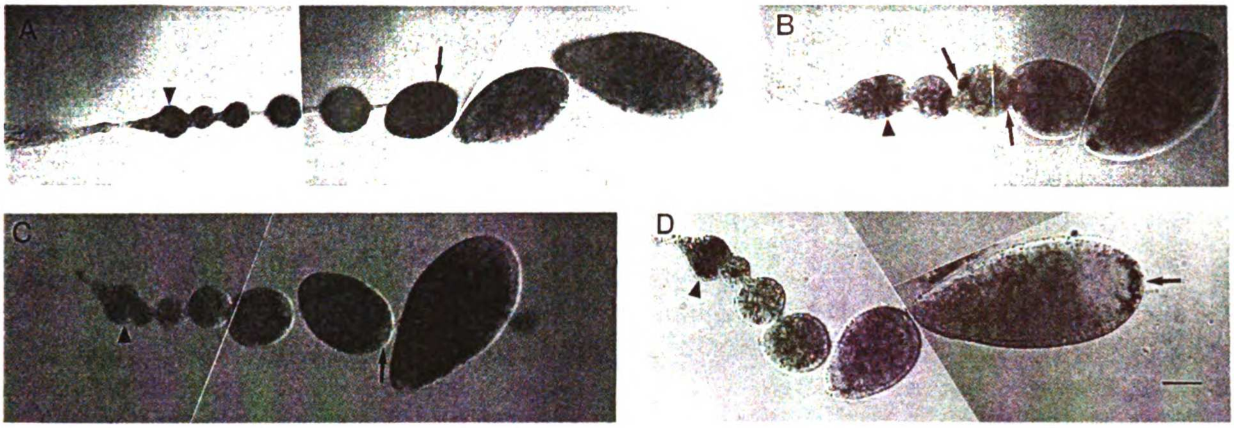

Figure 9. Expression of Neurogenic Genes during Oogenesis

The expression pattern of neurogenic genes in wild-type ovaries was revealed by whole-mount in situ hybridization.

(A) *N* mRNA is expressed in germline and somatic follicle cells. Expression is detected in the germarium (arrowhead) and in the follicle cells (arrow).

(B) *neu* expressed in germline and somatic polar follicle cells (arrows) and their precursors in the germarium (arrowhead).

(C) *Dl* expression is detected in germline and lateral follicle cells but not in the posterior follicle cells (arrow). *Dl* is also expressed in the germarium (arrowhead).

(D) *bib* is expressed in germarium (arrowhead) and later in posterior follicle cells (arrow). Scale bar is 250 µm.

sion of *m7* and *m8* was found, it remains possible that some of the other *Enhancer of split* transcripts are expressed in the ovary.

Temperature-sensitive mutations exist for one of these neurogenic genes (Dl^{6B37}) (Lehmann et al., 1983), making it possible to ask whether *Dl* is involved in oogenesis. Dl^{6B37}/Dl^{vial1} females at the restrictive temperature (32°C) showed phenotypes that were similar to but milder than those of N^{ts1}/N^{ts1} females, whereas control females that carried two copies of the wild-type allele in addition to the temperature-sensitive allele Dl^{6B37} showed none of these abnormalities.

The rate of egg laying was reduced by half after 40 hr at the restrictive temperature. After 82 hr at 32°C, egg laying by Dl^{6B37}/Dl^{vial1} females was reduced to 0.5% of the control (Figure 2B). One day at the restrictive temperature was also sufficient to block separation of the stage 1 egg chamber from the germarium in 50% of the ovarioles (Figures 3B and 3E). Later in oogenesis, mislocalization of *bcd* to the posterior pole of the oocyte (Figures 4C, 4E, and 4F) and excess fasciclin III– and *neu*-expressing cells (polar cells) (Figures 7G, 7H, and 7K), were also evident in ovaries from Dl^{6B37}/Dl^{vial1} mutants. Thus, qualitatively the phenotypes of the temperature-sensitive *Dl* mutation were similar to those of the temperature-sensitive *N* mutation. We emphasize that it will be of importance to establish the null phenotypes, so that the scope and strength of the null mutant phenotypes could be used as an index for the level and extent of normal gene function.

To determine whether *Dl* is required in somatic or germline cells, mosaic flies were generated using the yeast recombinase-based FLIP-FRT system (Golic, 1991). Mosaics with wild-type somatic cells and *Dl* mutant germline cells (24 analyzed) had no detectable morphological defects in oogenesis. However, the germarium phenotype observed in Dl^{6B37}/Dl^{vial1} (Figure 3E) was detected when the follicle cells required for pinching off were mutants for Dl^{6C3} (35 cases analyzed). Thus, as in the case of *N*, the mutant phenotypes are likely to result from perturbation of neurogenic gene function in somatic cells.

Discussion

Using conditional mutants of *N* and *Dl*, we have shown that these two neurogenic genes play an important role in oogenesis. Mosaic experiments suggest that the function of these genes is required in the somatic follicle cells, although distinct defects were observed in both somatic follicle cells and in the oocyte. Two separable phases of oogenesis, early in the germarium and later in the vitellarium, require *N* and *Dl* gene functions. In the germarium, separation between the stage 1 egg chamber and the immature egg chamber appears to involve the delamination and subsequent morphogenic movements of specialized follicle cells; these processes were abnormal in *N* and *Dl* mutants (Figure 11A). Later, in the vitellarium, there was

Figure 7. Hyperplasia of Polar Cells in N^{ts1}/N^{ts1} and Dl^{6B37}/Dl^{vial1} Ovaries

(A–H) Polar cells detected by whole-mount staining with fasciclin III antibody in N^{ts1}/N^{ts1} ovarioles (29 hr at 32°C; [A], [C], [E], and [F]) and in Dl^{6B37}/Dl^{vial1} ovarioles (48 hr at 32°C; [B], [D], [G], and [H]). An excess of follicle cells are positive with fasciclin III staining in the germarium (brackets in [C] and [D]) and in the posterior end of stage 6–8 egg chambers (brackets in [E]–[H]).

([I]–[K]) Polar cells detected by whole-mount in situ hybridization with a *neu* cDNA probe in wild-type ([I]), N^{ts1}/N^{ts1} (29 hr at 32°C; [J]), or Dl^{6B37}/Dl^{vial1} (48 hr at 32°C; [K]) stage 6–8 egg chambers. Only 2 posterior follicle cells (polar cells) express *neu* in wild-type egg chambers (arrowhead; [I]). Many more *neu*-expressing cells are detected in N^{ts1}/N^{ts1} ([J], bracket) and Dl^{6B37}/Dl^{vial1} ([K], bracket) egg chambers. Scale bar is 100 µm.

USAF LIBRARY

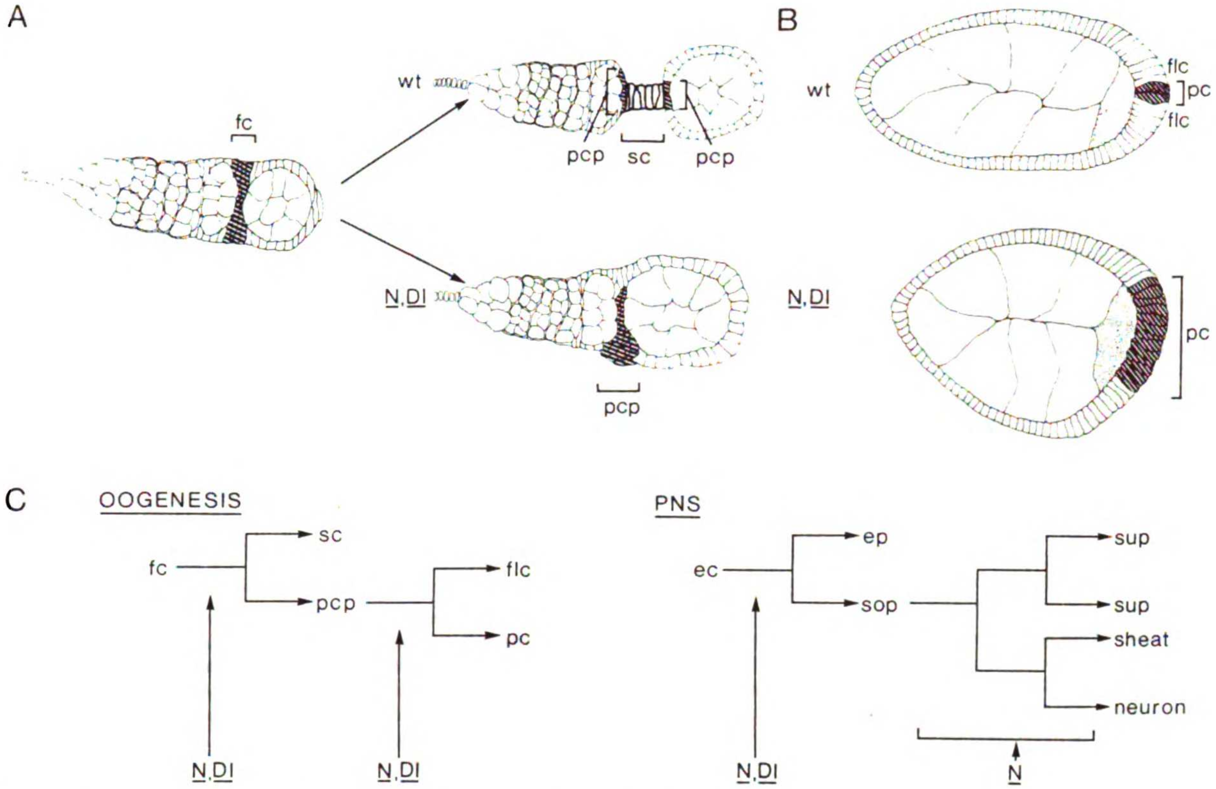

Figure 11. Schematic Summary of the Early and Late Defects in Oogenesis of *N* and *Dl* Mutants

(A) A diagram of the earliest detectable morphological differences between the wild-type (wt) ovary and the N^{ts1}/N^{ts1} (*N*) ovaries and Dl^{6B37}/Dl^{vial1} (*Dl*) ovaries. Follicle cells (fc) in the hatched region form stalk cells (sc) and polar cell precursors (pcp), causing the stage 1 egg chamber to pinch off from the germarium. No stalk is formed in *N* or *Dl* mutants.

(B) A diagram of the posterior polar cells (shaded) in egg chambers of the wild-type, N^{ts1}/N^{ts1}, or Dl^{6B37}/Dl^{vial1}. More cells that resemble posterior polar cells (pc) in their expression of *neu* and fasciclin III are found in *N* or *Dl* mutant egg chambers than in control egg chambers. In the wild-type ovary, follicle cells flanking the polar cells at the posterior end of the egg chamber (flanking cells, fc) are presumably derived from polar cell precursors.

(C) A model to explain the observed divergent mutant phenotypes. Early follicle cells (fc) differentiate into stalk cells (sc) and polar cell precursors (pcp). Polar cell precursors further differentiate into polar cells (pc) and flanking cells (flc). Our results suggest that *N* and *Dl* are required in both of these fate decisions in oogenesis. In the peripheral nervous system, an ectodermal cell (ec) either takes the fate of epidermoblast (ep) or sensory organ precursor (sop). The sensory organ precursors differentiate further into support cells (sup), sheath cells (sheat), and sensory neurons (neuron). *N* appears to be required in both of these cell fate decisions (Campos-Ortega, 1988; Hartenstein and Posakony, 1990). Similarly, we propose that the *N* and *Dl* functions in oogenesis are required to prevent stalk cells from adopting the fate of polar cell precursors early during oogenesis; these genes also function to prevent flanking cells from becoming posterior follicle cells later during oogenesis.

an apparent hyperplasia of posterior follicle cells. In the oocyte, the anterior morphogen *bcd* was mislocalized to the posterior pole, and the normal posterior localization of *osk* mRNA was disturbed. Based on the mosaic studies, it seems likely that the phenotypes in the germline reflect the defects in the somatic follicle cells. In the following, we first discuss the implications of the somatic influence over the anterior–posterior polarity of the oocyte, and then we propose a simple model that explains the observed divergent phenotypes as consequences of a primary defect in the specification of follicle cell fate.

Interactions between Follicle Cells and the Oocyte

bcd mislocalization to the posterior pole was found in N^{ts1} females but not in mosaics in which only the germ cells were homozygous for the N^{ts1} mutations. Thus, specification of the anterior–posterior axis of the oocyte appears to require *N* function in somatic cells, presumably follicle cells at the posterior end of the egg chamber.

The somatic requirement of *N* function for proper *bcd* localization was not anticipated. The nurse cells that provide *bcd* are localized at the anterior end of the oocyte. This has led to a simple model for *bcd* localization, which holds that *bcd* mRNA is passively trapped at the anterior pole by a uniformly distributed receptor as it is transferred from the nurse cells to the oocyte (Frohnhöfer and Nüsslein-Volhard, 1987). In this model the anterior localization of *bcd* is intrinsic to the germline, without somatic contribution. The localization of *bcd* to the posterior pole in the *N* mutant cannot be explained by this model. Our results suggest that the *bcd* mRNA is either actively transported to the posterior pole or is capable of interacting with receptors that are localized in both anterior and posterior poles of the oocyte in the mutants. Moreover, the require-

[illegible]
UCSF LIBRARY

by pulsing the blender three times at low speed (2 s per pulse). This treatment ruptures the cuticle but not the egg chambers. The homogenate was filtered through a loose mesh (1–2 mm mesh) to remove larger body parts. The material in the mesh was rehomogenized in 200 ml of modified Robbs buffer and refiltrated. The filtrates were pooled and gravity settled for 5 min. The egg chambers, which have a higher density than most other organs, will settle during that time. The supernatant was aspirated, and the body fragments were wiped off from the side of the beaker. The egg chambers were resuspended into 200 ml of modified Robbs buffer and filtered through a nylon mesh (250 μm mesh). The egg chambers were recovered in the filtrates. The filtrate was allowed to gravity settle for 5 min, and the supernatant was discarded. The egg chambers were resuspended into an additional 100 ml of modified Robbs, and the gravity settling was repeated. Supernatant was discarded, and the egg chambers were fixed (4% formaldehyde [EM grade, Ted Pella, Inc.] and 0.1% dimethyl sulfoxide in phosphate-buffered saline [PBS]) for 1 hr at room temperature. Thereafter the egg chambers were dehydrated through an ethanol series (25%, 50%, 75%, 95%, 100%, mixtures of ethanol and PBS) and stored at −20°C. For some experiments, the ovaries were prepared by hand dissection into modified Robbs buffer and thereafter fixed and dehydrated as described. These ovaries were used both for immunocytochemistry and whole-mount in situ assays.

Immunocytochemistry

The procedure for whole-mount staining of embryos was described previously (Bodmer et al., 1987); affinity-purified anti-HRP antibody was used in 1:500 dilution, anti-vasa antibody in 1:1000 dilution, and anti-fasciclin III monoclonal antibody in 1:15 dilution. For the whole-mount staining the ovaries were rehydrated, and the same procedure was used as for embryos. To detect the antigen inside the oocytes, a freeze fracture method (Hay et al., 1988) was used.

In Situ Hybridization for Ovaries

Whole-mount in situ hybridization of ovaries with digoxigenin-labeled (Boehringer Mannheim Biochemicals) probes was performed as described earlier (Tautz and Pfeiffle, 1989) with minor modifications. The ovaries were prepared as described, rehydrated, and protease treated. Whereas the embryos were treated with protease for 5 min, the ovaries were treated for 1 hr. The steps thereafter were as described earlier. The DNA fragments used for hybridization are: *bcd*, pGEM 3bcd (*bcd* cDNA, Driever et al., 1990); *N*, FAHB 4.0 (BamHI–HindIII fragment from the clone N2; Kidd et al., 1983); *Dl*, c3.2 (*Dl* cDNA, Haenlin et al., 1990); *neu*, pET3a/PCR (*neu* cDNA, a gift from G. Boulianne); *bib*, 9B (Rao et al., 1990); and *osk*, BSKS-osk (Ephrussi et al., 1991).

Other Staining Procedures

For the staining with DAPI the ovaries were fixed as described and thereafter washed in 1% Triton X-100, PBS for 30 min. The samples were washed in 3× PBS (30 mM sodium phosphate [pH 7.2], 0.45 M sodium chloride) and stained with 0.5 μg/ml DAPI (Polysciences, Inc) in 3× PBS for 3 hr. Thereafter, the samples were washed overnight in 3× PBS and mounted in glycerol.

For the X-Gal staining the ovaries were dissected in modified Robbs buffer and thereafter incubated over night at 37°C in 0.2% X-Gal solution (in 3.1 mM $K_3Fe(CN)_6$, 3.1 mM $K_4Fe(CN)_6$, 10 mM sodium phosphate [pH 7.2], 0.15 M sodium chloride, 1 mM magnesium chloride). Samples were washed in 1 × PBS, fixed for 30 min in 2.5% glutaraldehyde, 1 × PBS, and mounted in glycerol.

Egg Collections

As a control, N^{ts1}/N^{ts1}; *SM1 Cy Dp(1;2)*w^{+}51b7N^{+}/+; or *st* Dl^{6B37} *e/Dp(3;3)D2* bxd^{110} *pr e* flies were used in all the experiments. Eggs were collected on yeasted grape juice plates for 5 hr at 18°C or 32°C and counted thereafter. Each control datapoint in (Figure 2A) represents approximately 400 eggs per 100 females per 5 hr (18°C) or approximately 1100 eggs per 100 females per 5 hr (32°C).

Generation of Homozygous Germline Clones

The dominant female-sterile mutation ovo^{D1} was used as a tool to produce homozygous germline clones by mitotic recombination (Busson et al., 1983). N^{ts1}/*FM6* females were mated to ovo^{D1}, *v* males. Clones were produced by X-ray induced mitotic recombination (1000 rad, 5 min) 40 ± 16 hr after oviposition at 25°C. N^{ts1}/ovo^{D1} *v* females were mated to wild-type males and screened for N^{ts1}/N^{ts1} clones by checking their ability to lay eggs at the permissive temperature. The animals harboring homozygous N^{ts1} germline clones were shifted to the restrictive temperature, and the eggs were collected and stained with anti-HRP antibodies to test for the neurogenic phenotype, which is indicative of N^{ts1} homozygous germline clones instead of ovo^{D1} revertants (Busson et al., 1983). Thereafter the ovaries were dissected and stained with DAPI or anti-vasa antibody or hybridized with *bcd* cDNA probe. The clone size varied from 1 to 11 ovarioles out of approximately 40 ovarioles per female. We determined the frequency of reversion by mating the N^{ts1}/ovo^{D1}, *v* females to ovo^{D1}, *v* males and scoring adults that emerged from the cross for the *vermillion* eye pigment phenotype. ovo^{D1} revertants in these experiments represented less than 0.1% of the total, whereas N^{ts1} germline mosaics obtained were 5% of the total.

The yeast recombinase-based FLIP-FRT scheme (Golic, 1991; S. Shepherd, unpublished data) was used for *Dl* germline and somatic mosaics. Recombinase was induced by heat shocking second or third instar *FLP; FRT* Dl^{BC3}/*FRT* y^{+} larvae at 37°C for 1–1.5 hr. The adult ovaries were dissected, and X-Gal staining was performed as described. Homozygous Dl^{BC3} patches were readily distinguished by a greatly increased intensity of X-Gal reaction products relative to that of heterozygous cells.

Acknowledgments

We would like to thank Donald Ready for sending the N^{ts1} allele, José Campos-Ortega for the *Dp(3;3) D2* stock, and Bernd Kramatschek for *Dl* cDNA clone c3.2. We are indebted to Gabrielle Boulianne for sharing unpublished data on *neu* alleles and *neu* cDNA clone and to Hugo Bellen for discussions. We thank Yi Rao for the *bib* cDNA clone, Wolfgang Driever and Christian Nüsslein-Volhard for the *bcd* cDNA clone, Simon Kidd, Mike Young, and Susan Parmelee for the *N* clone, and especially Anne Ephrussi and Ruth Lehmann for *osk* cDNA prior to publication. Finally, we thank Ed Grell and Susan Shepherd for advice in genetics, Sandy Barbel and Bob Carretto for technical help, and Patrick O'Farrell, Bruce Hay, Ed Giniger, Vivian Siegel, Tom Jongens, and Harald Vaessin for constructive criticism on the manuscript. Also we would like to thank Kathi Prewitt for typing the manuscript and Larry Ackerman for illustrations. H. R. was supported by a Postdoctoral Fellowship from the European Molecular Biology Organization, and D. B. was supported by a Postdoctoral Fellowship from the Life Sciences Research Foundation. L. Y. J. and Y. N. J. are Investigators of the Howard Hughes Medical Institute.

The costs of publication of this article were defrayed in part by the payment of page charges. This article must therefore be hereby marked "*advertisement*" in accordance with 18 USC Section 1734 solely to indicate this fact.

Received February 26, 1991; revised June 5, 1991.

References

Anderson, K. V. (1987). Dorsal-ventral embryonic pattern genes of Drosophila. Trends Genet. *3*, 91–97.

Artavanis-Tsakonas, S. (1988). The molecular biology of the *Notch* locus and the fine tuning of differentiation in Drosophila. Trends Genet. *4*, 95–100.

Austin, J., and Kimble, J. (1989). Transcript analysis of *glp-1* and *lin-12*, homologous genes required for cell interactions during development of C. elegans. Cell *58*, 565–571.

Berleth, T., Burri, M., Thoma, G., Bopp, D., Richstein, S., Frigerio, G., Noll, M., and Nüsslein-Volhard, C. (1988). The role of localization of *bicoid* mRNA in organizing the anterior pattern of the Drosophila embryo. EMBO J. *7*, 1749–1756.

Bier, E., Vässin, H., Shepherd, S., Lee, K., McCall, K., Barbel, S., Ackerman, L., Carretto, R., Uemura, T., Grell, E., Jan, L., and Jan, Y. N. (1989). Searching for pattern and mutation in the Drosophila genome with a P-lacZ vector. Genes Dev. *3*, 1273–1287.

Bodmer, R., Barbel, S., Shepherd, S., Jack, J. W., Jan, L. Y., and Jan, Y. N. (1987). Transformation of sensory organs by mutations of the *cut* locus of D. melanogaster. Cell *51*, 293–307.

Brower, D. L., Smith, R. J., and Wilcox, M. (1981). Differentiation within the gonads of Drosophila revealed by immunofluorescence. J. Embryol. Exp. Morphol. *63*, 233–242.

Busson, D., Gans, M., Komitopoulou, K., and Masson, M. (1983). Genetic analysis of three dominant female sterile mutations located on the X chromosome of Drosophila melanogaster. Genetics *105*, 309–325.

Cagan, R. L., and Ready, D. F. (1989). *Notch* is required for successive cell decisions in the developing Drosophila eye. Genes Dev. *3*, 1099–1112.

Campos-Ortega, J. A. (1988). Cellular interactions during early neurogenesis of *Drosophila melanogaster*. Trends Neurosci. *11*, 400–405.

Campos-Ortega, J. A., and Jan, Y. N. (1991). Genetic and molecular bases of neurogenesis in Drosophila melanogaster. Annu. Rev. Neurosci., in press.

Cooley, L., Kelley, R., and Spradling, A. C. (1988). Insertional mutagenesis of the Drosophila genome with single P elements. Science *239*, 1121–1128.

de la Concha, A., Deitrich, U., Weigel, D., and Campos-Ortega, J. (1988). Functional interactions of neurogenic genes of Drosophila melanogaster. Genetics *118*, 499–508.

Doe, C. Q., and Goodman, C. S. (1985). Early events in insect neurogenesis. II. The role of cell interactions and cell lineages in the determination of neuronal precursor cells. Dev. Biol. *111*, 206–219.

Driever, W., Siegel, V., and Nüsslein-Volhard, C. (1990). Autonomous determination of anterior structures in the early Drosophila embryo by the *bicoid* morphogen. Development *109*, 811–820.

Ephrussi, A., Dickinson, L. K., and Lehmann, R. (1991). *oskar* organizes the germ plasm and directs localization of the posterior determinant *nanos*. Cell *66*, in press.

Fasano, L., and Kerridge, S. (1988). Monitoring positional information during oogenesis in adult Drosophila. Development *104*, 245–253.

Fehon, R. G., Kooh, P. J., Rebay, I., Regan, C. L., Xu, T., Muskavitch, M. A. T., and Artavanis-Tsakonas, S. (1990). Molecular interactions between the protein products of the neurogenic loci *Notch* and *Delta*, two EGF-homologous genes in Drosophila. Cell *61*, 523–534.

Frohnhöfer, H.-G., and Nüsslein-Volhard, C. (1987). Maternal genes required for the anterior localization of *bicoid* activity in the embryo of Drosophila. Genes Dev. *1*, 880–890.

Golic, K. G. (1991). Site-specific recombination between homologous chromosomes in Drosophila. Science *252*, 958–961.

Golic, K. G., and Lindquist, S. (1989). The FLP recombinase of yeast catalyzes site-specific recombination in the Drosophila genome. Cell *59*, 499–509.

Greenwald, I. S., Sternberg, P. W., and Horvitz, H. R. (1983). The *lin-12* locus specifies cell fates in Caenorhabditis elegans. Cell *34*, 435–444.

Grossniklaus, U., Bellen, H. J., Wilson, C., and Gehring, W. J. (1989). P-element-mediated enhancer detection applied to the study of oogenesis in Drosophila. Development *107*, 189–200.

Haenlin, M., Kramatschek, B., and Campos-Ortega, J. A. (1990). The pattern of transcription of the neurogenic gene *Delta* of Drosophila melanogaster. Development *110*, 905–914.

Hartenstein, V., and Posakony, J. (1990). A dual function of the *Notch* gene in Drosophila sensillum development. Dev. Biol. *142*, 13–30.

Hartley, D. A., Preiss, A., and Artavanis-Tsakonas, S. (1988). A deduced gene product from the Drosophila neurogenic locus, *Enhancer of split*, shows homology to mammalian G-protein β subunit. Cell *55*, 785–795.

Hay, B., Ackerman, L., Barbel, S., Jan, L., and Jan, Y. N. (1988). Identification of a component of Drosophila polar granules. Development *103*, 625–640.

Hay, B., Jan, L. Y., and Jan, Y. N. (1990). Localization of vasa, a component of Drosophila polar granules, in maternal-effect mutants that alter embryonic anteroposterior polarity. Development *109*, 425–433.

Jan, L. Y., and Jan, Y. N. (1982). Antibodies to horseradish peroxidase as specific neuronal markers in Drosophila and in grasshopper embryos. Proc. Natl. Acad. Sci. USA *72*, 2700–2704.

Jimenez, F., and Campos-Ortega, J. A. (1982). Maternal effects of zygotic mutants affecting early neurogenesis in Drosophila. Roux's Arch. Dev. Biol. *191*, 191–201.

Kidd, S., Kelley, M. R., and Young, M. W. (1986). Sequence of the *Notch* locus of Drosophila melanogaster: relationship of the encoded protein to mammalian clotting and growth factors. Mol. Cell. Biol. *6*, 3094–3108.

King, R. C. (1970). Ovarian Development in Drosophila melanogaster (New York: Academic Press).

Klämbt, C., Knust, E., Tietze, K., and Campos-Ortega, J. A. (1989). Closely related transcripts encoded by the neurogenic gene complex *Enhancer of split* of Drosophila melanogaster. EMBO J. *8*, 203–210.

Koch, E. A., and King, R. C. (1969). Further studies on the ring canal system of the ovarian cystocytes of Drosophila melanogaster. Z. Zellforsch. *102*, 129–152.

Kopczynski, C. C., Alton, A. K., Fechtel, K., Kooh, P. J., and Muskavitch, M. A. T. (1988). *Delta*, a Drosophila neurogenic gene, is transcriptionally complex and encodes a protein related to blood coagulation factors and epidermal growth factor in vertebrates. Genes Dev. *2*, 1723–1735.

Lehmann, R., and Nüsslein-Volhard, C. (1986). Abdominal segmentation, pole cell formation, and embryonic polarity require the localized activity of *oskar*, a maternal gene in Drosophila. Cell *47*, 141–152.

Lehmann, R., Jimenez, F., Dietrich, U., and Campos-Ortega, J. A. (1983). On the phenotype and development of mutants of early neurogenesis in Drosophila melanogaster. Roux's Arch. Dev. Biol. *192*, 62–74.

Lindsley, D. L., and Grell, E. H. (1968). Genetic variations of Drosophila melanogaster. Carnegie Institution of Washington Publication no. *627*.

Mahowald, A. P., and Kambysellis, M. P. (1978). Oogenesis. In Genetics and Biology of Drosophila, 2nd Vol., M. Ashburner and T. R. F. Wright, eds. (New York Academic Press), pp. 141–224.

Mahowald, A. P., Goralski, T. J., and Caulton, J. H. (1983). In vitro activation of Drosophila eggs. Dev. Biol. *98*, 437–445.

Manseau, L., and Schüpbach, T. (1989). The egg came first of course. Trends Genet. *5*, 400–405.

Nüsslein-Volhard, C., Frohnhöfer, H. G., and Lehmann, R. (1987). Determination of anteroposterior polarity in Drosophila. Science *238*, 1675–1681.

Patel, N. H., Snow, P. M., and Goodman, C. S. (1987). Characterization and cloning of fasciclin III: a glycoprotein expressed on a subset of neurons and axon pathways in Drosophila. Cell *48*, 975–988.

Price, J. V., Clifford, R. J., and Schüpbach, T. (1989). The maternal ventralizing locus *torpedo* is allelic to *faint little ball*, an embryonic lethal, and encodes the Drosophila EGF receptor homolog. Cell *56*, 1085–1092.

Rao, Y., Jan, L. Y., and Jan, Y. N. (1990). *big brain*, a gene involved in the choice between neurogenesis and epidermogenesis in Drosophila, encodes a protein with similarity with a family of transmembrane channels. Nature *345*, 163–167.

Schejter, E. D., and Shilo, B.-Z. (1989). The Drosophila EGF receptor homology (DER) is allelic to *faint little ball*, a locus essential for embryonic development. Cell *56*, 1093–1104.

Schüpbach, T. (1987). Germ line and soma cooperate during oogenesis to establish the dorsoventral pattern of egg shell and embryo in Drosophila melanogaster. Cell *49*, 699–707.

Seydoux, G., Schedl, T., and Greenwald, I. (1990). Cell–cell interactions prevent a potential inductive interaction between soma and germline in C. elegans. Cell *61*, 939–951.

Shellenbarger, D. L., and Mohler, J. D. (1975). Temperature-sensitive mutations of the *Notch* locus in Drosophila melanogaster. Genetics *81*, 143–162.

Smoller, D., Friedel, C., Schmid, A., Bettler, D., Lam, L., and Yedvobnick, B. (1990). The Drosophila neurogenic locus *mastermind* encodes a nuclear protein unusually rich in amino acid homopolymers. Genes Dev. *4*, 1688–1700.

St Johnston, D., Driever, W., Berleth, T., Richstein, S., and Nüsslein-Volhard, C. (1989). Multiple steps in the localization of *bicoid* mRNA to the anterior pole of the Drosophila oocyte. Development (Suppl.) *107*, 13–19.

Tautz, D., and Pfeifle, D. (1989). A nonradioactive in situ hybridization method for the localization of specific RNAs in Drosophila reveals a translational control of segmentation gene *hunchback*. Chromosoma *98*, 81–85.

Vässin, H., Vielmetter, J., and Campos-Ortega, J. A. (1985). Genetic interactions in early neurogenesis of Drosophila melanogaster. J. Neurogenet. *2*, 291–308.

Vässin, H., Bremer, K. A., Knust, E., and Campos-Ortega, J. A. (1987). The neurogenic locus *Delta* of Drosophila melanogaster is expressed in neurogenic territories and encodes a putative transmembrane protein with EGF-like repeats. EMBO J. *6*, 3431–3440.

Wharton, K. A., Johansen, K. M., Xu, T., and Artavanis-Tsakonas, S. (1985). Nucleotide sequence from the neurogenic locus Notch implies a gene product that shares homology with proteins containing EGF-like repeats. Cell *43*, 567–581.

Wieschaus, E. (1980). A combined genetic and mosaic approach to the study of oogenesis in Drosophila. In Development and Neurobiology of Drosophila, O. Siddiqi, P. Babu, L. M. Hall, and J. C. Hall, eds. (New York: Plenum Press), pp. 85–94.

Xu, T., Rebay, I., Fleming, R. J., Scotgale, F. N., and Artavanis-Tsakonas, S. (1990). The *Notch* locus and the genetic circuitry involved in early Drosophila neurogenesis. Genes Dev. *4*, 464–475.

Yochem, J., and Greenwald, I. (1989). *glp-1* and *lin-12*, genes implicated in distinct cell–cell interactions in C. elegans, encode similar transmembrane proteins. Cell *58*, 553–563.

Yochem, J., Weston, K., and Greenwald, I. (1988). The Caenorhabditis elegans lin-12 gene encodes a transmembrane protein with overall similarity to Drosophila Notch. Nature *335*, 547–550.

Note Added in Proof

The reference cited in the Experimental Procedures as Kidd et al., 1983, is as follows: Kidd, S., Lockett, T. J., and Young, M. W. (1983). The *Notch* locus of Drosophila melanogaster. Cell *34*, 421–433.

Appendix 3: Association of p60$^{c\text{-}src}$ with endosomal membranes in mammalian fibroblasts

Introduction

This appendix consists of an article published as Kaplan, K. B., Swedlow, J. R., Varmus, H. E., Morgan, D. O. (1992) Association of p60$^{c\text{-}src}$ with endosomal membranes in mammalian fibroblasts. J. Cell Biol. *118*:321-333 . The paper describes the biochemical and microscopic localization of c-src protein in endosomal membranes of Rat-1 fibroblasts. J. R. Swedlow's contribution to this work was the use of three-dimensional wide-field fluorescence microscopy to show that c-src concentrates in vesicles around the microtubule organizing center and coincides with the localization of the mannose-6-phosphate receptor, a marker for endosomes. Mutations that prevent the myristylation of c-src abolish this localization.

sociation of p60$^{c\text{-}src}$ with Endosomal Membranes Mammalian Fibroblasts

nneth B. Kaplan,* Jason R. Swedlow,‡ Harold E. Varmus,*§ and David O. Morgan‖

artments of *Microbiology and Immunology, §Biochemistry and Biophysics, and ‖Physiology, and ‡Graduate Program
iophysics, University of California, San Francisco, California 94143

stract. We have examined the subcellular localiza- n of p60$^{c\text{-}src}$ in mammalian fibroblasts. Analysis of irect immunofluorescence by three-dimensional op- al sectioning microscopy revealed a granular cyto- smic staining that co-localized with the microtubule anizing center. Immunofluorescence experiments h antibodies against a number of membrane mark- demonstrated a striking co-localization between)$^{c\text{-}src}$ and the cation-dependent mannose-6-phosphate eptor (CI-MPR), a marker that identifies endo- nes. Both p60$^{c\text{-}src}$ and the CI-MPR were found to ister at the spindle poles throughout mitosis. In ad- ion, treatment of interphase and mitotic cells with brefeldin A resulted in a clustering of p60$^{c\text{-}src}$ and CI-MPR at a peri-centriolar position. Biochemical fractionation of cellular membranes showed that a major proportion of p60$^{c\text{-}src}$ co-enriched with endocytic membranes. Treatment of membranes containing HRP to alter their apparent density also altered the density of p60$^{c\text{-}src}$-containing membranes. Similar density shift experiments with total cellular membranes revealed that the majority of membrane-associated p60$^{c\text{-}src}$ in the cell is associated with endosomes, while very little is associated with plasma membranes. These results support a role for p60$^{c\text{-}src}$ in the regulation of endosomal membranes and protein trafficking.

60$^{c\text{-}src}$ is a member of a family of cytoplasmic tyrosine kinases that are associated with cellular membranes and are thought to be involved in signal trans- ction events underlying growth control (for review see oper, 1989). The normal function of p60$^{c\text{-}src}$ is not clear, hough studies of mutant forms of the protein (e.g., the vi- l transforming protein p60$^{v\text{-}src}$) have implicated p60$^{c\text{-}src}$ in control of cell growth and proliferation. On the other nd, p60$^{c\text{-}src}$ is expressed at high levels in terminally fferentiated cells such as platelets and neurons (Cotton and ugge, 1983; Golden et al., 1986). In addition, p60$^{c\text{-}src}$ is tivated during mitosis in fibroblasts and thus may mediate rtain mitotic events (Chackalaparampil and Shalloway, 88; Morgan et al., 1989; Shenoy et al., 1989). Finally, a mozygous disruption of the c-src gene in mice is not le- al, but instead leads to defects in bone remodeling (proba- y as a result of defective osteoclast function) (Soriano et ., 1991).

Clues about p60$^{c\text{-}src}$ function have been obtained from udies of the subcellular location of src proteins. Immuno- uorescence and biochemical fractionation studies have sug- ested that both p60$^{c\text{-}src}$ and p60$^{v\text{-}src}$ are localized to peri- uclear and plasma membranes, while transforming proteins ave also been found in association with adhesion plaques Courtneidge et al., 1980; Resh and Erikson, 1985; Rohr- chneider, 1980). Immunofluorescence studies of p60$^{c\text{-}src}$ ave also revealed a punctate staining pattern that is depen- ent on membrane attachment domains in the amino-terminal region of the protein (Kaplan et al., 1990). This punctate pattern is characteristic of membrane vesicles, suggesting that p60$^{c\text{-}src}$ is associated with cellular membranes distinct from the plasma membrane. Although these membranes remain uncharacterized, analysis of p60$^{c\text{-}src}$ over expressed in 3T3 cells indicates a possible connection with endosomal membranes (David-Pfeuty and Nouvian-Dooghe, 1990). In addition, recent efforts to localize p60$^{c\text{-}src}$ in differentiated PC12 cells and neuroendocrine cells have shown that a significant proportion of p60$^{c\text{-}src}$ is associated with an endosomally derived population of vesicles (Linstedt et al., 1992; Grandori and Hanafusa, 1988).

To gain insight into the normal role of p60$^{c\text{-}src}$, we have used high resolution immunofluorescence analysis and biochemical fractionation to characterize the nature of p60$^{c\text{-}src}$-containing membranes. Our results indicate that p60$^{c\text{-}src}$ is mainly associated with endosomal membranes and is particularly enriched in a population of late endosomes.

Materials and Methods

Cells

The RTCS cell line was derived from a Rat-1 cell line infected with a retroviral construct expressing chicken p60$^{c\text{-}src}$ (Morgan et al., 1989) and expresses ∼7.5-fold more p60$^{c\text{-}src}$ than the parental Rat-1 cell line (determined by Western blot: our own unpublished observations). In some experiments, we used cell lines derived from the spontaneous immortalization of mouse embryo fibroblasts isolated from mice heterozygous or homozygous for a disruption of the c-src gene (cells kindly provided by P. Soriano, Bay-

) The Rockefeller University Press, 0021-9525/92/07/321/13 $2.00
he Journal of Cell Biology, Volume 118, Number 2, July 1992 321–333

lor College of Medicine, Houston, TX). Cells were cultured in DME H-16 with 10% FCS at 37°C in 5% CO_2.

Antibodies

mAbs against $p60^{c\text{-}src}$ were kindly provided by Joan Brugge (University of Pennsylvania, Philadelphia, PA) (mAb327) and Sara Courtneidge (mAb2-17) (Lipsich et al., 1983). Polyclonal rabbit sera against the cation-independent mannose 6-phosphate receptor (CI-MPR) were kindly provided by Peter Lobel (Rutgers University, New Brunswick, NJ) and Bill Brown (Cornell University, Ithaca, NY). mAbs against *cis/medial*-Golgi markers (10E6 and 8B3) were also kindly provided by Bill Brown (Cornell University). Antibodies against BiP binding protein were obtained from David Bole (University of Michigan). mAb against β-tubulin (tub2.1) was purchased from Sigma Chemical Co. (St. Louis, MO). Texas red and fluorescein-labeled secondary anti-rabbit and anti-mouse antibodies were purchased from Accurate Chemical and Scientific Corp. (Westbury, NY) and used at recommended dilutions.

Immunofluorescence

Cells were plated in six-well plates on glass coverslips 18-36 h before analysis. After specified treatments, cells were washed twice with PBS and then fixed for 20 min at 20°C in freshly made 3.7% paraformaldehyde/PBS (Polysciences Inc. Warrington, PA). Fixed cells were washed twice with PBS and permeabilized with 0.1% Triton X-100 in PBS. Cells were rinsed and then blocked in PBS + 0.2% gelatin + 0.02% NaN_3. Primary antibodies were used at the following dilutions for 20 min at 20°C in a humidified chamber: mAb 327 (1 mg/ml): 1/100; tub2.1: 1/200; CI-MPR; 1/200; mAb 2-17: 1/200; mAb 10E6/8B3: undiluted cell culture supernatants. Coverslips were then treated with secondary antibodies at the appropriate dilutions. Endogenous levels of $p60^{c\text{-}src}$ in Rat-1 fibroblasts were detected with an unlabeled rabbit anti-mouse antibody (used at 1 μg/ml) followed by goat anti-rabbit antibody labeled with Texas red. Controls performed with only secondary and tertiary antibodies resulted in negligible signals. Coverslips were washed in PBS + 0.2% gelatin + 0.02% NaN_3, followed by PBS, and finally incubated in Hoechst stain (No. 33258, Sigma Chemical Co.) for 5 min at 20°C before mounting in a solution of 3% *n*-propyl gallate in glycerol. The specificity of the $p60^{c\text{-}src}$ signal was demonstrated by adding excess amounts of purified baculovirus-produced chicken $p60^{c\text{-}src}$ (Morgan et al., 1991).

In costaining experiments with mAb tub2.1 and mAb 327, mAb tub2.1 was directly labeled with Texas red (Harlow and Lane, 1988). The labeled mAb tub2.1 was separated from unincorporated Texas red by gel filtration on a G-50 Sephadex column. Staining with mAb 327 was carried out as above and followed by an additional fixation step before incubation with mAb tub2.1-Texas red. This process fixed the anti-mouse antibody and ensured no cross-reactivity between the fluorescein-conjugated anti-mouse antibody and the mAb tub2.1. No tubulin staining was seen in the fluorescein channel, indicating that there was no interaction between fluorescein-labeled anti-mouse antibodies and mAb tub2.1.

Three-dimensional Optical Sectioning Microscopy and Image Processing

Data were recorded using a Peltier-cooled charge-coupled device (CCD) camera (Photometrics Ltd., Tucson, AZ) mounted on an inverted microscope (Olympus Corp., Lake Success, NY). Images were collected with a 60×/1.4 oil immersion lens (Olympus Corp.); the effective CCD pixel size was 0.074 μm × 0.074 μm. Optical sections were recorded at 0.2 μm intervals. Multiple-wavelength data were collected using a single dichroic mirror designed for DAPI (4',6-diamidino-2-phenylindole), fluorescein and Texas red wave lengths (Omega Optical Inc., Brattleboro, VT). This prevented large registration errors between images recorded with different wavelengths of light (Hiraoka et al., 1991). Excitation and barrier filters were mounted on motorized wheels; wavelength switching and all other aspects of microscope data collection were controlled by a MicroVax III workstation (Hiraoka et al., 1990, 1991). Once the three-dimensional data stacks were recorded, each was corrected for any photobleaching and lamp intensity variations which occurred during data collection (Paddy et al., 1990). Out-of-focus information was removed from each data stack by a three-dimensional, iterative deconvolution program with a non-negativity constraint (Agard et al., 1989). This method moves photons from their recorded positions (out-of-focus) to their points of origin without subtracting any of the information in the images. After the out-of-focus information was removed, projections representing the three-dimensional reconstruction of individual optical sections through the entire cell were generated. Data are presented both as projections of the entire set of optical sections, or as individual optical sections where noted. Some data are presented as unprocessed images recorded by the CCD camera.

Membrane Isolation and Fractionation

RTCS cells were plated 18-36 h before harvesting and allowed to reach a final confluency of 75-85%. Cells were loaded with HRP (Sigma Chemical Co.) (7.5-10 mg/ml in DME H-16, 10% FCS) at 37°C for 30 min (sufficient to saturate the endocytic pathway in these cells). Cells were chilled on ice, washed 4 times in ice-cold PBS and then scraped into homogenization buffer (20 mM Hepes, pH 7.4, 150 mM KCl, 2 mM $MgCl_2$, 10 mM EDTA, 1 mM PMSF, 1 μg/ml leupeptin, 10 μg/ml pepstatin, 0.1 mg/ml soybean trypsin inhibitor, 1 U/ml aprotinin, 0.25 M sucrose). Cells were homogenized in a 2-ml dounce (Wheaton Inds., Millville, NJ) with an A pestle for 30-40 strokes. After homogenization, nuclear membranes were pelleted for 10 min at 2,000 *g* in an SS-34 rotor (Sorvall, Dupont, Wilmington, DE) at 4°C. The postnuclear supernatant (S1) was collected and loaded over a 62% sucrose cushion and spun at 100,000 *g* in an SW50.1 rotor for 35 minutes at 4°C. Membranes at the interface were resuspended in the sucrose cushion (adjusted to 45% sucrose) and placed at the bottom of a sucrose step gradient consisting of 45, 32, and 18% steps. The gradient was centrifuged at 35,000 rpm in an SW50.1 rotor for 60 min at 4°C. The 18/32% interface was collected with a 23-gauge needle and a 2.5-ml syringe. The remaining fractions were collected from the top of the gradient with a pasteur pipette and analyzed for $p60^{c\text{-}src}$ and membrane markers.

Under these homogenization conditions (30-40 strokes) 30-40% of HRP activity was left in the nuclear pellet and plasma membranes were mainly observed in the 45% sucrose fraction. Harsher homogenization conditions (80 strokes) left <1% of the total HRP activity in the nuclear pellet and the majority of plasma membranes were observed in the 32% and interface (18/32%) fractions on sucrose gradients.

To analyze the 18/32% sucrose interface on percoll gradients, the fraction was mixed into a 27% percoll solution (8.5% sucrose) and centrifuged over a 62% sucrose cushion in a 50Ti rotor at 16,000 rpm for 60 min at 4°C. Fractions were collected from the bottom of the tube and assayed for membrane markers and $p60^{c\text{-}src}$ by immunoblotting.

Membrane markers were assayed as follows. The plasma membrane marker alkaline diphosphoesterase I (ADPE I) was measured with thymidine-5'-monophosphate-*p*-nitrophenyl ester (Sigma Chemical Co.) and assayed using a Beckman fluorometer at excitation 355 nM and emission 455 nM (Poole et al., 1983). The lysosomal marker β-hexosaminidase was measured with the fluorometric substrate 4-methyl umbelliferyl-*N*-acetyl-β-D-glucosaminide (Sigma Chemical Co.) and samples were read on a Beckman fluorometer at excitation 350 nM and emission 450 nM (ref). The Golgi marker galactosyl transferase was measured by incorporation of UDP-[3H]-galactose (Amersham Corp., Arlington Heights, IL) into BSA (Aoki et al., 1990). HRP activity was measured using *o*-dianisidine (Sigma Chemical Co.) prepared at 0.11 μg/ml in PBS, pH 5.0, 0.1% Triton X-100. Activity was measured at OD_{460} at several time points (or at several volumes of extract) to ensure linearity of the assay.

Density Shift and DAB Cytochemistry

HRP-containing membranes from the 18/32% interface or from the P100 fraction (isolated under relatively harsh homogenization conditions; see above) were treated with DAB in homogenization buffer to a final concentration of 6 μg/ml. 10 μl of 30% H_2O_2 was added and the mixture incubated in the dark at 0°C for 10 min. After treatment, membranes were loaded on another sucrose gradient or a percoll gradient as described above, centrifuged, and analyzed for $p60^{c\text{-}src}$ and membrane markers. In control experiments no density shift was observed if DAB or H_2O_2 were added separately.

To inhibit HRP entry in some experiments, cells were chilled on ice and cold media containing HRP was incubated with the cells at 0°C for 20 min. Half of the cells were placed at 37°C for 40 min. Both sets of plates were then washed and membranes harvested as above. DAB cytochemistry was carried out and fractions from percoll gradients were analyzed for $p60^{c\text{-}src}$ and membrane markers.

---

1. *Abbreviations used in this paper*: ADPE I, alkaline diphosphoesterase I; BFA, brefeldin A; CCD, charge-coupled device; CI-MPR, cation-independent mannose 6-phosphate receptor; MTOC, microtubule organizing center; TGN, *trans*-Golgi network.

onitoring of plasma membranes by surface iodination was performed
cells loaded for 30 min at 37°C with HRP. Cells were chilled on ice,
ed 4 times with ice cold PBS and then dislodged from the plate using
+ 1 mM EDTA. Cells were extensively washed in ice cold PBS and
abeled using sulfo-SHPP (Pierce Chemical Co. Rockford, IL) labeled
iodobeads (Thompson et al., 1987). Free ^{125}I counts were washed out
e cells using ice cold PBS. Membranes were isolated and DAB
hemistry was performed and analyzed as above.

ıunoprecipitation and Immunoblotting

mmunoprecipitating $p60^{c\text{-}src}$, fractions were diluted two times with
genization buffer and adjusted to 1% Triton X-100. mAb 327 was
l and incubated at 4°C for 1–4 h. Protein A–sepharose conjugated to
oit anti–mouse antibody was added (50 μl/fraction of 50% slurry) and
ated at 4°C for 1–2 h. After one wash with homogenization buffer +
riton X-100, protein A–sepharose beads were boiled in loading buffer,
ıpernatants were loaded onto 10% PAGE gels. After electrophoresis,
ns were transferred to nitrocellulose on an electroblot apparatus (Bio-
aboratories, Cambridge, MA), and blots were blocked in 2% BSA
h at 20°C. Blots were incubated in mAb327 (1 μg/ml) at 4°C for
h. Secondary ^{125}I-labeled goat anti–mouse IgG (New England Nu-
Boston, MA) was incubated for 1–4 h at 4°C and the blot washed and
adiography carried out at –70°C. Bands were cut from the blot and
ed to measure relative $p60^{c\text{-}src}$ signals. In some experiments, HRP-
l goat anti–mouse IgG (Amersham Corp.) was detected with a chemi-
escence procedure as described for the Amersham ECL detection sys-
To recognize antibodies against the CI-MPR, HRP-linked goat
abbit antibodies (Amersham Corp.) were used in the chemi-lumines-
protocol.

ılts

taining of $p60^{c\text{-}src}$ with Late Endosomes at the otubule Organizing Center

fibroblasts over-expressing chicken $p60^{c\text{-}src}$ (RTCS cell
were analyzed by indirect immunofluorescence with a
against $p60^{c\text{-}src}$ (mAb 327). To enhance resolution, im-
ofluorescence was recorded with an optical sectioning
oscope and both individual optical sections and three-
nsional reconstructions of the images were analyzed.
general populations of $p60^{c\text{-}src}$ were apparent: a granu-
aining throughout the cytoplasm and a concentrated
ng adjacent to the nucleus (Fig. 1 *A*). Staining with a
ent mAb against $p60^{c\text{-}src}$ (mAb 2-17) demonstrated a
ar staining pattern, and signals with either antibody
blocked by addition of purified chicken $p60^{c\text{-}src}$ pro-
l with the baculovirus expression system (Morgan et
991) (data not shown).
ining with antibodies against tubulin revealed that $p60^{c\text{-}src}$
calizes with the microtubule organizing center (MTOC),
gion of the cell where many membranous organelles are
d (Fig. 1 *B*). The concentration of $p60^{c\text{-}src}$ at the MTOC
ot simply because of the increased cell thickness in this
n of the cell, as analysis of optical sections showed a
ct region of staining along the vertical axis of the cell
: $p60^{c\text{-}src}$ is concentrated (Fig. 1 *C*). In addition, $p60^{c\text{-}src}$
ntrated at the MTOC co-stains with individual cellular
otubules when optical sections from cells stained with
odies against tubulin (Fig. 1 *D*) are compared to the iden-
sections stained with antibodies against $p60^{c\text{-}src}$ (Fig. 1
This staining pattern is also not because of the over-
ssion of chicken $p60^{c\text{-}src}$ in these cells, as endogenous
in Rat-1 fibroblasts exhibited an identical pattern (Fig.
In addition, the depolymerization of cellular microtu-
with the drug nocodazole dispersed $p60^{c\text{-}src}$ (Fig. 1 *E*) and suggested a direct association with the MTOC. $P60^{c\text{-}src}$ rapidly returned to the peri-nuclear region of the cell upon removal of nocodazole and the repolymerization of cellular microtubules (data not shown).

$P60^{c\text{-}src}$ is myristylated at its NH_2-terminus (Buss and Sefton, 1985), and the myristylation signal is necessary but not sufficient for association with cellular membranes (Kaplan et al., 1990). To address the issue of whether membrane association of $p60^{c\text{-}src}$ is required for the localization of $p60^{c\text{-}src}$ at the MTOC, we characterized a 3T3 fibroblast cell line expressing $p60^{c\text{-}src}$ in which the second amino acid glycine has been replaced with alanine. In $p60^{v\text{-}src}$, this amino acid change results in a protein that cannot be myristylated and therefore does not associate with cellular membranes (Buff et al., 1986; Kamps et al., 1986). Immunofluorescence analysis of cells expressing $p60^{c\text{-}src}$ containing this substitution showed a diffuse cytoplasmic staining, indicating that membrane attachment is required for localization at the MTOC, as previously suggested (Kaplan et al., 1990) (Fig. 2, *A* and *B*). We also failed to observe the granular cytoplasmic $p60^{c\text{-}src}$ staining pattern, indicating that membrane association is required for this localization as well. To determine whether membrane association alone is sufficient for localization of $p60^{c\text{-}src}$ at the MTOC, we analyzed a membrane-associated fusion protein comprising the first 14 amino acids of $p60^{c\text{-}src}$ fused to pyruvate kinase (Kaplan et al., 1990). When expressed in Rat-1 cells this protein exhibited a punctate staining pattern and did not co-localize with the MTOC (data not shown). We therefore conclude that myristylation is necessary but not sufficient to allow MTOC localization of $p60^{c\text{-}src}$, supporting the notion that there are other domains of $p60^{c\text{-}src}$ that contain information important for localization (Kaplan et al., 1990).

Membrane organelles involved in various secretory and endocytic processes have been localized to the MTOC. To identify candidate membranes that contain $p60^{c\text{-}src}$, co-localization studies were performed with a number of antibodies against markers of specific membrane compartments. The Golgi compartment was identified with several markers, including fluorescein-conjugated wheat germ agglutinin and two mAbs, 10E6 and 8B3, specific for *cis/medial*-Golgi elements (Wood et al., 1991). These markers stained a perinuclear region of the cell that was distinct from $p60^{c\text{-}src}$, suggesting that $p60^{c\text{-}src}$ is not found in *cis/medial*-Golgi membranes (Fig. 2 *C*). Similarly, staining of the ER with antibodies against BiP (Bole et al., 1989) and staining of lysosomes with antibodies against lgp120 (Lewis et al., 1985) revealed that these two membrane compartments are clearly distinct from $p60^{c\text{-}src}$ at the MTOC (data not shown).

In contrast, staining with antibodies to the CI-MPR, a marker of endosomes and *trans*-Golgi network (TGN), revealed a striking co-localization with $p60^{c\text{-}src}$ at the MTOC (Fig. 2, *D* and *E*). While all endosomal membranes are believed to contain the CI-MPR, the CI-MPR-positive endosomes located at the MTOC represent vesicles at a late stage in the endocytic pathway (late endosomes or pre-lysosomes) (Messner and Kreis, 1989). CI-MPR-positive vesicles also require intact microtubules for their localization, unlike early endosomes (K. Kaplan, unpublished observations) (Matteoni et al., 1987). Thus, our results suggest that $p60^{c\text{-}src}$ is associated with membranes at the MTOC that represent a late stage in the endocytic pathway. While no di-

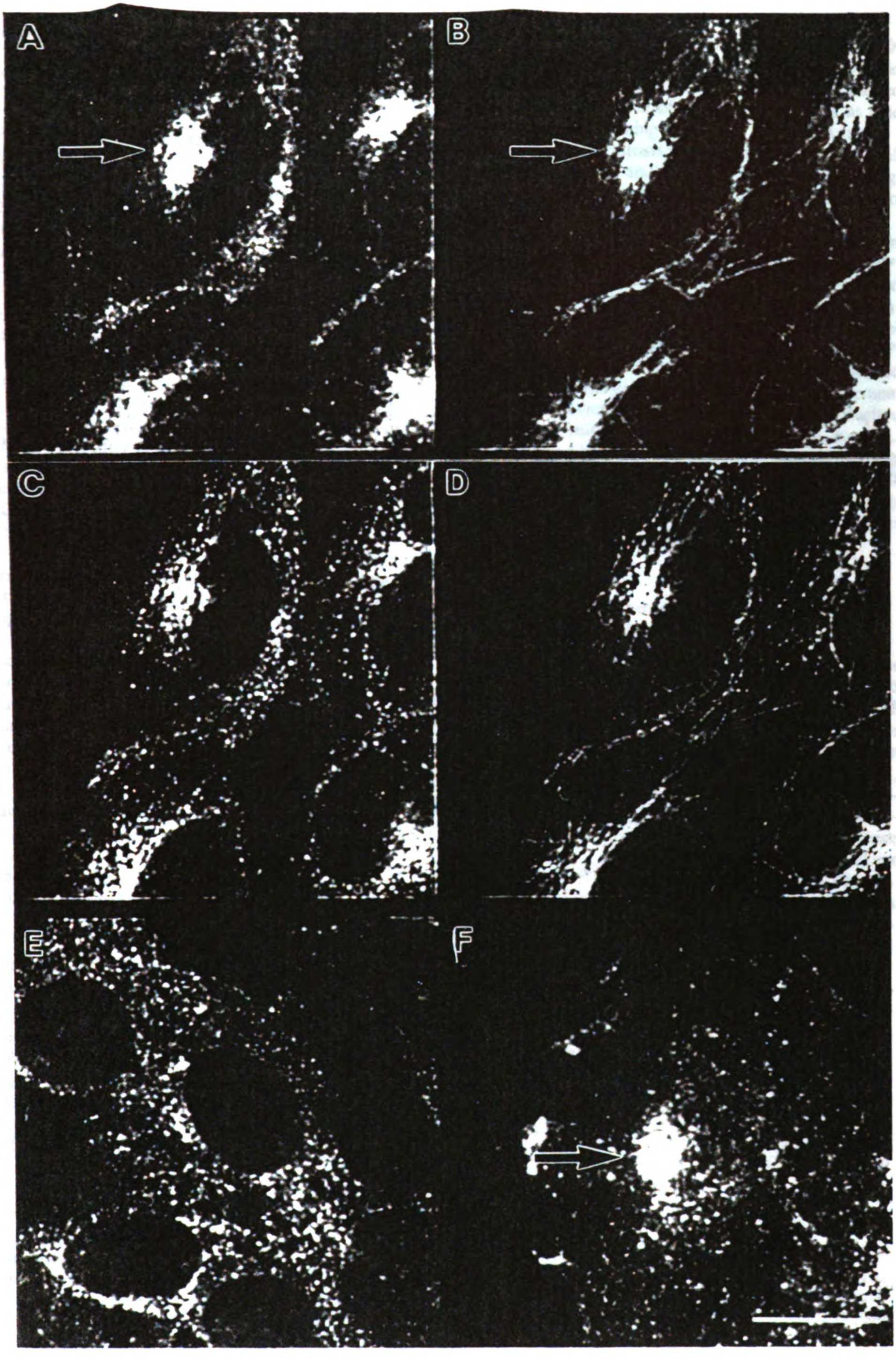
A
B
C
D
E
F

tempts were made to distinguish CI-MPR–positive en-
es from CI-MPR–positive TGN, we observed that
^{c} did not exhibit the tubular staining pattern charac-
c of the TGN (data not shown).

^{rc} and CI-MPR Co-localize after Treatment BFA

rther analyze $p60^{c-src}$-containing membranes and to guish these membranes from *cis/medial*-Golgi net-we treated cells with brefeldin A (BFA). BFA disrupts ɔrmal distribution of *cis/medial*-Golgi membranes, ıg retrograde transport to the ER. This results in a re-r staining pattern when the Golgi apparatus is visual-ɔy immunofluorescence (Lippincott-Schwartz et al., 1990). In contrast, BFA treatment does not result in ınsport of CI-MPR–containing membranes into the ER ;e and Pfeffer, 1990; Lippincott-Schwartz et al., 1991; et al., 1991). If $p60^{c-src}$ is associated with CI--containing late endosomes, then the behavior of ^{c} and CI-MPR after BFA treatment should be similar, et distinct from *cis/medial*-Golgi membranes.

ısistent with previous findings, we found that after BFA ıent the Golgi marker 10E6 exhibited a punctate/retic-taining pattern characteristic of ER staining in these (Fig. 3 *A*). We also observed that CI-MPR–positive ɔranes do not enter the ER after BFA treatment. After :reatment, both $p60^{c-src}$ and CI-MPR (Fig. 3, *B* and *C*) :d a tight cluster at the centrosome in a staining pattern .s distinct from *cis/medial*-Golgi membranes. This :ring of membranes containing $p60^{c-src}$ and CI-MPR at :ntrosome is less diffuse than the staining pattern at the C in untreated cells. The clustering occurs after 30 min 'A treatment, is reversible, and is dependent on intact ɔtubules, since pretreatment with nocodazole abolishes ffect (data not shown). In untreated populations of ɔlasts, some cells (5–10%) exhibit a similar clustering 0^{c-src} and CI-MPR staining at the centrosome, suggest-ıat the clustering of endosomes in this region can occur : absence of BFA. These results further support the no-:hat $p60^{c-src}$ and the CI-MPR are in a similar cellular ɔartment that is distinct from the *cis/medial*-Golgi ap-us.

ɔcalization of $p60^{c-src}$ and CI-MPR at the Spindle ; during Mitosis

ıctivation of $p60^{c-src}$ during mitosis suggests that it may ı role in mitosis. Therefore we also examined the local-ɔn of $p60^{c-src}$ in mitotic cells (identified by the state of chromatin after Hoechst staining; see Materials and ıods). During mitosis, $p60^{c-src}$ was observed to cluster : dividing centrosomes (Fig. 4 *A*; *arrows*). Co-staining anti–CI-MPR clearly demonstrated that the CI-MPR is clustered at the same peri-centriolar position as $p60^{c-src}$ (Fig. 4 *B*; *arrows*). Reconstructive analysis of three-dimensional optical sections confirmed that $p60^{c-src}$ staining corresponded to the position of migrating centrioles as determined by tubulin staining (data not shown). Analysis of additional stages of mitosis showed that the peri-centriolar populations of $p60^{c-src}$ and CI-MPR were present throughout mitosis and appear positioned to form membrane organelles at the MTOC after telophase.

Over-expression of $p60^{c-src}$ did not affect staining, as similar patterns were apparent when endogenous levels of $p60^{c-src}$ were examined in Rat-1 cells (Fig. 4, *D* and *E*). The mitotic localization of both CI-MPR and $p60^{c-src}$ is dependent on a properly formed spindle, since cells treated with nocodazole no longer show pericentriolar staining of $p60^{c-src}$ or CI-MPR (data not shown). In addition, staining of cells with antibodies specific for the Golgi apparatus revealed that Golgi membranes became vesicularized and were scattered throughout the cell during mitosis as previously reported for HeLa cells (Lucocq and Warren, 1987; Moskalewski and Thyberg, 1990). This contrast between Golgi staining and $p60^{c-src}$/CI-MPR staining during mitosis provides additional evidence that $p60^{c-src}$ associates with endosomal membranes and not with *cis/medial*-Golgi elements.

Biochemical Fractionation Reveals that $p60^{c-src}$ Co-enriches with Endosomal Membranes

We next examined the association of $p60^{c-src}$ with endosomal membranes by standard cell fractionation techniques. RTCS cells were allowed to internalize the fluid phase marker HRP to label the endocytic compartment. Cellular membranes isolated after a 100,000 *g* spin (P100 pellet) were placed at the bottom of a sucrose step gradient consisting of 45, 32, and 18% steps. Membranes were allowed to float to equilibrium during centrifugation. We determined that the endocytic marker HRP and thus endocytic membranes from these cells were enriched at the 18/32% interphase of the gradient (data not shown). We analyzed the fractions from the gradient by immunoblotting to identify $p60^{c-src}$ and observed a major peak at the 18/32% interface (Fig. 5 *A*). Based on immunoblots with ^{125}I-labeled antibody, we estimate that 65% of the total $p60^{c-src}$ on the gradient was at the 18/32% interface (Fig. 5 *B*). A similar pattern of enrichment was observed with cells expressing endogenous levels of $p60^{c-src}$ (data not shown). The density at the 18/32% interface is characteristic of endosomal membranes and is therefore consistent with the enrichment of $p60^{c-src}$ with endocytic vesicles. Analysis of markers for membrane compartments demonstrated that fractions enriched for $p60^{c-src}$ are distinct from lysosomal (data not shown), Golgi apparatus, and plasma membrane markers (Fig. 5, *C*–*E*), although a small

---

e 1. Co-staining of $p60^{c-src}$ and the MTOC. Projections comprising multiple optical sections of RTCS fibroblasts (see Materials and ods) were obtained with mAb 327 against $p60^{c-src}$ (*A*) and mAb tub 2.1 against tubulin (*B*). Individual optical sections that represent mation from the middle of the cells stained with mAb 327 against $p60^{c-src}$ (*C*) and mAb tub2.1 against tubulin (*D*) are also presented. ıgle optical section is presented from RTCS cells treated for 30 min with 0.5 μg/ml nocodazole to depolymerize microtubules, and ed with mAb 327 (*E*). A projection of Rat-1 fibroblasts expressing only endogenous c-src was obtained with mAb 327 against $p60^{c-src}$ Endogenous $p60^{c-src}$ signal was enhanced with a rabbit anti-mouse antiserum (sandwich antibody) between the primary mAb and ophore-conjugated secondary antibody. Arrows indicate the MTOC. Bar, 10 μm.

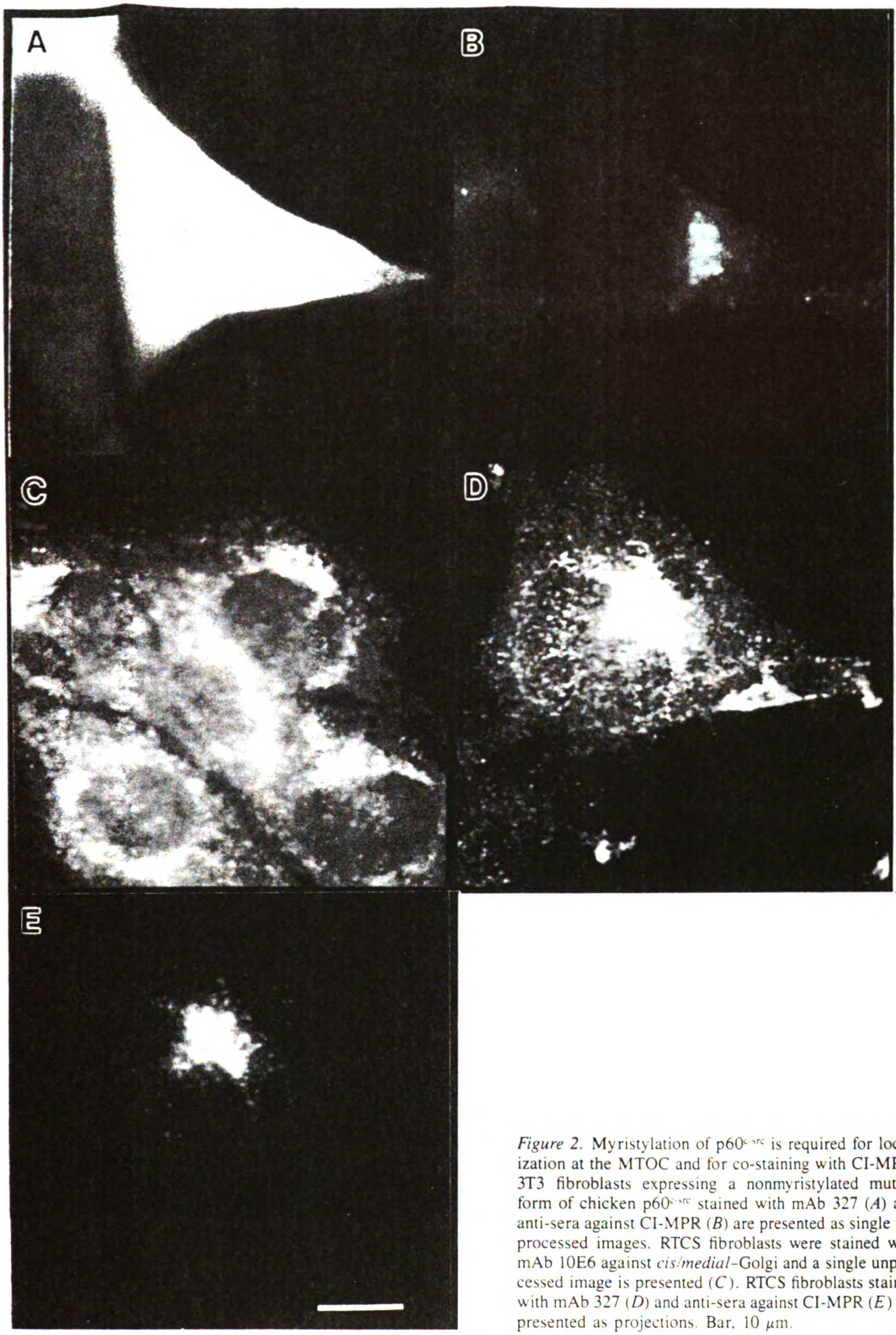

Figure 2. Myristylation of $p60^{c\text{-}src}$ is required for localization at the MTOC and for co-staining with CI-MPR. 3T3 fibroblasts expressing a nonmyristylated mutant form of chicken $p60^{c\text{-}src}$ stained with mAb 327 (*A*) and anti-sera against CI-MPR (*B*) are presented as single unprocessed images. RTCS fibroblasts were stained with mAb 10E6 against *cis/medial*–Golgi and a single unprocessed image is presented (*C*). RTCS fibroblasts stained with mAb 327 (*D*) and anti-sera against CI-MPR (*E*) are presented as projections. Bar, 10 μm.

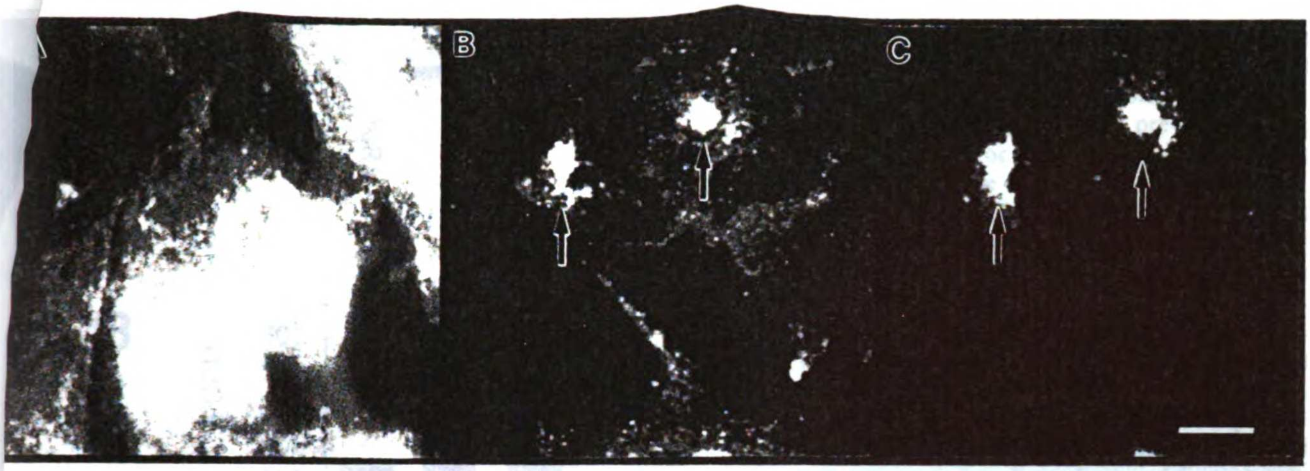

ure 3. Brefeldin A treatment causes p60$^{c\text{-}src}$ and CI-MPR membranes to cluster at the centrosome. RTCS fibroblasts were treated with g/ml brefeldin A for 30 min at 37°C and then processed for immunofluorescence. A single unprocessed image of staining with mAb E6 against *cis/medial*-Golgi is presented (*A*), while projections of multiple optical sections are presented for staining with mAb 327 ainst p60$^{c\text{-}src}$ (*B*) and anti-sera against CI-MPR (*C*). Arrows indicate clustered p60$^{c\text{-}src}$ and CI-MPR staining at the centrosome. Bar, μm.

ount of plasma membrane marker was found at the 18/32% erface (see Materials and Methods).

P60$^{c\text{-}src}$ was sometimes observed in the 45 and 32% frac ns. To address whether this material was membrane-associated, each fraction from the sucrose step gradient was diluted to a final concentration of 8.5% sucrose, pelleted at 100,000 *g* and the pellet analyzed for p60$^{c\text{-}src}$ by immunoblotting. Approximately 90% of the p60$^{c\text{-}src}$ in these frac-

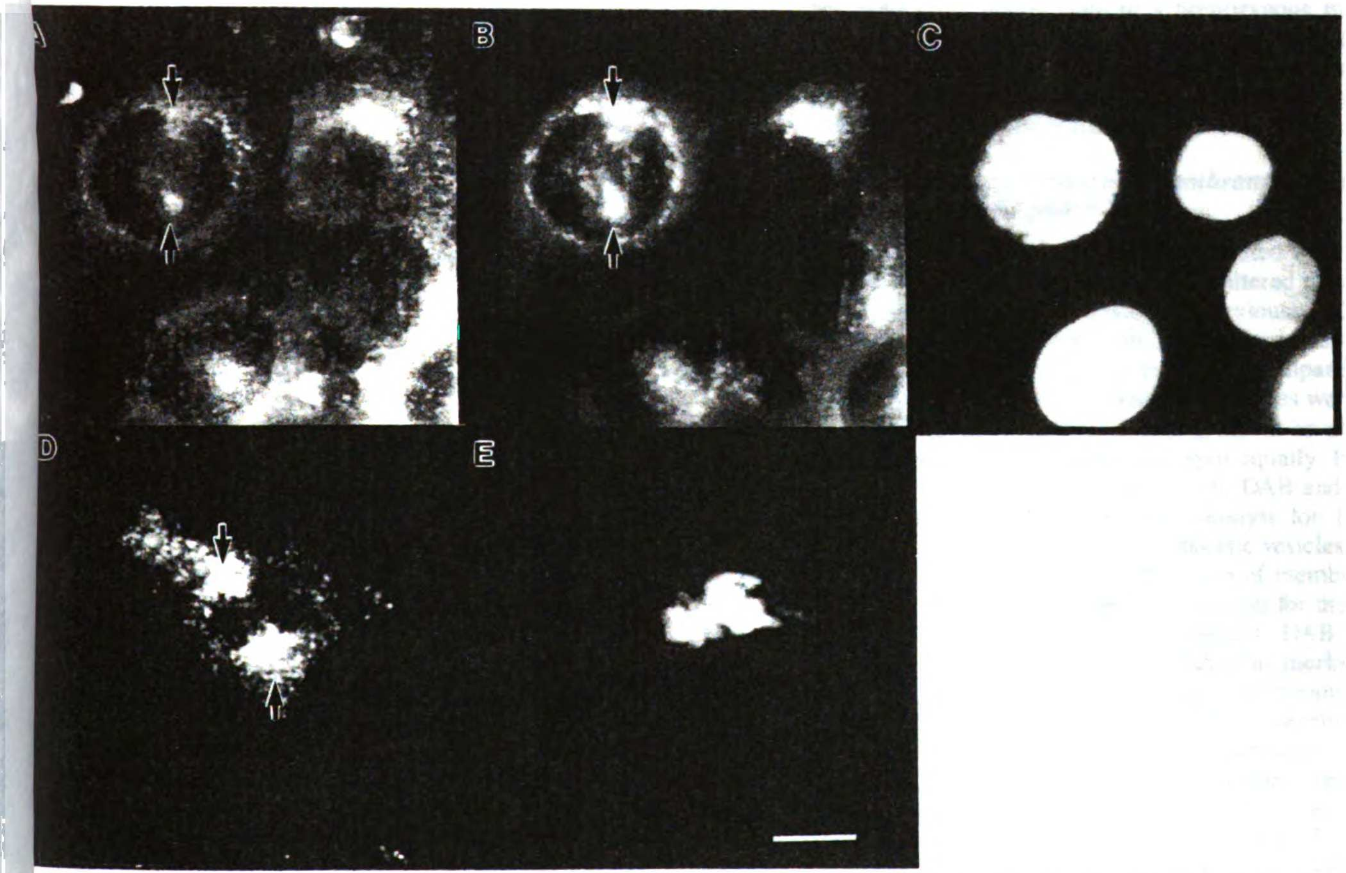

igure 4. Co-staining of p60$^{c\text{-}src}$ and CI-MPR at the spindle poles of mitotic cells. *A–C* represent projections of the same RTCS fibroblast rophase cell stained with mAb 327 against p60$^{c\text{-}src}$ (*A*), anti-sera against CI-MPR (*B*) and Hoechst stain (*C*) to reveal the chromatin. rojections were obtained of Rat-1 fibroblasts stained with mAb 327 against p60$^{c\text{-}src}$ plus a sandwich antibody (see legend to Fig. 1; *D*) nd with Hoechst stain to reveal the chromatin (*E*). Arrows indicate peri-centriolar staining in mitotic cells. Bar, 10 μm.

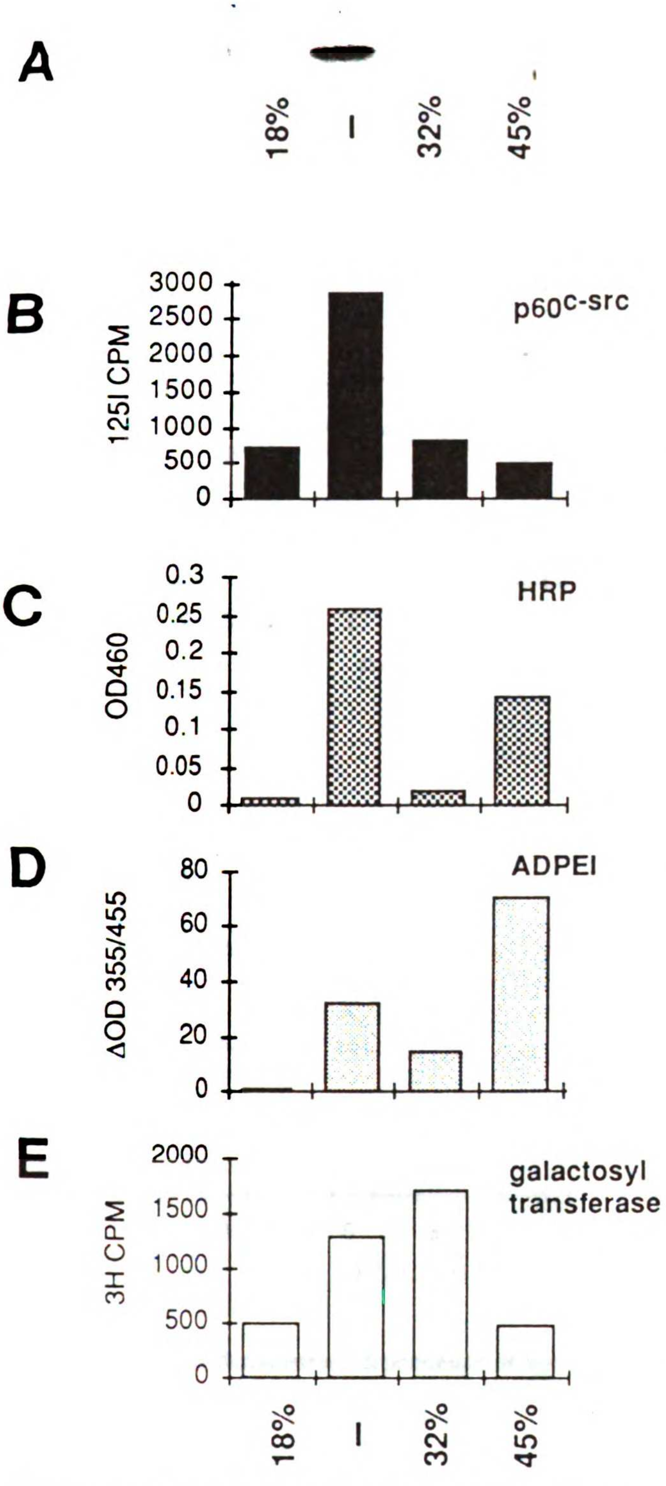

Figure 5. Enrichment of p60$^{c\text{-}src}$ and endosomal membranes on sucrose step gradients. RTCS fibroblasts were incubated with HRP for 30 min at 37°C and cell membranes were isolated and loaded on the bottom of a sucrose step gradient (see Materials and Methods). After centrifugation, fractions were analyzed by immunoblot with mAb 327 detected by ^{125}I labeled goat anti-mouse antibodies (*A*). Bands were cut from the blot and counted (*B*). Fractions were also analyzed for HRP activity (endosomal marker) (*C*), ADPE I activity (plasma membrane marker) (*D*), and galactosyl transferase activity (*cis/medial*-Golgi marker) (*E*).

tions remained in the supernatant and was therefore presumed to be soluble. In addition, treatment of cellular membranes with a water soluble, membrane impermeable cross-linking reagent (DTSSP) prevented the appearance of p60$^{c\text{-}src}$ in the 45 or 32% fractions, and resulted in a corresponding increase in the amount of p60$^{c\text{-}src}$ at the 18/32% interface. We therefore suspect that under normal homogenization conditions a minor fraction of p60$^{c\text{-}src}$ dissociates from cellular membranes and sediments near the bottom of the sucrose gradient.

We were particularly interested in separating plasma membranes and endosomal membranes because of the reported association of p60$^{c\text{-}src}$ with plasma membranes (Courtneidge et al., 1980). To further separate membranes, material from the 18/32% interface of the sucrose gradient was run on a percoll gradient and fractions were analyzed for the presence of p60$^{c\text{-}src}$. In multiple experiments, p60$^{c\text{-}src}$ migrated as a single peak in the low density fractions and paralleled the endocytic marker (HRP) profile (e.g., Fig. 6, *A* and *B*). In similar but separate experiments with total cellular membranes, p60$^{c\text{-}src}$ was also detected in low density fractions (data not shown) while Golgi markers, iodinated plasma membrane proteins (Fig. 6 *C*) and lysosomal markers (data not shown) were not enriched in p60$^{c\text{-}src}$-containing fractions. To rule out the possibility that soluble p60$^{c\text{-}src}$ present in cell homogenates was simply associating with endosomal membranes during cell lysis, we mixed p60$^{c\text{-}src}$ found in S100 fractions with membranes from cells not expressing p60$^{c\text{-}src}$ (due to a homozygous mutation at the src gene). P60$^{c\text{-}src}$ did not associate with endosomal membranes under these conditions, indicating that soluble p60$^{c\text{-}src}$ does not preferentially associate with endosomal membranes after cell lysis (data not shown).

Shift in Density of Endocytic Membranes Alters Membrane-Bound p60$^{c\text{-}src}$ Density

To determine if p60$^{c\text{-}src}$ is directly associated with endocytic vesicles inside the cell we specifically altered the density of endocytic membranes as described previously (Courtoy et al., 1984; Stoorvogel et al., 1991). Cells were allowed to internalize HRP to saturate the endocytic compartment (see Materials and Methods). Cellular membranes were isolated and sedimented on a sucrose step gradient as above. The 18/32% interface was isolated and split equally. Half of the interface membranes were treated with DAB and hydrogen peroxide (H_2O_2), a substrate and catalyst for HRP. The modification of DAB by HRP in endocytic vesicles results in an increase in vesicle density. Each set of membranes was analyzed on separate sucrose step gradients for the presence of p60$^{c\text{-}src}$ and HRP activity. As expected, DAB and H_2O_2 treatment resulted in a shift of the endocytic marker HRP to the 45% fraction (Fig. 7 *B*). Treatment of membranes with DAB and H_2O_2 also resulted in a shift of membranes containing p60$^{c\text{-}src}$ (Fig. 7 *A*) and CI-MPR (data not shown) to the 45% fraction. Other membrane markers present in the 18/32% interface did not undergo a shift in density to the 45% fraction after treatment with DAB (Fig. 7, *C* and *D*). The variation in the distribution of the Golgi marker galactosyl transferase (Fig. 7 *D*) was found to be dependent on homogenization conditions rather than DAB treatment, suggesting that the DAB-induced density shift was specific for

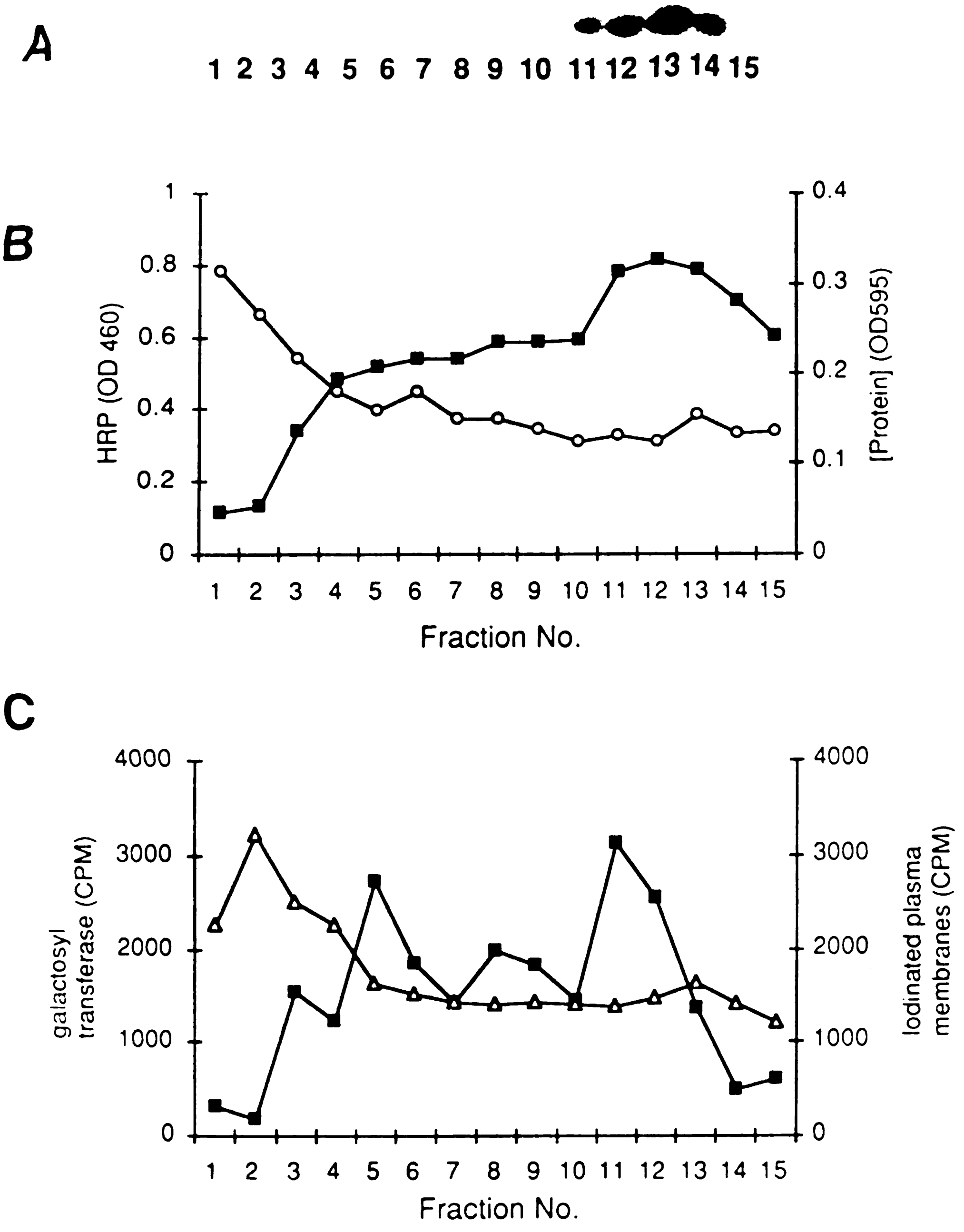

Figure 6. Separation of $p60^{c\text{-}src}$ from plasma membranes on percoll gradients. RTCS fibroblasts were incubated with HRP and cell membranes from the 18/32% interface of a sucrose step gradient were isolated and loaded on a percoll gradient (in the absence of $CaCl_2$; see Materials and Methods). Fractions were collected from the bottom of the gradient (1 = highest density and 15 = lowest density) and analyzed by immunoblot with mAb 327 against $p60^{c\text{-}src}$ (*A*), for protein concentration (*B*, ○) and HRP activity (*B*, ■). Whole cellular membranes from a p100 fraction were isolated in homogenization buffer (+2 mM $CaCl_2$; see Materials and Methods), run on parallel percoll gradients, analyzed for the Golgi marker galactosyl transferase (*C*, ■), and a gamma counter was used to detect the presence of iodinated plasma membrane proteins (*C*, △). The addition of $CaCl_2$ to the homogenization buffer in this experiment (see Materials and Methods; Fig. 6 *C*) further separated iodinated plasma membrane proteins from endosomal membranes by altering the apparent density of plasma membranes on the percoll gradient (Stoorvogel et al., 1989).

endosomal membranes. To demonstrate dependence of the density shift on the HRP reaction, samples treated only with DAB (or only with H_2O_2, data not shown) exhibited no shift in the apparent density of $p60^{c\text{-}src}$-associated membranes (Fig. 7 *A*, *left*).

Association of the Majority of $p60^{c\text{-}src}$ with Endosomal Membranes

All of the $p60^{c\text{-}src}$ isolated from the 18/32% fraction shifted density in these experiments, suggesting that all of the $p60^{c\text{-}src}$ in this fraction is associated with membranes accessible to the endocytic marker HRP. To determine the amount of $p60^{c\text{-}src}$ in the entire cell that is associated with endosomal membranes, we performed density shift experiments on the entire population of cellular membranes isolated from a 100,000 *g* pellet. The proportion of $p60^{c\text{-}src}$ in this pellet that undergoes a density shift should represent the proportion of membrane-bound $p60^{c\text{-}src}$ associated with endocytic membranes. After treatment with DAB and H_2O_2, total cellular membranes were separated on a percoll gradient and fractions were analyzed to identify $p60^{c\text{-}src}$ and relevant membrane markers. $P60^{c\text{-}src}$ from untreated membranes paralleled the peak of endosomal membranes (HRP) in low density fractions (Fig. 8 *A*). Treatment of membranes with DAB and H_2O_2 shifted the density of all detectable $p60^{c\text{-}src}$ and the endocytic marker HRP to higher density fractions (Fig. 8, *B* and *C*).

The shift in density of all detectable $p60^{c\text{-}src}$ suggested that the majority of $p60^{c\text{-}src}$ is associated with endosomal membranes and little or no $p60^{c\text{-}src}$ is associated with

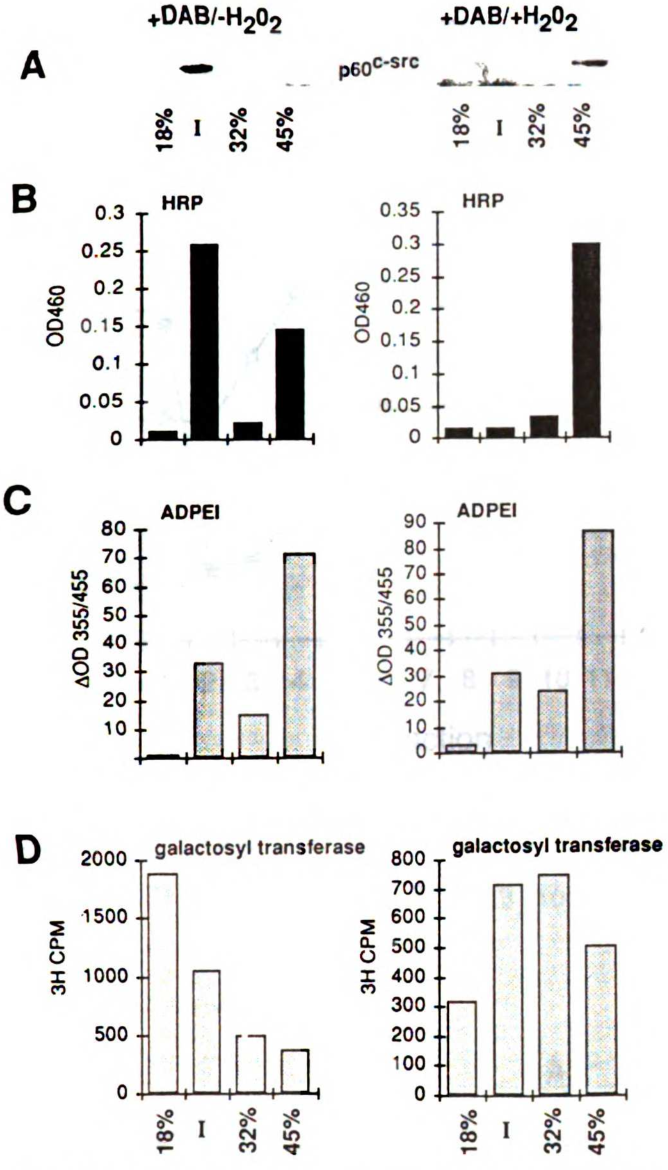

Figure 7. DAB-induced density shift of p60$^{c\text{-}src}$ in HRP-containing endosomes. Material from the 18/32% interface of a sucrose step gradient was treated with DAB in the presence (*right*) or absence (*left*) of H_2O_2. P60$^{c\text{-}src}$ was detected by immunoprecipitation and immunoblotting with mAb 327 (*A*). Fractions were also analyzed for HRP activity (*B*), ADPE I activity (plasma membrane marker) (*C*), and galactosyl transferase activity (*cis/medial*-Golgi marker) (*D*).

plasma membranes. However, it was possible that HRP bound to the plasma membrane was incorporated into vesicles, resulting in a shift in density of plasma membranes after DAB/H_2O_2 treatment. To address this possibility, attempts were made to determine the fate of plasma membranes after DAB/H_2O_2 treatment. Identification of plasma membranes by the measurement of enzymatic markers was impeded by low enzymatic activities in percoll. Instead, HRP-containing cells were surface iodinated at 0°C to identify plasma membranes. Measurement of ^{125}I after density shift revealed that there was no detectable shift in labeled plasma membrane proteins, while the p60$^{c\text{-}src}$-associated membranes underwent a shift in density as expected (Fig. 8).

To further address the specificity of the density shift, HRP was bound to the surface of cells at 0°C to prevent endocytosis and cell membranes were harvested and treated with DAB and H_2O_2. No detectable density shift of p60$^{c\text{-}src}$ was observed (data not shown) despite high levels of HRP activity in the membrane pellet. Thus, only HRP internalized into the endocytic pathway is able to shift the density of p60$^{c\text{-}src}$-containing membranes.

It was also possible that there was a preferential solubilization of plasma membrane-associated p60$^{c\text{-}src}$ during preparation of cellular membranes. The ~10–20% of total p60$^{c\text{-}src}$ that we detected in the soluble S100 fraction may therefore represent a plasma membrane-associated fraction of p60$^{c\text{-}src}$. To address this possibility, cell extracts were treated with DTSSP (as described above) to reduce the amount of p60$^{c\text{-}src}$ in the S100 fraction. P60$^{c\text{-}src}$ was fractionated on percoll gradients and did not cosediment with plasma membranes (data not shown). It is therefore unlikely that the population of soluble p60$^{c\text{-}src}$ came from the plasma membrane.

Discussion

We have found that the majority of membrane-associated p60$^{c\text{-}src}$ in mammalian fibroblasts is localized to a compartment that probably represents a population of endosomes. Our immunofluorescence experiments demonstrate that a significant proportion of p60$^{c\text{-}src}$ is found at the MTOC and co-localizes with CI-MPR, a marker of late endosomes. Biochemical fractionation and density shift experiments indicate that the majority of p60$^{c\text{-}src}$ in the cell associates with endosomal membranes accessible to the endocytic marker HRP. These results raise the possibility that p60$^{c\text{-}src}$ plays a role in endosomal function.

Previous immunofluorescence and electron microscopic studies of p60$^{v\text{-}src}$ tend to support localization of the viral src protein at the plasma membrane (Rohrschneider, 1979; Willingham et al., 1979). Some src family members are thought to interact with cell surface proteins, and a putative plasma membrane receptor for p60$^{v\text{-}src}$ has been identified in cross-linking experiments (Resh and Ling, 1990). In contrast, our results suggest that very little p60$^{c\text{-}src}$ is associated with plasma membranes. Although we sometimes observed p60$^{c\text{-}src}$ staining at cell–cell contacts, we suspect that this does not represent plasma membrane association but rather is because of enrichment of membranes at bundles of microtubules (Fig. 1). Dependence on intact microtubules for this localization further supports the notion that p60$^{c\text{-}src}$ is microtubule-associated at cell–cell contacts. The discrepancy between previous localization studies and our results may arise in part from differences between the transforming protein p60$^{v\text{-}src}$ and the nontransforming protein p60$^{c\text{-}src}$.

Our results also differ from previous studies that have used biochemical fractionation to localize src proteins. These studies demonstrate an enrichment of both p60$^{v\text{-}src}$ and p60$^{c\text{-}src}$ in plasma membranes (Courtneidge et al., 1980; Resh and Erikson, 1985). Fractionation techniques used in these studies did not differentiate between plasma membranes and endosomal membranes, which have similar densities and are likely to cosediment. We have used variable conditions during homogenization to alter the sedimentation of plasma membranes, allowing them to be separated from endosomes

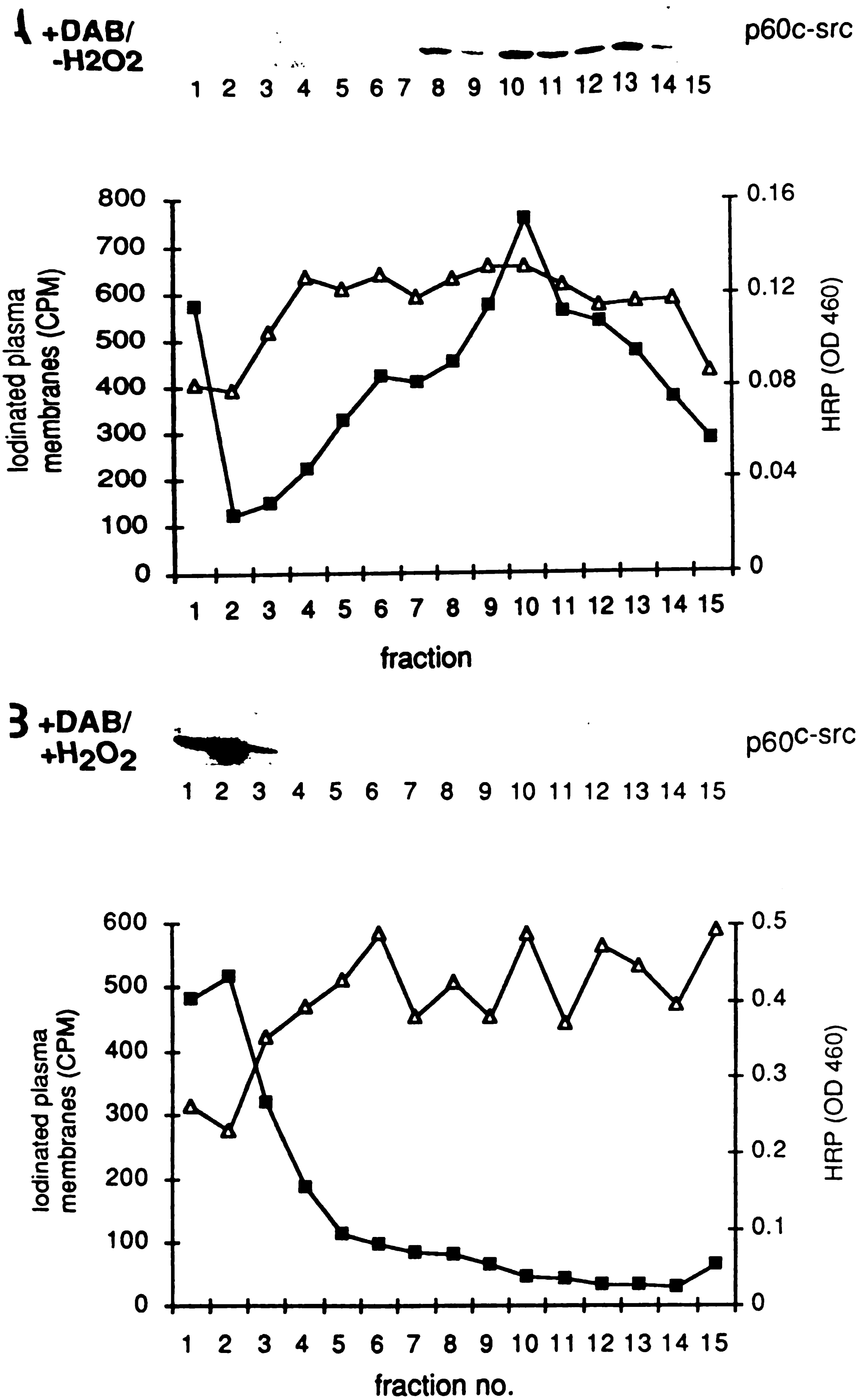

Figure 8. DAB-induced density shift of $p60^{c\text{-}src}$ from total cellular membranes. RTCS fibroblasts were incubated with HRP and total cellular membranes were isolated. Membranes were treated with DAB alone (*A*), or DAB/H_2O_2 (*B*) and then run on percoll gradients. Fractions were collected as in Fig. 6. $P60^{c\text{-}src}$ was detected by immunoprecipitation and immunoblotting with mAb 327. Fractions were also analyzed for HRP activity to detect endosomal membranes (■) and a gamma counter was used to detect the presence of iodinated plasma membrane proteins (△). Note that plasma membranes do not behave as in Fig. 6 due to the absence of $CaCl_2$ (see legend to Fig. 6).

see Materials and Methods). In addition, the specific shift n density of HRP-containing membranes convincingly separated endosomes from plasma membranes. Based on results from these fractionation experiments we have concluded that no detectable $p60^{c\text{-}src}$ is associated with plasma membranes. It remains possible that a very small proportion of $p60^{c\text{-}src}$ is associated with plasma membranes but is undetectable under our conditions.

Our results suggest that $p60^{c-src}$ is associated with the microtubule cytoskeleton via endocytic vesicles, in contrast to previous localization and biochemical studies suggesting an association of $p60^{v-src}$ with the actin cytoskeleton (Hamaguchi and Hanafusa, 1987; Henderson and Rohrschneider, 1987; Resh and Erickson, 1985; Rohrschneider, 1979, 1980). Analysis of optical sections near the bottom of cells over-expressing chicken $p60^{c-src}$ showed only punctate, microtubule-associated staining and no localization to adhesion plaques. We found that $p60^{c-src}$ co-localizes with a number of microtubule-related structures, including microtubule bundles at points of cell–cell contact, the microtubule organizing center, and a region associated with the spindle pole during mitosis (Figs. 1 and 4). In all cases this staining is dependent on intact microtubules. Ample evidence has demonstrated that endocytic membranes can be transported along microtubules (DeBrabander et al., 1988; Goergi et al., 1990; Matteoni and Kreis, 1987). It is therefore likely that co-localization of $p60^{c-src}$ with various microtubule structures reflects the transport of endosomal membranes along cellular microtubules. It is even conceivable that $p60^{c-src}$ may regulate microtubules or microtubule-associated motors involved in endosomal membrane transport.

The microtubule-dependent alteration of $p60^{c-src}$ staining induced by BFA treatment provides additional evidence for $p60^{c-src}$ transport along microtubules. BFA is known to cause microtubule-dependent retrograde transport of Golgi elements into the ER (Lippincott-Schwartz et al., 1989, 1990). We have shown that treatment of cells with BFA also affects the transport of endosomal membranes containing $p60^{c-src}$. BFA treatment results in the clustering of $p60^{c-src}$-containing membranes at the centrosome, which is distinct from the normally diffuse staining of $p60^{c-src}$ at the MTOC (Fig. 3). Similar findings have been reported for the effect of BFA on a wide range of endocytic membranes in both rat and canine cells (Lippincott-Schwartz et al., 1991; Wood et al., 1991). While the mechanism of action of BFA remains unclear, the behavior of $p60^{c-src}$ and CI-MPR after BFA treatment emphasizes the similar nature of the membrane compartment occupied by these proteins.

Studies of cells in early stages of mitosis show that $p60^{c-src}$ and CI-MPR are found at the dividing centrosomes (Fig. 4). The presence of both CI-MPR and $p60^{c-src}$ at the spindle poles during mitosis further suggests that both of these proteins reside in a similar membrane compartment that is distinct from *cis/medial*-Golgi membranes, which are scattered throughout the cell during mitosis (K. Kaplan, unpublished observations) (Lucocq and Warren, 1987; Moskalewski and Thyberg, 1990). Since $p60^{c-src}$ is known to be activated during mitosis and phosphorylated by $p34^{cdc2}$ (Chackalaparampil and Shalloway, 1988; Morgan et al., 1989), it is possible that $p60^{c-src}$ is mediating mitotic effects of $p34^{cdc2}$ at the pericentriolar region of the cell. Several processes associated with endosomal membranes are known to be regulated during mitosis. For example, it has been shown in vitro that early endosomal fusion events are inhibited by addition of active *Xenopus* $p34^{cdc2}$ (Tuomikoski et al., 1989; Woodman et al., 1992).

Work with secretory cells suggests that $p60^{c-src}$ may be involved in regulating the function of specialized secretory vesicles. In addition to being enriched in secretory granules of chromaffin cells, $p60^{c-src}$ is associated with a 38-kD protein that may be important in the function of these secretory organelles (Grandori and Hanafusa, 1988). These compartments may be analogous to the endosomal compartment in fibroblasts. The association of $p60^{c-src}$ with endosomally derived synaptic vesicles in PC-12 cells is consistent with this proposal (Johnston et al., 1989; Linstedt et al., 1992).

Endosomal membranes are dynamic structures involved in the trafficking of proteins throughout the cell and are known to be regulated at the level of both transport and fusion. In this regard it may be relevant to consider the phenotype of mice that are genetically null for the c-src gene through homologous recombination (Soriano et al., 1991). The defect in bone modeling (osteopetrosis) exhibited by these mice arises ultimately from an inability to dissolve bone tissue during development. The osteoclasts responsible for dissolving bone tissue are known to be highly specialized secretory cells that secrete lysosomal enzymes. In the absence of $p60^{c-src}$ these cells may be defective in regulating the trafficking of lysosomal proteins.

We would like to thank David Agard and John Sedat for the use of their microscopy facilities, Peter Lobel and William Brown for antisera against the CI-MPR, Josh Kaplan for the RTCS cell line, and Phil Soriano for mouse embryo fibroblasts from transgenic mice. We are grateful to members of the Src group and Frances Brodsky for helpful discussions and to Inke Näthke and John Young for valuable comments on the manuscript.

This work was supported by grants to D. O. Morgan and H. E. Varmus from the National Institutes of Health, a Searle Scholars Award from the Chicago Community Trust (D. O. Morgan) and a Basil O'Connor Starter Scholar Award from the March of Dimes Birth Defects Foundation (D. O. Morgan). H. E. Varmus is an American Cancer Society Research Professor.

Received for publication 31 January 1992 and in revised form 4 April 1992.

References

Agard, D. A., P. Hiraoka, P. Shaw, and J. W. Sedat. 1989. Fluorescence microscopy in three dimensions. *Methods Cell Biol.* 30:353–377.

Aoki, D., H. E. Apperti, D. Johnson, S. S. Wong, and M. N. Fukada. 1990. Analysis of the substrate binding sites of human galactosyl transferase by protein engineering. *EMBO (Eur. Mol. Biol. Organ.) J.* 9:3171–3178.

Bole, D. G., L. M. Hendershot, and J. F. Kearney. 1989. Post-translational association of immunoglobulin heavy chain binding protein with nascent heavy chains in nonsecreting hybridomas. *J. Cell Biol.* 102:1558–1566.

Buss, J. E., and B. M. Sefton. 1985. Myristic acid, a rare fatty acid, is the lipid attached to the transforming protein of Rous sarcoma virus and its cellular homolog. *J. Virol.* 53:7–12.

Buss, J. E., M. P. Kamps, K. Gould, and B. M. Sefton. 1986. The absence of myristic acid decreases membrane binding of $p60^{src}$ but does not affect tyrosine protein kinase activity. *J. Virol.* 58:468–474.

Chackalaparampil, I., and D. Shalloway. 1988. Altered phosphorylation and activation of $pp60^{c-src}$ during fibroblast mitosis. *Cell.* 52:801–810.

Chege, W. N., and S. R. Pfeffer. 1990. Compartmentation of the golgi complex: brefeldin-A distinguishes trans-golgi cisternae from the trans-golgi network. *J. Cell Biol.* 111:893–899.

Cooper, J. A. 1989. The src-family of protein-tryosine kinases. *In* Peptides and Protein Phosphorylation. B. Kemp and P. F. Alewood, editors. CRC Press, Boca Raton, FL. 85–113.

Cotton, P. C., and J. S. Brugge. 1983. Neural tissues express high levels of the cellular src gene product $pp60^{c-src}$. *Mol. Cell. Biol.* 3:1157–1162.

Courtneidge, S. A., A. D. Levinson, and J. M. Bishop. 1980. The protein encoded by the transforming gene of avian sarcoma virus ($pp60^{src}$) and a homologous protein in normal cells ($pp60^{proto-src}$) are associated with the plasma membrane. *Proc. Natl. Acad. Sci. USA.* 77:3783–3787.

Courtoy, P. J., J. Quintart, and P. Baudhuin. 1984. Shift of equilibrium density induced by 3,3'-diaminobenzidine cytochemistry: a new procedure for the analysis and purification of peroxidase-containing organelles. *J. Cell Biol.* 98:870–876.

David-Pfeuty, T., and Y. Nouvian-Dooghe. 1990. Immunolocalization of the cellular src protein in interphase and NIH c-src overexpressor cells. *J. Cell Biol.* 111:3097–3116.

DeBrabander, M., R. Nuydens, H. Geerts, and C. R. Hopkins. 1988. Dynamic behavior of the transferrin receptor followed in living epidermoid carcinoma

(A431) cells with nonovid microscopy. *Cell Motil. Cytoskeleton.* 9:30–47.

Goergi, A., C. Mottola-Harthshorn, A. Warner, B. Fields, and L. B. Chen. 1990. Detection of individual fluorescently labeled reovirions in living cells. *Proc. Natl. Acad. Sci. USA.* 87:6579–6583.

Golden, A., S. P. Nemeth, and J. S. Brugge. 1986. Blood platelets express high levels of pp60^{c-src} specific tyrosine kinase activity. *Proc. Natl. Acad. Sci. USA.* 83:852–856.

Grandori, C., and H. Hanafusa. 1988. P60^{c-src} is complexed with a cellular protein in subcellular compartments involved in exocytosis. *J. Cell Biol.* 107:2125–2135.

Hamaguchi, M., and H. Hanafusa. 1987. Association of p60^{src} with Triton X-100-resistant cellular structure correlates with morphological transformation. *Proc. Natl. Acad. Sci. USA.* 84:2312–2316.

Harlow, E., and D. Lane. 1988. Antibodies: A Laboratory Manual. Cold Spring Harbor Laboratory, Cold Spring Harbor, NY. 726 pp.

Henderson, D., and L. Rohrschneider. 1987. Cytoskeletal association of pp60^{src}, the transforming protein of the Rous sarcoma virus. *Exp. Cell Res.* 168:411–421.

Hiraoka, Y., D. A. Agard, and J. W. Sedat. 1990. Temporal and spatial coordination of chromosome movement, spindle formation, and nuclear envelope breakdown during prometaphase in *Drosophila melanogaster* embryos. *J. Cell Biol.* 111:2815–2828.

Hiraoka, Y., J. R. Swedlow, M. R. Paddy, D. A. Agard, and J. W. Sedat. 1991. Three-dimensional multiple wavelength microscopy for the structural analysis of biological phenomena. *Sem. Cell Biol.* 2:153–165.

Johnston, P. A., P. L. Cameron, H. Stukenbrok, R. Jahn, P. De Camilli, and T. C. Sudhof. 1989. Synaptophysin is targeted to similar microvesicles in CHO and PC12 cells. *EMBO (Eur. Mol. Biol. Organ.) J.* 8:2863–2872.

Kamps, M. P., J. E. Buss, and B. M. Sefton. 1986. Rous sarcoma virus transforming protein lacking myristic acid phosphorylates known polypeptide substrates without inducing transformation. *Cell.* 45:105–112.

Kaplan, J. M., H. E. Varmus, and J. M. Bishop. 1990. The src protein contains multiple domains for specific attachment to membranes. *Mol. Cell Biol.* 10:1000–1009.

Lewis, V., S. A. Green, M. Marsh, P. Vihko, A. Helenius, and I. Mellman. 1985. Glycoproteins of the lysosomal membrane. *J. Cell Biol.* 100:1839–1847.

Linstedt, L. D., M. L. Vetter, J. M. Bishop, and R. B. Kelly. 1992. Specific association of the proto-oncogene product pp60^{c-src} with intracellular organelle, the PC12 synaptic vesicle. *J. Cell Biol.* 117:1077–1084.

Lippincott-Schwartz, J., L. C. Yuan, J. S. Bonifacino, and R. D. Klausner. 1989. Rapid redistribution of golgi proteins into the ER in cells treated with Brefeldin A: evidence for membrane cycling from golgi to ER. *Cell.* 56: 801–813.

Lippincott-Schwartz, J., J. G. Donaldson, A. Schweizer, E. G. Berger, H.-P. Hauri, L. C. Yuan, and R. D. Klausner. 1990. Microtubule-dependent retrograde transport of proteins into the ER in the presence of Brefeldin A suggests an ER recycling pathway. *Cell.* 60:821–836.

Lippincott-Schwartz, J., L. Yuan, C. Tipper, M. Amherdt, L. Orci, and R. D. Klausner. 1991. Brefeldin A's effect on endosomes, lysosomes and the TGN: a general mechanism for regulating organelle structure and membrane traffic. *Cell.* 67:601–616.

Lipsich, L. A., A. J. Lewis, and J. S. Brugge. 1983. Isolation of monoclonal antibodies that recognize the transforming proteins of avian sarcoma virus. *J. Virol.* 48:352–360.

Lucocq, J. M., and G. Warren. 1987. Fragmentation and partitioning of the Golgi apparatus during mitosis in Hela cells. *EMBO (Eur. Mol. Biol. Organ.) J.* 6:3239–3246.

Matteoni, R., and T. E. Kreis. 1987. Translocation and clustering of endosomes and lysosomes depends on microtubules. *J. Cell Biol.* 105:1253–1265.

Messner, D. J., G. Griffiths, and S. Kornfeld. 1989. Isolation and characterization of membranes from bovine liver which are highly enriched in mannose 6-phosphate receptors. *J. Cell Biol.* 108:2149–2162.

Morgan, D. O., J. M. Kaplan, J. M. Bishop, and H. E. Varmus. 1989. Mitosis-specific phosphorylation of p60^{c-src} by p34^{cdc2}-associated protein kinase. *Cell.* 57:775–786.

Morgan, D. O., J. M. Kaplan, J. M. Bishop, and H. E. Varmus. 1991. Production of p60^{c-src} by baculovirus expression and immuno-affinity purification. *Methods Enzymol.* 200:645–660.

Moskalewski, S., and J. Thyberg. 1990. Disorganization and reorganization of the golgi complex and the lysosomal system in association with mitosis. *J. Submicrosc. Cytol. Pathol.* 22:159–171.

Paddy, M. R., A. S. Belmont, H. Saumweber, D. A. Agard, and J. W. Sedat. 1990. Interphase nuclear envelope lamins form a discontinuous network that interacts with only a fraction of the chromatin in the nuclear periphery. *Cell.* 62:89–106.

Poole, R. R. J., K. M. Maurey, and B. Storrie. 1983. Characterization of pinocytic vesicles from CHO cells: resolution of pinosomes from lysosomes by analytical centrifugation. *Cell Biol. Int. Rep.* 7:361–367.

Resh, M. D., and R. L. Erikson. 1985. Highly specific antibody to Rous sarcoma virus src gene product recognizes a novel population of pp60^{v-src} and pp60^{c-src} molecules. *J. Cell Biol.* 100:409–417.

Resh, M. D., and H. Ling. 1990. Identification of a 32K plasma membrane protein that binds to the myristylated amino-terminal sequence of p60^{v-src}. *Nature (Lond.).* 346:84–86.

Rohrschneider, L. R. 1979. Immunofluorescence on avian sarcoma virus-transformed cells: localization of the src gene product. *Cell.* 16:11–24.

Rohrschneider, L. R. 1980. Adhesion plaques of Rous sarcoma virus-transformed cells contain the src gene product. *Proc. Natl. Acad. Sci. USA.* 77: 3514–3518.

Shenoy, S., J. K. Choi, S. Bagrodia, T. D. Copeland, J. L. Maller, and D. Shalloway. 1989. Purified maturation promoting factor phosphorylates pp60^{c-src} at the sites phosphorylated during fibroblast mitosis. *Cell.* 57: 761–772.

Soriano, P., C. Montgomery, R. Geske, and A. Bradley. 1991. Targeted disruption of the c-src proto-oncogene leads to osteopetrosis in mice. *Cell.* 64: 693–702.

Stoorvogel, W., H. J. Geuze, J. M. Griffith, A. L. Schwartz, and G. J. Strous. 1989. Relations between the intracellular pathways of the receptors for transferrin, asialoglycoprotein, and mannose 6-phosphate in human hepatoma cells. *J. Cell Biol.* 108:2137–2148.

Stoorvogel, W., G. J. Strous, H. J. Geuze, V. Oorschot, and A. L. Schwartz. 1991. Late endosomes derive from early endosomes by maturation. *Cell.* 65: 417–427.

Thompson, J. A., A. L. Lau, and D. D. Cunningham. 1987. Selective radiolabeling of cell surface proteins to a high specific activity. *Biochemistry.* 26: 743–750.

Tuomikoski, T., M.-A. Felix, M. Doree, and J. Gruenberg. 1989. Inhibition of endocytic vesicle fusion *in vitro* by the cell cycle control protein kinase cdc2. *Nature (Lond.).* 342:942–945.

Willingham, M. C., G. Jay, and I. Pastan. 1979. Localization of the ASV src gene product to the plasma membrane of transformed cells by electron microscopic immunocytochemistry. *Cell.* 18:125–134.

Wood, S. A., J. E. Park, and W. J. Brown. 1991. Brefeldin A causes a microtubule-mediated fusion of the trans-golgi network and early endosomes. *Cell.* 67:591–600.

Woodman, P. G., D. I. Mundy, P. Cohen, and G. Warren. 1992. Cell-free fusion of endocytic vesicles is regulated by phosphorylation. *J. Cell Biol.* 116: 331–338.

Appendix 4: Defining interactions and distributions of cadherin and catenin complexes in polarized epithelial cells

Introduction

This appendix consists of a manuscript submitted for publication as Näthke, I. S., Hinck, L., Swedlow, J. R., Papkoff, J. Nelson, W. J. (1994) Defining interactions and distributions of cadherin and catenin complexes in polarized epithelial cells. The paper describes the biochemical fractionation and microscopic localization of E-cadherin, α–catenin, β–catenin, and plakoglobin in MDCK epithelial cells before and after Triton X-100 extraction. J. R. Swedlow's contribution to this work was the use of three-dimensional wide-field fluorescence microscopy to show striking differences in the localization of the E-cadherin with the two catenins and plakoglobin. E-cadherin and both catenins localize to the lateral membrane of polarized epithelial cells and concentrate in the apical junctional complex. Only the figures containing microscopic data are included in this Appendix.

ABSTRACT

The cadherin/catenin complex plays important roles in cell adhesion, signal transduction, and the initiation and maintenance of structural and functional organization of cells in tissues. In the preceding study, we showed that the assembly of the cadherin/catenin complex is temporally regulated, and that novel combinations of catenin and cadherin complexes are formed in both Triton X-100 soluble and insoluble fractions; we proposed a model in which pools of catenins are important in regulating assembly of E-cadherin/catenin and catenin complexes. Here, we sought to determine the spatial distributions of E-cadherin, α–catenin, β–catenin and plakoglobin and whether different complexes of these proteins accumulate at steady state in polarized MDCK cells. Protein distributions were visualized by wide field, optical sectioning, double immunofluorescence microscopy, followed by reconstruction of three dimensional images. In cells that were extracted with Triton X-100 and then fixed (Triton X-100 insoluble fraction), more E-cadherin is concentrated at the apical junction relative to other areas of the lateral membrane. Alpha-catenin and β–catenin co-localize with E-cadherin at the apical junctional complex. There is some overlap in the distribution of these proteins in the lateral membrane, but there are also areas where the distributions are distinct. Plakoglobin is excluded from the apical junctional complex, and its distribution in the lateral membrane is different from that of E-cadherin. Cells were also fixed and then permeabilized to reveal the total cellular pool of each protein (Triton X-100 soluble and insoluble fractions). This analysis showed lateral membrane localization of α–catenin, β–catenin and plakoglobin, and also revealed that they are distributed throughout the cell. Chemical cross-linking of proteins and analysis with specific antibodies confirmed the presence at steady state of E-cadherin/catenin complexes containing either β–catenin or plakoglobin, and catenin complexes devoid of E-cadherin. Complexes containing E-cadherin/β–catenin and E-cadherin/α–catenin are present in both the Triton

X-100 soluble and insoluble fractions, but E-cadherin/plakoglobin complexes are not detected in the Triton X-100 insoluble fraction. Taken together these results show that different complexes of cadherin and catenins accumulate in fully polarized epithelial cells and that they distribute to different sites. We suggest that cadherin/catenin, and catenin complexes at different sites have specialized roles in establishing and maintaining the structural and functional organization of polarized epithelial cells.

INTRODUCTION

Cadherins are a multifunctional family of transmembrane glycoproteins important in the morphogenesis of multicellular organisms (Takeichi, 1991, Kemler, 1992). During recognition and adhesion between cells, cadherins regulate homophilic, Ca^{++}-dependent interactions in epithelial cells. This initiates a cascade of events that leads to the structural and functional reorganization of cells, including: formation of junctional complexes (tight junction, *zonula adherens*, desmosomes); organization of the actin cytoskeleton at the apical junctional complex; assembly of the membrane cytoskeleton; and development of membrane domains (Rodriguez-Boulan and Nelson, 1989, Nelson, 1992).

Recent studies have identified three cytoplasmic proteins, α–catenin, β–catenin, and plakoglobin, that bind non-covalently to the cytoplasmic domain of cadherins (Nagafuchi and Takeichi, 1989, Ozawa *et al.*, 1989). Formation of the cadherin/catenin complex is required for cadherin functions in cell-cell adhesion and cellular reorganization (Nagafuchi and Takeichi, 1988, Ozawa *et al.*, 1990). Alpha-catenin has sequence similarities to vinculin and is a candidate for linking the cadherin/catenin complex to the cytoskeleton (Herrenknecht *et al.*, 1991, Nagafuchi *et al.*, 1991). Beta-catenin and plakoglobin are mammalian homologs of armadillo, a *Drosophila* protein involved in a signal transduction pathway leading to specification of segmental identity in the embryo (Riggleman *et al.*, 1990, McCrea *et al.*, 1991, Butz *et al.*, 1992). Plakoglobin was originally identified as a component of desmosomes (Cowin *et al.*, 1986).

Little is known about how interactions between cadherins at the cell surface of neighboring cells during cell recognition and adhesion leads to the reorganization of membrane and cytoskeletal proteins. Evidence has accumulated that other cytoplasmic proteins, including actin, fodrin, and src and yes kinases also interact with the cadherin/catenin complex (Tsukita *et al.*, 1993). These interactions may link the cadherin/catenin complex with the cytoskeleton and intracellular signaling pathways. In addition, recent studies have shown that cadherin/catenin interactions are modulated by the proto-oncogene Wnt-1 (Bradley *et al.*, 1993, Hinck *et al.*, 1994b), the mammalian homologue of the *Drosophila wingless* gene, which is part of the armadillo transduction pathway (for review see Nusse and Varmus, 1992).

From these observations, two minimal models of cadherin/catenin function can be postulated: a single cadherin/catenin complex that initiates a signaling pathway resulting in a cascade of independent intracellular events; alternatively, multiple cadherin/catenin complexes that have different distributions and regulate each of these events individually. We can discriminate between these models by analyzing the composition of cadherin/catenin complexes and their distributions in polarized epithelial cells.

In the preceding paper, we showed that assembly of newly synthesized E-cadherin with catenins in MDCK epithelial cells is temporally regulated (Hinck *et al.*, 1994a). Complexes of cadherin and catenins are present in the Triton X-100 (TX-100) insoluble fraction of proteins. There also appear to be pools of α–catenin, β–catenin and plakoglobin that are distinct from the cadherin/catenin complex. In this paper, we have examined the accumulation of these complexes, and tested whether they have different spatial distributions. We used wide field optical sectioning fluorescence microscopy in combination with three dimensional image reconstruction to localize complexes, and chemical cross-linking to study the composition of the cadherin/catenin complexes. Our results show that there are multiple cadherin/catenin complexes, and cadherin independent pools of catenin complexes which have different distributions at the lateral membrane and throughout the cell, supporting the second model of cadherin/catenin function (see above). We suggest that the distributions of different complexes are related to specific functions in cell adhesion, signal transduction, and cellular reorganization.

MATERIALS AND METHODS

General methods and reagents

Cell culture, immunoprecipitations and cross-linking were performed as described in the preceding paper (Hinck *et al.*, 1994a). A monoclonal antibody against the extracellular domain of E-cadherin from MDCK cells (3G8) was the generous gift of Dr. Warren Gallin (University of Alberta, Canada). Two different polyclonal antisera against the cytoplasmic portion of P-cadherin (Pcad 1 and 2) were provided by Dr. Dietmar Vestweber, Max Planck Institut für Immunbiologie, Freiburg. Specific antibodies against each of the catenins (Hinck *et al.*, 1994) and the cytoplasmic domain of E-cadherin (Marrs *et al.*, 1993) have been described previously.

Affinity purification of catenin antibodies

The cognate peptides for the α–catenin, β–catenin and plakoglobin antibodies were coupled to SulfoLink® coupling gel (Pierce) according to the manufacturer's instructions. Antisera were incubated with the immobilized peptides. After washing the resins extensively with PBS, affinity pure antibodies were eluted with 0.2 M glycine, pH 2.5. The pH of antibody containing fractions was adjusted to 7.5 with 1 M Tris, pH 8.0.

Immunoblotting

Immunoblotting was performed as described in the preceding paper (Hinck *et al.*, 1994a). The antibodies were used at the following dilutions: α–catenin, 1:100; β–catenin, plakoglobin, and E-cadherin, 1:500; 3G8 (tissue culture supernatant), 1:100, P-cadherin 1 and 2, 1:200. Binding of the mouse monoclonal antibody 3G8 was detected by first incubating the membranes with a rabbit-anti mouse antiserum (DAKO Corp.) at a dilution of 1:100 for 1 hour prior to incubation with ^{125}I-protein-A.

Immunofluorescence microscopy

Confluent monolayers of MDCK cells were maintained on collagen–coated Transwell polycarbonate filters (Costar) for 8 days. Cells were extracted with CSK buffer (50mM NaCl, 300 mM sucrose, 10mM Pipes pH 6.8, 3mM $MgCl_2$, 0.5% Triton X-100, 10 μg/ml leupeptin, 1 mM Pefabloc (Boehringer Mannheim)) for 15 minutes at 4°C and then fixed with 3.75% formaldehyde in PBS for 30 minutes. Alternatively, cells were fixed with 3.75% formaldehyde and then permeabilized with CSK buffer for 15 minutes at 4°C. Cells were blocked in PBS, 0.2%BSA, 1% normal goat serum for one hour and then incubated with a monoclonal antibody against E-cadherin (3G8, 1:100), and affinity purified antibodies against α–catenin (1:200), β–catenin (1:500), or plakoglobin (1:750) in PBS, 0.2%BSA. After washing three times with PBS, 0.2%BSA, binding of the primary antibodies was detected with rhodamine coupled goat anti-mouse (E-cadherin) and FITC coupled goat anti-rabbit antibodies (catenin) (Boehringer Mannheim) diluted 1:100 in PBS, 0.2% BSA. When cells were fixed in -20°C methanol and stained as described above, the staining was similar to the staining of cells that were extracted with CSK buffer prior to fixation with formaldehyde (data not shown).

Three-dimensional images of immunostained epithelial monolayers were recorded using a Peltier-cooled charge-coupled device (CCD) camera (Photometrics Ltd., Tucson, AZ) with a 1,340 x 1,037 pixel CCD chip (Kodak-Videk; Eastman Kodak Co., Rochester, NY). The camera was mounted on a fluorescence microscope workstation equipped with bandpass excitation and emission filters mounted on motorized wheels and a multi-wavelength dichroic mirror (Chroma, Inc., Brattleboro, VT). All aspects of data collection were controlled by a SGI 4D-35 computer (Silicon Graphics Corp., Mountain View, CA). The design and specifications of the system have been described previously (Hiraoka *et al.*, 1991). Optical sections (512x512 pixels; effective pixel size = 0.0744 µm x 0.0744 µm) were recorded with a Plan ApoChromat 60x/NA1.4 (Olympus, Inc.) at 0.2 µm intervals by changing the microscope focus with a computer-controlled Nanomover motor (Melles Griot, Inc., Rochester, NY). Dual wavelength three-dimensional images were recorded in a single focal series by alternating the appropriate excitation and emission filters for fluorescein isothiocyanate and tetramethylrhodamine at each focal plane. To correct for temporal fluctuations in illumination intensity due to power instabilities in the Hg-arc lamp, the intensity of the lamp was directly measured using an avalanche photodiode-based photon counting module (EG & G, Vaudreuil, Quebec). The out-of-focus information in these images was then removed using iterative, constrained, three-dimensional deconvolution, a technique that deblurs an image by moving out-of-focus intensity back to its originating point based on an empirical measure of the "point spread" function, which is the blurring of an image caused by the limited resolution of the objective lens (Agard *et al.*, 1989, Hiraoka *et al.*, 1991). The volume rendered images of the three dimensional data were calculated as previously described (Levoy, 1991).

RESULTS

Three dimensional distributions of E-cadherin and catenins in polarized monolayers of MDCK cells

The spatial distributions of E-cadherin, α–catenin, β–catenin, and plakoglobin in MDCK cells were analyzed by immunofluorescence using a wide field optical sectioning microscope (Agard *et al.*, 1989, Hiraoka *et al.*, 1991). To ensure that the cellular junctions had formed completely and cells were fully polarized, MDCK cells were grown in confluent monolayers on Transwell filters for 8 days. We examined the distributions of both the TX-100 soluble and insoluble fractions in order to correlate these studies with those in the preceding paper (Hinck *et al.*, 1994a). The TX-100 insoluble fraction was examined by extraction of cells followed by fixation (Figs. 1-3: "Extracted"); the combination of TX-100 soluble and insoluble fractions were examined in cells that were first fixed and then permeabilized (Figs 1-3: "Total"). Cells were stained with both a mouse monoclonal antibody against E-cadherin, and affinity purified rabbit polyclonal antibodies specific for either α–catenin (Fig. 1), β–catenin (Fig. 2) or plakoglobin (Fig. 3). Optical sections were recorded at 0.2 μm intervals from at least 2 μm below to 2 μm above the cell layer (total of 15-18 μm). Out of focus information was removed by a deconvolution algorithm and the resulting images were displayed using a 3-D volume rendering algorithm (Agard *et al.*, 1989, Hiraoka *et al.*, 1991, Levoy, 1991). Figures 1, 2, and 3 display three dimensional images tilted by 10-15 degrees to visualize the lateral membranes. The images are oriented with the apical membrane at the top and the basal membrane at the bottom. Extracted cells that were stained with antibodies to E-cadherin (on the left) and either of the three catenins (on the right) are shown in the top panels, and unextracted ("Total") cells are shown in the bottom panels.

The degree of co-localization of E-cadherin and each of the three catenins is shown by the overlay of optical sections from cells stained with antibodies against E-cadherin and either α–catenin (top), β–catenin (middle) or plakoglobin (bottom) (Fig. 4). To illustrate the similarities and differences in the distributions of these proteins in extracted cells, individual optical sections are shown from the middle of the cell (left panels; 6-6.5 μm above the substratum), and at the apex of the lateral membrane (8.4-10 μm above the substratum), where the tight junction and the *zonula adherens* are located (apical junctional complex) (right panels). E-cadherin staining is shown in purple, catenin staining in green, and areas of overlapping staining are indicated in white.

In unextracted cells, E-cadherin is localized to the lateral membrane, with little or no staining detectable at the basal or apical membranes. When three dimensional images (Fig. 1: "Total") and individual optical sections are examined (not shown), E-cadherin staining appears closely punctate at the lateral membrane. In extracted cells, both three dimensional images (Fig. 1: "Extracted") and individual optical sections (Fig. 4) show an openly punctate staining at the lateral membrane. At the apical junctional complex, E-cadherin staining is almost continuous and there appears to be an enrichment of E-cadherin at this area relative to other areas of the lateral membrane. The difference in E-cadherin staining between unextracted and extracted cells indicates that a higher proportion of E-cadherin is insoluble in TX-100 in the apical junctional complex, than in the lateral membrane below the apical junctional complex.

In unextracted cells, α–catenin staining appears punctate throughout the cell and in the plane of the lateral membrane (Fig. 1: "Total"). In extracted cells, α–catenin staining is restricted to the lateral membrane in a punctate pattern (Fig. 1: "Extracted"). Alpha-catenin also appears to be enriched at the level of the apical junctional complex, similar to E-cadherin (Fig. 1: "Extracted"). In the area of the membrane below the apical junctional complex, some of the staining for α–catenin is coincident with that of E-cadherin (Fig. 4). However, other regions of the lateral membrane exhibit staining for either α–catenin or E-cadherin, indicating that in these cases both proteins are independently associated with the membrane (Fig. 4).

In unextracted cells, β–catenin staining is punctate throughout the cell and in the plane of the lateral membrane (Fig. 2: "Total"). In extracted cells, β–catenin staining is restricted to the lateral membrane in a punctate pattern. Some enrichment of β–catenin is also observed at the apical junctional complex, but this enrichment appears to be less than that of E-cadherin and α–catenin (Fig. 2: "Extracted"). As in the case of α–catenin, some areas of the lateral membrane exhibit patterns of β–catenin and E-cadherin staining that are similar, but staining for β–catenin that is different from E-cadherin staining is predominant (Fig. 4).

In unextracted cells, plakoglobin staining is punctate throughout the cell (Fig. 3: "Total"). In extracted cells, plakoglobin staining appears in a punctate pattern restricted to the lateral membranes. The sizes of the individual spots of plakoglobin staining are larger and less uniform than those of E-cadherin, α–catenin and β–catenin (Fig. 3: "Extracted"). The punctate staining patterns of E-cadherin and plakoglobin do not overlap, and there appears to be no enrichment of plakoglobin at the apical junctional complex of extracted cells (Fig. 4).

In summary, we have found that in many cases, and particularly at the apical junctional complex, the spatial distributions of E-cadherin, α–catenin, and β–catenin in the lateral membrane are similar. However, our results show unequivocally that both α–catenin and β–catenin are present in regions of the lateral membrane that do not appear to contain E-cadherin, and that plakoglobin does not co-localize with E-cadherin in the lateral membrane of TX-100 extracted cells. Furthermore, α–catenin, β–catenin and plakoglobin are present in a TX-100 soluble fraction that is distributed throughout the cell. These results, in combination with those presented in the preceding paper (Hinck *et al.*, 1994a), strongly indicate that there are cadherin independent pools of catenins. In the next series of experiments we have sought to demonstrate biochemically the accumulation at steady state of cadherin/catenin complexes in the TX-100 insoluble fraction, and of cadherin independent pools of catenins.

Protein composition of cadherin/catenin complexes and cadherin independent catenin complexes

The protein composition of cadherin/catenin complexes was examined in polarized MDCK cells with established cell contacts. We used the bifunctional cross-linking reagent, dithiobis(succinimidylpropionate) (DSP), to preserve protein complexes in both the TX-100 soluble and insoluble fractions. MDCK cells were grown in confluent monolayers on collagen–coated Transwell filters for 8 days, like those cells that were analyzed by high resolution immunofluorescence microscopy. Cells were incubated in the presence of DSP, and extracted sequentially with buffers containing TX-100 and SDS to generate TX-100 soluble (S) and insoluble (P) fractions, as described in the preceding paper (Hinck *et al.*, 1994a). Equal aliquots of each fraction were immunoprecipitated with E-cadherin (E-cad), α–catenin (α–cat), β–catenin (β–cat) or plakoglobin (PG) antibodies. Immunoprecipitates were reduced to reverse the cross-linking, separated by SDS-PAGE, transferred to Immobilon-P membranes and probed with each of the four antibodies.

Figure 5A reveals that >85% of E-cadherin is located in the TX-100 insoluble fraction; relatively little E-cadherin is detected in the E-cadherin immunoprecipitate from the TX-100 soluble fraction. E-cadherin is detected in the α–catenin, β–catenin, and plakoglobin immunoprecipitates from the TX-100 soluble fraction. Little E-cadherin is detected in either the α–catenin and β–catenin of the TX-100 insoluble fraction. No E-cadherin is detected in plakoglobin immunoprecipitates of the TX-100 insoluble fraction.

Figure 5B shows that α–catenin is present in the E-cadherin immunoprecipitate from both the TX-100 soluble and insoluble fractions, but relatively more (85%) is detected in the TX-100 soluble fraction. Large amounts of α–catenin co-immunoprecipitate with β–catenin and plakoglobin from both the TX-100 soluble fraction. Alpha–catenin is also detected in the β–catenin and plakoglobin immunoprecipitates from the TX-100 insoluble fraction.

Figure 5C shows that the fraction of β–catenin that is associated with E-cadherin is predominantly distributed in the TX-100 soluble fraction (84%). However, 60% of the total β–catenin is present in the TX-100 insoluble fraction. Beta-catenin is detected in the α–catenin immunoprecipitate from the TX-100 soluble and insoluble fraction, although the amount is low. Little or no β–catenin is detected in the plakoglobin immunoprecipitate from either the TX-100 soluble or insoluble fractions. The absence of β–catenin from these immunoprecipitated complexes reflects the formation of mutually exclusive complexes containing either plakoglobin or β–catenin (PG IP) also shown by Hinck et al. (Hinck *et al.*, 1994a, Hinck *et al.*, 1994b).

Figure 5D shows that 70% of plakoglobin is present in the TX-100 insoluble pool. Little plakoglobin is detected in the E-cadherin and α–catenin immunoprecipitates from the TX-100 soluble fraction, and no plakoglobin is present in the β–catenin immunoprecipitations from the TX-100 soluble and insoluble fractions.

These biochemical studies confirm the existence of cadherin/catenin complexes in both the TX-100 soluble and insoluble fractions. However, the experiment described above, and those in the preceding paper (Hinck *et al.*, 1994a), provide only indirect evidence for the existence of catenin complexes that are independent of cadherin. In order to demonstrate this directly, we cleared cell extracts of E-cadherin and then examined the remaining proteins for complexes containing different combinations of catenins. MDCK cells were established in confluent monolayers on collagen–coated Transwell filters for 8 days. They were incubated with the reducible cross-linking reagent DSP and TX-100 soluble (S) and insoluble (P) fractions were prepared. Each fraction was sequentially immunoprecipitated six times with the anti-cadherin antibody. This E-cadherin antibody (E-cad) was raised against the cytoplasmic domain of E-cadherin and recognizes the cytoplasmic domain of many cadherins (Marrs *et al.*, 1993). To determine whether cadherin, and E-cadherin in particular, were quantitatively removed from these cell fractions, the depleted extracts were subjected to SDS-PAGE, transferred to Immobilon-P membranes, and probed with different cadherin antibodies: antibody to cadherin cytoplasmic domain (E-cad) (Marrs *et al.*, 1993); a monoclonal antibody that specifically binds to the extracellular domain of E-cadherin (3G8); and antibodies raised against the intracellular domain of P-cadherin (P-cad1 and 2) and which also crossreact with other cadherins (Dietmar Vestweber, personal communication).

The first immunoprecipitation removed >90% of cadherins from the TX-100 insoluble fraction (Fig. 6A); subsequent immunoprecipitations removed all of the remaining cadherins. A similar quantitative removal of cadherins from the TX-100 soluble fraction was performed. We did not detect any cadherins in the final cadherin immunoprecipitates from the TX-100 insoluble or soluble fractions (Fig. 6A). To ensure that the extracts were indeed cadherin-depleted, they were probed with the panel of cadherin antibodies described above. Neither E- nor P-cadherin were detected (Fig. 6B), demonstrating that the cell extracts were cleared of cadherins

To determine if cadherin-depleted extracts contained catenins they were probed with antibodies against α–catenin (α–cat), β–catenin (β–cat), or plakoglobin (PG) (Fig. 6B). All three proteins were detected in both the TX-100 soluble and insoluble protein fractions, indicating that pools of catenins exist independently of cadherin. To determine if these cadherin–independent catenins are associated with one another, we again performed immunoprecipitations followed by immunoblotting with different antibodies. Cadherin–depleted extracts were immunoprecipitated with antibodies against plakoglobin or β–catenin. These immunoprecipitates were probed with α–catenin antibodies (Fig. 6C). Plakoglobin and β–catenin antibodies co-immunoprecipitate α–catenin in similar amounts from the TX-100 soluble and insoluble fractions (Fig. 6C).

Since cross-linking reactions are not always quantitative, conclusions about the cadherin–independence of catenin complexes in the TX-100 insoluble fraction have to be drawn with caution. It is possible that cadherin–independent catenins detected in the TX-100 insoluble fraction were originally bound to a cadherin/catenin complex but were not covalently cross-linked to it so that they dissociated from the complex during the subsequent solubilization step. As a consequence, the amount of cadherin–independent catenins in the TX-100 insoluble fraction shown in Figure 6B may be higher than that originally present in the cell. However, we note that complexes of catenins are detected in the TX-100 insoluble fraction in this experiment (Fig. 6C), demonstrating that catenins were cross-linked to each other (immunoprecipitations from the TX-100 insoluble fraction of non-cross-linked cells using catenin antibodies only contain the catenin against which the antibody is directed (Hinck *et al.*, 1994a, Figs. 1 and 4). In addition, the microscopy analysis, taken together with the biochemical experiments shown in this and the preceding paper (Hinck *et al.*, 1994a), provide strong evidence for cadherin–independent pools of catenins in the TX-100 insoluble fraction. We conclude that there are catenin complexes independent of cadherin in the TX-100 soluble and insoluble fractions.

DISCUSSION

The cadherin/catenin complex is a key component in the initiation of cell-cell recognition and adhesion, and the elaboration of structural and functional organization in multicellular tissues and organs (Takeichi, 1991, Kemler, 1992). The complex transduces information from extracellular contacts made by cadherins, to the cytoskeleton and intracellular signaling pathways (Nelson, 1992, Tsukita *et al.*, 1993). We propose two minimal models of cadherin/catenin function: a single cadherin/catenin complex that initiates a signaling pathway resulting in a cascade of independent intracellular events; alternatively, multiple cadherin/catenin complexes that have different distributions and regulate each of these events individually. Based upon previous studies, the cadherin/catenin complex at steady state is considered to be of a single type containing E-cadherin, α–catenin, β–catenin and g-catenin (plakoglobin) (Takeichi, 1991, Kemler, 1992). This view is based on the protein complex co-immunoprecipitated with E-cadherin from cells extracted with TX-100. The composition of the cadherin/complex in the TX-100 insoluble fraction has not been investigated until now (Hinck *et al.*, 1994a). Previous studies also examined the distribution of E-cadherin in polarized epithelial cells where it was shown to be enriched at the apical junctional complex (Boller *et al.*, 1985). The distributions of α–catenin and β–catenin were not investigated. The availability of catenin specific antibodies has allowed us to analyze cadherin/catenin complexes independently of cadherin. High resolution microscopy using these antibodies provides a

detailed, comparative analysis of protein distributions. Our results demonstrate that there are multiple cadherin/catenin and catenin complexes that have different subcellular distributions.

Multiple cadherin/catenin complexes at steady state in MDCK cells

In MDCK cells, we detect cadherin/catenin complexes at steady state that contain E-cadherin and α–catenin, and either β–catenin or plakoglobin. This result demonstrates that there are mutually exclusive associations of β–catenin and plakoglobin with E-cadherin (see also Hinck *et al.*, 1994a, Fig. 1). Since β–catenin and plakoglobin share ~66% sequence identity (McCrea *et al.*, 1991), they may bind to the same site on E-cadherin. However, there are differences in the distribution of these complexes in cells. We found that the E-cadherin/β–catenin complex, but not the E-cadherin/plakoglobin complex, is present in the TX-100 insoluble fraction (Figs. 4 and 5). Since formation of stable cell-cell contacts correlates with TX-100 insolubility (McNeill *et al.*, 1993), we suggest that E-cadherin/plakoglobin complexes do not participate in the formation and maintenance of stable, E-cadherin–mediated cell-cell contacts in MDCK cells. Additionally, plakoglobin and E-cadherin do not co-localize in the TX-100 insoluble fraction (Fig. 3: "Extracted"; and Fig. 4). The lack of E-cadherin/plakoglobin complexes in the TX-100 insoluble pool may represent disassembly of plakoglobin and exchange with β–catenin (see also Hinck *et al.*, 1994a). Alternatively, the E-cadherin/plakoglobin complex may be degraded more rapidly than the E-cadherin/β–catenin complex resulting in the accumulation of only the latter. Note that plakoglobin is principally involved in cell adhesion through desmosomes (Fig. 7) (Cowin *et al.*, 1986). It is possible that binding of plakoglobin to desmosomal cadherins (desmoglein, desmocollin) is more stable than plakoglobin binding to E-cadherin. Differences in the affinity of plakoglobin and β–catenin for different cadherins may be responsible for sorting of these proteins to

UCSF LIBRARY

either the *zonula* (ZA; E-cadherin/β–catenin) or *macula adherens* (MA; desmoglein/plakoglobin), as discussed below (Fig. 7).

Complexes containing α–catenin and plakoglobin or β–catenin, but not E-cadherin were detected in cadherin–depleted cell extracts. Microscopy analysis demonstrated that E-cadherin independent pools of α–catenin and β–catenin are localized in the lateral membrane below the apical junctional complex of TX-100 extracted cells. In addition, α–catenin, β–catenin and plakoglobin are distributed throughout the cell in the TX-100 soluble pool. These data confirm the existence of cadherin-independent pools of catenins that were identified in the preceding paper (Hinck *et al.*, 1994a). The fact that these pools of catenins accumulate at steady state shows that they are not assembly intermediates or incorrectly processed proteins. Possible functions of these complexes will be discussed below.

Different spatial distributions of cadherin/catenin complexes and functions in cellular organization

Microscopy observations define the distributions of cadherin/catenin and catenin complexes in both the TX-100 soluble and insoluble fractions. There are three principal locations: throughout the cell; along the lateral membrane below the apical junctional complex; and, at the apical junctional complex (Fig. 7). We propose that these distributions are related to specific functions.

All three catenins were distributed throughout the cell interior in patterns that were different from that of E-cadherin (Fig. 7). These intracellular pools of catenins were completely extracted from cells with TX-100. Biochemically, we showed that these

UCSF LIBRARY
UCSF LIBRARY

pools contain α–catenin/β–catenin and α–catenin/plakoglobin complexes. It is also possible that pools of individual catenins are present. We showed by sucrose gradient analysis of proteins extracted from cells with TX-100 that a portion of α–catenin is not associated with either E-cadherin, plakoglobin or β–catenin; this may represent an individual pool of α–catenin (Hinck *et al.*, 1994a). We propose two functions for these intracellular pools of catenins. First, intracellular pools of catenins may provide reservoirs for the exchange and assembly of the catenins that were proposed in the preceding paper to participate in regulating the assembly of cadherin/catenin complexes (Hinck *et al.*, 1994a). Second, intracellular pools of catenins may bind to other proteins (Fig. 7). We do not know if these cadherin–independent pools of catenins are cytosolic, or whether they are associated with cytoskeletal components or membrane organelles. It is interesting to note that the product of a tumor suppresser gene, APC, forms a cytosolic complex with α–catenin and β–catenin that is independent of cadherin (Rubinfeld *et al.*, 1993, Su *et al.*, 1993). Such interactions may play a role in sequestering catenins to prevent them from binding to cadherins, or linking other proteins to signaling pathways common to cadherins.

A second location for E-cadherin/catenin, and catenin complexes is the lateral membrane (Fig. 7). In addition to roles in maintaining cell-cell contacts, we suggest that each of these complexes play at least one other role. The cadherin/catenin complex provides a link between cell adhesion molecules, the cytoskeleton and other integral membrane proteins that is important in generating polarized distributions of proteins to the lateral plasma membrane. For example, Na^+/K^+-ATPase is restricted to the lateral membrane upon induction of E-cadherin–mediated cell adhesion. The common link between the cadherin/catenin complex and Na^+/K^+-ATPase is the membrane cytoskeleton, which is composed of ankyrin and spectrin (Nelson *et al.*, 1990). When linkage of the cadherin/catenin complex to the cytoskeleton is lost, Na^+/K^+-ATPase

UCSF LIBRARY

remains uniformly distributed over the cell surface (McNeill *et al.*, 1990). The cadherin independent pools of catenins may function through binding to other membrane proteins (Fig. 7). In the preceding paper we demonstrated by chemical cross-linking that five other proteins are part of the cadherin/catenin complex (Hinck *et al.*, 1994a). Although unidentified as yet, these proteins may bind catenins directly. Recently, other membrane proteins have been identified in association with catenins, including desmosomal cadherins (Korman *et al.*, 1989) and the EGF receptor (Näthke, Hinck, Papkoff and Nelson, unpublished result). Linkage of catenins to these membrane proteins, which are located on the lateral membrane of polarized epithelial cells (Brändli *et al.*, 1991), may play a role in regulating receptor distribution through binding of these proteins to the cytoskeleton, similar to a mechanism for localizing Na^+/K^+-ATPase to the lateral membrane (see above). In addition, since growth factor receptors are involved in transducing mitogenic responses, their association with catenins may also indicate a role for catenins in this signal transduction pathway (see also Hinck *et al.*, 1994a).

The highest concentration of E-cadherin, α–catenin and β–catenin in TX-100 extracted cell is in the region of the apical junctional complex. There are several reasons for the concentration of cadherin/catenin complexes at this location. The apical junctional complex contains the tight junction which requires cadherin–mediated cell adhesion and actin filament organization for formation and regulation (Madara, 1987). The apical junctional complex is also the site for organization of a circumferential ring of actin filaments (Fig. 7) (Wessels *et al.*, 1971). It has been proposed that actin filaments and the apical junctional complex are important in morphogenetic movements of cells through a "purse string" type contractile action (Wessels *et al.*, 1971). Several actin accessory proteins have been identified in the apical junctional complex where it is thought that they play a role in actin filament organization (Tsukita *et al.*, 1992, Tsukita *et al.*, 1993). E-cadherin/catenin complexes that localize to the apical junctional complex

UCSF LIBRARY
UCSF LIBRARY

may interact directly or indirectly with these molecules to regulate the assembly of the cytoskeleton at this location and maintain the structural integrity at cell-cell interactions during changes in actin filament organization.

Members of the src family of protein kinases, c-src and c-yes, are also localized at the apical junctional complex (Fig. 7) (Tsukita *et al.*, 1991, Tsukita *et al.*, 1993). The mechanism of localization, and function of these tyrosine kinases are unknown. One possibility is that they regulate the function of the E-cadherin/catenin complex (Matsuyoshi *et al.*, 1992, Behrens *et al.*, 1993). Overexpression of v-src leads to a decrease in cell adhesion and correlates with an increase in the level of tyrosine phosphorylation of the proteins in the cadherin/catenin complex, particularly β–catenin (Matsuyoshi *et al.*, 1992, Behrens *et al.*, 1993). We do not know whether these tyrosine kinases are activated by another protein to phosphorylate the cadherin/catenin complex, or if the cadherin/catenin complex itself can activate src kinases. Together these observations indicate that, in addition to its structural role, the apical junctional complex has important regulatory functions. It is interesting to note that the enrichment of E-cadherin and catenins at the apical junctional complex is only observed in cells that have been growing in confluent monolayers for >5 days. In cells grown in confluent monolayer for 5 days or less, the distribution of E-cadherin, α–catenin and β–catenin is still uniform throughout the lateral membrane of TX-100 extracted cells (Näthke and Swedlow, unpublished data). Lateral membrane localization of cadherins and catenins may be related to cell adhesion and organization of membrane proteins that are initiated immediately following cell contact and recognition. Complete development of the apical junctional complex may require longer and is involved in specialized structural and regulatory functions of the epithelium.

UCSF LIBRARY

In summary, cadherin-mediated cell-cell adhesion initiates a cascade of intracellular events that leads to the structural and functional reorganization of cells, including: formation of junctional complexes; organization of the actin cytoskeleton at the apical junctional complex; assembly of the membrane cytoskeleton; and development of membrane domains (Rodriguez-Boulan and Nelson, 1989, Nelson, 1992). We speculated that there is either a single cadherin/catenin complex involved in initiating all of these events, or that there are multiple complexes each of which initiate a single event. Our data show that there are multiple cadherin/catenin, and catenin complexes that have different distributions in the cell.

Acknowledgments: We thank Drs. David A. Agard and John W. Sedat for our use of their wide field optical sectioning microscope and image processing software. We also thank Dr. Dietmar Vestweber for providing antibodies against P-cadherin and Dr. James A. Marrs for providing the antibody against the cytoplasmic domain of E-cadherin. Inke S. Näthke was supported by a Cancer Research Fund of the Damon Runyon–Walter Winchell Foundation Fellowship, DRG-1171. Lindsay Hinck was the recipient of a Cancer Biology Predoctoral Fellowship. This work was supported by a grant to W. J. Nelson from the American Cancer Society, and in part by Syntex Corporation. W. J. Nelson was the recipient of an Established Investigator Award form the American Heart Association.

UCSF LIBRARY
UCSF LIBRARY

References:

Agard, D. A., Y. Hiraoka, P. Shaw and J. W. Sedat. 1989. Fluorescence microscopy in three dimensions. *Methods in Cell Biol.* 30:353-377.

Behrens, J., L. Vakaet, R. Friis, E. Winterhager, F. Van Roy, M. M. Mareel and W. Birchmeier. 1993. Loss of epithelial differentiation and gain of invasiveness correlates with tyrosine phosphorylation of the E-cadherin/β–catenin complex in cells transformed with a temperature-sensitive v-SRC gene. *J. Cell Biol.* 120:757-766.

Boller, K., D. Vestweber and R. Kemler. 1985. Cell adhesion molecule uvomorulin is localized in the intermediate junctions of adult epithelial intestinal cells. *J. Cell Biol.* 100:327-323.

Bradley, R. S., P. Cowin and A. M. C. Brown. 1993. Expression of Wnt-1 in PC12 cells results in modulation of plakoglobin and E-cadherin and increased cellular adhesion. *J. Cell Biol.* 123:1857-1866.

Brändli, A. W., E. D. Adamson and K. Simons. 1991. Transcytosis of epidermal growth factor. The epidermal growth factor receptor mediates uptake but not transcytosis. *J. Biol. Chem.* 266:8560-8566.

Butz, S., J. Stappert, H. Weissig and R. Kemler. 1992. Plakoglobin and beta-catenin: distinct but closely related [letter]. *Science* 257:1013-1176.

Cowin, P., H.-P. Kapprell, W. W. Franke, J. Tamkun and R. O. Hynes. 1986. Plakoglobin: a protein common to different kinds of intercellular adhering junctions. *Cell* 46:1063-1073.

UCSF LIBRARY
UCSF LIBRARY

Herrenknecht, K., M. Ozawa, C. Eckerskorn, F. Lottspeich, M. Lenter and R. Kemler. 1991. The uvomorulin-anchorage protein alpha-catenin is a vinculin homologue. *Proc. Natl. Acad. Sci. USA* 88:9156-9160.

Hinck, L., I. S. Näthke, J. Papkoff and W. J. Nelson. 1994a. Dynamics of cadherin/catenin complex formation: novel protein interactions and pathways of complex assembly. submitted.

Hinck, L., W. J. Nelson and J. Papkoff. 1994b. Wnt-1 modulates cell-cell adhesion in mammalian cells by stabilizing β–catenin binding to the cell adhesion protein cadherin. *J. Cell Biol.* in press.

Hiraoka, Y., J. R. Swedlow, M. R. Paddy, D. A. Agard and J. W. Sedat. 1991. Three-dimensional multiple-wavelength fluorescence microscopy for the structural analysis of biological phenomena. *Sem. Cell Biol.* 2:153-165.

Kemler, R. 1992. Classical cadherins. *Sem. Cell Biol.* 3:149-155.

Korman, N. J., W. E. Russell, M. D. Eyre, V. Klaus-Kovtun and J. R. Stanley. 1989. Demonstration of an adhering-junction molecule (plakoglobin) in the autoantigens of pemphigus foliaceus and pemphis vulgaris. *New Eng. J. Med.* 321:631-635.

Levoy, M. 1991. Display of surfaces from volume data. *In* Volume visualization. A. Kaufman, editor. ICEE Comp. Soc. Press, Washington. 135-143.

UCSF LIBRARY

Madara, J. L. 1987. Intestinal absorptive cell tight junctions are linked to cytoskeleton. *American J. Physiology* 253:C171-175.

Marrs, J. A., E. W. Napolitano, C. Murphy-Erdosh, R. A. Mays, L. F. Reichardt and W. J. Nelson. 1993. Distinguishing roles of the membrane-cytoskeleton and cadherin mediated cell-cell adhesion in generating different Na^+, K^+-ATPase distribution in polarized epithelia. *J. Cell Biol.* 123:149-164.

Matsuyoshi, N., M. Hamaguchi, S. Taniguchi, A. Nagafuchi, S. Tsukita and M. Takeichi. 1992. Cadherin-mediated cell-cell adhesion is perturbed by v-src tyrosine phosphorylation in metastatic fibroblasts. *J. Cell Biol.* 118:703-714.

McCrea, P. D., C. W. Turck and B. Gumbiner. 1991. A homolog of the *armadillo* protein in *Drosophila* (plakoglobin) associated with E-cadherin. *Science* 254:1359-1361.

McNeill, H., M. Ozawa, R. Kemler and W. J. Nelson. 1990. Novel function of the cell adhesion molecule uvomorulin as an inducer of cell surface polarity. *Cell* 62:309-316.

McNeill, H., T. A. Ryan, S. J. Smith and W. J. Nelson. 1993. Spatial and temporal dissection of immediate and early events following cadherin-mediated epithelial cell adhesion. *J. Cell Biol.* 120:1217-1226.

Nagafuchi, A. and M. Takeichi. 1988. Cell binding function of E-cadherin is regulated by the cytoplasmic domain. *EMBO J.* 7:3679-3684.

UCSF LIBRARY
UCSF LIBRARY

Nagafuchi, A. and M. Takeichi. 1989. Transmembrane control of cadherin-mediated cell adhesion: a 94Kd protein functionally associates with a specific region of the cytoplasmic domain of E-cadherin. *Cell Regul.* 1:37-44.

Nagafuchi, A., M. Takeichi and S. Tsukita. 1991. The 102 kd cadherin-associated protein: similarity to vinculin and posttranscriptional regulation of expression. *Cell* 65:849-857.

Nelson, W. J. 1992. Regulation of surface polarity from bacteria to mammals. *Science* 258:948-955.

Nelson, W. J., E. M. Shore, A. Z. Wang and R. W. Hammerton. 1990. Identification of a membrane-cytoskeletal complex containing the cell adhesion molecule uvomorulin (E-cadherin), ankyrin, and fodrin in Madin-Darby canine kidney epithelial cells. *J. Cell Biol.* 110:349-357.

Nusse, R. and H. E. Varmus. 1992. Wnt Genes. *Cell* 69:1073-1087.

Ozawa, M., H. Baribault and R. Kemler. 1989. The cytoplasmic domain of the cell adhesion molecule uvomorulin associates with three independent proteins structurally related in different species. *EMBO J.* 8:1711-1717.

Ozawa, M., M. Ringwald and R. Kemler. 1990. Uvomorulin-catenin complex formation is regulated by a specific domain in the cytoplasmic region of the cell adhesion molecule. *Proc. Natl. Acad. Sci. U S A* 87:4246-4250.

UCSF LIBRARY
UCSF LIBRARY

Riggleman, B., P. Schedl and E. Wieschaus. 1990. Spatial expression of the *Drosophila* segments polarity gene *armadillo* is posttranscriptionally regulated by *wingless*. *Cell* 63:549-560.

Rodriguez-Boulan, E. and W. J. Nelson. 1989. Morphogenesis of the polarized epithelial cell phenotype. *Science* 245:718-725.

Rubinfeld, B., B. Souza, I. Albert, O. Müller, S. H. Chamberlain, F. R. Masiarz, S. Munemitsu and P. Polakis. 1993. Association of the APC gene product with β–catenin. *Science* 262:1731-1734.

Su, L.-K., B. Vogelstein and K. W. Kinzler. 1993. Association of the APC tumor suppressor protein with catenins. *Science* 262:1734-1737.

Takeichi, M. 1991. Cadherin cell adhesion receptors as a morphogenetic regulator. *Science* 251:1451-1455.

Tsukita, S., M. Itoh, A. Nagafuchi, S. Yonemura and S. Tsukita. 1993. Submembranous junctional plaque proteins include potential tumor suppressor molecules. *J. Cell Biol.* 123:1049-1053.

Tsukita, S., K. Oishi, T. Akiyama, Y. Yamanashi, T. Yamamoto and S. Tsukita. 1991. Specific proto-oncogenic tyrosine kinases of src family are enriched in cell-to-cell adherens junctions where the level of tyrosine phosphorylation is elevated. *J. Cell Biol.* 113:867-879.

UCSF LIBRARY
UCSF LIBRARY

Tsukita, S., S. Tsukita, A. Nagafuchi and S. Yonemura. 1992. Molecular linkage between cadherins and actin filaments in cell-cell adherens junction. *Curr.Opin.Cell Biol.* 4:835-839.

Wessels, N. K., B. S. Spooner, J. F. Ash, M. O. Bradley, M. A. Ludena, E. L. Taylor, J. T. Wrenn and K. M. Yamada. 1971. Microfilaments in cellular and developmental processes. *Science* 171:135-143.

UCSF LIBRARY
UCSF LIBRARY

Figure legends:

Figure 1: Double staining of MDCK cells for E-cadherin and α–catenin. Confluent monolayers of MDCK cells were established on collagen–coated Transwell filters and maintained for 8 days in HCM. Growth medium was replaced daily. The cells were washed with PBS, 0.5mM $CaCl_2$ and either fixed with formaldehyde and extracted with CSK buffer ("Total") or extracted with CSK buffer and then fixed with formaldehyde ("Extracted"). Cells were labeled with a mouse monoclonal antibody against E-cadherin and affinity purified rabbit polyclonal antibodies against α–catenin followed by rhodamine conjugated anti-mouse and fluorescein conjugated anti-rabbit antibodies. Optical sections were recorded at 0.2 µm intervals. After removal of the out of focus information by deconvolution, three dimensional images were generated using a volume rendering algorithm and are displayed rotated at an angle of 10-15°. The bar in the lower right hand corner of the first panel represents 5 µm.

Figure 2: Double labeling of MDCK cells for E-cadherin and β–catenin. MDCK cells were treated as described in Figure 1 but they were double stained with affinity purified polyclonal antibodies against β–catenin and a mouse monoclonal antibody against E-cadherin.

Figure 3: Double staining of MDCK cells for E-cadherin and plakoglobin. As in Figures 1 and 2, but cells were double labeled with affinity purified rabbit polyclonal antibodies against plakoglobin and a mouse monoclonal antibody against E-cadherin.

Figure 4: Co-localization of E-cadherin and the catenins in extracted MDCK cells. Confluent monolayers of MDCK cells were maintained on collagen–coated Transwell filters for 8 days. Cells were extracted with TX-100 containing buffer and fixed with formaldehyde. They were stained with both mouse monoclonal antibodies against E-

UCSF LIBRARY

UCSF LIBRARY

cadherin and affinity purified rabbit polyclonal antibodies against α–catenin, β–catenin or plakoglobin as indicated. To detect the primary antibodies, secondary antibodies coupled to rhodamine (E-cadherin) or FITC (catenins) were used. Staining for E-cadherin is indicated by purple, staining for catenins is shown in green and overlapping areas are indicated by white. Individual optical sections from either the middle of the cells (6-6.5 µm above the substratum) or the apical junctional complex (8.4-10 µm above the substratum) are displayed.

Figure 5: The composition of E-cadherin/catenin complexes in the TX-100 soluble and insoluble pool at steady state. Confluent monlayers of MDCK cells were maintained on collagen–coated Transwell filters for 8 days. They were cross-linked with the reducible cross-linking reagent DSP and harvested in TX-100 containing lysis buffer. Soluble (S) and insoluble (P) fractions were immunoprecipitated (IP) with antibodies against E-cadherin (E-cad), α–catenin (α–cat), β–catenin (β–cat), and plakoglobin (PG). Each immunoprecipitate was subjected to SDS-PAGE and transferred to Immobilon-P membranes for immunoblotting (Blot) with the same panel of antibodies (Panel A: E-cadherin immunoblot; Panel B: α–catenin immunoblot; Panel C: β–catenin immunoblot; Panel C: Plakoglobin immunoblot). Molecular weight standards (116, 97, and 68 kD) are indicated on the left.

Figure 6: Catenins associate with each other in an E-cadherin independent pool in the TX-100 soluble and insoluble fractions. Confluent monolayers of MDCK cells were maintained on collagen–coated Transwell filters for 8 days. They were cross-linked with the reducible cross-linking reagent DSP and TX-100 soluble (S) and insoluble (P) fractions were harvested. Each fraction was sequentially immunoprecipitated with antibodies against cadherin six times. The immunoprecipitated material from each cycle (#1-6) was subjected to SDS-PAGE, transferred to Immobilon-P membranes and immunoblotted with antibodies to cadherin to establish that cadherin had been removed (Panel A). One fraction of the

UCSF LIBRARY
UCSF LIBRARY

remaining lysates was subjected to SDS-PAGE and immunoblotted with antibodies against E-cadherin (E-cad and 3G8), P-cadherin (P-cad 1 and 2), α–catenin (α–cat), β–catenin (β–cat), and plakoglobin (PG) (Panel B). Another fraction of the remaining lysates was immunoprecipitated (IP) with antibodies against plakoglobin (PG) or β–catenin (β–cat). The immunoprecipitated material was separated by SDS-PAGE, transferred to Immobilon-P membranes and immunoblotted (Blot) with antibodies against α–catenin (α–cat) (Panel C).

The identity of the lower molecular weight protein that is reactive with antibodies against E-cadherin in Panel B is not known. The lower molecular weight proteins that are detected by immunoblotting TX-100 soluble extracts with the monoclonal antibody 3G8 against E-cadherin (Panel B) are background bands that are non-specifically bound by the rabbit-anti-mouse secondary antibody used for the detection of the primary, mouse monoclonal antibody with ^{125}I-protein A (see Materials and Methods).

Figure 7: Subcellular distribution of different cadherin/catenin complexes in completely polarized MDCK cells. Complexes containing E-cadherin, α–catenin and β–catenin are distributed throughout the lateral plasma membrane (Lateral-PM). In TX-100 extracted cells, the concentration of these complexes is highest at the apical junctional complex (AJ, indicated by the shaded box). This region contains the *zonula adherens* and the *zonula occludens*. Also shown is the belt of actin filaments at the apical junctional complex. The triangle depicted at the apical junctional complex represents actin accessory proteins as well as tyrosine kinases which are concentrated at this site (see text).

Both α–catenin and β–catenin bind to the lateral membrane independently of E-cadherin in the TX-100 insoluble fraction. They associate with unknown membrane proteins, denoted by "Y". We cannot formally exclude the possibility that α–catenin and β–catenin associate with "Y" individually. Plakoglobin does not associate with E-cadherin in the TX-100 insoluble fraction but it is found in desmosomes (*macula adherens*, MA) in association with desmosomal cadherins like desmoglein. The association of plakoglobin

UCSF LIBRARY
UCSF LIBRARY

with E-cadherin in the TX-100 soluble fraction is not shown here because the localization of these complexes was not investigated. In the TX-100 soluble fraction α–catenin is free or bound to either β–catenin or plakoglobin with or without cadherin. Catenin complexes also associate with other cytosolic proteins denoted by “X”. One candidate for “X” is the APC protein (see text).

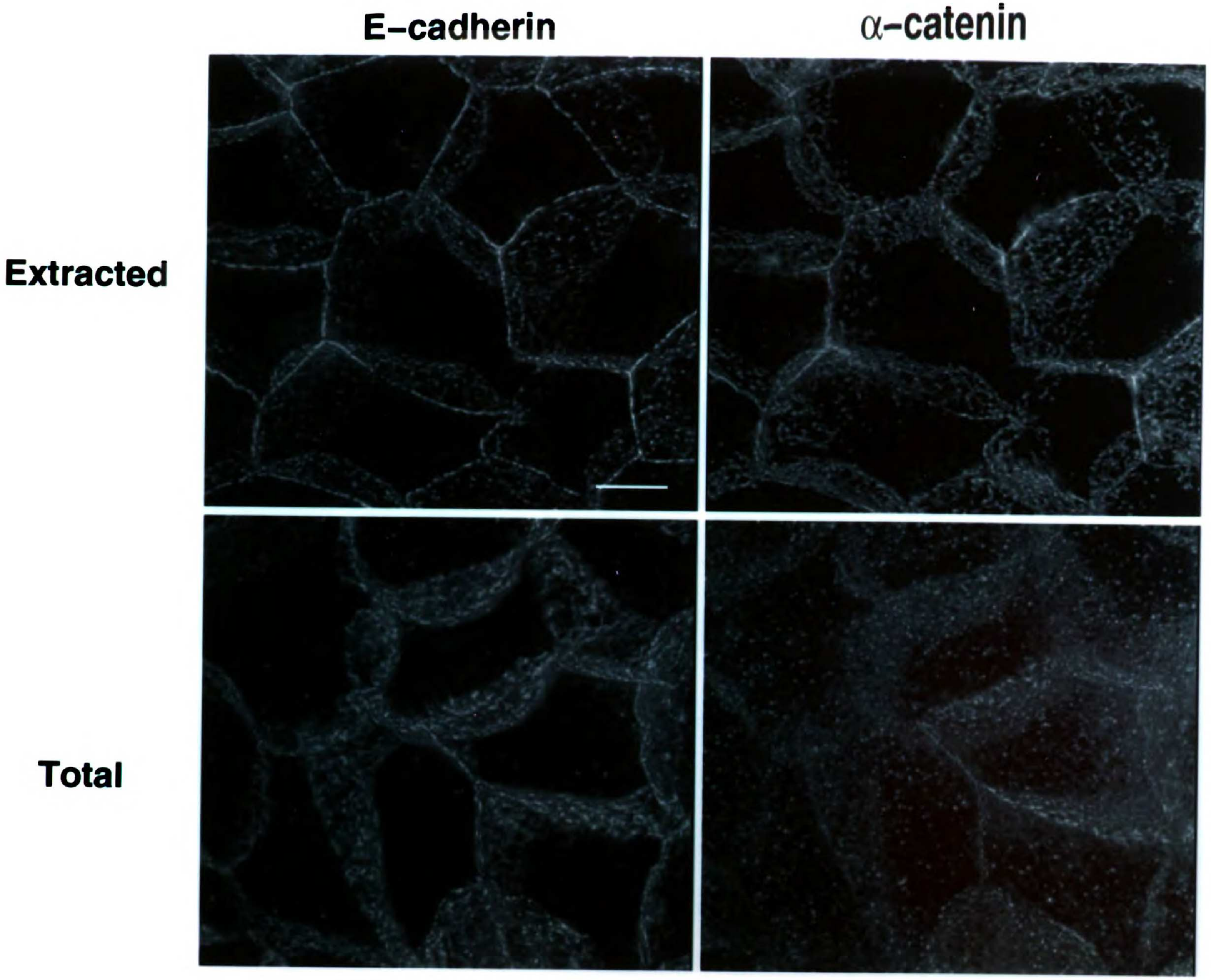
E–cadherin
α–catenin
Extracted
Total

UCSF LIBRARY
UCSF LIBRARY

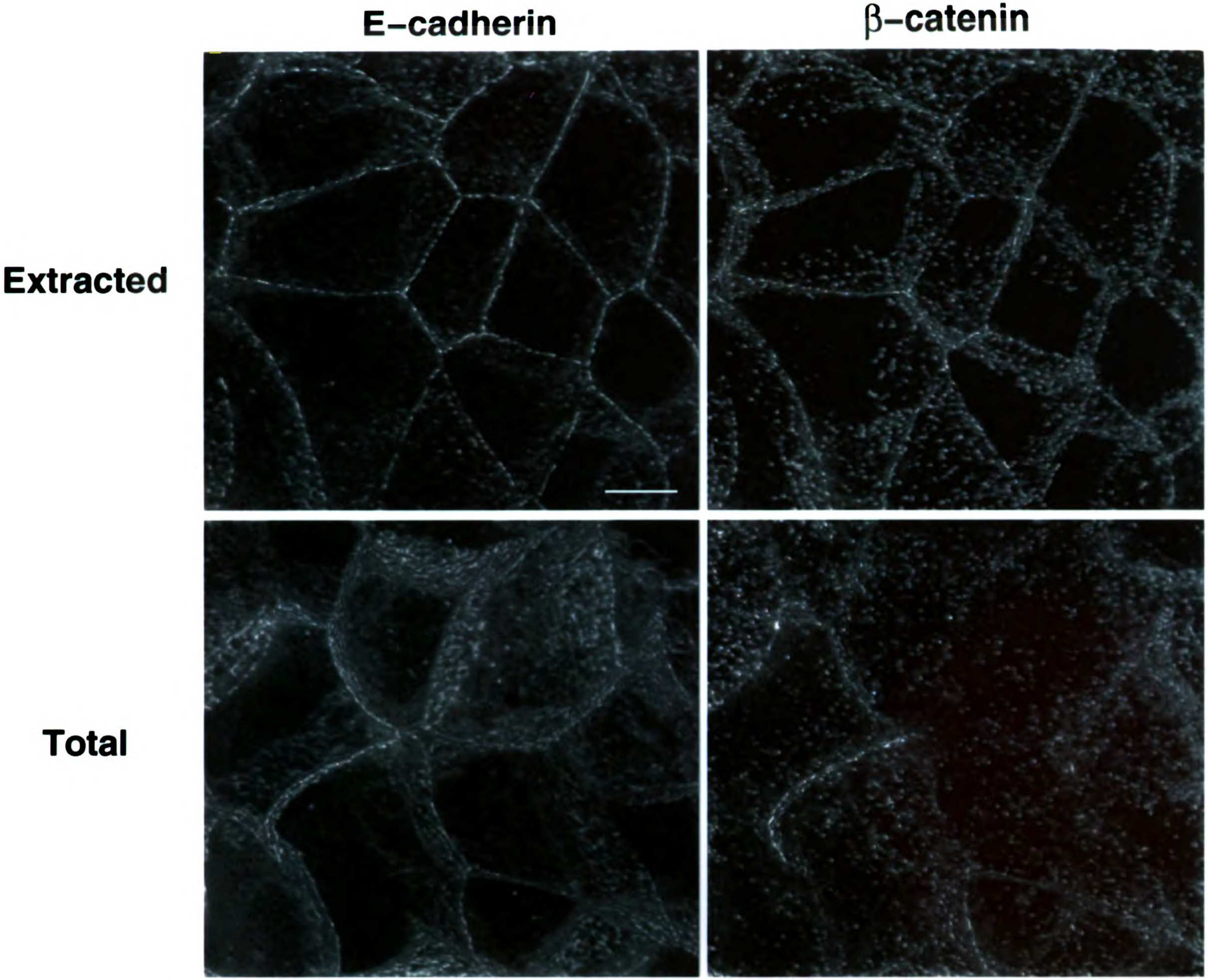
E–cadherin
β–catenin
Extracted
Total

UCSF LIBRARY
UCSF LIBRARY

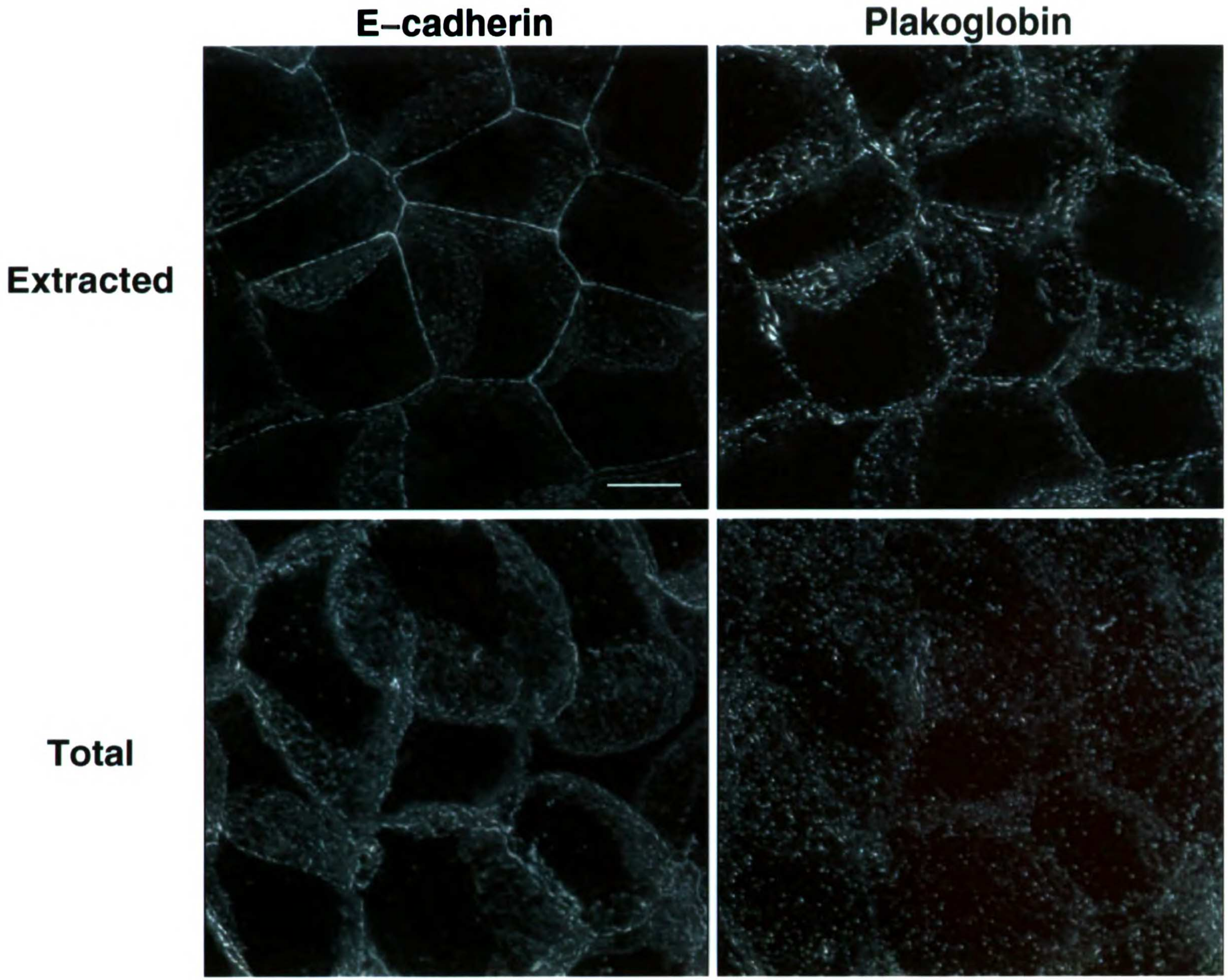
E–cadherin
Plakoglobin
Extracted
Total

UCSF LIBRARY
UCSF LIBRARY

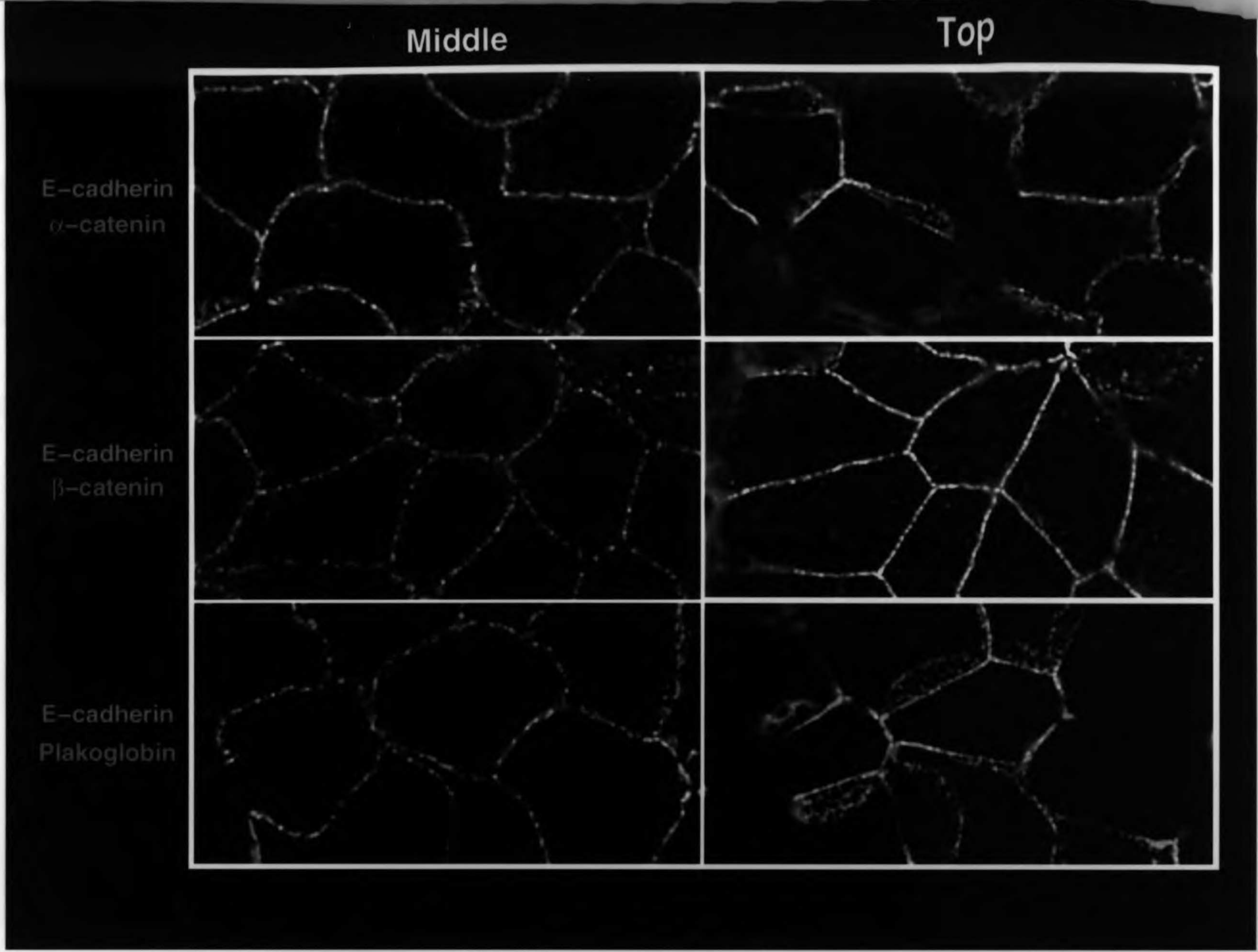
Middle
Top
E–cadherin
α–catenin
E–cadherin
β–catenin
E–cadherin
Plakoglobin

UCSF LIBRARY

11 36R

UCSF LIBRARY

UCSF LIBRARY

For reference

Not to be taken from the room.

629761

3 1378 00629 7611